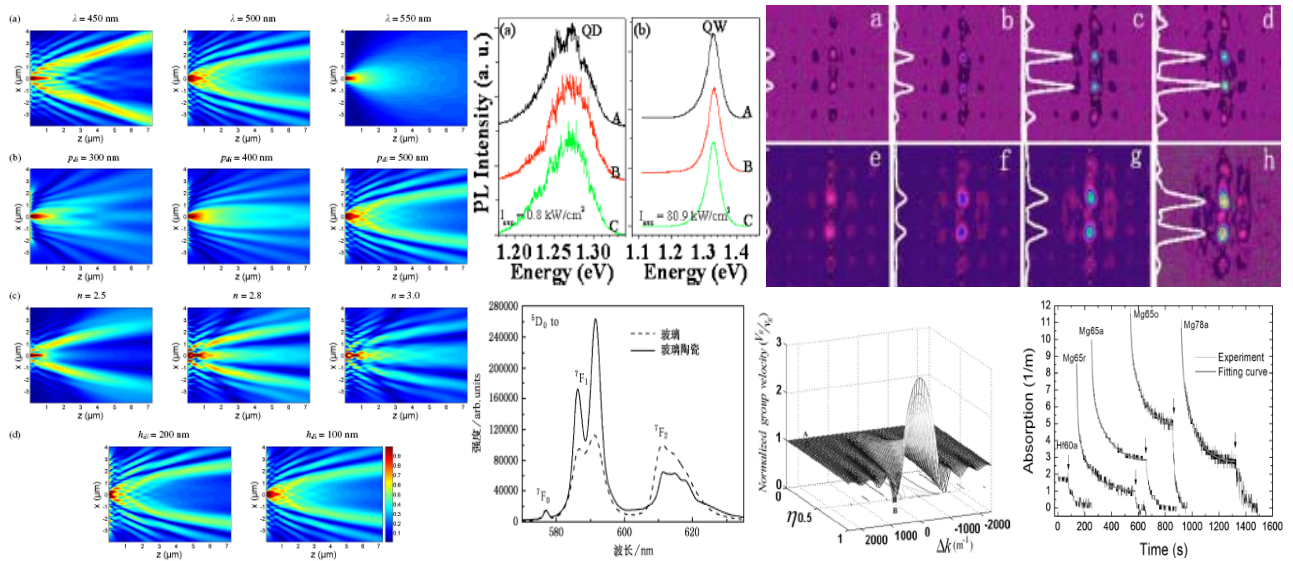


Annual Report 2006



南开大学弱光非线性光子学

教育部重点实验室

Annual Report 2006

The Key Laboratory of Weak Light Nonlinear Photonics,
Ministry of Education



南开大学弱光非线性光子学
教育部重点实验室

- ▼ 英国伦敦国王学院物理系 Klaus Suhling 博士来实验室进行学术交流。

(2006.6.4-5)



- ▶ 美国阿肯色大学物理系肖敏教授来实验室进行短期工作访问并做学术报告。

(2006.6.23-25)



- ◀ 乌克兰国家科学院 Svetlana Bugaychuk 研究员对实验室进行工作访问并探讨了长期合作问题。

(2006.8.21-9.3)

▶▶ 甘子钊院士为组长的专家组对实验室的建设工作进行验收，专家组听取了实验室主任许京军教授的实验室建设总结报告。
(2006.11.18)



▼ 美国马里兰大学 Wendell T. Hill III 教授对实验室进行工作访问并做学术报告。
(2006.11.25)



- ▼ 实验室召开年度学术研讨会，实验室主任及各方向负责人作了年度工作总结报告及学术报告。

(2006.12.30)



目 录

实验室概况/Overview of the Laboratory of Weak Light Nonlinear Photonics.....	1
人员结构/Organization	2
承担课题/Projects under Researching.....	5
仪器设备/Facilities	9
研究报告/Scientific Report.....	10
专利/Patents	15
发表论文/Publications in Journal	16
国际合作与交流/International Cooperation and Exchange.....	22
国内、国际会议报告/Talks at Conferences	24
主办/协办国内、国际会议/Conferences Sponsored by the Laboratory.....	26
学术组织与期刊任职/Academic Service	27
获奖情况/Awards & Honors.....	28
学位论文/Dissertations.....	29
选录论文/Selected Papers.....	31

实验室概况/Overview of the Laboratory of Weak Light Nonlinear Photonics

本实验室主要由非线性物理与光子技术、光子学材料及先进制备技术、弱光非线性及量子相干光学、光谱表征及传感技术、半导体生长技术和半导体器件等五个方向组成，有研究人员 50 人，专职技术人员 4 人。其中教育部长江奖励计划特聘教授 2 名，国家杰出青年基金获得者 3 人，天津市授衔专家称号获得者 2 人，首批新世纪百千万人才工程国家级人选 1 人，教育部跨世纪/新世纪优秀人才支持计划获得者 8 人，教育部优秀青年教师资助计划入选者 2 人。团队获得教育部“长江学者和创新团队发展计划”创新团队基金资助。

2006 年实验室共承担“973”计划，“863”计划，国家自然科学基金等各类科研基金 44 项，总经费达近一千万元。共发表论文 83 篇，申请国家发明专利 5 项，获得国家发明专利 2 项。获得天津市技术发明奖二等奖 1 项（2006 年），国家自然科学基金二等奖 1 项（2005 年），许京军教授获得第六届“中国青年科学家奖”（2006 年）。

实验室和国内外学术界开展了广泛的合作与交流，邀请了美国、英国、日本和乌克兰等国家和地区的学者来实验室讲学，有 8 人次出国访问或者进行合作研究。主办/协办 SPIE Photonics West Conference，中国物理学会 2006 年秋季学术会议，第十三届全国凝聚态物质光学性质学术会议等国际国内学术会议，在国际国内学术会议上作报告 29 人次，其中孔勇发教授在第十三届全国凝聚态物质光学性质学术会议作大会报告。宋峰、孔勇发、孙骞等多名教授在国内各种学术组织中担任职务，许京军、张国权、孔勇发、孙骞等教授在多种国际国内学术刊物担任编委。

实验室目前有在读博士生 60 人，在读硕士生 149 人。2006 年共有 16 人获得博士学位，29 人获得硕士学位。其中博士生任相魁获得 2006 年全国博士论坛优秀论文奖，薄方获得泰达奖教金优秀学生奖一等奖，有多名研究生获得南开大学奖学金。

实验室在 2006 年共引进各类人才 6 名。

人员结构/Organization

实验室主任/Director

许京军 教授

实验室副主任/Deputy Directors

张国权 教授

孙 骞 教授

学术秘书/Academical Secretary

禹宣伊 副教授

研究方向负责人/Research Group Leaders

弱光非线性及量子相干光学 许京军 教授

非线性物理与光子技术 田建国 教授

光子学材料及先进制备技术 孔勇发 教授

光谱表征及传感技术 臧维平 教授

半导体生长技术和半导体器件 舒永春 教授

学术委员会/Academic Committee

主任/Chairman

王占国 院士

委员/Committee Members

沈德忠 院士

薛其坤 院士

姚建年 院士

陈志刚 教授

龚旗煌 教授

陆 卫 研究员

田建国 教授

王慧田 教授

徐现刚 教授

许京军 教授

许宁生 教授

资 剑 教授

外籍学术顾问委员

D. Kip 教授 德国 Cauthburge 大学

L. Hessenlink 教授 美国斯坦福大学物理系

R. A. Rupp 教授 奥地利维也纳大学实验物理所

T. Volk 教授 俄罗斯国家晶体研究所

Y. Tomita 教授 日本电气通信大学

杰出人才/Intelligent Staff

教育部“长江奖励计划”特聘教授

1999 许京军

2006 陈志刚

国家杰出青年基金获得者

1998 许京军

2001 田建国

教育部“优秀青年教师资助计划”入选者

2002 张国权

2003 宋 峰

教育部“跨世纪优秀人才培养计划”入选者

1998 许京军

2000 田建国

2001 孙 骞

2002 孔勇发

教育部“新世纪优秀人才支持计划”入选者

2004 张国权

2004 宋 峰

2005 臧维平

2005 李宝会

首批新世纪百千万人才工程国家级人选

2004 田建国

国家海外青年学者合作研究基金获得者

2005 陈志刚

“天津市授衔专家”称号获得者

2005 许京军

2005 田建国

教育部“长江学者和创新团队发展计划”创新团队基金资助

弱光非线性光子学重点实验室人员名录/Name List

研究人员/Scientific Staff (50 人)

王占国 张光寅 许京军 田建国 Romano A. Rupp 陈志刚 张国权 孔勇发 刘思敏
 郭儒 孙骞 宋峰 臧维平 舒永春 徐章程 姚江宏 赵丽娟 刘士国 张玲
 李宝会 朱箭 李任植 曹亚安 张春平 孙甲明 张天浩 李玉栋 徐晓轩 张心正
 周文远 乔海军 曹学伟 邢晓东 禹宣伊 余华 吴强 孙同庆 武莉 楼慈波
 高峰 唐柏权 刘智波 李祖斌 范万德 李乙刚 丁镭 冯鸣 张万林 冯敏

技术人员/Technical Staff (4 人)

黄自恒 陈绍林 马玉祥 梁建

博士生/Ph.D Students (60 人)

高峰 申岩 楼慈波 高垣梅 黄春福 高国祥 蔡卫 刘建彬 祁轶舫 唐莉勤
 孙立萍 薄方 付博 涂燕飞 潘雷霆 朱登松 李威 王振华 李俊 宋道宏
 胡毅 刘照红 柳永亮 刘玮 杨光 李福新 陈树琪 叶青 孙美秀 程化
 郝召锋 鄢小卿 李林枫 张冰 刘智波 李祖斌 温宏胜 阎文博 王文杰 曹永强
 刘宏德 李晓春 张冠杰 皮彪 贾国治 舒强 刘如彬 施曙东 于小晨 任相魁
 吴朝晖 苏静 刘淑静 韩琳 杨嘉 黄春福 高垣梅 林海波 武中臣 杨秀芹

硕士生/M.S. Students (149 人)

王铁铮 车蔚玥 董嵘 宋涛 曲迪 朱楠 殷长秋 鄢飞润 刘龙昌 杨程亮
 许宁宁 王慎之 钱学波 刘祥明 刘海旭 陈聪 韩彬 王喆 王俊俏 石艳丽
 陈楠 陈星宇 边飞 齐新元 周立鹏 李源 刘莹莹 郭磊 冯蕾 贾峰
 荣华 胡志健 王恒 白香港 邵伟伟 徐玉惠 刘宇 钱坤 王秉慧 吴超
 刘春锋 王文娟 孟扬 潘立彬 杨一宏 付世鹏 邢冲 张力舟 张校亮 李行
 安保国 贺珍妮 南晓宇 朱宝刚 潘君成 张森 张婷 彭灏 宋宇 孙磊
 赵迪 王占银 闫卫国 周斌斌 李剑韬 李树奇 孙亮 胡茜 窦树岗 陈喜杰
 王磊磊 董江舟 袁继翔 刘刚 詹鹤 吕玮 于晓明 孙建成 肖罗生 吴日雯
 安亚南 林军海 王超 宁海波 王艳丽 张雅婷 张玲 马晓明 张兰兰 赵路松
 王玲玲 翟晓辉 王恩君 王栋栋 王淑香 陈天琳 方扩军 谈绍峰 王红旗 赵艳军
 吴胜青 赵延雷 叶志诚 陈晨 崔楠 罗青青 薛亮平 刘国梁 陈琳 李丹
 柏天国 王影 刘志伟 张雁 程振洲 李腾 曲菲菲 王青如 侯春宵 宋令枝
 李俊梅 弭志强 刘宝荣 孙健 邹万芳 伍雁雄 闫立华 苏瑞渊 蔡虹 邹昌光
 田彬 张鑫 宋杰 陈凯 周凯迪 孙秀峰 范伟 杨威 朱楠 宋涛
 杨大鹏 张攀 曲迪 尹美荣 李奇楠 梁兴 祁国春 杨正广 梅灿

承担课题/Projects under Researching

序号	项目名称	项目来源	起止时间	负责人
1	有机化合物给体受体间弱相互作用光学非线性的研究	973 项目	2004.10-2006.10	田建国
2	光泵浦 1064nm 半导体垂直外腔表面发射激光器芯片材料的制备	863 项目	2006.12-2008.12	舒永春
3	光波相位耦合过程中的光速变化问题的研究	国家自然科学基金	2004.1-2006.12	张国权
4	非相干光的非线性光学效应研究	国家自然科学基金	2004.1-2006.12	刘思敏
5	新型结构高活性的纳米 TiO ₂ 可见光催化剂的制备	国家自然科学基金	2005.1-2007.12	曹亚安
6	半导体量子点激光材料瞬态光谱特性及超快现象研究	国家自然科学基金	2005.1-2007.12	姚江宏
7	光感应阵列波导中的分立衍射与分立孤子	国家自然科学基金	2005.1-2007.12	刘思敏
8	掺镁铌酸锂光学微结构级联二阶非线性频率变换的研究	国家自然科学基金	2006.1-2007.1	陈云琳
9	光强与时间控制的光学图像和信息处理器件的原理及技术研究	国家自然科学基金	2006.1-2008.12	张春平
10	光感应二维非线性光子晶体及其性能的研究	国家自然科学基金	2006.1-2008.12	孔勇发
11	卟啉有机超分子激发态光学非线性研究	国家自然科学基金	2006.1-2008.12	田建国

12	高活性可见光催化剂界面光生电荷转移的原位瞬态分析	国家自然科学基金	2006.1-2008.12	曹亚安
13	980nm InGaAs 亚单层量子点激光器	国家自然科学基金	2006.1-2008.12	徐章程
14	用宽带荧光上转换飞秒时间分辨光谱技术研究 CdS 纳米体系中超快弛豫过程	国家自然科学基金	2006.1-2008.12	赵丽娟
15	基于一维光自带隙结构的光限制效应研究	国家自然科学基金	2007.1-2009.12	臧维平
16	弱关联光子晶格体系中飞秒光传播特性及其导致的非线性光学效应	国家自然科学基金	2007.1-2009.12	吴强
17	光耦合过程的色散效应及光速变化的研究	教育部科学技术研究重点项目	2004.1-2006.12	张国权
18	空间光孤子与光子微结构的相互作用及其应用	海外杰出青年基金	2004.1-2006.12	陈志刚
19	砷酸锂晶体光子学基质平台的研究	教育部跨世纪优秀人才培养计划基金	2003.1-2007.12	孔勇发
20	弱关联光子学晶格体系中光波传播特性的研究	教育部新世纪优秀人才支持计划	2005.1-2007.12	张国权
21	稀土掺杂材料的发光与激光特性的研究	教育部新世纪优秀人才支持计划	2005.1-2007.12	宋峰
22	非线性光学机制研究	教育部新世纪优秀人才支持计划	2006.1-2008.12	臧维平
23	近红外有机/无机量子点复合材料和器件	教育部新世纪优秀人才支持计划	2006.1-2008.12	徐章程
24	激光二极管泵浦的自适应固体激光器的研究	教育部优秀青年教师资助计划	2004.1-2006.12	宋峰
25	医用生物芯片检测分析系统的研究与开发	天津市科技发展计划	2003.4-2006.4	田建国

26	多功能高分辨率 OCT 成像系统	天津市科技发展计划	2005.4-2007.12	田建国
27	高增益短长度光纤器件的研究	天津市攻关培育项目	2005.1-2007.12	宋峰
28	光泵浦 980nm 半导体垂直外腔表面发射激光器芯片的制备	天津市重点基金项目	2006.4-2008.12	舒永春
29	若干新型弱光非线性效应及其应用的研究	天津市国际科技合作项目	2006.4-2009.3	张国权
30	弱光非线性光学新效应和机制	天津市科技创新能力与环境建设平台项目	2006.7-2009.6	孙骞
31	双相掺杂高活性纳米 TiO ₂ 可见光催化剂制备的研究 (043612411)	天津市自然科学基金	2004.4-2006.12	曹亚安
32	混合光限制器的理论和实验研究	天津市自然科学基金	2004.4-2006.12	臧维平
33	长江学者启动基金	985	2006.3-2009.2	陈志刚
34	钽酸锂晶体的非挥发双色全息存储研究	教育部留学回国人员启动基金	2003.8-2006.8	张国权
35	高增益玻璃光学特性的研究	国家留学回国基金	2005.1-2006.12	宋峰
36	InGaAs/GaAs 亚单层量子点的分子束外延生长	教育部留学回国人员科研启动基金	2005.1-2007.12	徐章程
37	熔体注入法生长近化学比铌酸锂的工艺研究	横向课题	2005.10-2006.10	孔勇发
38	高品质铌酸锂晶棒产业化工艺研究	横向课题	2005.10-2006.10	刘士国
39	钽酸锂晶体的生长技术研究	横向课题	2005.10-2006.10	张玲

40	InGaAs/GaAs 亚单层量子点的光学性质	中科院上海技物所红外物理国家重点实验室开放课题	2005.10-2007.10	徐章程
41	高直流电导钽 / 铌酸锂晶片制备技术研究	南开大学创新基金	2005.4-2006.12	张玲
42	新型非线性光学晶体五磷酸镧二钾的生长与性质研究	南开大学创新基金	2005.4-2006.12	孙同庆
43	无动态扫描傅立叶变换光谱技术的研究与开发	南开大学创新基金	2005.4-2006.12	周文远
44	掺铈铌酸锂晶体抗光折变性能研究	南开大学创新基金	2006.12-2008.12	刘士国

仪器设备/Facilities

仪器设备名称	规格型号	购置时间
激光器工作站	899-29	2005.09
飞秒激光器	VF-T2S	2000.08
皮秒激光器	PY61	2003.11
纳秒激光器	Panther OPO	2003.11
光纤激光器	PLY-20-M	2003.11
可调频再生放大器	Spitfire F-1K	2000.04
时间分辨光谱及瞬态吸收光谱系统	Spectrapro.300i	2000.04
光谱分析仪	AQ6315A	2005.09
显微拉曼光谱仪	MKI2000	1998.09
分子速外延生长炉	Riber Compact 21T	2003.09
提拉法晶体生长炉	研制	2002.04
晶体切割研磨抛光系统	Logitech 系列	2001.06
扫描探针显微镜	Nanoscope IIIa	2006.08

注：除开放基金外，所有仪器设备均为有偿使用

研究工作报告/Scientific Report

非线性物理与光子技术/Nonlinear Physics and Photonics Techniques

负责人：田建国

1. 有机及超分子材料光学非线性研究

相对于传统的有机化合物，超分子材料不仅有着更丰富的结构形式，而且是一种可编程的、动态的、组合的材料，从而可以提供更为灵活地改善材料光学非线性的途径。首先，通过对卟啉自组装分子结构的光学非线性的研究，发现卟啉自组装结构中配位溶剂吡啶的添加会引起非线性吸收的提高，而锌原子对卟啉的金属化导致了非线性折射的剧烈变化；其次，我们通过三种不同溴化的锌卟啉与吡啶之间的动态平衡过程实现了对非线性吸收的精细调整，即利用超分子的动态概念获得了对卟啉光学非线性在一定范围内的控制。

2. 周期性亚波长结构的光学性质的研究

我们在原有的金属小孔凹槽结构的基础上，引入周期调制介质膜和周期排列介质突起，提出了两种新的亚波长狭缝结构，研究了这些新结构的增强透过效应及准直光束发射和方向性光发射效应，并对这些效应提出了理论分析。引入介质结构的意义在于当对于直接在金属表面制备的结构，介质结构更容易加工，并且可以获得更好的增强透过效果。分析了凹槽周期性在亚波长狭缝增强透过现象中的作用。发现凹槽周期性不是增强透过现象的必要条件，在非周期凹槽的作用下同样得到了增强透过现象；凹槽周期性是获得强的增强效果的充分条件。在近似周期凹槽作用下得到了与绝对周期凹槽时十分相似的结果，特别当凹槽相对于绝对周期变化较小时。这些结果对现实中的亚波长结构的加工有重要的指导意义。

3. 生物光子学

(1)利用 532 nm 的半导体激光束作为激发光，利用 632.8nm 的 He-Ne 激光束作为探测光束，激发光和探测光的偏振方向互相垂直且照射到细菌视紫红质膜的相同位置处。在一定的光强范围内，在探测光束中加入输入图象，由调节激发光的强度可以开关输入图象并能对输出图象的强度进行连续调节。(2)利用空间分辨技术无损测量了尼龙棒在不同的表面粗糙度下的有效散射系数。一般情况下生物组织具有一定的粗糙度，因此由空间分辨无损测量得到的有效散射系数并不是生物组织真正的有效散射系数，这个有效散射系数需要修正，修正系数依赖于生物组织的表面粗糙度。(3)用 Z-扫描的方法研究了新合成的一种二芳基乙烯化合物的光学非线性性质。(4)提出了三种新型激光器光束整形器件：改进的圆锥形光锥导管；哑铃形导管和牛角形光锥导管。对于牛角形光锥和哑铃形导管的特性进行了测量，讨论了利用牛角形光锥制作高亮点光源和通过哑铃形导管合成多束激光束的两个创新设计。

2006 年毕业博士研究生 3 名，硕士研究生 2 名；2006 年招收博士研究生 3 名，硕士研究生 5 名。一名博士研究生留校，开展周期性亚波长结构的光学性质的研究。

光子学材料及先进制备技术/ Photonics Materials and Advanced Fabrication Techniques

负责人：孔勇发

本年度在国内外主要学术期刊上发明论文二十余篇；其中 Appl. Phys. Lett. 2 篇, Opt. Express 一篇, J. Phys. Chem. 一篇。获得发明专利两项；申请发明专利两项。大尺寸光学铌酸锂晶体获得 2005 年度天津市技术发明二等奖。完成各类科研基金六项，启动国家自然科学基金四项。徐章程教授入选教育部新世纪优秀人才培养计划。

开发了具有自主知识产权的熔体注入式双坩埚技术，生长了直径 3 英寸近化学计量比铌酸锂晶体。在国内率先生长了具有高抗光折变能力的掺铪铌酸锂晶体。发明了铪铁双掺铌酸锂晶体，在显著提高晶体响应速度的同时，并不降低其衍射效率，大幅提高了晶体的光折变灵敏度。发现新化合物 NaSrBO_3 和 NaMgBO_3 ，并用粉末从头算法进行了晶体结构解析，构建了 $\text{Na}_2\text{O-SrO-B}_2\text{O}_3$ 体系富硼区相图。

在氟氧化物玻璃陶瓷中发现较宽的 1530nm 荧光发射，适于用作光纤材料。制备出 $\text{Tm}^{3+}/\text{Yb}^{3+}$ 的掺杂蓝色上转换发光玻璃陶瓷材料，其上转换蓝色荧光肉眼可见。发现可以通过热处理的方式在玻璃基体中构造纳米级的微晶，并可通过腐蚀的方式获得粉末状纳米团簇。

采用溶胶-凝胶制备方法和掺杂调控技术，研制出系列掺杂复合纳米 TiO_2 紫外-可见光催化剂，其紫外-可见光催化活性已超过单掺杂可见光催化剂；研制出具有 W 和 N 双离子掺杂和微观表面多元组分协同作用的“新型结构高活性的纳米 TiO_2 可见光催化剂”，该催化剂的紫外-可见光催化活性已超过 N 离子掺杂 TiO_2 可见光催化剂。

研究了亚单层 InGaAs 量子点中的载流子动力学，发现材料中的局域声子模以及量子点基态的辐射寿命和俘获载流子的时间与量子点尺寸的关系。在国内率先开展了有机/无机量子点红外复合材料的制备工作。在自制 MEH-PPV 的基础上，采用原位复合技术成功合成了 MEH-PPV/PbS 量子点复合材料。

采用在热处理条件下结合外加电场极化技术，在 3mm 厚铌酸锂晶体上实现了铁电畴极化反转，使极化开关电场降低了 3 个数量级；在 1mm 厚掺镁铌酸锂晶体上制备出周期为 $1.5\mu\text{m}$ 的均匀亚微米周期结构。用全固态激光抽运多周期掺镁铌酸锂微结构晶体，实现了 $1.45\sim 1.72\mu\text{m}$ 波段输出。在温度 30°C ，抽运光功率 300mW 时，信号光输出功率达 56mW，斜率效率 18.7%。

武莉博士以“洪堡学者”身份到德国亚琛工业大学进修一年；陈云琳教授到美国作访问学者；徐章程教授获得日本丸文国际交流基金的资助，赴日本早稻田大学进行学术访问。参加学术会议 9 人次；其中孔勇发教授在第 13 届全国凝聚态物质光学性质学术会议作大会报告，在中国光学学会 2006 年学术大会作邀请报告。招收研究生 14 名，其中博士生 2 名；毕业研究生 10 名，其中博士生一名。

弱光非线性及量子相干光学/ Weak Light Nonlinear Optics and Quantum Coherent Optics

负责人：许京军

2006 年度“弱光非线性及量子相干光学”方向主要在以下方面取得了进展。

张国权教授研究组利用光折变相位耦合的色散效应实现了单脉冲的光速减慢和加快，并在红宝石晶体中观测到超光速传输现象；研究了掺镁铌酸锂晶体的紫外光激发载流子霍尔效应，初步证实光激发载流子的霍尔迁移率远大于热激发载流子的迁移率。

陈志刚教授研究组和许京军教授研究组在多种无机和有机材料中成功制备出各种结构和缺陷的光子晶格，对光波在各种光子晶格中的传播特性作了详细的研究，实现了反对称离散孤子、离散涡旋孤子态、旋转式离散孤子以及缺陷孤子态等多种形式的新型离散孤子，相关结果在 *Physical Review Letters*、*Optics & Photonics News*、*Optics Letters* 等高水平学术刊物上发表。

孙骞教授研究组系统研究了磁场对掺铁铌酸锂晶体弱光非线性效应的影响；利用熔体扩散法成功提高了铌酸锂晶体的锂浓度；利用真空高温强还原缩短了铌酸锂晶体的光折变响应时间至毫秒量级；并在表面等离子激元、基于纳米光纤的纳米尺度定向耦合器光耦合和光镊效应等方面开展了研究。

本方向在 2006 年度获得国家自然科学基金面上项目 1 项，“973”计划 1 项，天津市重点基金项目 2 项。目前在研经费约 330 万元。2006 年度共有 6 人获得博士学位，8 人获得硕士学位，毕业生就业去向主要分布在高等院校和高科技产业。本年度新引进教师 2 人（楼慈波博士，高峰博士），出国进修教师 2 人（乔海军副教授，吴强博士）。许京军教授为《*Frontiers of Physics in China*》、《物理》、《激光技术》、《红外与毫米波学报》等多种专业学术刊物编委，中国物理学会秋季会议等国内外大型学术会议组委。孙骞教授和张国权教授新增为《激光技术》第九届编委。

光谱表征及传感技术/Spectral Characterization and Sensing Techniques

负责人：臧维平

本年度在国内外主要学术期刊上发明论文十九篇；其中 Appl. Phys. 1 篇，物理学报 2 篇。申请发明专利两项，完成各类科研基金四项，在研科研项目五项。

在 NaY(WO₄)₂ 晶体材料中的上转换特性研究方面发表论文三篇，集中在光谱性能分析和发光机理方面（宋峰教授小组）。在激光清洗领域发表了三篇论文并在第六届全国清洗行业进步与发展研讨会上做了大会报告（宋峰教授）。

在光传播理论方面，臧维平教授发表一篇 Appl. Phys 论文一篇。

赵丽娟教授小组在光子学材料和生物光子学领域，对荧光探针材料和 DNA 检验方面研究发表论文两篇。

周文远副教授小组在光谱仪器领域，对高灵敏度多通道分析仪器研究持续进行，并发表文章一篇。

徐晓轩副教授小组在应用光谱学领域，主要涉及近红外光谱学数据处理方法、三维荧光光谱学方法、乳腺组织拉曼光谱表征、有机半导体材料光谱表征以及材料相变过程光谱表征，共发表论文 7 篇。

申请“自适应热透镜焦距变化固体激光器”发明专利一项，“红外激光检测卡及其制备方法”发明专利一项。

宋峰教授承担教育部高等学校物理基础课程教学指导分委员会委员以及国家自然科学基金委信息科学学部四处流动项目主任，并任 SPIE Photonics West 会议执行委员，并在第六届全国清洗行业技术进步与发展研讨会上做特邀大会报告。

招收研究生 11 名，其中博士生 3 名；毕业研究生 3 名，其中博士生 1 名。

半导体生长技术和半导体器件/ Semiconductor Growth and Devices

负责人：舒永春

1、科研进展

针对 MBE 系统使用固体磷源的技术难题和设备状况，首先对磷回收系统和液氮循环系统进行改造，改造完成后，立即开展了含磷化合物半导体材料制备的研究工作。通过生长参数对 InP/InP 材料制备工艺参数和性能与表面状态影响的综合研究，认识到含磷化合物材料生长的关键是控制背景杂质含量和界面质量，并掌握了这些关键点的控制与工艺参数相互影响的关系，取得了良好实验结果。随后进行了 InGaP/GaAs、InGaAs/InP、GaAs/InGaAsP 等含磷半导体材料的匹配生长及其性质进行了细致研究，为下一年度开发新型含磷化合物半导体器件奠定了基础。

围绕新获批的国家 863 项目和天津基金重点项目开展研究工作。优化了传输矩阵的方法计算拟合出多层分布式布拉格反射镜 (DBR) 和垂直外腔激光器 (VECSEL) 芯片结构的反射谱曲线，并研究了结构与生长工艺条件，制备出中心波长与理论计算基本吻合的 DBR 和 VECSEL 芯片高反射率 (995%) 材料。同时开展了 InGaAs/GaAs 量子阱及其应力补偿的深入研究，并取得了阶段性进展。

对 InAs/GaAs 量子点材料制备的工艺参数和光学性质的相互影响关系进行了深入研究，制备出 1200nm 量子点激光器。

2、获批项目

- (1) 国家 863 项目 (2006~2008): “光泵浦 1064nm 半导体垂直外腔表面发射激光器芯片材料的制备”; 项目编号: 2006AA03Z413。
- (2) 天津市重点基金项目 (2006~2008): “光泵浦 980nm 半导体垂直外腔表面发射激光器芯片的制备”; 项目编号: 06YFJZJC01100。

3、学术交流

2006 年本组人员共参加会议等学术交流活动 3 次，发表会议论文 5 篇。

4、学生情况

2006 年毕业研究生 3 人，其中博士 1 人，硕士生 2 人。2006 年新招研究生 4 人，由硕士转攻博士 1 人。

专利/Patents

申请专利/ Patents Applied

- [1] 200610013956.0; 用于快速生物芯片检测的成像镜头; 发明; 田建国。
- [2] 200610013955.6; 智能大功率半导体激光器驱动装置; 发明; 田建国。
- [3] 200610129356.0; 掺锆铌酸锂晶体; 发明; 刘士国, 孔勇发, 赵艳军, 许京军, 陈绍林, 黄自恒, 张玲。
- [4] 200610014585.8; 一种自适应热透镜焦距变化的固体激光器; 发明; 宋 峰, 伍雁雄, 张鑫, 覃斌, 田建国。
- [5] 200710056669.2; 红外激光检测卡及其制备方法; 发明; 赵丽娟, 余华。

授权专利/ Patents Approved

- [1] ZL200410019732.1; 近化学比铌酸锂晶体制备工艺; 发明; 孙军, 张玲, 孔勇发, 李兵, 刘士国, 黄自恒, 陈绍林, 许京军。
- [2] ZL200410019454.X; 熔体注入法生长近化学比铌酸锂晶体系统及其工艺; 发明; 孙军, 孔勇发, 张玲, 许京军, 阎文博, 黄自恒, 刘士国, 陈绍林, 李剑韬, 李兵。

发表论文/Publications in Journal

1. X. Wang, Z. Chen, P. G. Kevrekidis, "Observation of discrete solitons and soliton rotation in periodic ring lattices", *Phys. Rev. Lett.* 96, 083904 (2006).
2. J. Yang, Z. Chen, "Defect solitons in optically-induced photonic lattices", *Phys. Rev. E* 73, 026609 (2006).
3. I. Makasyuk, Z. Chen, J. Yang, "Bandgap guidance in optically-induced photonic lattices with a negative defect", *Phys. Rev. Lett.* 96, 223903, 1-4 (2006).
4. Zhangcheng Xu, Yating Zhang, Jorn M. Hvam, Jingjun Xu, Xiaoshuang Chen and Wei Lu, "Carrier dynamics in submonolayer InGaAs/GaAs quantum dots", *Appl. Phys. Lett.* 89(1), Art.No.013113 (2006).
5. Shuqi Li, Shiguo Liu, Yongfa Kong, Jingjun Xu and Guangyin Zhang, "Enhanced photorefractive properties of LiNbO₃:Fe crystals by HfO₂ co-doping", *Appl. Phys. Lett.* 89(10), Art.No.101126 (2006).
6. X. Wang, J. Young, Z. Chen and J. Yang "Observation of lower to higher bandgap transition of one-dimensional defect modes", *Opt. Exp.* 14, 7362-7367 (2006).
7. Zhi-Bo Liu, Jian-Guo Tian, Jian-Yu Zheng, Zhi-Yun Li, Shu-Qi Chen and Yan Zhu, "Active tuning of nonlinear absorption in a supramolecular zinc diphenylporphyrin-pyridine system", *Opt. Exp.* 14, 2770-2775 (2006).
8. Zu-Bin Li, Jian-Guo Tian, Wen-Yuan Zhou, Wei-Ping Zang, and Chunping Zhang, "Periodic dielectric bars assisted enhanced transmission and directional light emission from a single subwavelength slit", *Opt. Exp.* 14(18),8037-8042 (2006).
9. X. Wang, I. Makasyuk, Z. Chen and J. Yang "Guiding light in optically induced PCF-like structures", *Optics & Photonics News* December 27 (2006).
10. Tao Song, Simin Liu, Ru Guo, Zhaohong Liu, Nan Zhu, Yuanmei Gao, "Observation of composite gap solitons in optically induced nonlinear lattices in LiNbO₃: Fe crystal", *Opt. Exp.* 14(5), 1924 (2006).
11. Wenbo Yan, Yongfa Kong, Lihong Shi, Hongde Liu, Xiaochun Li, Jingjun Xu, Shaolin Chen, Ling Zhang, Ziheng Huang, Shiguo Liu and Guangyin Zhang, "Investigations of centers formed in UV-light-induced absorption for LiNbO₃ highly doped with Mg and Hf", *Opt. Exp.* 14(22), 10898-10906 (2006).
12. Feng Song, Kang Zhang, Jing Su, et. al., "Three-photon indirect sensitization in green upconversion luminescence of Er/Tm codoped NaY(WO₄)₂ crystal", *Opt. Exp.* 14(26),12584 (2006).
13. C. Lou, J. Xu, L. Tang, Z. Chen, P. G. Kevrekidis, "Symmetric and anti-symmetric solitons in two-dimensional lattices", *Opt. Lett.* 31, 492-494 (2006).
14. X. Wang, Z. Chen, J. Yang, "Guiding light in optically induced ring lattices with a low-refractive-index core", *Opt. Lett.* 31, 1887-1889 (2006).
15. Guiying Chen, Yizhe Yuan, Chunping Zhang, Guan Yang, Jian Guo Tian, Tang Xu, Qi Wang. Song, "All-optical time-delay relay based on a bacteriorhodopsin film", *Opt. Lett.* 31(10), 1531-1534 (2006).

16. T. H. Zhang, J. Yang, H. Z. Kang, L. Feng, J. J. Xu, C. P. Zhang, X. K. Ren, B. H. Wang, Y. Z. Lu, F. Jia and W. W. Shao, "Surface second-harmonic generation in Sr_{0.6}Ba_{0.4}NbO₃ with a nonlinear diffusion mechanism", *Phys. Rev. B* 73, 153402 (2006).
17. Zubin Li, Jianguo Tian, Wenyuan Zhou, Zhibo Liu, Weiping Zang, "Effect of groove periodicity on the enhanced transmission through a single subwavelength slit", *J. Opt. Soc. Am. B* 23, 1517-1523 (2006).
18. Zhibo Liu, Yizhou Zhu, Yan Zhu, Shuqi Chen, Jianyu Zheng, Jianguo Tian, "Nonlinear absorption and nonlinear refraction of self-assembled porphyrins", *J. Phys. Chem. B* 110, 15140-15145 (2006).
19. Bifen Gao, Ying Ma, Yaan Cao, Wensheng Yang, and Jiannian Yao, "Great Enhancement of Photocatalytic Activity of Nitrogen-Doped Titania by Coupling with Tungsten Oxide", *J. Phys. Chem. B* 110(29), 14391-14397 (2006).
20. Li Wu, Xiaolong Chen, Y Zhang, Yongfa Kong, Jingjun Xu and YP Xu, "Ab Initio Structure determination of novel borate NaSrBO₃", *J. Solid State Chem.*, 179(4), 1219-1224 (2006).
21. Bifen Gao, Ying Ma, Yaan Cao, Jincai Zhao and Jiannian Yao, "Effect of Ultraviolet Irradiation on Crystallization Behavior and Surface Microstructure of Titania in the Sol-Gel Process", *J. Solid State Chem.*, 179(1), 41-48 (2006).
22. Wenbo Yan, Lihong Shi, Yongfa Kong, Yufang Wang, Hongde Liu, Jingjun Xu, Shaolin Chen, Ling Zhang, Ziheng Huang, Shiguo Liu and Guangyin Zhang, "The electrostatic depinning mechanism of domain wall for near-stoichiometric lithium niobate crystals", *J. Phys. D: Appl. Phys.*, 39(19), 4245-4249 (2006).
23. Wenbo Yan, Yongfa Kong, Lihong Shi, Lei Sun, Hongde Liu, Xiaochun Li, Di Zhao, Jingjun Xu, Shaolin Chen, Ling Zhang, Ziheng Huang, Shiguo Liu and Guangyin Zhang, "The relationship between the switching field and the intrinsic defects in near-stoichiometric lithium niobate crystals", *J. Phys. D: Appl. Phys.*, 39(1), 21-24 (2006).
24. Jing Su, Song F., Hao Tan, et al., "Phonon-assisted mechanisms and concentration dependence of Tm³⁺ blue upconversion luminescence in codoped NaY(WO₄)₂ crystals", *J. Phys. D: Appl. Phys.* 39, 2094-2099 (2006)
25. Shuqi Li, Shiguo Liu, Yongfa Kong, Dongling Deng, Guangyu Gao, Yanbo Li, Hongchen Gao, Ling Zhang, Ziheng Hang, Shaolin Chen and Jingjun Xu, "The optical damage resistance and absorption spectra of LiNbO₃:Hf crystals", *J. Phys.: Condens. Matter*, 18(3), 3527-3534 (2006).
26. Jun Sun, Yongfa Kong, Ling Zhang, Wenbo Yan, Xueze Wang, Jingjun Xu and Guangyin Zhang, "Growth of large diameter nearly stoichiometric lithium niobate crystals by continuous melt supplying system", *J. Crystal Growth*, 292(2), 351-354 (2006).
27. Shaolin Chen, Hongde Liu, Yongfa Kong, Ziheng Huang and Jingjun Xu, "High photorefractive sensitivity and fast response time of near-stoichiometric and MgO doped LiNbO₃:Fe crystal", *Crys. Res. Tech.* 41(8), 790-794 (2006).
28. Wenbo Yan, Yongfa Kong, Lihong Shi, Lei Sun, Hongde Liu, Xiaochun Li, Di Zhao and Jingjun Xu, "The influence of composition on the photorefractive centers in pure LiNbO₃ at

- low light intensity” , *Appl. Opt.*, 45(11), 2453-2458 (2006).
29. Di Qu, Ru Guo, Simin Liu, Zhaohong Liu, Yuanmei Gao, “Simple optical method for determination of crystal orientation in photorefractive crystals”, *Appl. Opt.* 45(24), 6218-6222 (2006).
 30. Dongsong Zhu, Jingjun Xu, Haijun Qiao, Yanli Shi, Feng Gao, Wei Li, Bo Fu, Guaquan Zhang, Ke Zheng, “Ultraviolet photorefractive effect in Mg-doped near-stoichiometric LiNbO₃”, *Opt. Commun.* 266 (2), 582-585 (2006).
 31. Fang Bo, Guoquan Zhang, Jingjun Xu, “Ultraslow Gaussian pulse propagation induced by a dispersive phase coupling in photorefractive bismuth silicon oxide crystals at room temperature”, *Opt. Commun.* 261, 349-352 (2006).
 32. Feng Gao, Jingjun Xu, Haijun Qiao, Qiang Wu, Yin Xu, Guoquan Zhang, “Observation of superluminal and slowdown light propagation in doped lithium niobate crystals”, *Opt. Commun.* 257, 185-190 (2006).
 33. Yuanmei Gao, Simin Liu, Ru Guo, Zhaohong Liu, Tao Song, Nan Zhu, “The circular and elliptic white-light dark spatial solitons in a photovoltaic self-defocusing nonlinear medium”, *Opt. Commun.* 259, 738-743 (2006).
 34. Song F., Han, L., Tan H., et. al., “Spectral performance and intensive green upconversion luminescence in Er³⁺/Yb³⁺-codoped NaY(WO₄)₂ crystal”, *Opt. Commun.* 259(1), 179-186 (2006)
 35. T.H. Zhang, B.H. Wang, X.K. Ren, W.W. Shao, Y.H. Xu, Z.J. Hu, H.Z. Kang, J. Yang, L. Feng, F. Jia, “Influence of the external field on photorefractive surface waves”, *Opt. Commun.* 265(2), 649-654 (2006).
 36. Weiping Zang, Jianguo Tian, Zhibo Liu, Wenyuan Zhou, Feng Song, Chunping Zhang, “High-accuracy finite-difference beam-propagation method for cylindrical geometry”, *Appl. Phys. B* 82, 99-104 (2006).
 37. Xinzheng Zhang, Gernot Berger, Mathias Dietz, Cornelia Denz, “Cross-talk in phase encoded volume holographic memories employing unitary matrices”, *Appl. Phys. B* 85(4), 575-579 (2006).
 38. Nan Zhu, Ru Guo, Simin Liu, Zhaohong Liu, Tao Song, “Modulation instability of broad beam in self-defocusing photorefractive crystal LiNbO₃: Fe”, *J. Opt. A* 8149-154 (2006).
 39. Ru Guo, Chun-Fu Huang and Si-Min Liu, “Interactions of partially incoherent spatial solitons in logarithmic saturable nonlinear media”, *J. Opt. A (Pure Appl. Opt.)* 8, 695-702 (2006).
 40. Hongde Liu, Xiang Xie, Yongfa Kong, Wenbo Yan, Xiaochun Li, Lihong Shi, Jingjun Xu and Guangyin Zhang, “Photorefractive properties of near-stoichiometric lithium niobate crystals doped with iron” , *Opt. Mat.*, 28(3), 212-215 (2006).
 41. Lihong Shi, Yongfa Kong, Wenbo Yan, Jun Sun, Shaolin Chen, Ling Zhang, Wanlin Zhang, Hongde Liu, Xiaochun Li, Xiang Xie, Di Zhao, Lei Sun, Zhanyin Wang, Jingjun Xu and Guangyin Zhang, “Determination of the composition of lithium tantalate by means of Raman and OH⁻ absorption measurements” , *Mater. Chem. Phys.*, 95(2-3), 229-234 (2006).
 42. Venugopal Karunakaran, J. Luis Perez Lustres, Lijuan Zhao, Nikolaus P. Ernsting, Oliver Seitz, “Large dynamic stokes shift of DNA intercalation dye thiazole orange has contribution from a high-frequency mode”, *J. Am. Chem. Soc.* 128, 2954-2962 (2006).

43. Chen Guiying, Yuan Yizhe, Liang Xin, Xu Tang, Zhang Chunping, Song Qiwan, "The behaviours of optical novelty filter based on bacteriorhodopsin film", *Chin. Phys.*15(9), 2007-2011 (2006).
44. Qiang Wu, Jingjun Xu, Romano Rupp, Xinzheng Zhang, CiBo Lou, Sveta Bugaychuk, "Transition from backscattering speckles to phase conjugation in LiNbO₃:Fe", *Chin. Phys. Lett.* 23(8), 2101-2104 (2006).
45. Guoxiang Gao, Jingjun Xu, Shu Zhang, Wenhui Liu, Hongde Liu, Yongfa Kong, Shaolin Chen, Guangyin Zhang, Qian Sun, "Photo-Induced Carriers in Near-Stoichiometric LiNbO₃:Fe Crystal", *Chin. Phys. Lett.* 23(2), 443-445 (2006).
46. Zubin Li, Jianguo Tian, Wenyuan Zhou, Zhibo Liu, Weiping Zang, Chunping Zhang, "Role of evanescent waves in highly directional emission from a subwavelength slit in metal-dielectric layered films", *Chin. Phys. Lett.* 23(5), 1207-1210 (2006).
47. Shu Qiang, Lin Yaowang, Xing Xiaodong, Yao Jianghong, "Effect of Small-angle scattering on the integer quantum Hall plateau", *Chin. Phys. Lett.* 23(2), 436-439 (2006).
48. Song Feng, Wu Zhaohui, Liu Shujing, et. al., "A passive Q-switched microchip Er/Yb Glass Laser Pumped by laser diode", *Chin. Phys. Lett.* 23(5), 1195-7 (2006)
49. Guang Yang, Guiying Chen, Xing Liang, Chunping Zhang, Jianguo Tian, Chengmei Zhao, Qiwan Song, "The influence of the velocity and the size of an object on the quality of an optical novelty filter designed using a bacteriorhodopsin film", *J. Mod. Optic.* 3(8), 1177-1185 (2006).
50. J. L. Zhao, L. Ernsting, N. P. Seitz, arge, Karunakaran, V., Perez Lustres, "Dynamic Stokes Shift of DNA Intercalation Dye Thiazole Orange has Contribution from a High-Frequency Mode", *O.J. Am. Chem. Soc.* 128(9), 2954-2962 (2006).
51. Yunlin Chen, Juan Guo, Cibo Lou, Ziheng Huang, Shaolin Chen and Guangyin Zhang, "Low external electric field periodic poling of thick LiTaO₃", *J. Rare Earth* 24, 128-130 (2006).
52. 黄春福, 郭儒, 刘思敏, "饱和对数非线性介质中非相干孤子碰撞对相干性的改善", *物理学报* 55(3), 1218-1223 (2006)。
53. 张国权, 薄方, 涂燕飞, 许京军, "光波位相耦合色散效应与固态介质中室温下的光速调控", *物理* 35(10), 845-851 (2006)。
54. 陈树琪, 刘智波, 臧维平, 周文远, 张春平, 田建国, "大非线性相移下 Z-扫描特性的研究", *物理学报* 55, 1211-1217 (2006)。
55. 余华, 孙健, 刘宝荣, 宋杰, 赵丽娟, 许京军, "Eu³⁺离子在微晶玻璃研究中的探针作用", *物理学报* 55(11), 6152-6155 (2006)。
56. 闫卫国, 陈云琳, 王栋栋, 郭娟, 张光寅, "掺镁铈酸锂亚微米结构畴反转的研究", *物理学报* 55(11), 5855-5858 (2006)。
57. 舒强, 舒永春, 张冠杰, 刘如彬, "调制掺杂 GaAs/AlGaAs 2DEG 材料持久光电导及子带电子特性研究", *物理学报* 55(3), 1379-1383 (2006)。
58. 吴朝晖, 宋峰, 刘淑静, "LD抽运Er³⁺、Yb³⁺共掺磷酸盐玻璃被动调Q激光器的理论分析和数值计算", *物理学报* 55(9), 4659-06 (2006)。

59. 李奇楠, 徐晓轩, 武中臣, 宋宁, 张存洲, 俞钢, “FTIR 发射光谱中室内气体热辐射源的优化设计及辐射特性研究”, 红外与毫米波学报 25 (1), 56-59 (2006)。
60. 高碧芬, 马颖, 曹亚安, 姚建年, “热处理温度对铬掺杂二氧化钛表面结构和性质的影响”, 化学学报 64(13), 1329-1333 (2006)。
61. 王占银, 孔勇发, 陈绍林, 许京军, “大直径铈酸锂晶片的化学机械抛光研究”, 人工晶体学报 35(1), 99-103 (2006)。
62. 李树奇, 刘士国, 孔勇发, 阎文博, 刘宏德, 邓东灵, 高光宇, 李彦波, 高宏臣, 许京军, “四价掺杂铈酸锂晶体抗光折变性能研究”, 人工晶体学报 35(3), 474-477 (2006)。
63. 王铁铮, 吴强, 王振华, 张心正, 许京军, “LiNbO₃:Fe 晶体中飞秒二波耦合光栅衍射自增强现象的研究”, 中国激光 33(7), 918-921 (2006)。
64. 高国祥, 孙骞, 许京军, 陆文强, 张姝, 刘文辉, 孔勇发, 刘宏德, “LiNbO₃:Fe,Zn 晶体不同温度下的扇形噪音研究”, 光电子·激光 17 (2), 203-206 (2006)。
65. 唐柏权, 许京军, 陈志刚, 张国权, 乔海军, 孙骞, 孔勇发, “若干弱光非线性光学效应及其应用”, 激光技术 30(6), 581-588 (2006)。
66. 张冠杰, 舒永春, 刘如彬, 舒强等, “光抽运垂直外腔面发射激光器特性与研究进展”, 激光技术 30(4), 351-354 (2006)。
67. 张雅婷, 徐章程, 李菲晖, “Si 基上电沉积 Cu 薄膜的形貌与择优取向”, 人工晶体学报 35(4), 728-731 (2006)。
68. 张冠杰, 徐波, 陈涌海, 姚江宏等, “不同淀积厚度 InAs 量子点的喇曼散射”, 半导体学报 27(6), 1012-1015 (2006)。
69. 张静, 徐晓轩, 武中臣, 杨仁杰, 俞钢, 张存洲, “近红外光谱法检测聚醚多元醇伯羟基与仲羟基的相对含量”, 光谱学与光谱分析 26 (1), 37-39 (2006)。
70. 杨仁杰, 徐晓轩, 尚丽平, 许家林, 杨延勇, 张存洲, “三维荧光光谱差谱法测定柴油中溶剂油”, 光谱学与光谱分析 26 (1), 94-96 (2006)。
71. 林海波, 徐晓轩, 王斌, 吴彬麟, 许家林, 俞钢, 杨延勇, “Poly(3,4-ethylene dioxithiophene):Poly(styrene sulfonate)的共振拉曼光谱研究”, 光谱学与光谱分析 26 (4), 646-648 (2006)。
72. 宋宇, 周文远, 叶青, 臧维平, 田建国, “高灵敏度光学多通道分析仪的研究”, 光谱学与光谱分析 26 (5), 775-778 (2006)。
73. 于舸, 徐晓轩, 吕淑华, 宋增福, 张存洲, 张春平, “乳腺组织形态基元共焦拉曼光谱的研究”, 光谱学与光谱分析 26 (5), 869-873 (2006)。
74. 张攀, 徐晓轩, 刘燕楠, 邓大为, 梁骏, 张存洲, “应用光纤生物传感器测量肿瘤的自体荧光光谱”, 发光学报 27 (4), 581-584 (2006)。
75. 许家林, 徐晓轩, 张攀, 张存洲, 俞钢, “PbS 及其光致氧化产物的显微成像拉曼散射研究”, 光散射学报 18 (3), 219-224 (2006)。
76. 张冠杰, 陈涌海, 姚江宏, 舒强等, “InAlAs 量子点材料的 AFM 和拉曼散射研究”, 激光和光电子学进展 43(4), 68-72 (2006)。
77. 曲迪, 刘思敏, 陆猗, 郭儒, 汪大云, “部分空间非相干光光生伏打暗空间孤子及其定向耦合器”, 南开大学学报(自然科学版) 39(2), 11-15 (2006)。

78. 梁兴, 杨秀芹, 杨光, 田建国, 张春平, 许棠, 李晓霞, “偶氮样品折射率变化的测量与计算”, 南开大学学报(自然科学版) 39(4), 74-77 (2006)。
79. 张小华, 刘思敏, 高垣梅, 刘照红, “二维非相干白光波导阵列的制作”, 南开大学学报(自然科学版) 39(5), 6-9 (2006)。
80. 刘如彬, 舒永春, 张冠杰, 舒强等, “产生超短脉冲的光泵浦垂直外腔面发射激光器的研究进展”, 激光杂志 27(2), 9-10 (2006)。
81. 宋峰, 邹万芳, 刘淑静, 田彬, “激光清洗——微电子元件”, 清洗世界 22 (1), 38-40 (2006)。
82. 宋峰, 邹万芳, 刘淑静, 田彬, “激光清洗的其它应用”, 清洗世界 22 (3), 38-40 (2006)。
83. 宋峰, 田彬, 邹万芳, 刘淑静, “激光清洗设备介绍”, 清洗世界 22 (4), 27-32 (2006)。

国际合作与交流/International Cooperation and Exchange

来访人员名单/Visitors List

序号	姓名	国家或地区	单位	职称或职位	来访时间	来访目的
1.	Klaus Suhling	英国	伦敦国王学院物理系	博士	2006.6.4-5	工作访问 学术交流
2.	肖敏	美国	阿肯色大学物理系	教授	2006.6.23-25	工作访问 讲学
3.	S.Jiang	美国	Optical Sciences Center in University of Arizona	Associate Professor	2006.8.	学术交流
4.	Svetlana Bugaychuk	乌克兰	乌克兰国家科学院	研究员	2006.8.21-9.3	工作访问 讲学
5.	汤上登	日本	宇都宫大学能量与环境科学系	教授(Prof.)	2006.11.9	工作访问
6.	Wendell T. Hill III	美国	马里兰大学	教授	2006.11.25	工作访问

出访人员名单/Personnel exchange Researchers List

序号	姓名	国家或地区	单位	职称或职位	出访时间	出访目的
1.	张心正	德国	明斯特大学应用物理学院	副教授	2004.4-2006.8	洪堡研究学者
2.	楼慈波	美国	旧金山州立大学物理天文系	讲师	2006.10-2007.2	访问学习
3.	徐章程	日本	早稻田大学	教授	2006.3	合作研究
4.	徐章程	日本	早稻田大学	教授	2006.11	合作研究
5.	武莉	德国	亚琛工业大学	讲师	2006.7-2007.8	洪堡研究学者
6.	吴强	美国	麻省理工	讲师	2006.12-2008.4	合作研究
7.	乔海军	加拿大	加拿大维多利亚大学	副教授	2006.04-2008.03	合作研究
8.	陈云琳	美国	阿肯色大学	教授	2006.11-2007.11	合作研究

引进人才名单

序号	姓名	性别	出生年月	职称	研究方向
1	李祖斌	男	1978.11	讲师	亚波长材料光学性质
2	高峰	男	1978.7	讲师	色散调控
3	楼慈波	男	1979.1	讲师	光子微结构及光动力学
4	陈志刚	男	1964.1	教授	光孤子
5	Romano A. Rupp	男	1952.1	教授	光折变非线性光学
6	孙甲明	男	1968.11	教授	硅基光电子材料和器件, 半导体 THz 材料和物理

国内、国际会议报告/Talks at Conferences

1. 孔勇发, 许京军, 张光寅, “缺陷结构调控与铌酸锂晶体的光折变性能”, 第 13 届全国凝聚态物质光学性质学术会议, 厦门 (2006.8.4-6)。(大会报告)
2. 孔勇发, 许京军, “光折变全息存储材料的研究进展”, 中国光学学会 2006 年学术大会, 广州 (2006.9.3-5)。(邀请报告)
3. 宋峰, “激光在除锈中的应用”, 第六届全国清洗行业技术进步与发展研讨会暨企业创新与产业升级高峰论坛, 青岛 (2006.6)。(邀请报告)
4. 张国权, “南开大学物理科学学院光学学科工作报告”, 第 13 届全国激光物理讨论会, 湖南, 张家界 (2006.10.21-23)。
5. 高峰, “Condensed matter dispersion and light group velocity control”, 2006 年第五届亚太激光研讨会, 桂林 (2006.11.23-27)。
6. 崔国新, 李玉栋, 郭小枝, 陈靖, 刘洪冰, 许京军, 孙骞, “铌酸锂铁电畴波导的制备”, 第十三届全国凝聚态物质光学性质学术会议, 厦门 (2006.8.4-9)。
7. 齐继伟, 李玉栋, 许京军, 崔国新, 孙骞, “磁场对光折变光栅擦除过程影响的研究”, 第十三届全国凝聚态物质光学性质学术会议, 厦门 (2006.8.4-9)。
8. 刘照红, 刘思敏, 郭儒, 齐新元, 周立鹏, 李源, “二维白光圆形暗空间孤子及其相互作用”, 中国物理学会秋季学术会议, 清华大学 (2006.9.15-17)
9. 汪大云, 刘思敏, 刘照红, 郭儒, 高垣梅, 黄春福, 朱楠, 宋涛, “高斯光束传播在 $\text{LiNbO}_3:\text{Fe}$ 晶体中的时间行为的实验研究”, 中国物理学会秋季学术会议, 清华大学 (2006.9.15-17)
10. 李源, 郭儒, 刘思敏, 刘照红, 齐新元, 周立鹏, “暗孤子在扩散场中的偏折”, 中国物理学会秋季学术会议, 清华大学 (2006.9.15-17)
11. 齐新元, 刘思敏, 郭儒, 刘照红, 周立鹏, 李源, “光感应一维光子晶格中的缺陷模分立孤子”, 中国物理学会秋季学术会议, 清华大学 (2006.9.15-17)
12. 周立鹏, 刘思敏, 郭儒, 刘照红, 齐新元, 李源, “掺铁铌酸锂晶体中的二维波导阵列的制作及分立衍射分立孤子的观察”, 中国物理学会秋季学术会议, 清华大学 (2006.9.15-17)
13. 黄春福, 郭儒, 刘思敏, “部分非相干光和白光在抛物型平面波导中的自陷行为”, 中国物理学会秋季学术会议, 清华大学 (2006.9.15-17)
14. 张春平, “偶氮染料掺杂聚合物薄膜的全光开关特性”, 全国光子—光电子学系列主题学术与发展战略研讨, 三亚 (2006.12)。
15. 张春平, “表面粗糙度对有效散射系数影响的实验研究”, 中国光学学会 2006 年学术大会, 广州 (2006.9.3-6)。
16. 孔勇发, 孙军, 李兵, 黄自恒, 陈绍林, 张玲, 刘士国, 舒永春, 许京军, “大尺寸光学级铌酸锂晶体”, 第 14 届全国晶体生长与材料学术会议, 福州 (2006.11.5-9)。
17. 李晓春, 孔勇发, 安亚南, 刘宏德, “近化学计量比双掺铜铈铌酸锂非挥发性全息存储性能的研究”, 中国光学学会 2006 年学术大会, 广州 (2006.9.3-5)。
18. 李晓春, 孔勇发, 刘宏德, 许京军, “组分对掺铁铌酸锂晶体光折变中心的影响”, 中国物理学会 2005 年秋季学术会议, 北京 (2006.9.15-17)。
19. 刘宏德, 孔勇发, 李晓春, 吴日雯, 肖罗生, 陈绍林, 刘士国, 黄自恒, 张玲, 许京军, “近化学计量比掺杂铌酸锂晶体的非线性光学性能研究”, 中国物理学会 2006 年秋季学术会议, 北京 (2006.9.15-17)。
20. 刘宏德, 孔勇发, 吴日雯, 胡茜, 王文杰, 陈绍林, 刘士国, 黄自恒, 张玲, 许京军, 张光寅, “光诱导铌酸锂晶体畴反转的研究”, 第 13 届全国凝聚态物质光学性质学术会

- 议, 厦门 (2006.8.4-6)。
21. 何龙, 赵迪, 孙同庆, 张康, 陈绍林, 孔勇发, 宋峰, “Er:KLa(WO₄)₂晶体的生长与光谱性质”, 第 14 届全国晶体生长与材料学术会议, 福州 (2006.11.5-9)。
 22. 高碧芬, 马颖, 曹亚安, 谷战军, 姚建年, “Ti(1-x)ZrxO₂ 固溶体的制备和光催化性能的研究”, 中国化学会第二十五届学术年会, 长春 (2006.7.11-15)。
 23. 姚江宏, 刘志伟, 薛亮平, 许京军, 张光寅, “准相位匹配掺镁铌酸锂晶体红外光学参量振荡特性”, 第十三届全国凝聚态物质光学性质学术会议, 厦门 (2006.8)。
 24. 贾国治, 姚江宏, 舒永春, 许京军, 王占国, “近红外波段 InAs 量子点 MBE 生长及发光特性研究”, 第十三届全国凝聚态物质光学性质学术会议, 厦门 (2006.8)。
 25. 贾国治, 姚江宏, 舒永春, 王占国, “生长温度对双模量子点尺寸分布和光学性质的影响”, 第十四届全国化合物半导体材料、微波器件和光电器件学术会议, 北海 (2006.11)。
 26. 姚江宏, 贾国治, 舒永春, 王占国, “InAs/GaAs 量子点形貌与光学性质研究”, 第十四届全国化合物半导体材料、微波器件和光电器件学术会议, 北海 (2006.11)。
 27. 贾国治, 姚江宏, 王占国, “近红外波段 InAs 量子点 MBE 生长及发光特性研究”, 光子—光电子学系列主题学术与发展战略研讨会, 主题 (II): 先进光电子器件及其应用, 海南三亚 (2006.12)。
 28. 宋峰, 全国光学大会, 广州 (2006.9)。
 29. 宋峰, 第二届国际光纤传感与产业化研讨会, 哈尔滨 (2006.9)。

主办/协办国内、国际会议/Conferences Sponsored by the Laboratory

序号	姓名	会议名称	职位
1	宋峰	SPIE Photonics West Conference	Program Committee Member
2	许京军	中国物理学会 2006 年秋季学术会议	会议组委
3	孙骞	中国物理学会 2006 年秋季学术会议	分会主席
4	孙骞	第十三届全国凝聚态物质光学性质学术会议	分会主席

学术组织与期刊任职/Academic Service**国内学术组织任职/Service to the Domestic Professional Societies**

序号	姓名	任职机构	职位	任期
1	许京军	天津市物理学会	理事	
2	宋峰	国家自然科学基金委信息科学学部四处	流动项目主任	2006.5~2007.2
3	宋峰	教育部高等学校物理基础课程教学指导分委员会	委员	2006~2010
4	孔勇发	天津市硅酸盐学会	晶体生长与材料专业委员会副主任	2005-
5	孙骞	天津市光电子学会	常委	2006-
6	孙骞	中国光学学会光电技术委员会	委员	2006-

国内期刊任职/Service to the Domestic Journals

序号	姓名	任职机构	职位	任期
1	许京军	Frontiers of Physics in China-Selected publications from Chinese Universities	编委	2005-
2	许京军	《激光技术》	编委	2006-2010
3	许京军	《红外与毫米波学报》	编委	
4	许京军	《物理》	编委	
5	孔勇发	《激光技术》编委会	编委	2006-2010
6	张国权	《激光技术》	编委	2007-2011
7	孙骞	《激光技术》	编委	2006-2010

获奖情况/Awards & Honors

大尺寸光学级铌酸锂晶体

2006 年天津市技术发明奖二等奖 (2005FM-2-003-D1)

获奖者: 孔勇发 许京军 孙军 孙骞 张光寅



光折变新效应、机理与器件的研究

南开大学科技成果特别奖

获奖者: 许京军 张光寅 刘思敏 张国权 孔勇发

获奖个人/Award for distinguished scientists

第六届“中国青年科学家奖”

获得者: 许京军



获奖研究生/Award for excellent students

2006 年全国博士论坛优秀论文奖: 任相魁

泰达奖教金优秀学生奖一等奖: 薄方

南开大学党员标兵: 薄方

南开大学优秀党员: 刘宏德

南开大学优秀学生干部: 潘雷霆

南开大学优秀学生干部: 肖罗生 张兰兰

南开大学优秀毕业生: 孙亮 董嵘 曲迪 申岩

南开大学三好学生: 刘宏德 苏静

南开大学奖学金:

一等奖学金 张雅婷

二等奖学金 王秉慧

三等奖学金 薄方 舒强 刘宏德 苏静 王喆 吴日雯 苏瑞渊 刘燕楠
田彬 刘宝荣 孙健 贾峰 孟扬 郭磊

学位论文/Dissertations

1. 博士学位论文 Dissertation for Doctoral Degree

- [1] 吴朝晖, 激光二极管抽运 Er-Yb 共掺磷酸盐玻璃激光器的研究; 导师: 宋峰
- [2] 杨嘉, 光折变光学表面波及其在二次谐波产生中的应用; 导师: 张春平
- [3] 楼慈波, 光子晶格微结构及其光传播动力学研究; 导师: 许京军
- [4] 高峰, 时空周期调制与光群速调控; 导师: 许京军
- [5] 阎文博, 近化学计量比铌酸锂晶体的生长与性能研究; 导师: 孔勇发
- [6] 黄春福, 非相干光空间孤子及其相互作用研究; 导师: 郭儒
- [7] 高垣梅, 在 LiNbO₃:Fe 晶体中白光暗空间孤子及其应用和由反射光栅引起的二波耦合的实验研究; 导师: 刘思敏
- [8] 李祖斌, 周期性亚波长结构的光学透过性质研究; 导师: 田建国
- [9] 刘智波, 有机及超分子材料光学非线性研究; 导师: 田建国
- [10] 张冠杰, GaAs 基多量子阱和自组织量子点材料的 MBE 优化生长及其特性的研究; 导师: 王占国
- [11] 高国祥, 铌酸锂晶体低温光折变性质研究; 导师: 许京军
- [12] 申岩, 光折变空间电荷场演变与非线性效应的理论研究; 导师: 许京军
- [13] 林海波, 聚合物电致发光器件的老化机理和发光性能光谱研究; 导师: 俞钢
- [14] 武中臣, 复杂凝聚态体系中近红外光谱信号的信息提取及定量表示; 导师: 俞钢
- [15] 温宏胜, 以 Monte Carlo 方法研究粗糙表面效应对生物组织光散射的影响; 导师: 田建国
- [16] 杨秀芹, 有机光色材料的光学非线性及其应用; 导师: 张春平

2. 硕士学位论文 Dissertation for Master Degree

- [1] 杨威, 液相外延法生长铌酸锂薄膜中助熔剂对衬底材料的影响; 导师: 孙骞
- [2] 车蔚玥, 具有光学缓冲层的周期层叠全息光栅的光学性质及应用; 导师: 张国权
- [3] 朱楠, 铌酸锂晶体中的调制不稳定性与灰孤子的研究; 导师: 郭儒
- [4] 周斌斌, 掺铬镁橄榄石激光器及准相位匹配光学参量振荡器研究; 导师: 陈云琳
- [5] 李剑韬, 熔体注入-双坩埚提拉法生长近化学计量比铌酸锂晶体研究; 导师: 张玲
- [6] 李树奇, 掺铪铌酸锂晶体抗光折变性能研究; 导师: 刘士国
- [7] 宋涛, 光感应一维阵列波导中复合态分立孤子的实验观察; 导师: 刘思敏
- [8] 杨大鹏, 铁电类晶体非线性表面电磁波与表面非线性光学效应研究; 导师: 张天浩
- [9] 张攀, 人体乳腺肿瘤诊断的新技术研究; 导师: 俞钢
- [10] 孙磊, 近化学计量比掺锰铌酸锂晶体光折变特性研究; 导师: 孔勇发
- [11] 杨正广, DCG 全息在光信息学中的应用; 导师: 田建国
- [12] 梅灿, 光传播与坐标变换方法; 导师: 田建国
- [13] 赵迪, 掺铟钨酸镧钾晶体生长与性质研究; 导师: 孔勇发
- [14] 曲迪, 二维非线性光子晶格中缺陷模的实验和理论研究; 导师: 刘思敏
- [15] 王占银, 大直径铌酸锂晶片化学机械抛光研究; 导师: 孔勇发

- [16] 鄢飞润, 光学微结构的性质研究; 导师: 孙骞
- [17] 彭灏, 纳秒光学参量振荡系统的激光光束整形研究; 导师: 田建国
- [18] 孙亮, 量子点-量子点光放大器的增益特性; 导师: 王占国
- [19] 尹美荣, 探针-样品间剪切力作用机制的研究; 导师: 张天浩
- [20] 薛亮平, 周期极化掺镁铌酸锂晶体光参量振荡研究; 导师: 姚江宏
- [21] 闫卫国, 掺镁铌酸锂准周期结构的研究; 导师: 陈云琳
- [22] 刘国梁, GaAs 基 In(Ga,Al)As 量子点材料生长与性质研究; 导师: 姚江宏
- [23] 李奇楠, 微量有机物热解气 FTIR 红外光谱分析研究; 导师: 俞钢
- [24] 董嵘, 光波位相耦合过程中的色散效应及其应用; 导师: 张国权
- [25] 殷长秋, 光折变体三维全息存储器编解码方式和寻址方式的研究; 导师: 孙骞
- [26] 梁兴, 有机光色材料光学性质的研究与应用; 导师: 张春平
- [27] 宋宇, CCD 在微光成像领域中的应用研究; 导师: 田建国
- [28] 王铁铮, 光折变光栅瞬态特性研究; 导师: 许京军
- [29] 徐音, 电扩散法制备近化学计量比铌酸锂晶体; 导师: 许京军

选录论文/Selected Papers

- [1] Zhangcheng Xu, Yating Zhang, Jorn M. Hvam, Jingjun Xu, Xiaoshuang Chen and Wei Lu, “Carrier dynamics in submonolayer InGaAs/GaAs quantum dots”, *Appl. Phys. Lett.* 89(1), Art.No.013113 (2006).
- [2] Shuqi Li, Shiguo Liu, Yongfa Kong, Jingjun Xu and Guangyin Zhang, “Enhanced photorefractive properties of LiNbO₃:Fe crystals by HfO₂ co-doping”, *Appl. Phys. Lett.* 89(10), Art.No.101126 (2006).
- [3] Zhi-Bo Liu, Jian-Guo Tian, Jian-Yu Zheng, Zhi-Yun Li, Shu-Qi Chen and Yan Zhu, “Active tuning of nonlinear absorption in a supramolecular zinc diphenylporphyrin-pyridine system”, *Opt. Exp.* 14, 2770-2775 (2006).
- [4] Zu-Bin Li, Jian-Guo Tian, Wen-Yuan Zhou, Wei-Ping Zang, and Chunping Zhang, “Periodic dielectric bars assisted enhanced transmission and directional light emission from a single subwavelength slit”, *Opt. Exp.* 14(18),8037-8042 (2006).
- [5] Wenbo Yan, Yongfa Kong, Lihong Shi, Hongde Liu, Xiaochun Li, Jingjun Xu, Shaolin Chen, Ling Zhang, Ziheng Huang, Shiguo Liu and Guangyin Zhang, “Investigations of centers formed in UV-light-induced absorption for LiNbO₃ highly doped with Mg and Hf”, *Opt. Exp.* 14(22), 10898-10906 (2006).
- [6] C. Lou, J. Xu, L. Tang, Z. Chen, P. G. Kevrekidis, “Symmetric and anti-symmetric solitons in two-dimensional lattices”, *Opt. Lett.* 31, 492-494 (2006).
- [7] Dengsong Zhu, Jingjun Xu, Haijun Qiao, Yanli Shi, Feng Gao, Wei Li, Bo Fu, Guoquan Zhang, Ke Zheng, “Ultraviolet photorefractive effect in Mg-doped near-stoichiometric LiNbO₃”, *Opt. Commun.* 266 (2), 582-585 (2006).
- [8] Fang Bo, Guoquan Zhang, Jingjun Xu, “Ultraslow Gaussian pulse propagation induced by a dispersive phase coupling in photorefractive bismuth silicon oxide crystals at room temperature”, *Opt. Commun.* 261, 349-352 (2006).
- [9] Feng Gao, Jingjun Xu, Haijun Qiao, Qiang Wu, Yin Xu, Guoquan Zhang, “Observation of superluminal and slowdown light propagation in doped lithium niobate crystals”, *Opt. Commun.* 257, 185-190 (2006).
- [10] Weiping Zang, Jianguo Tian, Zhibo Liu, Wenyuan Zhou, Feng Song, Chunping Zhang, “High-accuracy finite-difference beam-propagation method for cylindrical geometry”, *Appl. Phys. B* 82, 99-104 (2006).
- [11] Zhibo Liu, Yizhou Zhu, Yan Zhu, Shuqi Chen, Jianyu Zheng, Jianguo Tian, “Nonlinear absorption and nonlinear refraction of self-assembled porphyrins”, *J. Phys. Chem.* B110, 15140-15145 (2006).
- [12] Shu Qiang, Lin Yaowang, Xing Xiaodong, Yao Jianghong, “Effect of Small-angle scattering on the integer quantum Hall plateau”, *Chin. Phys. Lett.* 23(2), 436-439 (2006).
- [13] 余华, 孙健, 刘宝荣, 宋杰, 赵丽娟, 许京军, “Eu³⁺离子在微晶玻璃研究中的探针作用”, *物理学报* 55(11), 6152-6155 (2006)。

- [14] 舒强, 舒永春, 张冠杰, 刘如彬, “调制掺杂 GaAs/AlGaAs 2DEG 材料持久光电导及子带电子特性研究”, 物理学报 55(3), 1379-1383 (2006)。
- [15] 张冠杰, 徐波, 陈涌海, 姚江宏等, “不同淀积厚度 InAs 量子点的喇曼散射”, 半导体学报 27(6), 1012-1015 (2006)。
- [16] 林海波, 徐晓轩, 王斌, 吴彬麟, 许家林, 俞钢, 杨延勇, “Poly(3,4-ethylene dioxythiophene):Poly(styrene sulfonate)的共振拉曼光谱研究”, 光谱学与光谱分析 26(4), 646-648 (2006)。
- [17] 于舸, 徐晓轩, 吕淑华, 宋增福, 张存洲, 张春平, “乳腺组织形态基元共焦拉曼光谱的研究”, 光谱学与光谱分析 26 (5), 869-873 (2006)。
- [18] 张冠杰, 舒永春, 刘如彬, 舒强等, “光抽运垂直外腔面发射激光器特性与研究进展”, 激光技术 30(4), 351-354 (2006)。
- [19] 张冠杰, 陈涌海, 姚江宏, 舒强等, “InAlAs 量子点材料的 AFM 和拉曼散射研究”, 激光和光电子学进展 43(4), 68-72 (2006)。

Carrier dynamics in submonolayer InGaAs/GaAs quantum dots

Zhangcheng Xu^{a)} and Yating Zhang

Key Laboratory of Advanced Technique and Fabrication for Weak-Light Nonlinear Photonics Materials (Ministry of Education), TEDA College, Nankai University, Tianjin 300457, People's Republic of China and National Laboratory for Infrared Physics, Chinese Academy of Sciences, Yutian Road No. 500, Shanghai 200083, People's Republic of China

Jørn M. Hvam

Department of Communications, Optics and Materials, and Nano.DTU, Technical University of Denmark, DK-2800 Lyngby, Denmark

Jingjun Xu

Key Laboratory of Advanced Technique and Fabrication for Weak-Light Nonlinear Photonics Materials (Ministry of Education), Nankai University, Tianjin 300457, People's Republic of China

Xiaoshuang Chen and Wei Lu

National Laboratory for Infrared Physics, Chinese Academy of Sciences, Yutian Road No. 500, Shanghai 200083, People's Republic of China

(Received 4 March 2006; accepted 2 June 2006; published online 6 July 2006)

Carrier dynamics of submonolayer InGaAs/GaAs quantum dots (QDs) were studied by microphotoluminescence (MPL), selectively excited photoluminescence (SEPL), and time-resolved photoluminescence (TRPL). MPL and SEPL show the coexistence of localized and delocalized states, and different local phonon modes. TRPL reveals shorter recombination lifetimes and longer capture times for the QDs with higher emission energy. This suggests that the smallest SML QDs are formed by perfectly vertically correlated two-dimensional InAs islands, having the highest In content and the lowest emission energy, while a slight deviation from the perfectly vertical correlation produces larger QDs with lower In content and higher emission energy. © 2006 American Institute of Physics. [DOI: 10.1063/1.2219394]

Self-assembled quantum dots (QDs) can be grown either in the conventional Stranski-Krastanow (SK) mode or via submonolayer (SML) deposition.¹⁻⁵ SML InGaAs/GaAs QD heterostructures are verified to be a quantum-dot-quantum-well structure (QDQW), in which local clusters with higher In content are embedded in a lateral quantum well with lower In content.^{6,7} Although SML InGaAs QD lasers with high gain or power have been realized recently,^{5,8,9} very few works have been carried out on the carrier dynamics of SML QDs, as compared with SK QDs.^{1,10-12} The study of the carrier dynamics of SML QD structures is of great interest not only for the understanding of the fundamental physics of zero-dimensional structures but also for optoelectronic device applications.

In this letter, we use microphotoluminescence (MPL), selectively excited photoluminescence (SEPL), and time resolved photoluminescence (TRPL) to explore the localization, capture, and recombination of carriers in SML QD structures, at low temperature. We found that the capture time and the recombination lifetime of SML QDs depend strongly on the emission energy, which could be explained by analyzing the growth mechanism of SML QDs.

SML InGaAs/GaAs QDs was formed by alternate deposition of 0.5 ML InAs and 2.5 ML GaAs for ten times (see Ref. 6 for the details of the sample preparation). The MPL and SEPL were measured at 10 K, and the TRPL measurements were carried out at 5 K. In MPL, the incident light from a He-Ne laser at the wavelength of 632.8 nm was focused on the sample to a spot of around 2 μm in diameter. In

SEPL, a wavelength-tunable Ti:sapphire laser was used for excitation. In the TRPL setup, the sample was cooled in a liquid helium cryostat and excited in the GaAs barriers with 120 fs pulses from a Ti:sapphire laser at the wavelength of 800 nm and the PL signal was collected, dispersed, and synchronously detected using a streak camera with 2.5 ps time resolution. The excitation spots in both REPL and TRPL are about 50 μm in diameter.

The size distribution of QD ensembles could vary slightly with the position on the wafer as seen in Fig. 1(a) at low excitation density. The fine structures for the three spectra are different from each other showing emission from individual QDs. These features are reproducible so we could rule out the effect of noise. As the areal density of the SML

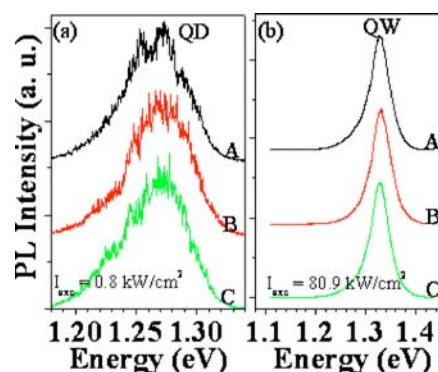


FIG. 1. (Color online) Microphotoluminescence spectra at 10 K at three different points on the wafer (A, B, and C) 1 mm apart, at low excitation power density (a) and at high excitation power density (b).

^{a)}Electronic mail: zcxu@nankai.edu.cn

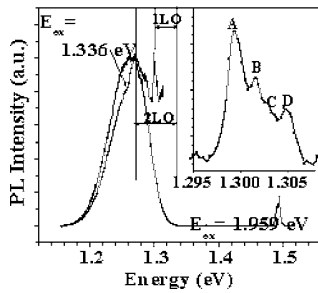


FIG. 2. (Color online) The PL spectra of the SML QD structure at the excitation energies of 1.959 eV above the GaAs barrier band gap and 1.336 eV just above the edge energy of the QW at 10 K. The inset zooms in the 1LO parts, and the solid line is a guide for the eye.

QDs is about $5 \times 10^{11} \text{ cm}^{-2}$ as reported in Ref. 6, about 15 000 SML QDs are probed at the same time. This explains the high density of sharp lines throughout the whole contour of the QD PL emission. At high excitation power density, a peak at 1.326 eV dominates the whole spectrum, and the peak energies for the three excitation points are identical, as shown in Fig. 1(b). This indicates that the peak at 1.326 eV originates from the delocalized states in the studied structure, corresponding to the QW states.⁷

In SEPL measurement with the excitation energy E_{ex} tuned near to the edge of the density of states (DOS) in the QW ($E_{\text{ex}} = 1.336 \text{ eV}$), a few sharp resonant lines and a resonant PL band appear within the broad PL band, near to one longitudinal optical [LO] (31–36 meV) and 2LO (66 meV) phonon energies below the excitation energy, respectively, as shown in Fig. 2. To confirm that these sharp lines are not attributed to resonant Raman scattering, the polarization directions of the incident laser beam and the detected PL signal were set to be along the [110] and the $[1, \bar{1}, 0]$ directions, respectively, in the backscattering geometry, as in Ref. 13. A Raman signal cannot be detected in this geometry, according to the selection rules.¹⁴ When the excitation energy is less than one GaAs LO-phonon energy above the lateral QW ground state in the SML-grown QDQW structure, the probability for the photon-excited carriers (excitons) to relax within the QW states by emission of only longitudinal acoustic (LA) phonons is less than the carrier (exciton) capture probability from QW to QDs by emission of LO phonons. Dots which can be accessed by emission of LO phonons are populated more efficiently, since their delta-function-like DOS can be accessed directly from the excited energy level in the QW by LO phonon emission.

The complex structure in the 1LO resonant peaks consists of several optical phonon modes whose energies are 36.7, 34.5, 32.9, and 31.3 meV, respectively, as shown in the inset of Fig. 2. We assign these lines to the LO phonon modes in the GaAs barrier, the GaAs/InAs interface, the InGaAs lateral QW, and the InGaAs QDs, respectively. The 2LO resonance occurs at the energy of 66 meV below the excitation energy, nearly two times the LO phonon energies of QW. The coexistence of several optical phonon modes indicates the complex structure of SML QDs.

The electron-hole ($e-h$) pairs (or excitons) generated in the GaAs barrier are either captured directly into the QW where they relax and are finally captured by the QDs, or they are directly captured by the QDs or recombine in the QW. Then the captured carriers will recombine inside the QDs.

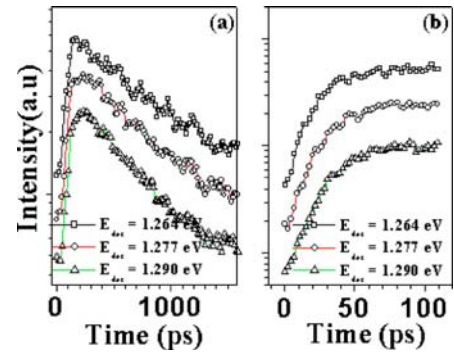


FIG. 3. (Color online) TRPL detected at different ground states of SML QDs at 5 K, (a) in the long time scale for the evaluation of the decay time; (b) in the short time scale for the evaluation of the rise time.

Figure 3 shows the PL transient of QD states in SML InGaAs/GaAs QD structures, at an excitation density of 101 W/cm^2 (corresponding to 10^{17} electron-hole pairs/ cm^3 pulse). On the long timescale [Fig. 3(a)], the PL decay can be well fitted by a monoexponential function, and the decay time τ_d can be evaluated. On the short timescale [Fig. 3(b)], the PL transients can be fitted by the expression¹⁵

$$I(t) \propto [\exp(-t/\tau_r) - \exp(-t/\tau_d)]/(\tau_r - \tau_d), \quad (1)$$

where τ_r is the rise time of PL transients, which can provide information on carrier capture into the QDs.

Fig. 4 shows the values of τ_d and τ_r plotted against the QD emission energy. With increasing QD transition energy, τ_d decreases from 840 to 500 ps, while τ_r increases from 35 to 60 ps.

For SK QDs, QDs with higher emission energy are believed to be smaller, and stronger electron-hole overlap occurs inside the QDs, resulting in longer lifetime.¹⁶ Recently, a reduction of the radiative lifetime for smaller SK QDs with higher emission energy has been observed, which was explained by the reduced electron-hole overlap integral due to the larger piezoelectric effect in larger QDs.¹⁷ However, in

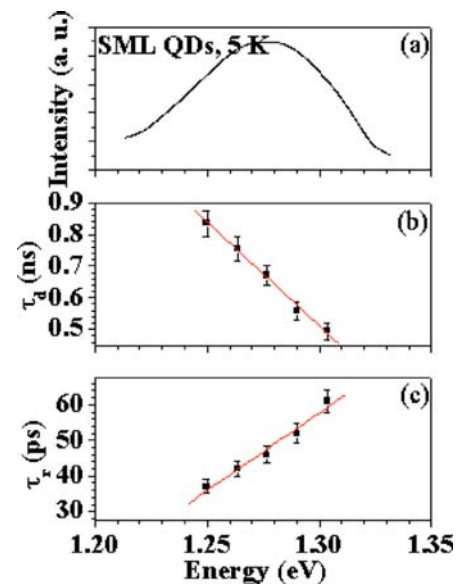


FIG. 4. (Color online) Dependence of the decay (rise) time with respect to the QD emission energy for SML QDs. (a) the integrated PL spectra; (b) the decay time; and (c) the rise time.

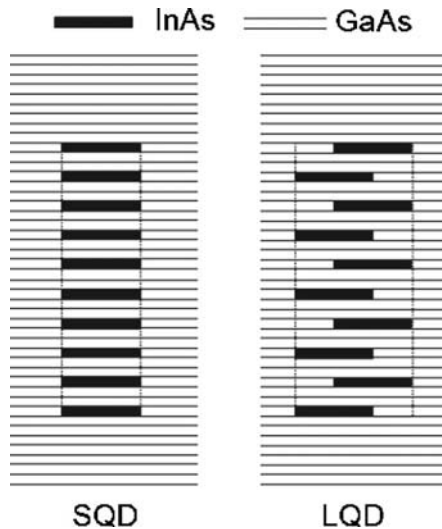


FIG. 5. (Color online) The schematic diagram showing the relationship between the size and average In content inside SML QDs. The QD regions are circled by the dotted lines. SJD and LQD are referred to as small QDs and larger QDs.

the case of SML QDs, the smallest QDs are formed by perfectly vertically correlated two-dimensional (2D) InAs islands,^{2,3,6,8} and have the highest In content, while slight deviation from the perfect vertical correlation produces larger QDs with lower In content, as schematically shown in Fig. 5. SML QDs with higher emission energy have larger lateral dimensions but the same height, as suggested by the in-plane transmission electron microscope (TEM) image in Ref. 6. The contrast of the image comes from the difference of In contents, the brighter parts have less In contents than the darker parts. Although it is not easy to distinguish the difference of In contents between the smaller and larger QDs, we can clearly see the contrast difference between the lateral InGaAs QWs (bright parts) with lower In contents and the QDs (darker papers) with higher In content. The lateral InGaAs QW structure is formed due to the random distribution of InAs 2D islands within the GaAs matrix. In some sense, the QW structure can be regarded as the largest QDs with the lowest In content. The observed shorter PL decay time for larger SML QDs with higher emission energy may thus be due to the enhanced overlap of the electron-hole wave functions. On the other hand, it is also possible that the exciton wave function extension increases, due to the coupling to QW states, with the increase of the QD emission energy, which will make the PL decay time even shorter.

Since thermalization and relaxation processes with the three-dimensional GaAs and the two dimensional QW occur on a much faster time scale,¹⁸ the measured rise time mainly reflects the capture process into the QD. When the density of carriers generated by each pulse is much higher than the QD density as in the present case, the carrier capture is mediated by Coulomb scattering (Auger process). According to Ref. 19, the Auger coefficient (capture time) decreases (increases) with the increase of the QD diameter, which coincides with the present result.

In summary, we have explored the carrier dynamics of an InGaAs/GaAs QDQW structure formed by submonolayer deposition. The coexistence of the localized states of QDs

and the delocalized states of QWs are revealed clearly in the MPL spectra. Different local phonon energies of the QDQW structure are obtained when the excitation energy is tuned close to the edge of DOS of QWs, indicating the complex structure of SML QDs. The recombination lifetime of SML QDs decreases with the increase of QD emission energy. This can be explained by assuming that SML QDs with higher emission energy have lower average In content and larger volume. The Auger carrier capture time for SML QDs increases with the increase of QD volume, which coincides with theoretical predictions.¹⁹

Enlightening discussions with Vadim Lyssenko and Dan Birkedal are gratefully acknowledged. This work has been supported in part by the National Natural Science Foundation of China (Grant Nos. 60444010, and 60506013), the Danish Technical Science Research Council, the SRF for ROCS (SEM), the Startup fund for new employees of Nankai University, the Marubun Research Promotion Foundation and the PCSIRT.

¹D. Bimberg, M. Grundmann, and N. N. Ledentsov, *Quantum Dot Heterostructures* (Wiley, New York, 1999).

²V. A. Shchukin and D. Bimberg, *Rev. Mod. Phys.* **71**, 1125 (1999).

³V. Bressler-Hill, A. Lorke, S. Varma, P. M. Petroff, K. Pond, and W. H. Weinberg, *Phys. Rev. B* **50**, 8479 (1994).

⁴N. N. Ledentsov, I. L. Krestnikov, M. Strabburg, R. Engelhardt, S. Rodt, R. Heitz, U. W. Pohl, A. Hoffmann, D. Bimberg, A. V. Sakharov, W. V. Lundin, A. S. Usikov, Z. I. Alferov, D. Litvinov, A. Rosenauer, and D. Gerthsen, *Thin Solid Films* **367**, 40 (2000).

⁵A. F. Zhukov, A. R. Kovsh, S. S. Mikhlin, N. A. Maleev, V. M. Ustinov, D. A. Livshits, I. S. Tarasov, D. A. Bedarev, M. V. Maximov, A. F. Tsatsulnikov, I. P. Soshnikov, P. S. Kopev, Z. I. Alferov, N. N. Ledentsov, and D. Bimberg, *Electron. Lett.* **35**, 1845 (1999).

⁶Z. C. Xu, D. Birkedal, J. M. Hvam, Z. Y. Zhao, Y. M. Liu, K. T. Yang, A. Kanjilal, and J. Sadowski, *Appl. Phys. Lett.* **82**, 3859 (2003).

⁷Z. C. Xu, K. Leosson, D. Birkedal, V. Lyssenko, J. M. Hvam, and J. Sadowski, *Nanotechnology* **14**, 1259 (2003).

⁸S. S. Mikhlin, A. E. Zhukov, A. R. Kovsh, N. A. Maleev, V. M. Ustinov, Y. M. Shernyakov, I. P. Soshnikov, D. A. Livshits, I. S. Tarasov, D. A. Bedarev, B. V. Volovik, M. V. Maximov, A. F. Tsatsulnikov, N. N. Ledentsov, P. S. Kopev, D. Bimberg, and Z. I. Alferov, *Semicond. Sci. Technol.* **15**, 1061 (2000).

⁹Z. C. Xu, D. Birkedal, M. Juhl, and J. M. Hvam, *Appl. Phys. Lett.* **85**, 3259 (2004).

¹⁰Thomas F. Boggess, L. Zhang, D. G. Deppe, D. L. Huffaker, and C. Cao, *Appl. Phys. Lett.* **78**, 276 (2001).

¹¹M. De Giorgi, C. Ling, G. von Plessen, J. Feldmann, S. De Rinaldis, A. Passaseo, M. De Vittorio, R. Cingolani, and M. Lomascolo, *Appl. Phys. Lett.* **79**, 3968 (2001).

¹²L. Ya. Karachinsky, S. Pellegrini, G. S. Buller, A. S. Shkolnik, N. Yu. Gordeev, V. P. Evtikhiev, and V. B. Novikov, *Appl. Phys. Lett.* **84**, 7 (2004).

¹³P. D. Wang, N. N. Ledentsov, and C. M. Sotomayor Torres, *J. Appl. Phys.* **79**, 7166 (1996).

¹⁴P. Y. Yu and Manuel Cardona, *Fundamentals of Semiconductors* (Springer, Berlin, 1996).

¹⁵B. Ohnesorge, M. Albrecht, J. Oshinowo, A. Forchel, and Y. Arakawa, *Phys. Rev. B* **54**, 11532 (1996).

¹⁶Gustavo A. Narvaez, Gabriel Bester, and Alex Zunger, *Phys. Rev. B* **72**, 245318 (2005).

¹⁷L. Ya. Karachinsky, S. Pellegrini, G. S. Buller, A. S. Shkolnik, N. Yu. Gordeev, V. P. Evtikhiev, and V. B. Novikov, *Appl. Phys. Lett.* **84**, 7 (2004).

¹⁸J. Shah, *Ultrafast Spectroscopy of Semiconductors and Semiconductor Nanostructures, Solid-State Sciences* (Springer-Verlag, Berlin 1999).

¹⁹I. Magnusdottir, S. Bischoff, A. V. Uskov, and J. Mørk, *Phys. Rev. B* **67**, 205326 (2003).

Enhanced photorefractive properties of LiNbO₃:Fe crystals by HfO₂ codoping

Shuqi Li, Shiguo Liu, Yongfa Kong,^{a)} Jingjun Xu, and Guangyin Zhang

The MOE Key Laboratory of Advanced Technique and Fabrication for Weak-Light Nonlinear Photonics Material, Nankai University, Tianjin 300457, China

(Received 5 June 2006; accepted 17 July 2006; published online 8 September 2006)

Photorefractive properties of congruent lithium niobate crystals codoped with HfO₂ and Fe₂O₃ were investigated and it was found that Fe ions are still located at Li sites as photorefractive centers when the doping concentration of HfO₂ goes above the threshold value. As a result, their photorefractive response speed and sensitivity are significantly enhanced. Meanwhile, the high saturation diffraction efficiency is still maintained. Experimental results definitely show that Hf is now the most effective doping element for LiNbO₃:Fe crystal to improve its photorefractive properties. © 2006 American Institute of Physics. [DOI: 10.1063/1.2349306]

Lithium niobate (LiNbO₃, LN) crystal is one of the most widely used photorefractive materials in the holographic volume storage. Transition-metal elements, such as Fe, Cu, and Mn, are usually added into LiNbO₃ to improve its photorefractive characteristics.¹ Among them, Fe₂O₃ doped LiNbO₃ (LiNbO₃:Fe) is one of the most excellent candidate materials for optical data storage due to its high diffraction efficiency, high photorefractive sensitivity, high data storage density, long storage lifetime, and well-considered thermally fixing method. However, several problems, such as low response speed and strong light-induced scattering, impede the application of LiNbO₃:Fe crystal in holographic volume storage. Doping with damage-resistant elements, such as Mg, Zn, In, and Sc, has been found to be a useful way to solve these problems.²⁻⁵ It has been known that there exist threshold concentrations for these dopants. When the doping concentrations are above the threshold values, most of the Fe ions on the Li sites will be repelled by these damage-resistant ions to the Nb sites. As a result, response speed and photorefractive sensitivity are remarkably improved, nevertheless diffraction efficiency will apparently decrease.

Recently, hafnium was found to be another optical damage-resistant element and its doping threshold concentration is about 4 mol % in the melt.⁶⁻⁸ Dissimilar to Mg²⁺, Zn²⁺, In³⁺, and Sc³⁺, Hf⁴⁺ is a tetravalent ion and its valence is higher than that of Fe^{2+/3+}, which suggests that the photorefractive properties of LiNbO₃:Fe crystals codoped with HfO₂ are likely to be different from those codoped with other damage-resistant elements. In this letter, the holographic properties of LiNbO₃ codoped with HfO₂ and Fe₂O₃ (LiNbO₃:Fe:Hf) are investigated by holographically recording experiments. It is very interesting to find that Fe ions still locate at Li sites when the doping concentration of HfO₂ exceeds the threshold value, and therefore the photorefractive response speed and sensitivity are greatly improved while the high diffraction efficiency is maintained.

In the experiments, three congruent LiNbO₃ crystals codoped with 0.03% Fe and different concentrations of HfO₂ were investigated. The congruent composition was selected as [Li]/[Nb]=48.38/51.62. Their HfO₂-doping concentra-

tions are 2, 4, and 5 mol %, respectively, with which the samples are marked as LN:Fe:Hf₂, LN:Fe:Hf₄, and LN:Fe:Hf₅, as in Table I. The crystals were grown in air by the Czochralski method along the *c* axis with the pulling rate of 1 mm/h and the rotation speed of 12 rpm. After the annealing treatment and artificial polarization, the crystal sheets with the thicknesses of 1 and 3 mm were cut along the *y* faces and optically polished.

Holographic experiment was carried out with the 3 mm thick plates in a traditional holographically recording configuration, in which a 532 nm diode laser was used. Two mutually coherent and extraordinary polarized beams with equal intensity of 250 mW/cm² were used as writing beams at a crossing angle of 23° on the incident crystal surface. The grating vector was aligned along the *c* axis to utilize the largest electro-optic coefficient *r*₃₃. The measured diffraction efficiency η was defined as $I_d/(I_d+I_t)$, where I_d and I_t were the diffracted and transmitted intensities of the readout beam, respectively.

The recording behavior of the single grating in LiNbO₃:Fe:Hf could be well described by a function of $\eta(t) = \eta_{\text{sat}}[1 - \exp(-t/\tau_r)]$, where τ_r is the recording time constant and η_{sat} is the saturation diffraction efficiency. The photorefractive sensitivity *S* was defined as $S = (d\sqrt{\eta}/dt)_{t=0}/(IL)$, where *I* is the total recording light intensity and *L* is the crystal thickness. Table I describes the photorefractive properties of LiNbO₃:Fe:Hf crystals, in which the data for Fe doped and Mg and Fe codoped LiNbO₃ crystals are also listed for comparison.

Under low illumination intensity (in mW/cm²), the holographically recording time in LiNbO₃:Fe is usually of the order of minutes. However, our experimental results in Table I show that the response rate and sensitivity in our samples increase greatly with the increase of Hf-doping concentrations. When the HfO₂-doping concentration is 2 mol % in the melt, i.e., below its threshold value, the maximum diffraction efficiency of 68% is obtained. Meanwhile, the response time is reduced to 17.2 s. When the HfO₂-doping concentration increased to 5 mol %, the response time decreased to 10.7 s while the saturation diffraction efficiency was kept as high as 55.4%. But for Mg and Fe codoped LiNbO₃,² when MgO-doping concentration increases from 2 to 6 mol %, namely, from below to above its threshold

^{a)} Author to whom correspondence should be addressed; electronic mail: kongyf@nankai.edu.cn

TABLE I. Photorefractive properties of Fe doped, Mg and Fe codoped, and Hf and Fe codoped LN crystals. Incident power density of a single beam used for Hf and Fe codoped samples was approximately 250 mW/cm².

Sample	Doping concentrations			Photorefractive properties			Refs.
	Fe (wt %)	Mg (mol %)	Hf (mol %)	η_{sat} (%)	τ_r (s)	S (cm/J)	
LN:Fe	0.01			70	160		2
LN:Fe:Mg ₂	0.01	2		70	60		2
LN:Fe:Mg ₆	0.01	6		15	15		2
LN:Fe:Hf ₂	0.03		2	68.0	17.2	3.99	This work
LN:Fe:Hf ₄	0.03		4	47.6	12.6	4.36	This work
LN:Fe:Hf ₅	0.03		5	55.4	10.7	5.23	This work

concentration (the threshold concentration of MgO is about 4.6 mol % in melt⁹), the recording speed is increased 4 times, while the maximum diffraction efficiency is reduced 4.7 times.

The holographic properties of LiNbO₃ crystal mainly depend on its photorefractive centers. In LiNbO₃:Fe crystal, the photovoltaic effect is the dominant charge-transport mechanism¹⁰ and the dominant charge carriers are electrons.¹¹ Hence in our samples, Hf ions do not participate in the charge-transport process and Fe ions also play a dominant role. However, the codoped hafnium ions may affect concentrations and incorporation of other ions, which contribute to the photoconductivity σ_{ph} . As for LN:Fe:Hf₂, 2 mol % of the Hf-doping concentration is below its threshold concentration, thus there exists a small portion of antisite Nb ions (Nb on Li sites, Nb_{Li}) in the sample, which is the most probable electron acceptor in a Li-deficient LiNbO₃ host. When the HfO₂-doping concentration is above its threshold value, Nb_{Li} are completely removed and photoconductivity σ_{ph} greatly increases,⁷ which makes the response speed and the photorefractive sensitivity enhanced.

The OH⁻ absorption spectra and UV-visible absorption spectra of our 1 mm thick plates were measured with a Magna-560 Fourier transform infrared spectrophotometer and a Beckman DU-8B spectrophotometer, respectively, with the incident light transmitting along the *y* axis at room temperatures. Figure 1 shows the OH⁻ absorption spectra of our samples, in which the absorption band is situated at about 3484 cm⁻¹ for LN:Fe:Hf₂ and located near 3487 cm⁻¹ for LN:Fe:Hf₄ and LN:Fe:Hf₅. These experimental results are the same as those obtained in single doped LiNbO₃:Hf crystals,⁸ where the presence of 3487 cm⁻¹ absorption band indicates that the Hf-doping concentration has reached its

threshold level and Hf has occupied normal Nb sites. In Mg and Fe codoped LiNbO₃ crystals with its MgO-doping concentrations above threshold, besides 3535 cm⁻¹ absorption band related with Mg_{Nb}²⁺-OH⁻ complex, another peak corresponding to the vibration of Fe_{Nb}³⁺-OH⁻ appears at 3507 cm⁻¹.^{12,13} It should be noted that 3507 cm⁻¹ absorption band is not present in LN:Fe:Hf₄ and LN:Fe:Hf₅, which suggests that the lattice locations of Fe³⁺ ions are unaltered and still located at Li sites in spite of HfO₂-doping concentrations above its threshold value. As we know, when Mg-doping concentration goes above its threshold, Fe³⁺ ions will move from Li sites to Nb sites and the light-induced refractive index change can be greatly reduced. Some researchers^{14,15} attribute this reduction of photorefractive properties to an abrupt decrease of the capture cross section of electrons by Fe³⁺ and therefore the sharp increase of photoconductivity. When the concentration of Hf exceeds its threshold concentration, all antisite defects Nb_{Li} are cleared up and thus response time is shortened greatly, nevertheless Fe³⁺ ions are still located at Li sites acting as electron acceptors, therefore, the saturation diffraction efficiency of LN:Fe:Hf₅ crystal does not greatly decrease with respect to the sample of LN:Fe:Hf₂. However, η_{sat} for LN:Fe:Hf₄ is somewhat lower than that for LN:Fe:Hf₅, which might be due to slightly lower Fe concentration in LN:Fe:Hf₄, especially those of Fe²⁺ ions. This supposition is partly proved by the UV-visible absorption spectra.

Figure 2 shows UV-visible transmission curves of these crystals, from which we can see that there is an apparent absorption band from the absorption edge to the wavelength of longer than 700 nm for LN:Fe:Hf₂ and LN:Fe:Hf₅ crystals, corresponding to Fe²⁺ ion absorption.¹⁶ It is easily shown that the shape for LN:Fe:Hf₅ is almost similar to that

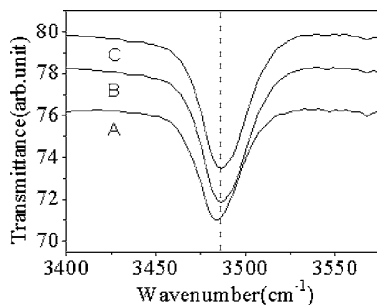


FIG. 1. OH⁻ absorption spectra of LiNbO₃ crystals codoped with 0.03% Fe and different concentrations of Hf. A, B, and C is for 2, 4, and 5 mol % Hf, respectively.

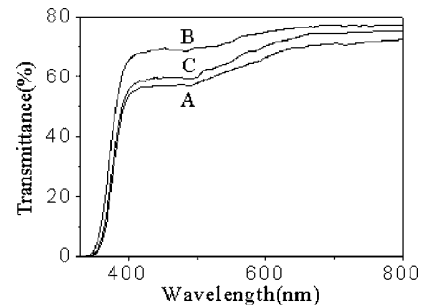


FIG. 2. Transmittance curves for as-grown LiNbO₃ crystals codoped with 0.03% Fe and 2 mol % Hf (curve A), 4 mol % Hf (curve B), and 5 mol % Hf (curve C), respectively.

TABLE II. Photorefractive properties for reduced LN:Fe:Hf crystals.

Sample	η_{sat} (%)	τ_r (s)	S (cm/J)
LN:Fe:Hf ₂	51.2	9.9	6.77
LN:Fe:Hf ₄	47.0	6.7	7.65
LN:Fe:Hf ₅	45.4	2.6	12.6

for LN:Fe:Hf₂, which means that the optical properties of Fe²⁺ ions are unchanged with the increase of HfO₂-doping concentration up to 5 mol %. As it has been commented above, Fe³⁺ ions also remain at Li sites in LN:Fe:Hf₅ crystal, and the valence state of Fe²⁺ is lower than that of Fe³⁺ ions. We believe that Fe²⁺ ions are also located at Li sites as donor centers. But for LN:Fe:Hf₄, there is no such an obvious broadband absorption, and a noticeable blueshift of its absorption edge can be observed. This observed difference implies that the involvement of total Fe as well as Fe²⁺ ions in LN:Fe:Hf₄ is somewhat lower than those of our other two samples and hence the small number of effective electrons is available. As a result, LN:Fe:Hf₄ crystal shows a lower η_{sat} .

It is known that the photoconductivity and photorefractive sensitivity of Fe doped LiNbO₃ crystals can be optimized for holographic data storage by thermally reducing or oxidizing treatments. The reduction treatment for our samples was also accomplished in an argon atmosphere at 750 °C for 30 min. The holographic properties for these reduced crystals are shown in Table II. As expected, the maximum diffraction efficiency slightly decreases, while the response speed and sensitivity are further improved by reduction treatment. It is obvious that photorefractive properties for LN:Fe:Hf₅ are much more excellent than those for LN:Fe:Mg₆. The shortest response time exhibited in LN:Fe:Hf₅ is only 2.6 s while it still shows a large saturation diffraction efficiency of 45.4%. In iron doped LN crystals, the heavy reduction will aggravate absorption, which results in strong record light energy loss. Doping with HfO₂ is a good solution for this problem. In our experiments, the ratio of the transmitting intensity to the incident intensity could be as high as 40% for the reduced LN:Fe:Hf₅.

In summary, the effects of incorporating Hf⁴⁺ ions into LiNbO₃:Fe crystals were studied by holographic measurement. Dissimilar to Mg²⁺ (or Zn²⁺, In³⁺) and Fe codoped LiNbO₃ crystals, Fe ions still remain at Li sites in LiNbO₃:Fe:Hf crystals when the HfO₂-doping concentration goes above its threshold value, as a result, the response rate and sensitivity are greatly improved. Meanwhile, the saturation diffraction efficiency remains at a high value. Therefore, hafnium ion is now the most efficient one among optical damage-resistant ions to improve the photorefractive properties of LiNbO₃:Fe crystal.

This work was partly supported by Program for Changjiang Scholars and Innovative Research Team in University and the National Natural Science Foundation of China (60578019 and 90501004).

- ¹W. Phillips, J. J. Amodei, and D. L. Staebler, *RCA Rev.* **33**, 94 (1972).
- ²G. Zhang, J. Xu, S. Liu, Q. Sun, G. Zhang, Q. Fang, and C. Ma, *Proc. SPIE* **14**, 2529 (1995).
- ³T. R. Volk, N. V. Razumovski, A. V. Mamaev, and N. M. Rubinina, *J. Opt. Soc. Am. B* **13**, 1457 (1996).
- ⁴Y. Guo, Y. Liao, L. Cao, G. Liu, Q. He, and G. Jin, *Opt. Express* **12**, 5556 (2004).
- ⁵W. Zheng, B. Liu, J. Bi, and Y. Xu, *Opt. Commun.* **246**, 297 (2005).
- ⁶E. P. Kokanyan, L. Razzari, I. Cristiani, V. Degiorgio, and J. B. Gruber, *Appl. Phys. Lett.* **84**, 1880 (2004).
- ⁷L. Razzari, P. Minzioni, I. Cristiani, V. Degiorgio, and E. P. Kokanyan, *Appl. Phys. Lett.* **86**, 131914 (2005).
- ⁸S. Li, S. Liu, Y. Kong, D. Deng, G. Gao, Y. Li, H. Gao, L. Zhang, Z. Hang, S. Chen, and J. Xu, *J. Phys.: Condens. Matter* **18**, 3527 (2006).
- ⁹G. Zhong, J. Jin, and Z. Wu, *Proceedings of the 11th International Quantum Electronics Conference*, IEEE Cat. No. 80 CH1561-0, New York, 1980, p. 631.
- ¹⁰A. M. Glass, D. von der Linder, and T. J. Negran, *Appl. Phys. Lett.* **25**, 233 (1974).
- ¹¹D. L. Staebler and J. J. Amodei, *J. Appl. Phys.* **43**, 1042 (1972).
- ¹²L. Kovács, Zs. Szaller, I. Cravero, I. Földvari, and C. Zaldo, *J. Phys. Chem. Solids* **51**, 417 (1990).
- ¹³Y. Kong, J. Xu, W. Zhang, and G. Zhang, *J. Phys. Chem. Solids* **61**, 1331 (2000).
- ¹⁴D. A. Bryan, R. Gerson, and H. E. Tomaschke, *Appl. Phys. Lett.* **44**, 847 (1984).
- ¹⁵T. R. Volk, V. I. Pryalkin, and N. M. Rubinina, *Opt. Lett.* **15**, 996 (1990).
- ¹⁶O. F. Schirmer, O. Thiemann, and M. Wöhlecke, *J. Phys. Chem. Solids* **52**, 185 (1991).

Active tuning of nonlinear absorption in a supramolecular zinc diphenylporphyrin-pyridine system

Zhi-Bo Liu¹, Jian-Guo Tian^{1*}, Jian-Yu Zheng², Zhi-Yun Li², Shu-Qi Chen¹, and Yan Zhu²

1 The Key Laboratory of Advanced Technique and Fabrication for Weak-Light Nonlinear Photonics Materials, Ministry of Education, and TEDA Applied Physical School, Nankai University, Tianjin 300457, China

2 State Key Laboratory of Elemento-Organic Chemistry, Nankai University, Tianjin, 300071, China
jjtian@nankai.edu.cn

Abstract: We report on an active tuning of nonlinear absorption from reverse saturable absorption to saturable absorption in supramolecular zinc diphenylporphyrins by the combination of molecular and supramolecular levels at 532, 542 and 552 nm. Firstly, the modifications of molecular structures with bromination result in a discrete but regular change in magnitude and sign of nonlinear absorption (NLA). Furthermore, a fine tuning of NLA was obtained by the intermolecular weak interaction of pyridine and zinc porphyrins. Using an association model, we theoretically simulate the change of NLA. Compared with modifying molecular structures of conventional organic materials, the weak intermolecular interaction of supramolecular porphyrins has another advantage that it can be realized more easily and flexibly to change NLA.

©2006 Optical Society of America

OCIS codes: (190.4710) Optical nonlinearities in organic materials; Reverse saturable absorption; Saturable absorption; (160.4330) Nonlinear optical materials; (300.1030) Absorption.

References and links

1. D. S. Chemla, and J. Zyss, eds. *Nonlinear Optical Properties of Organic Molecules and Crystals*. (Academic Press, Orlando, FL, 1987)
2. P. N. Prasad and D. J. Williams, *Introduction to Nonlinear Optical Effects in Molecules and Polymers*. (Wiley, New York 1991).
3. H. S. Nalwa, S. Miyata, eds. *Nonlinear Optics of Organic Molecules and Polymers*. (CRC Press, Boca Raton, FL, 1997).
4. G. de la Torre, P. Vazquez, F. Agullo-Lopez, and T. Torres, "Role of structural factors in the nonlinear optical properties of phthalocyanines and related compounds," *Chem. Rev.* **104**, 3723 (2004).
5. S. R. Marder, C. B. Gorman, F. Meyers, J. W. Perry, G. Bourhill, J. L. Bredas, and B. M. Pierce, "A unified description of linear and nonlinear polarization in organic polymethine dyes," *Science* **256**, 632 (1994).
6. K. McEwan, K. Lewis, G. Y. Yang, L. L. Chng, Y. W. Lee, W. P. Lau, and K. S. Lai, "Synthesis, characterization, and nonlinear optical study of metalloporphyrins," *Adv. Funct. Mater.* **13**, 863 (2003).
7. A. Karotki, M. Drobizhev, M. Kruk, C. Spangler, E. Nickel, N. Mamardashvili, and A. Rrbane, "Enhancement of two-photon absorption in tetrapyrrolic compounds," *J. Opt. Soc. Am. B* **20**, 321 (2003).
8. C. Bosshard, R. Spreiter, P. Gunter, R. R. Tykwinski, M. Schreiber, and F. Diederich, "Structure-property relationships in nonlinear optical tetraethynylethenes," *Adv. Mater.* **8**, 231 (1996).
9. M. Calvete, G. Y. Yang, and M. Hanack, "Porphyrins and phthalocyanines as materials for optical limiting," *Synth. Met.* **141**, 231 (2004).
10. J. M. Lehn, "Perspectives in supramolecular chemistry: from molecular recognition towards molecular information processing and self-organization," *Angew. Chem. Int. Ed. Engl.* **29**, 1304 (1990).
11. S. M. Kuebler, R. G. Denning, H. L. Anderson, "Large third-order electronic polarizability of a conjugated porphyrin polymer," *J. Am. Chem. Soc.* **122**, 339 (2000).
12. K. Ogawa, T. Zhang, K. Yoshihara, Y. Kobuke, "Large third-order optical nonlinearity of self-assembled porphyrin oligomers," *J. Am. Chem. Soc.* **124**, 22 (2002).

13. K. Ogawa, A. Ohashi, Y. Kobuke, K. Kamada, and K. Ohta, "Strong two-photon absorption of self-assembled butadiyne-linked bisporphyrin," *J. Am. Chem. Soc.* **125**, 13356(2003).
14. W. Blau, H. Byrne, W. M. Dennis, and J. M. Kelly, Reverse saturable absorption in tetraphenylporphyrins. *Opt. Commun.* **56**, 25 (1985).
15. N. M. B. Neto, L. D. Boni, C. R. Mendonca, L. Misoguti, S. L. Queiroz, L. R. Dinelli, A. A. Batista, and S. C. Zilio, "Nonlinear absorption dynamics in tetrapyrrolyl metalloporphyrins," *J. Phys. Chem. B* **109**, 17340 (2005).
16. K. McEwan, P. Fleitz, J. Rogers, J. Slagle, D. McLean, H. Akdas, M. Katterle, I. Blake, and H. Anderson, "Reverse saturable absorption in the near-infrared by fused porphyrin dimmers," *Adv. Mater.* **16**, 1933 (2004).
17. W. J. Su, T. M. Cooper, and M. C. Brant, "Investigation of reverse-saturable absorption in brominated porphyrins," *Chem. Mater.* **10**, 1212 (1998).
18. L. W. Tutt, and A. Kost, "Optical limiting performance of C₆₀ and C₇₀ solutions," *Nature* **356**, 225 (1992).
19. J. W. Perry, K. Mansour, I. Y. S. Lee, X. L. Wu, P. V. Bedworth, C. T. Chen, D. Ng, S. R. Marder, P. Miles, T. Wanda, M. Tian, and H. Sasabe, "Organic optical limiter with a strong nonlinear absorptive response," *Science* **273**, 1533 (1996).
20. C. P. Singh, K. S. Bindra, B. Jain, and S. M. Oak, "All-optical switching characteristics of metalloporphyrins," *Opt. Commun.* **245**, 407 (2005).
21. S. Roy, and K. Kulshrestha, "Theoretical analysis of all-optical spatial light modulation in organometallics based on triplet state absorption dynamics," *Opt. Commun.* **252**, 275 (2005).
22. M. Sheik-Bahae, A. A. Said, T. H. Wei, D. J. Hagan, and E. W. Van Stryland, "Sensitive measurement of optical nonlinearities using a single beam," *IEEE J. Quantum Electron* **26**, 760 (1990).
23. P. P. Kiran, D. R. Reddy, B. G. Maiya, A. K. Dharmadhikari, G. R. Kumar, and N. R. Desai, "Enhanced optical limiting and nonlinear absorption properties of azoarene-appended phosphorus (V) tetratolylporphyrins," *Appl. Opt.* **41**, 7631 (2002).
24. Z. B. Liu, J. G. Tian, W. P. Zang, W. Y. Zhou, F. Song, C. P. Zhang, J. Y. Zheng, and H. Xu, "Flexible alteration of optical nonlinearities of iodine charge-transfer complexes in solutions," *Opt. Lett.* **29**, 1099 (2004).
25. A. Satake, and Y. Kobuke, "Dynamic supramolecular porphyrin systems," *Tetrahedron* **61**, 13 (2005).
26. H. J. Schneider, R. Kramer, S. Simova, and U. Schneider, "Solvent and salt effects on binding constants of organic substrates in macrocyclic host compounds. a general equation measuring hydrophobic binding contributions," *J. Am. Chem. Soc.* **110**, 6442 (1988).
27. P. Bhyrappa, V. Krishnan, and M. Nethaji, "Solvation and axial ligation properties of (2,3,7,8,12,13,17,18-octabromo-5,10,15,20-tetraphenylporphyrinato)zinc(II)," *J. Chem. Soc. Dalton Trans.* **12**, 1901 (1993).

1. Introduction

Organic nonlinear optical (NLO) materials have been thought of as one of prospective materials because of their potential flexibility and variability [1-3]. To enhance and control optical nonlinearities, the structure-nonlinearity relationship has been investigated in large numbers of organic materials [4-9]. However, it is difficult to realize a fine-tuning and large enhancement of optical nonlinear coefficients, if only depending on the modifications of molecular structures. The emergence of supramolecular chemistry, the chemistry beyond the molecule, brought a new chance to the development of organic NLO materials due to the introduction of a weak intermolecular interaction called non-covalent bond [10]. For example, optical nonlinearities have been enhanced about 2-3 orders of magnitude in supramolecular porphyrins [11-13].

Porphyrins are well known to exhibit excited state absorption (ESA), including reverse saturable absorption (RSA) and saturable absorption (SA), in the visible wavelength range [14, 15] and even near-infrared wavelength range [16]. As a type of nonlinear absorption (NLA), ESA is usually described by a five-level model [17]. It is caused by the further promotion of the excited electron from the first excited state (S_1 or T_1) to a higher-lying state (S_n or T_n) after the electrons in ground state were excited. The singlet excited state cross-section σ_S and triplet excited state cross-section σ_T are larger or smaller than that of ground state σ_0 for RSA or SA, respectively. In this paper, we report an active tuning of NLA from RSA to SA by supramolecular incorporation of pyridine into zinc diphenylporphyrins at 532, 542, and 552 nm. This method can provide a simple and convenient route to change NLA of porphyrins materials in practical applications, such as optical limiting [18, 19], optical switching [20], and spatial light modulation [21], etc.

2. Experiment section

A series of diphenylporphyrins we synthesized have been characterized by ^1H NMR recorded on a Bruker Av300 spectrometer and MALDI-TOF-MS spectra using a Thermo Finnign LCQ Advantage mass spectrometer. UV absorption spectra and titration spectra were recorded at 25°C on a Cary 300 UV spectrophotometer, using a quartz cell of 1cm path length. The concentrations of all porphyrins are 1.0×10^{-6} M for UV spectra in chloroform. In titration measurements, a aliquot of a solution of pyridine (5.0×10^{-3} M in chloroform) was added to a solution of zinc porphyrins (2.0×10^{-5} M in chloroform), and the resulting solutions were subjected to linear absorption spectroscopy at 25°C . Each spectrum was corrected with a dilution factor and background subtraction. In measurements of nonlinear absorption using Z-scan technique, a Q-switched Nd:YAG laser (Continuum Surelite-II) and a mode-locked Nd:YAG laser (Continuum Model PY61) were used to generate 5-ns pulses and 30-ps pulses at the wavelength of 532 nm. The lasers at 512 nm, 542 nm, and 552 nm are from a commercial optical parametric oscillator (Continuum Panther OPO) pumped by the third harmonic (355 nm) from Continuum Surelite-II with a repetition rate of 10 Hz and tunable in the range of 420-2500 nm, and the pulse duration is about 4-5 ns. The beam waist was 18-24 μm for different wavelengths and different pulse duration. The incident and transmitted pulse energies were measured simultaneously with two energy detectors (Molelectron J3S-10). All of solutions of porphyrins used in Z-scan measurements had a concentration of 2.0×10^{-4} M and were poured in a 1-mm quartz cuvette.

3. Results and discussion

The spectra and structures of diphenylporphyrins used in our experiments are shown in Fig. 1(a). There are about 10nm red-shift in both Soret and Q bands as bromination increases. Nonlinear absorption measurements were carried out by the open-aperture Z-scan technique [22]. Figure 1(b) gives the open-aperture Z-scan curves of three porphyrins with 5-ns pulse duration at 532 nm, and the solid lines are theoretical fitting curves. The change of open-aperture Z-scan curves from peak to valley indicated that a transition from SA to RSA happens with bromination. Since the ESA is dominated by absorption of triplet excited states ($T_1 \rightarrow T_n$) in the case of nanosecond pulsed laser incidence, and by absorption of singlet excited states ($S_1 \rightarrow S_n$) in the case of picosecond pulsed laser incidence [23], to exactly obtain the value of σ_S , we have also performed Z-scan experiments of picosecond pulsed laser. The photophysical parameters of ZnDPP, ZnDPPBr, and ZnDPPBr₂ obtained are shown in Tab. 1, where τ_0 and τ_{ISC} are the lifetime of S_1 and the intersystem crossing time of $S_1 \rightarrow T_1$, respectively.

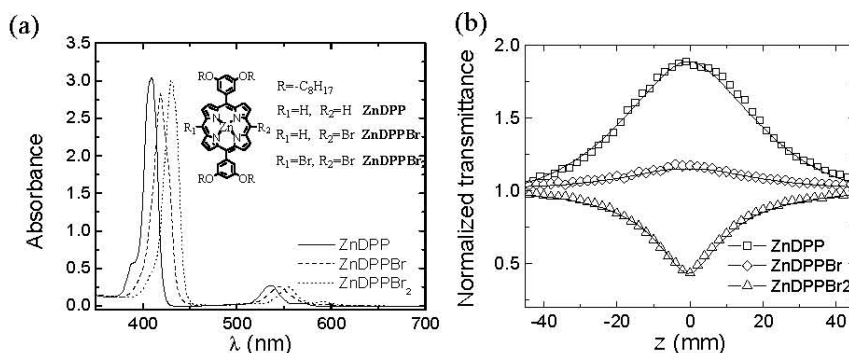


Fig. 1. The linear and nonlinear absorption data of ZnDPP, ZnDPPBr, and ZnDPPBr₂. (a) Molecular structures and Linear absorption spectra. (b) Open-aperture Z-scan curves with 5-ns pulse duration at 532nm. Symbols represent experimental data; solid lines are theoretical fittings using a five-level model.

Table 1. Photophysical parameters of ZnDPP, ZnDPPBr, and ZnDPPBr₂

Material	Soret-bands λ_{\max} (nm)	Q-bands λ_{\max} (nm)	σ_0 (10^{-17}cm^2)	σ_s (10^{-17}cm^2)	σ_T (10^{-17}cm^2)	τ_0 (ns)	τ_{ISC} (ns)
ZnDPP	409	536	8.72	2.5	2.7	5.0	3.0
ZnDPPBr	419	545	4.25	3.4	3.6	3.0	7.0
ZnDPPBr ₂	430	554	1.26	4.6	4.8	0.7	5.0

The modifications of molecular structures by bromination result in a discrete but regular change in magnitude and sign of NLA. However, in practical application of NLA, such as optical limiting, all optical switching, and spatial light modulation, it may be necessary to continuously tune NLA. Using solvent effect, we have obtained flexible alteration of optical nonlinearities in the solutions of iodine [24], but the nature of solvent effect remains unclear. Since weak interactions in supramolecular porphyrins can provide a sufficient thermodynamic driving force to influence optical properties of system, here we utilize the binding model of the pyridine group coordinated to zinc porphyrins, which has been intensively investigated [25], to manipulate the fine-tuning process. Pyridine is chosen as a ligand in our study because it has almost no nonlinear response in visible-wavelength region, and simple 1:1 porphyrin-pyridine (Por-Py) complexes can be obtained.

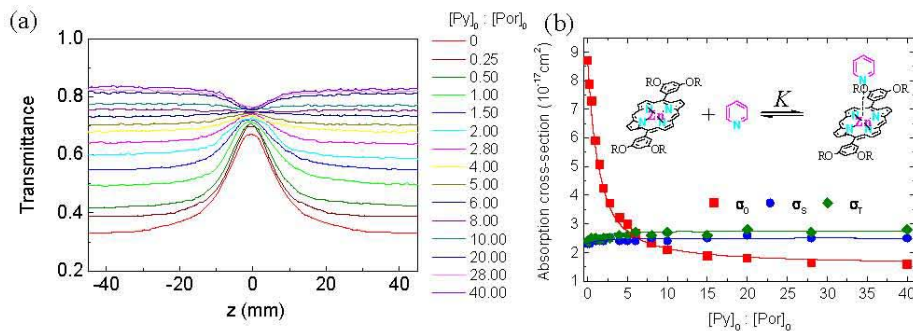


Fig. 2. Change of nonlinear absorption for ZnDPP with various concentration of pyridine. (a) Open-aperture Z-scan curves of at 532nm. (b) Absorption cross-sections of ground and excited states vs $[\text{Py}]_0:[\text{Por}]_0$. The solid lines are fittings with $K=0.48 \times 10^4 \text{ M}^{-1}$ using association model. Inset gives the equilibrium equation between zinc porphyrins and pyridine.

Figure 2 shows the open-aperture Z-scan curves in the case of nanosecond pulsed laser incidence and absorption cross-sections of ground and excited states of ZnDPP with the change of concentration of pyridine at 532 nm. In our measurements, the concentration of zinc porphyrins was kept unchanged. It should be noted that the transmittances in Fig. 2(a) are not normalized by linear transmittance, not like that in Fig. 1(b). As the concentration of pyridine increased, more Por-Py was formed, which led to a drastic decrease of linear absorption (see the transmittance change at both sides of Z-scan curves), but a small change of ESA in nonlinear region (see the transmittance change at the focus). Under the co-effect of linear absorption and ESA, a transition from SA to RSA with gradual change is shown in Fig. 2(a). From Fig. 2(b), we can see the changes of linear absorption and ESA more clearly.

The equilibrium equation between porphyrin and pyridine due to zinc-pyridine interaction is given in the inset of Fig. 2(b), where

$$K = \frac{[\text{Por} \cdot \text{Py}]}{[\text{Por}][\text{Py}]} = \frac{[\text{Por} \cdot \text{Py}]}{([\text{Por}]_0 - [\text{Por} \cdot \text{Py}])([\text{Py}]_0 - [\text{Por} \cdot \text{Py}])} \quad (1)$$

is the association constant [26], and $[\text{Por}\cdot\text{Py}]$, $[\text{Por}]$, and $[\text{Py}]$ are the equilibrium concentrations of zinc Por-Py complex, zinc porphyrin, and pyridine, while $[\text{Por}]_0$ and $[\text{Py}]_0$ are the total concentrations of zinc porphyrin and pyridine, respectively. Because the $[\text{Por}]_0$ ($2.0\times 10^{-4}\text{ M}$) was kept unchanged in our experiments, when pyridine was added in excess amounts, $[\text{Por}\cdot\text{Py}]\rightarrow[\text{Por}]_0$ and optical properties of system tended to saturate gradually. When the ratio of $[\text{Py}]_0$ to $[\text{Por}]_0$ is about larger than 20, the changes of Z-scan curves and σ_0 became very slow, as shown in Fig. 2.

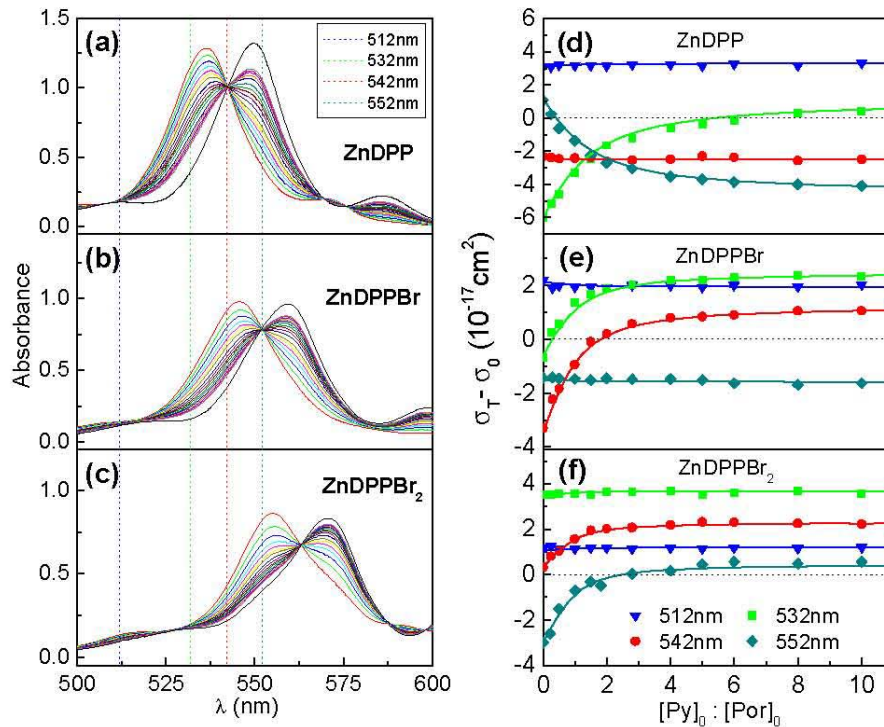


Fig. 3. Spectrophotometric titrations of (a) ZnDPP, (b) ZnDPPBr, and (c) ZnDPPBr₂ with pyridine. The cross section difference ($\sigma_T - \sigma_0$) of (d) ZnDPP, (e) ZnDPPBr, and (f) ZnDPPBr₂ vs the concentration of pyridine $[\text{Py}]_0 : [\text{Por}]_0$. The dotted lines represent $\sigma_T - \sigma_0 = 0$. If $\sigma_T - \sigma_0 > 0$, RSA will occur, and if $\sigma_T - \sigma_0 < 0$, SA will occur. The solid fitting curves are obtained directly from the association model.

To obtain the value of K , titrations of ZnDPP, ZnDPPBr, and ZnDPPBr₂ with pyridine were performed, and such absorption spectral changes are illustrated in Figs. 3(a)-3(c). Upon the addition of pyridine, the Q bands at 536 nm, 546 nm, and 555 nm corresponding to the unbound zinc porphyrins gradually disappeared and new bands appeared at 550 nm, 560 nm, and 570 nm for ZnDPP, ZnDPPBr, and ZnDPPBr₂. The new bands are characteristics of Por-Py complexes. Clear isosbestic points are observed at 542 nm, 552 nm, and 563 nm for ZnDPP, ZnDPPBr, and ZnDPPBr₂, respectively, and this is indicative of sequential two-state equilibria. The black lines are the absorption spectra with extreme excessive pyridine, which can be thought that the coordination interaction between pyridine and zinc porphyrins is sufficient. The calculated K for pyridine ligation to the zinc are $0.48\times 10^4\text{ M}^{-1}$, $1.03\times 10^4\text{ M}^{-1}$, and $1.55\times 10^4\text{ M}^{-1}$ for ZnDPP, ZnDPPBr, and ZnDPPBr₂, respectively. If $[\text{Py}]_0$, $[\text{Por}]_0$ and K are given, $[\text{Por}\cdot\text{Py}]$ can be derived from Eq. (1). And then, we can easily predict the change of nonlinear absorption of system according to the ratio of porphyrins to Por-Py complexes. The

theoretical fittings using the model above, called association model, agree well with the experimental data, as shown in Fig. 2(b). The similar results can be also observed for ZnDPPBr at 542nm and ZnDPPBr₂ at 552nm due to about 10 nm red-shift of absorption band.

For ZnDPP, as pyridine is added, absorption spectral changes at 512 nm, 542 nm, and 552 nm are different from that at 532 nm in Fig. 3(a). We now consider the tuning of NLA at other three wavelengths (512 nm, 542 nm, and 552 nm), and Z-scan experiments with nanosecond pulsed laser incidence were performed to obtain values of σ_T at different wavelengths. It should be noted that σ_T has also a dependence on [Por·Py], but it is much weaker than σ_0 as shown in Fig. 2(b). Here, the cross section difference ($\sigma_T - \sigma_0$) is introduced as a useful indicator of NLA. Because the weak interaction between porphyrin and pyridine has a larger effect on σ_0 than on σ_T , it can be predicted how the nonlinear absorption of ZnDPP changes at these wavelengths. As the ratio of [Py]₀ to [Por]₀ increases, there is an opposite change of NLA at 552 nm compared with that at 532 nm, as shown in Fig. 3(d), but RSA at 512 nm and SA at 542 nm almost remain unchanged. In the same way, Figs. 3(e) and 3(f) give the regularity of changes of $\sigma_T - \sigma_0$ for ZnDPPBr and ZnDPPBr₂ at different wavelengths. For ZnDPPBr and ZnDPPBr₂, faster tendency to saturation of $\sigma_T - \sigma_0$ can be caused by a larger K compared with ZnDPP, which indicates that they have a stronger association with pyridine than ZnDPP. The agreement between the experimental data and the fitting curves seems to support the association model. The red-shift of linear absorption band can arise from a destabilization of the highest occupied molecular orbital (HOMO) with little effect on the lowest unoccupied molecular orbital (LUMO) due to a flow of charge from the axial ligand to the porphyrin ring through the zinc ion [27]. Therefore, the addition of pyridine to zinc porphyrin can cause a destabilization of ground state, but has little effect on excited states. We believe that this is why there is a major drop in linear absorption whereas σ_T almost remains unchanged when the complex Py:Por is formed.

4. Conclusion

In summary, it is feasible for a fine-tuning of NLA in a large range shown in Fig. 3, and we can easily realize a flexible alteration from a positive NLA (RSA) to a negative NLA (SA) or a reverse alteration at 532, 542 and 552 nm, based on the bromination of zinc diphenylporphyrins and the weak interaction between zinc porphyrins and pyridine. Compared with modifying molecular structures of conventional organic materials, the weak intermolecular interaction of supramolecular porphyrins or other supramolecular materials has another advantage that it can be realized more easily and flexibly. In applications of NLO materials, such as optical limiting, optical switching, etc, a fine-tunable nonlinear response should be more useful, and it makes designs of NLO devices more convenient.

With the rapid development of supramolecular chemistry, more means using weak interaction will be utilized to control and tune optical nonlinearities of materials, which may be not easy or even impossible for traditional molecular chemistry. Besides absorption bands, tuning of polarization, polarizability, and extent of charge transfer in supramolecular system will be expected to lead to a change of other optical nonlinearities, such as nonlinear refraction and two-photon absorption. Even we expect to use optical nonlinearities to characterize supramolecular system. Supramolecular materials have demonstrated better tailorable optical nonlinearities than conventional organic NLO materials. Therefore, we think that supramolecular porphyrins are strong candidates for future NLO materials.

Acknowledgments

This work was supported by the Preparatory Project of the National Key Fundamental Research Program (grant 2004CCA04400), the Natural Science Foundation of China (grant 10574075, 20172028 and 20421202) and the Program for Changjiang Scholars and Innovative Research Team in University.

Periodic dielectric bars assisted enhanced transmission and directional light emission from a single subwavelength slit

Zu-Bin Li, Jian-Guo Tian, Wen-Yuan Zhou, Wei-Ping Zang, and Chungping Zhang

The MOE Key Lab of Advanced Technique & Fabrication for Weak-Light Nonlinear Photonics Materials, and Tianjin Key Lab of Photonics Materials & Technology for Information Science, Nankai University, Tianjin 300457, China

jjitian@nankai.edu.cn

Abstract: The transmission from a single subwavelength slit in a metal film with periodic dielectric bars on its surfaces has been analyzed numerically by the finite-difference time-domain method. Results show that the role of the periodic dielectric bars is just the same as that of the periodic grooves directly on the surfaces. With the modulations of dielectric bars on the input and output surfaces of the metal film, light transmission through the subwavelength slit is enhanced extraordinarily and confined to directional emission. The CDEW model is employed to explain the mechanism of the transmission enhancement and directional emission caused by the periodic dielectric bars.

©2006 Optical Society of America

OCIS codes: (050.1940) Diffraction; (050.1220) Apertures; (240.6690) Surface waves.

References and links

1. T. Thio, K. M. Pellerin, R. A. Linke, H. J. Lezec, and T. W. Ebbesen, "Enhanced light transmission through a single subwavelength aperture," *Opt. Lett.* **26**, 1972-1974 (2001).
2. H. J. Lezec, A. Degiron, E. Devaux, R. A. Linke, L. Martin-Moreno, F. J. Garcia-Vidal, and T. W. Ebbesen, "Beaming light from a subwavelength aperture," *Science* **297**, 820-822 (2002).
3. T. Thio, H. J. Lezec, and T. W. Ebbesen, "Strongly enhanced optical transmission through subwavelength holes in metal films," *Physica B* **279**, 90-93 (2000).
4. G. Gbur, H. F. Schouten, and T. D. Visser, "Achieving superresolution in near-field optical data readout systems using surface plasmons," *Appl. Phys. Lett.* **87**, 191105 (2005).
5. C. H. Gan and G. Gbur, "Strategies for employing surface plasmons in near-field optical readout systems," *Opt. Express* **14**, 2385-2397 (2006), <http://www.opticsexpress.org/abstract.cfm?URI=OPEX-14-6-2385>.
6. K. Ishihara, T. Ikari, H. Minamide, J. Shikata, K. Ohashi, H. Yokoyama, and H. Ito, "Terahertz near-field imaging using enhanced transmission through a single subwavelength aperture," *Jpn. J. Appl. Phys.* **44**, L929-L931 (2005).
7. S. Shinada, J. Hashizume, and F. Koyama, "Surface plasmon resonance on microaperture vertical-cavity surface-emitting laser with metal grating," *Appl. Phys. Lett.* **83**, 836-838 (2003).
8. H. Caglayan, I. Bulu, and E. Ozbay, "Extraordinary grating-coupled microwave transmission through a subwavelength annular aperture," *Opt. Express* **13**, 1666-1671 (2005), <http://www.opticsexpress.org/abstract.cfm?URI=OPEX-13-5-1666>.
9. M. J. Lockyear, A. P. Hibbins, and J. R. Sambles, "Microwave transmission through a single subwavelength annular aperture in a metal plate," *Phys. Rev. Lett.* **94**, 193902 (2005).
10. H. Caglayan, I. Bulu, and E. Ozbay, "Beaming of electromagnetic waves emitted through a subwavelength annular aperture," *J. Opt. Soc. Am.* **23**, 419-422 (2006).
11. B. Wang and G. P. Wang, "Directional beaming of light from a nanoslit surrounded by metallic heterostructures," *Appl. Phys. Lett.* **88**, 013114 (2006).
12. A. V. Zayats and I. I. Smolyaninov, "High-optical-throughput individual nanoscale aperture in a multilayered metallic film," *Opt. Lett.* **31**, 398-400 (2006).
13. Z.-B. Li, J.-G. Tian, Z.-B. Liu, W.-Y. Zhou, and C.-P. Zhang, "Enhanced light transmission through a single subwavelength aperture in layered films consisting of metal and dielectric," *Opt. Express* **13**, 9071-9077 (2005), <http://www.opticsexpress.org/abstract.cfm?URI=OPEX-13-22-9071>.
14. Z.-B. Li, J.-G. Tian, W.-Y. Zhou, Z.-B. Liu, W.-P. Zang, and C.-P. Zhang, "Highly directional emission from a subwavelength slit in metal-dielectric layered films," *Chin. Phys. Lett.* **23**, 1207-1210 (2006).

#70998 - \$15.00 USD
(C) 2006 OSA

Received 15 May 2006; revised 26 June 2006; accepted 21 July 2006
4 September 2006 / Vol. 14, No. 18 / OPTICS EXPRESS 8037

15. E. Moreno, F. J. Garcia-Vidal, and L. Martin-Moreno, "Enhanced transmission and beaming of light via photonic crystal surface modes," *Phys. Rev. B* **69**, 121402(R) (2004).
16. P. Kramper, M. Agio, C. M. Soukoulis, A. Birner, F. Muller, R. B. Wehrspohn, U. Gosele, and V. Sandoghdar, "Highly directional emission from photonic crystal waveguides of subwavelength width," *Phys. Rev. Lett.* **92**, 113903 (2004).
17. S. K. Morrison and Y. S. Kivshar, "Engineering of directional emission from photonic-crystal waveguides," *Appl. Phys. Lett.* **86**, 081110 (2005).
18. H. J. Lezec and T. Thio, "Diffracted evanescent wave model for enhanced and suppressed optical transmission through subwavelength hole arrays," *Opt. Express* **12**, 3629-3651 (2004), <http://www.opticsexpress.org/abstract.cfm?URI=OPEX-12-16-3629>.
19. A. P. Hibbins, J. R. Sambles, and C. R. Lawrence, "Gratingless enhanced microwave transmission through a subwavelength aperture in a thick metal plate," *Appl. Phys. Lett.* **81**, 4661-4663 (2002).

It is generally known that light transmission through a subwavelength aperture is very poor and diffracted to all directions according to the standard diffraction theory. Recently, extraordinarily enhanced transmission was observed through a single subwavelength aperture in a metal film if surrounded by periodic corrugations on the illuminating side [1]. With periodic grooves on the output side of the metal film, the transmission was confined to be a beaming light from a single hole or directional emission from a single slit [2]. These findings attracted a lot of interest because of their extensive potential applications such as optimized probe for near-field microscopy [3], near-field optical data readout systems [4-5], near-field imaging [6], and micro-aperture laser [7]. Furthermore, enhanced transmission and beaming light were also reported from annular aperture with grooves surrounded [8-10]. Besides these aperture-groove structures, beaming light from a nanoslit surrounded by metallic heterostructures [11] and enhanced transmission from an aperture in a multilayered metallic film [12] were reported very recently.

In our previous works [13-14], some new structures of layered metal-dielectric films were studied numerically. By the modulation of dielectric film, transmission through the subwavelength slit in layered films was enhanced and confined to beaming light. Actually, enhanced transmission and beaming light are not the particular properties of pure metallic structures, and they were also obtained through a subwavelength waveguide in photonic crystal with modulated surface aspects [15-17]. These new findings extend the view of transmission enhancement phenomena, and are very important to understand the underlying mechanism of transmission enhancement.

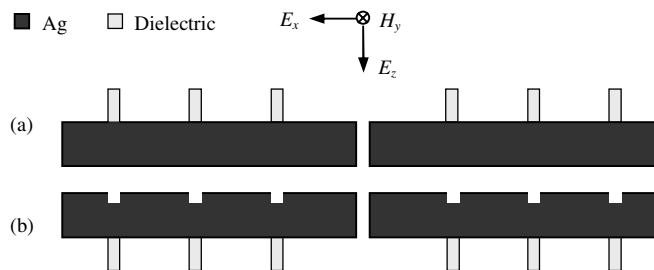


Fig. 1. Sketch maps of a slit in a metal film with periodic dielectric bars (a) on the input surface and (b) on the output surface.

In this letter, we change the dielectric film in structures of Ref. [13-14] to periodic dielectric bars with subwavelength width and analyze the transmission from subwavelength slits in these new structures numerically by finite-difference time-domain (FDTD) method. The sketch maps are shown in Fig. 1. In our simulation, we use metal Ag and its permittivity is given by Drude model: $\varepsilon(\omega) = 1 - [\omega_p^2 / (\omega^2 + i\omega\gamma)]$ with $\omega_p = 1.346 \times 10^{16}$ rad/s and $\gamma = 9.617 \times 10^{13}$ rad/s. The geometry of the metal film is fixed for comparison [2] and simplicity as thickness $h_{Ag} = 300$ nm and slit width $w = 40$ nm. The slit is surrounded by $2N_{di}$ dielectric

bars and the dielectric is supposed to be isotropic, and without dispersion and absorption. Referred to the results in our works [13-14], N_{di} is set to be 5. A TM polarized plane wave is incident perpendicularly on the structures. The dielectric bars will be put on the input or output surface of the metal film respectively to discuss their effects on the transmission enhancement or directional light emission.

At first, we put dielectric bars on the input surface of the metal film and the output surface is smooth [see Fig. 1(a)]. Under this condition, the transmission through the slit is totally determined by the dielectric bars on the input surface. In Fig. 2, we show area-normalized transmission spectra of three structures in metal films: a bare slit without any structure on its surfaces, a slit with dielectric bars on the input surface, and a slit with periodic grooves on the input surface. The parameters of the dielectric bars are period $p_{di} = 500$ nm, height $h_{di} = 100$ nm, width $w_{di} = 40$ nm, refractive index $n = 2.0$, and these parameters are set to be default if not mentioned additionally. The slit-groove metal structure has ± 5 grooves directly on the input surface with period of 500 nm, width of 40nm, and depth of 60 nm.

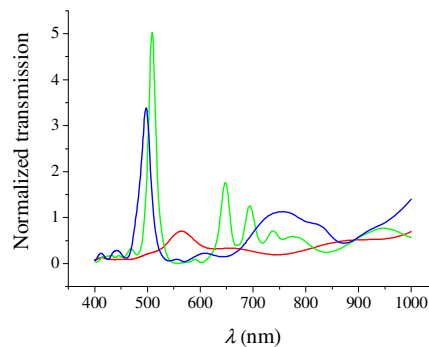


Fig. 2. Area-normalized transmission spectra of a bare slit (red line), a slit with dielectric bars (green line) and a slit with periodic grooves (blue line). All three slits are in the same metal film with thickness of 300 nm and slit width of 40 nm. The spectra are normalized by the fraction of the surface occupied by the slit.

From Fig. 2, we can see clearly that the transmission through the subwavelength slit in our structure is extraordinarily enhanced by the modulation of the periodic dielectric bars on the input surface of the metal film. Compared with the enhancement caused by grooves directly on the metal surface with same period and width, the peak enhancement by the dielectric bars is stronger and the peak wavelength is a little longer. However, despite these small differences, the properties of their transmission peaks are very similar, and we suppose that the periodic dielectric bars play the same role in the transmission enhancement through the subwavelength slit as what the periodic grooves do.

Although the resonant excitation of surface plasmons was used widely to explain the mechanism of transmission enhancement, it doesn't fit our result obtained from the structure of metal slit and dielectric bars. As we know, the frequency of the surface plasmon is determined by the permittivities of the metal and the dielectric at the interface. However, with large difference of dielectric properties ($n = 1$ for air grooves and $n = 2$ for dielectric bars), the resonant wavelengths of the slit with grooves and the slit with dielectric bars are very close (see Fig. 2). This cannot be explained by the surface plasmons model. In this letter, the CDEW (composite diffracted evanescent waves) model presented by Lezec and Thio [18] is employed to explain the mechanism of transmission enhancement. In the CDEW model, the transmission enhancement is due to the constructive interference of composite diffracted evanescent waves generated by subwavelength features on the surface. Just as shown in Fig. 3, when light illuminates on the metal-dielectric structure, it will be diffracted into evanescent waves by subwavelength-scaled dielectric bars. These composite evanescent waves propagate to the slit and interfere with the light incident directly on the slit, leading to field enhancement

when the interference is constructive at selected wavelength. Based on the CDEW model, the stronger enhancement and the little longer peak wavelength can be explained easily. The stronger enhancement is because the dielectric bars are transparent, which affect little on the propagation of evanescent waves from far side. And the longer peak wavelength is caused by the increase of the effective refractive index n_{eff} at the interface of the dielectric bars and the metal film {see Eq. (4) in Ref. [18]}.

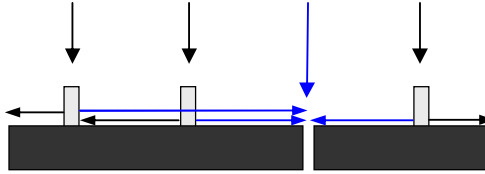


Fig. 3. The schematic diagram of transmission enhancement by CDEW model.

Furthermore, we simulate the influences of the characters of dielectric bars on the transmission enhancement. In Fig. 4 are shown the normalized transmission and the wavelength at peak (T_{max} and λ_{max}) as a function of h_{di} . As h_{di} increases, T_{max} increases first and then trends to saturation. This is attributed to the exponential decay of the evanescent waves along the direction perpendicular to the interface. The composite diffracted evanescent waves have an imaginary component $k_z = i(k_x^2 - k_0^2)$ along the direction perpendicular to the interface [18]. λ_{max} increases a little with the increment of h_{di} , which is due to the increase of the light path.

In Fig. 5 are shown T_{max} and λ_{max} as a function of n . As n increases, T_{max} increases first and then decreases. This is because that when n increases, the diffractive ability of the

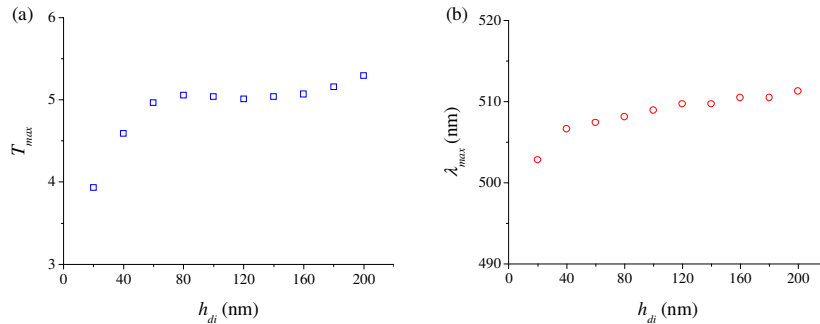


Fig. 4. (a) Normalized transmittance and (b) wavelength at peak as a function of the height of dielectric bars. Other parameters of the dielectric bars are set as default.

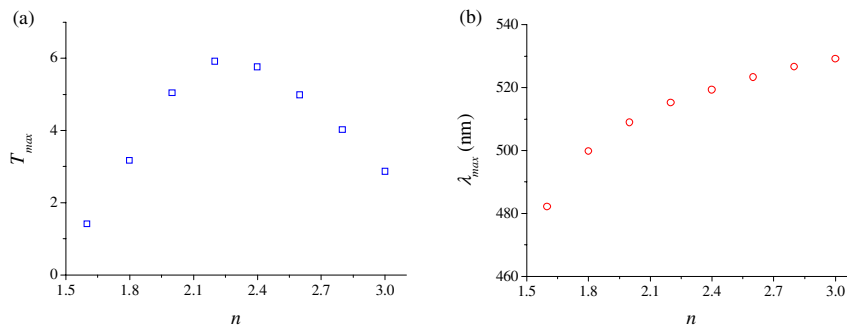


Fig. 5. (a) Normalized transmittance and (b) wavelength at peak as a function of the refractive index of dielectric bars. Other parameters of the dielectric bars are set as default.

dielectric bars increases, leading to more evanescent waves and stronger transmission enhancement. However, larger n leads to stronger reflection at the dielectric surface, which weakens the contribution to enhancement from dielectric bars far away from the slit. These two contrary processes act together and lead to this variation finally. λ_{max} increases as n increases, which is due to the increase of the effective refractive index n_{eff} at the interface.

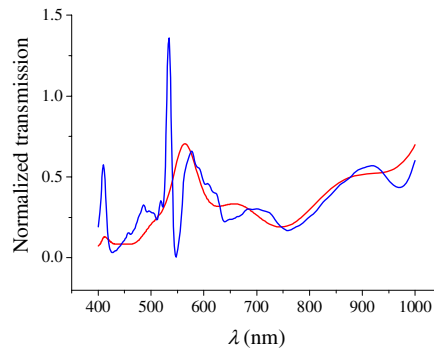


Fig. 6. Area-normalized transmission spectra of a bare slit (red line) and a slit with metal bars on the input surface (blue line). The metal bars have a period of 500 nm, height of 40 nm and width of 40 nm.

As a comparison, we change the dielectric bars to metal bars and simulate the transmission. As shown in Fig. 6, the transmission through the slit with periodic metal bars is also enhanced, but the enhancement is quite low. Actually, the evanescent waves can also be generated by the diffraction of the metal bars, but the metal bars interrupt the propagation of the evanescent waves and block the contributions to the enhancement from bars out of the first pair. Thus the enhancement by metal bars is mostly due to the first pair of bars. The enhancement factor of the transmission peak in Fig. 6 is 3.4, which is very similar to the result obtained from slit with only one pair of grooves [19].

From results above, we know that the transmission through a subwavelength slit is extraordinarily enhanced by the modulation of the periodic dielectric bars on the input surface. As we already knew [14], the features on the output surface can modulate the distribution of the light transmitted through the slit. We simulate the field distributions through the slit with periodic dielectric bars on the output surface under different parameters, which are shown in Fig. 7. The grooves [see Fig. 1(b)] on the input surface of the metal film have period of 500 nm, width of 40 nm and depth of 60 nm. The incident light is 500 nm if not mentioned especially. From the plots in Fig. 7, we can see clearly that the transmission through the slit is confined to directional emission by the modulation of the dielectric bars on the output surface. The plot of $p_{di} = 400$ nm presents a beaming light emission. Just same as the effect of dielectric film with grooves [14], the dielectric bars diffract the evanescent waves (which are generated by the diffraction of the subwavelength slit) into propagating waves and these diffracted waves interfere with each other leading to the beaming light or directional emission. However, it must be noticed that the dielectric bars are of very small width compared with the incident wavelength and the bar period. Thus the variation of the dielectric parameters will not affect the field distribution too much. As shown in Fig. 7, although the incident wavelength, period, refractive index, and height of the dielectric bars vary greatly, the distributions of output fields vary much slowly, especially compared with the results modulated by the dielectric film [14].

In conclusion, we have analyzed numerically the properties of the transmission from a single subwavelength slit in a metal film with periodic dielectric bars on the input and output surface respectively by the FDTD method. Results show that the transmission is strongly enhanced by the modulation of the dielectric bars on the input surface, and confined to beaming light or directional emission by the modulation of the dielectric bars on the output

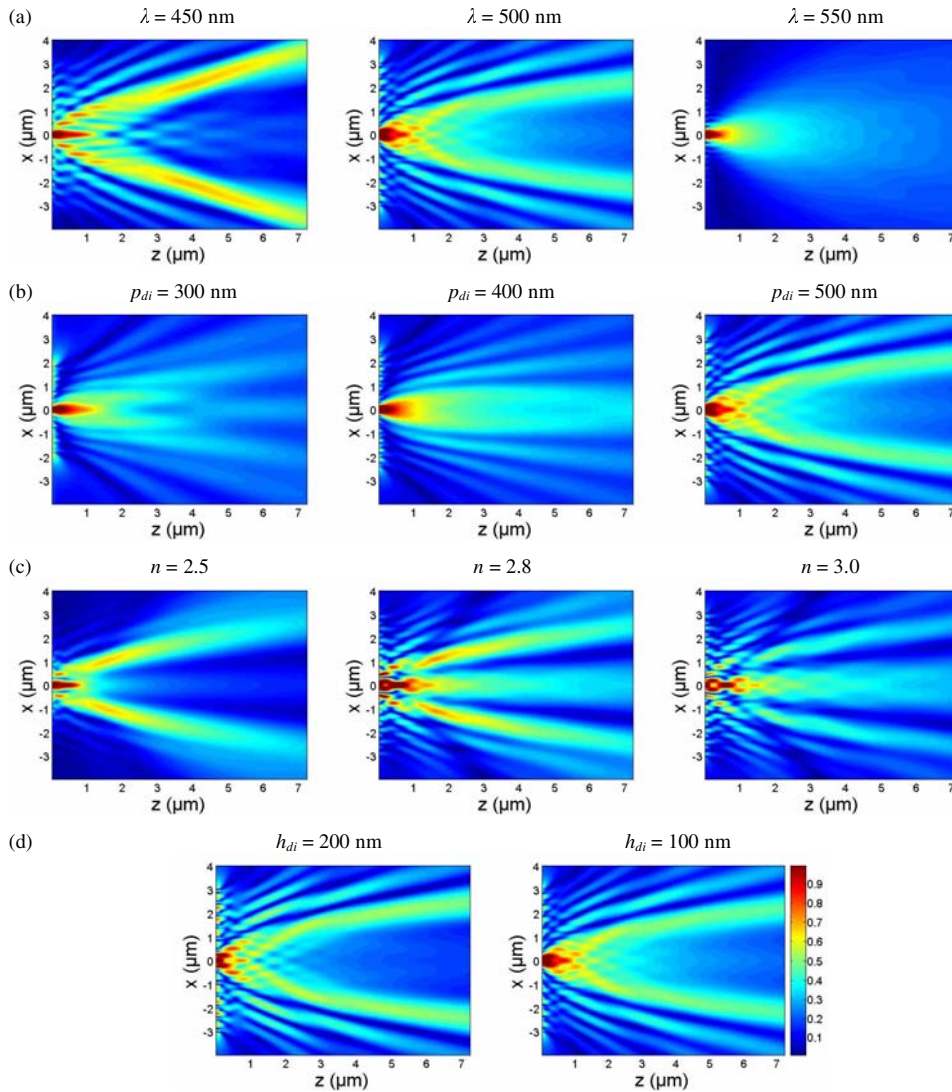


Fig. 7. Patterns of light emitting from the slit under different incident wavelength and parameters of dielectric bars. Other parameters are set as default.

surface. The dielectric bars play the same role as the periodic grooves directly on the surfaces. We employ the CDEW model to explain the mechanism of the transmission enhancement and the directional emission. The structure with periodic dielectric particles is very efficient to obtain strong transmission enhancement. And we think our results will be very helpful for the applications of subwavelength optical devices.

Acknowledgement

This research is supported by Science & Technology Development Project of Tianjin (grant 033104311), the Preparatory Project of the National Key Fundamental Research Program (grant 2004CCA04400), and the Program for Changjiang Scholars and Innovative Research Team in University.

Investigations of centers formed in UV-light-induced absorption for LiNbO₃ highly doped with Mg and Hf

Wenbo Yan, Yongfa Kong, Lihong Shi, Hongde Liu, Xiaochun Li, and Jingjun Xu

*The Key Lab of Advanced Technique and Fabrication for Weak-Light Nonlinear Photonics Materials, Ministry of Education,
Nankai University, Tianjin 300457, China*

Shaolin Chen, Ling Zhang, Ziheng Huang, Shiguo Liu, and Guangyin Zhang

*Tianjin Key Lab of Photonics Material and Technology for Information Science, Nankai University, Tianjin 300457, China
kongyf@nankai.edu.cn*

Abstract: UV-light-induced absorption in LiNbO₃ highly doped with Mg and Hf was investigated. Distinct decay behavior was attributed to the different centers formed under UV illumination, i.e., the shallow and intermediate deep centers for trapping holes. O[•] formed near doped cation at the niobium site was suggested to be the origin of the shallow center, whereas that formed near cation vacancy was suggested to be the origin of the intermediate deep center. The influence of the sample status (oxidized or reduced) on the UV-light-induced absorption was demonstrated to support our suggestion. Two different dark decay processes were associated with relaxations of holes from the shallow centers to two nonequivalent Nb_{Nb} adjacent to the doped cations at niobium sites.

©2006 Optical Society of America

OCIS codes: (130.3730) Lithium niobate; (300.1030) Absorption; (190.5330) Photorefractive.

References and links

1. A. Rüber, *Current Topics in Materials Science*, V.1 (North-Holland, Amsterdam, 1978).
2. P. Günter and J. P. Huignard, *Photorefractive Materials and Their Applications*, Vols. I and II (Springer-Verlag, Heidelberg, 1989).
3. K. Buse, A. Adibi, and D. Psaltis, "Non-volatile holographic storage in doubly doped lithium niobate crystals," *Nature* **393**, 665–668 (1998).
4. Y. S. Bai and R. Kachru, "Nonvolatile holographic storage with two-step recording in lithium niobate using cw lasers," *Phys. Rev. Lett.* **78**, 2944–2947 (1997).
5. L. Hesselink, S. Orlov, A. Liu, A. Akella, D. Lande, and R. Neurgaonkar, "Photorefractive materials for nonvolatile volume holographic data storage," *Science* **282**, 1089–1094 (1998).
6. H. Guenther, R. Macfarlane, Y. Furukawa, K. Kitamura, and R. Neurgaonkar, "Two-color holography in reduced near-stoichiometric lithium niobate," *Appl. Opt.* **37**, 7611–7623 (1998).
7. M. Lee, S. Takekawa, Y. Furukawa, K. Kitamura, H. Hatano, and S. Tanaka, "Nonvolatile two-color holographic recording in Tb-doped LiNbO₃," *Appl. Phys. Lett.* **76**, 1653–1655 (2000).
8. G. Zhang and Y. Tomita, "Broadband absorption changes and sensitization of near-infrared photorefractivity induced by ultraviolet light in LiNbO₃:Mg," *J. Appl. Phys.* **91**, 4177–4180 (2002).
9. G. Zhang and Y. Tomita, "Ultraviolet-light-induced nearinfrared photorefractivity and two-color holography in highly Mg-doped LiNbO₃," *J. Appl. Phys.* **93**, 9456–9459 (2003).
10. Y. Tomita, S. Sunarno, and G. Zhang, "Ultraviolet-light-gating two-color photorefractive effect in Mg-doped near-stoichiometric LiNbO₃," *J. Opt. Soc. Am. B* **21**, 753–760 (2004).
11. E. P. Kokanyan, L. Razzari, I. Cristiani, V. Degiorgio, and J. B. Gruber, "Reduced photorefraction in hafnium-doped single-domain and periodically poled lithium niobate crystals," *Appl. Phys. Lett.* **84**, 1880–1882 (2004).

12. L. Razzari, P. Minzioni, I. Cristiani, V. Degiorgio, and E. P. Kokanyan, "Photorefractivity of Hafnium-doped congruent lithium-niobate crystals," *Appl. Phys. Lett.* **86**, 131914 (2005).
13. S. Li, S. Liu, Y. Kong, D. Deng, G. Gao, Y. Li, H. Gao, L. Zhang, Z. Hang, S. Chen, and Jingjun Xu, "The optical damage resistance and absorption spectra of $\text{LiNbO}_3\text{:Hf}$ crystals," *J. Phys.: Condens. Matter* **18**, 3527–3534 (2006).
14. N. Iyi, K. Kitamura, Y. Yajima, S. Kimura, Y. Furukawa, and M. Sato, "Defect structure model of MgO-doped LiNbO_3 ," *J. Solid State Chem.* **118**, 148–152 (1995).
15. Q. Xu, G. Zhang, H. Qiao, B. Fu, Y. Shen, and J. Xu, "Studies on thermal activation energy of ultraviolet-induced small polarons O^- in damage-resistant lithium niobate crystals," *Trends Opt. Photon.* **99**, 121–126 (2005).
16. A. Winnacker, R. M. Macfarlane, Y. Furukawa, and K. Kitamura, "Two-color photorefractive effect in Mg-doped lithium niobate," *Appl. Opt.* **41**, 4891–4896 (2002).
17. O. Schirmer, O. Thiemann, and M. Wöhlecke, "Defects in LiNbO_3 . I. experimental aspects," *J. Phys. Chem. Solids* **52**, 185–200 (1991).
18. B. Faust, H. Muller, and O. F. Schirmer, "Free small polarons in LiNbO_3 ," *Ferroelectrics* **153**, 297–302 (1994).
19. G. K. Kitaeva, K. A. Kuznetsov, A. N. Penin, and A. V. Shepelev, "Influence of small polarons on the optical properties of Mg: LiNbO_3 crystals," *Phys. Rev. B* **65**, 054304 (2002).
20. O. F. Schirmer and D. Von der Linde, "Two-photon- and x-ray-induced Nb^{4+} and O^- small polarons in LiNbO_3 ," *Appl. Phys. Lett.* **33**, 35–38 (1978).
21. H. Qiao and Y. Tomita, "Ultraviolet-light-induced absorption changes in highly Zn-doped LiNbO_3 ," *Opt. Express* **14**, 5773–5778 (2006).
22. S. Li, S. Liu, Y. Kong, J. Xu, and G. Zhang are preparing a paper to be called "Enhanced photorefractive properties of $\text{LiNbO}_3\text{:Fe}$ crystals by HfO_2 co-doping," *Appl. Phys. Lett.* (to be published).

1. Introduction

Lithium niobate (LiNbO_3 , LN) crystals are extensively studied for their many important applications [1, 2], e.g., holographic volume storage, optical image and signal processing, coherent optical amplification, and phase conjugation. In particular, holographic volume storage has attracted increasing attention for the past three decades. One crucial problem with this application is the volatility of stored information, because during readout carriers are redistributed homogeneously, which leads to erasure of the recorded hologram. To solve this problem, two-color recording was proposed and has been the focus of research in recent years [3–10].

The two-color recording process in LN doubly doped with Fe and Mn was interpreted as a two-center picture (Fe and Mn centers) [3]. For nominally pure near-stoichiometric LN, this process was proved to be connected with the small polaron (the intermediate state) formed at the antisite defect Nb_{Li} [4–7]. The small polaron together with the bipolaron (electrons trapped at adjacent Nb_{Li} and Nb_{Nb} sites) plays a key role in the realization of two-color holography [5]. Recently, UV-light-induced absorption and two-color holography in LN highly doped with damage-resistant impurity have been demonstrated by many researchers [8–10]. Since Nb_{Li} has been eliminated completely in these samples, small polarons are excluded as the origin of these phenomena. The researchers attributed it to the creation of intermediate shallow centers O^- (i.e., bound small polarons), where UV-excited holes were trapped at O^{2-} sites near cation vacancies charged negatively with respect to the lattice [8–10]. In particular, Tomita *et al.* [10] investigated the UV-light-induced two-color photorefractivity in a near-stoichiometric LN doped with Mg and found that there are at least four types of centers participated in this two-color photorefractive effect, but the exact nature of all these centers was not given. For clarifying their essence, further investigations on LN samples with other damage-resistant impurity are needed. Recently, Kokanyan *et al.* found that doping of tetravalent elements Hf can substantively suppress the optical damage of LN in the visible spectral region [11]. Razzari *et al.* reported that the light-induced birefringence changes observed for LN doped with 4 mol% of Hf are comparable to those found for 6 mol% Mg-doped crystals and suggested that the so-called damage-resistant threshold was close to 4 mol% for Hf-doped LN [12]. Later, Li *et al.* gave the UV-visible and infrared absorption

spectra of highly Hf-doped LN [13]. However, information is still lacking with regard to its optical properties in the UV spectral region.

In this paper we investigated the UV-light-induced absorption (ULIA) in LN highly doped with Mg and Hf, respectively and demonstrated their distinct decay behavior. The influence of the sample status (oxidized or reduced) on the ULIA was also studied. Based on these experimental results, the origin of the different centers participated in the ULIA process was discussed in detail.

2. Experimental procedure

Samples used in this study were LN doped with 6.5, 7.8 mol% MgO and 4.0, 6.0 mol% HfO₂, respectively. The highly doped LN single crystals were grown along the *z* axis from the congruent melt by using the Czochralski technique. The as-grown crystals were cut to rectangular-shaped Y-oriented plates, which were then polished to optical grade. To get the reduction state, the samples were treated in an argon atmosphere at 700°C for 6 h, and oxidation required treatment in air at 800°C for 10 h. The labels and material parameters of the samples are shown in Table 1.

Table 1. The labels and material parameters of the samples used in this study.

Sample	Doping level	Status	Thickness (mm)
Hf40a	4.0 mol% HfO ₂	As grown	2.86
Hf60a	6.0 mol% HfO ₂	As grown	2.86
Mg65r	6.5 mol% MgO	Reduced	2.86
Mg65a	6.5 mol% MgO	As grown	2.86
Mg65o	6.5 mol% MgO	Oxidized	2.86
Mg78a	7.8 mol% MgO	As grown	4.14

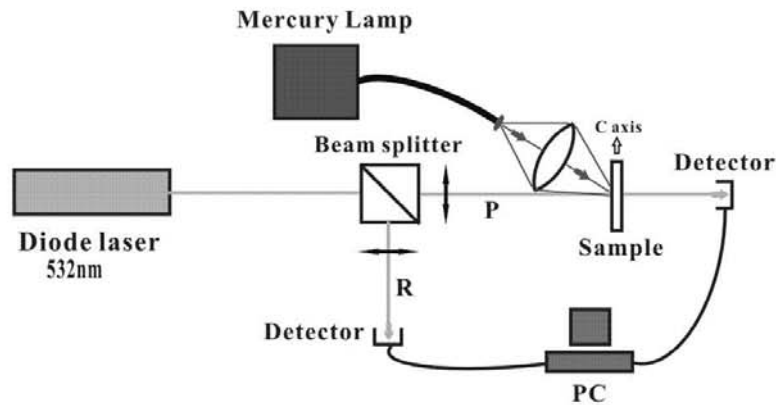


Fig. 1. Schematic of the experimental arrangement for the ULIA measurement. Details of uniform illumination of strong green light were omitted. UV light intensity was 500 mW/cm², intensity of strong green light was 200 mW/cm², and that of the probe-light (denoted as "P") 1mW/cm². Another reference light (denoted as "R") was used to reduce the drifts caused by power fluctuation of the semiconductor laser.

Figure 1 shows a schematic experimental arrangement for the ULIA measurement. A 10 W mercury lamp was used as the incoherent UV light source. The spectrum of UV light was

selected to peak at 365 nm by use of an appropriate optical filter. The UV light was loosely focused by a lens and irradiated the sample for pump. We used an e-polarized 532 nm light beam emitted from semiconductor laser as probe light, which impinged on the sample along the direction orthogonal to the Y plane of the sample. The transmitted light was detected by a photo-detector with a green filter placed in the front to block scattered 365 nm pump UV light. Additionally, another strong incoherent 532 nm light beam was expanded for uniformly illuminating the sample. Since the changes of the sample transmission during the ULIA process are very small (sometimes less than 1%), it is necessary to avoid external influences on the ULIA measurement. In our experiments the samples were kept at a steady temperature (295 K), and the absorption induced by the temperature change could be eliminated. In addition, another reference light was taken out from probe light before the sample. Also, the ULIA coefficient changes were obtained from $\ln[(I_{R1}/I_{R0})/(I_{P1}/I_{P0})]/d$, where I_{P1} (I_{P0}) and I_{R1} (I_{R0}) are measured intensities of transmission and reference beams with (without) UV light illumination, respectively, and d is the sample's thickness. This way we were able to reduce as much as possible the drifts caused by power fluctuation of the semiconductor laser. In order to test the reliability of our experiments, the absorption change of background was measured ahead for a long time. The absorption change was found to be nearly zero all the time, which indicates the external influences on the ULIA measurement had been effectively suppressed.

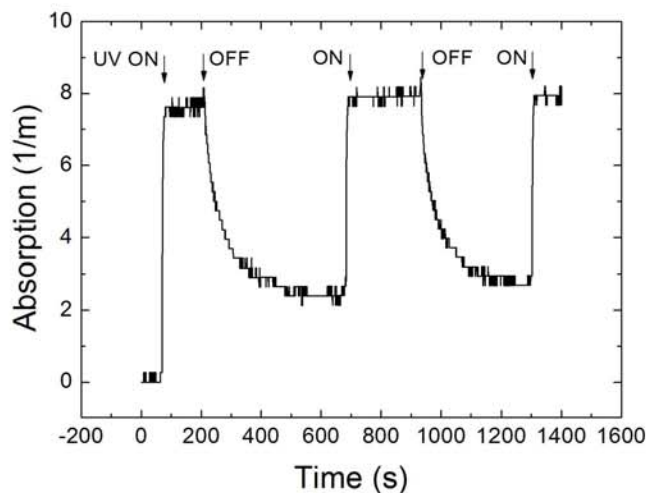


Fig. 2. Typical ULIA curve for highly Mg-doped LN crystal. ON- and OFF-states of UV light are denoted as arrows in the figure.

3. Results and discussion

Figure 2 is the typical ULIA curve for a highly Mg-doped LN sample, which increases rapidly at the beginning of UV light irradiation, achieves a saturation value for several seconds, and decays partly to another stationary value in the dark after shutting down of UV light. It should be noted that “in the dark” mentioned here and later is only an approximation in the experimental condition. In other words, the samples are not situated in absolute darkness, even after the shutting down of UV light, because the green probe is still irradiating it in order to monitor the absorption. In our experiment, however, the probe light with the intensity of $1\text{mW}/\text{cm}^2$ is very weak and can be neglected. This suggestion is supported by nearly the same results obtained when detecting the absorption from time to time instead of

using a continuing probe. In Fig. 2, the most noticeable phenomenon is the nondecayed part of the ULIA in the dark, which can, however, be erased completely by uniformly strong illumination with 532 nm green light (as shown in Fig. 3). This result means that at least two type of centers participated in the ULIA process: one is unstable and decays in the dark, which corresponds to the shallow centers reported previously [8, 10]; the other can exist stably in the dark but is sensitive to the green light, which seems in agreement with the intermediate deep centers suggested by Tomita *et al.* [10]. The terms “shallow”, “intermediate deep”, and “deep” used here and later are concerning energy level for holes but not electrons. The complete decay of the ULIA for LN highly doped with Mg was reported by Zhang *et al.* [8], and the nondecayed part was not observed in their experiments. We think two factors should account for this discrepancy. First, higher intensity adopted for the green probe light may lead to the complete decay of the ULIA, because a relatively strong probe light can erase undesignedly the nondecayed part mentioned above. Another factor is the oxidation status of the sample used in experiments, which also influences the nondecayed part of the ULIA as discussed in the following paragraphs.

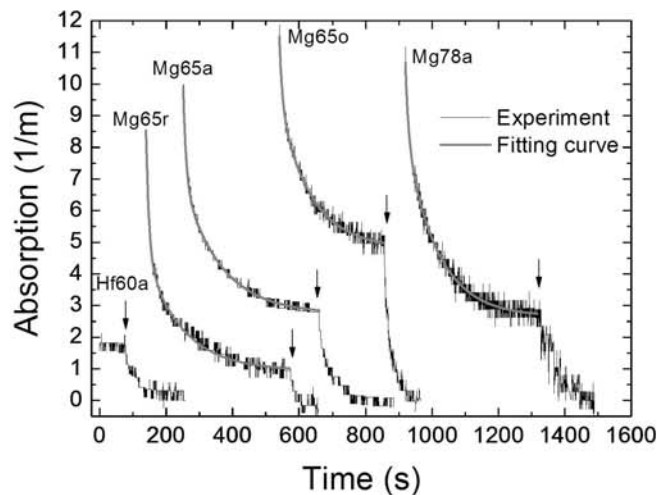


Fig. 3. Dark decay and green-light-induced decay curves for ULIA. ON-state of strong uniform illumination with 532-nm green light is denoted as arrows, black curves correspond to the experimental data, and red curves are the fitting results of the dark decay curves with bi-exponential form given by Eq. (2).

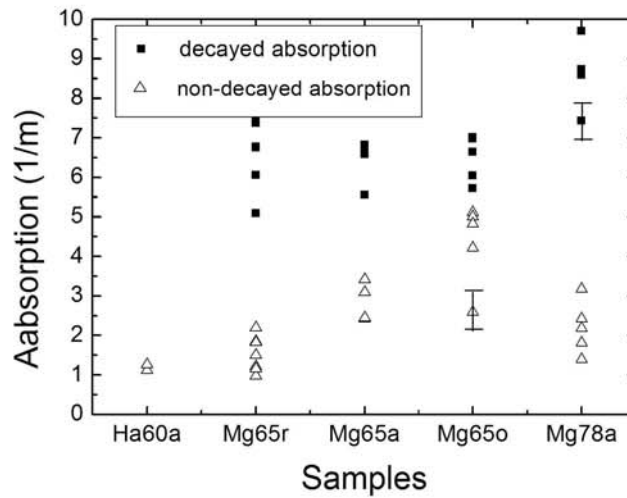


Fig. 4. Experiment data for decayed and nondecayed parts of the ULIA in the dark.

Figure 4 gives the detailed experiment data for decayed and nondecayed parts of the ULIA in the dark. First, we can see that the decayed part for Mg78a is obviously larger than Mg65a, which indicates Mg78a has more shallow centers than Mg65a. Assuming O^- near cation vacancy (V_{Li}^- for LN) as the shallow center just like the previous suggestion [8–10], we can deduce more V_{Li}^- existing in Mg78a than Mg65a, which conflicts with the fact that the amount of V_{Li}^- will decrease with Mg concentration above the so-called damage-resistant threshold [14]. Therefore, the origin of shallow centers should be considered again. We know, except V_{Li}^- , highly Mg-doped LN has another type of defect: Mg_{Nb}^{3-} . It is also charged negatively with respect to the lattice and may trap the holes at O^{2-} sites. Considering more and more Mg_{Nb}^{3-} appears with the increase of Mg concentration, assuming O^- formed near Mg_{Nb}^{3-} as the shallow center becomes reasonable. In the view of defect structure, O^- formed near V_{Li}^- is more stable than Mg_{Nb}^{3-} because of the loss of Li cation, and it may be corresponding to the intermediate deep center.

Another noticeable result comes from highly Hf-doped LN crystals. In contrast to highly Mg-doped LN, the dark decay of the ULIA was absent for both Hf40a and Hf60a, and only the similar green-light-induced decay curves can be observed. For simplicity, merely the experimental data of Hf60a are given in Figs. 2 and 3. This absence of the dark decay means the corresponding shallow centers have disappeared in these samples, which further weakens the possibility of O^- formed near V_{Li}^- as the shallow center because of a large amount of V_{Li}^- existing in LN highly doped with tetravalent hafnium ions [13]. Also, Xu *et al.* [15] investigated the ULIA for LN highly doped with trivalent In, and gave the much smaller dark decay as compared with LN highly doped with bivalent Mg. These results indicate that the shallow center is related to the valence of doped ions, which can be explained by our assumption about the shallow center in the previous paragraph. In LN highly doped with Mg, In, and Hf, the corresponding impurity defects formed at niobate sites are Mg_{Nb}^{3-} , In_{Nb}^{2-} , and Hf_{Nb}^{1-} , respectively. For their decreasing electrical negativity, the ability of Mg_{Nb}^{3-} , In_{Nb}^{2-} , and Hf_{Nb}^{1-} for trapping holes goes down in turn. Thus, as the shallow centers formed in LN highly

doped with Mg, In, and Hf reduce accordingly, so does the dark decay caused by them. For the extreme case of LN highly doped with Hf, the shallow centers responsible for the dark decay disappear completely.

In order to confirm our suggestion about the intermediate deep centers, we studied the influence of oxidation/reduction treatment on the ULIA of highly Mg-doped LN samples. Obviously, the treatment has no obvious effect on the dark decay of the ULIA, but it influences the nondecay part tremendously. From Fig. 3, we can see that the reduction process leads to the sharp decrease of the nondecay part. Generally, LN may lose oxygen near cation vacancies more easily than elsewhere during the reduction process. Thus, the amount of O^- formed near V_{Li}^- will reduce after the reduction treatment, which causes the decrease of the intermediate deep centers.

Table 2. The fitting results of the dark decay curves in Fig. 3 using bi-exponential form given by Eq. (2).

Parameters	Mg65r	Mg65a	Mg65o	Mg78a
A_0 (m^{-1})	0.95	2.74	4.83	2.65
A_1 (m^{-1})	4.05	2.99	2.08	2.30
τ_1 (s)	9.33	9.05	8.61	9.40
A_2 (m^{-1})	3.60	4.14	4.58	5.73
τ_2 (s)	110	114	93.2	95.3

For the further analysis of shallow centers, we fitted the dark decay curves for all samples. These curves cannot be well described by the functional form used by Zhang *et al.* [8]:

$$\Delta\alpha(t) = \frac{\Delta\alpha_0}{\sqrt{1 + 2\gamma\Delta\alpha_0^2 t}} \quad (1)$$

but can be perfectly fitted with bi-exponential form given as following:

$$\Delta\alpha(t) = A_0 + A_1 \exp(-t/\tau_1) + A_2 \exp(-t/\tau_2) \quad (2)$$

where A_0 denotes the nondecay part of ULIA.

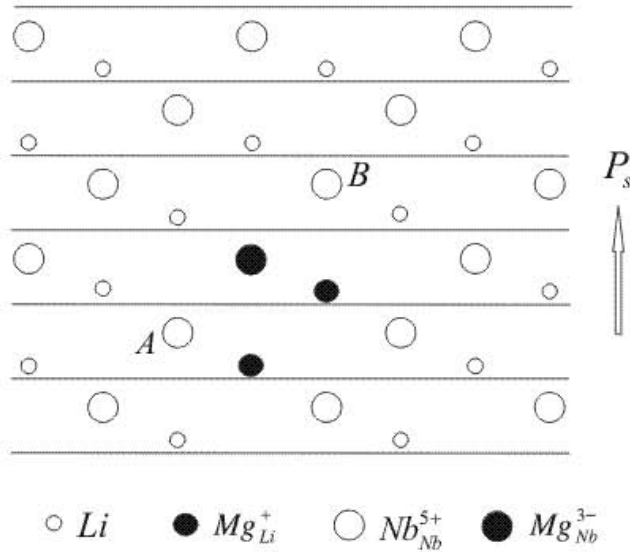


Fig. 5. Structural schematics of lattice for highly Mg-doped LN. Mg_{Li}^+ is located near Mg_{Nb}^{3-} for the balance of electric charge, but it doesn't participate in the charge transfer process of ULIA.

Tomita *et al.* [10] also approximated the dark-decay trend of the shallow-center grating to an exponential form rather than from Eq. (1) and gave a good fit to their data. Table 2 lists our fitting results. We can see the values of A_0 in this table have the similar trend as given in Fig. 4. In addition, all samples have nearly identical τ_1 (about 9 s) and τ_2 (about 100 s), which indicates the existence of two different dark decay processes, $A_1 \exp(-t/\tau_1)$ and $A_2 \exp(-t/\tau_2)$. In nature, the dark decay can be interpreted as the relaxation process of holes from shallow traps to deep ones in the dark. However, the origin of deep traps in highly Mg-doped LN remains disputable. These traps should be quite close to the conduction band but have an ability to supply holes (be able to trap electrons). Some researchers [10, 16] considered Nb_{Nb}^{5+} as the hole-supplying deep center, but the direct evidence of Nb_{Nb}^{5+} close to the conduction band is absent until now. The broad band centered near 0.9–1 eV (1.1–1.3 μm) was always observed in reduced highly Mg-doped LN and attributed to small polaron absorption via polaron hopping at Nb_{Nb} sites [17–19]. It indicates that Nb_{Nb}^{5+} has an ability to trap electrons (supply holes), can form a level relatively close to the conduction band, and perhaps play the role of the hole-supplying deep centers in highly Mg-doped LN. This suggestion is also supported by the fact that holes have been found by ESR (Electron Spin Resonance) to be created together with electrons trapped at Nb_{Nb}^{5+} (forming Nb^{4+}) [20]. Now, we tentatively take Nb_{Nb}^{5+} as the hole-supplying deep centers and give a description of one possible mechanism for ULIA decay in highly Mg-doped LN. UV light excites holes from Nb_{Nb}^{5+} (the deep centers) to the valence band. After their migration in the valence band, part of them are trapped by O^{2-} near V_{Li}^- and Mg_{Nb}^{3-} , which leads to the creation of O^- and the corresponding ULIA. After the UV light is shut down, the ULIA caused by stable O^- near V_{Li}^- (the intermediate deep centers) remain nondecayed, but the holes at the relatively unstable O^- near Mg_{Nb}^{3-} (the shallow centers) relax rapidly to neighborhood Nb_{Nb}^{5+} (the deep centers), which corresponds to the dark decay process of ULIA. Figure 5 shows a hypothetical model for Mg_{Nb}^{3-} surrounded by two nearest Nb_{Nb} (six nearest Nb_{Nb} in all because of the threefold

symmetry of LN). Due to the presence of a spontaneous polarization P_s in LN, Nb_{Nb} A and B are not equivalent in the view of energy. In comparison with A, holes trapped near Mg_{Nb}^{3-} relax to Nb_{Nb} B more easily, which leads to two dark decay processes with different time constants (τ_1 and τ_2). Here, traps (for holes) at Nb_{Nb} A, B and O^{2-} near Mg_{Nb}^{3-} constitute a three-level band scheme. Recently, Qiao *et al.* [21] suggested another three-level model to interpret their ULIA results for highly Zn-doped LN. However, using such a model to explain our experimental results is difficult. Just as they emphasized, more experimental support and further investigation are of great necessity to clarify the mechanism of the ULIA for highly doped LN.

4. Conclusion

The ULIA in LN highly doped with Mg and Hf was investigated, respectively. Both dark decay and nondecay parts of ULIA were observed in highly Mg-doped LN, but only a nondecay part was observed in Hf-doped LN. This distinct behavior was attributed to different centers (the shallow centers and the intermediate deep centers for trapping holes) formed under UV illumination. O^- near doped cation at the niobium site was suggested to be the origin of the shallow center, which is responsible for the dark decay and disappears in Hf-doped LN due to the very weak electrical negativity of Hf_{Nb}^- . Meanwhile, O^- near cation vacancy corresponds to the intermediate deep center for the nondecay part. The influence of the sample status (oxidized or reduced) on the ULIA was demonstrated to support our argument. In addition, two different dark decay processes were associated with relaxations of holes from the shallow centers to two nonequivalent Nb_{Nb} adjacent to the doped cations at niobium sites.

As a tetravalent ion, Hf has different photorefractive properties from Mg^{2+} , Zn^{2+} , or In^{3+} . At the time this paper was being written, Li *et al.* [22] found that Fe ions remain at Li sites in Hf- and Fe-codoped LN crystals when the HfO_2 doping concentration goes above its threshold value; as a result the photorefractive response rate and sensitivity are greatly improved, and the saturation diffraction efficiency remains at a high value. The different ULIA behavior of highly Mg- and Hf-doped LN observed in this work helped us to clarify the nature of different centers formed under UV illumination and reveal the detailed kinetics of the ULIA process involved in UV light-gating nondestructive two-color holography. For highly Hf-doped LN, the absence of the dark decay process means that no shallow centers form under UV illumination. It implies that the migration speed of holes in highly Hf-doped LN should be faster than that in highly Mg-doped crystal, which is important for improving the response speed of UV photorefractive holographic storage in LN.

Acknowledgments

This work is partly supported by the Program for Changjiang Scholars and Innovative Research Team in University and the National Natural Science Foundation of China (Grant No. 60578019 and 90501004). The authors are indebted to the referees for their valuable comments.

Symmetric and antisymmetric soliton states in two-dimensional photonic lattices

Cibo Lou, Jingjun Xu, Liqin Tang, and Zhigang Chen

Key Laboratory for Weak-Light Nonlinear Photonics Materials, Ministry of Education, and TEDA Applied Physical School, Nankai University, Tianjin 300457, China

P. G. Kevrekidis

Department of Mathematics and Statistics, University of Massachusetts Amherst, Amherst, Massachusetts 01003

Received September 21, 2005; revised November 8, 2005; accepted November 23, 2005; posted December 1, 2005 (Doc. ID 64943)

We study the dynamics of off-site excitation in an optically induced waveguide lattice. A single beam centered between two waveguides leads to an asymmetric beam profile as the nonlinearity reaches a threshold. When two probe beams are launched in parallel into two nearby off-site locations, they form symmetric or antisymmetric (twisted) soliton states, depending on their relative phase. A transition of intensity pattern from on-site to off-site locations is also observed as the lattice is excited by a quasi-one-dimensional plane wave. © 2006 Optical Society of America
OCIS codes: 190.4420, 230.3990.

The dynamics of soliton propagation in coupled optical waveguides, from two coupled waveguides such as dual-core fiber couplers and directional couplers to three coupled waveguides and multiwaveguide arrays, has been studied extensively during the past decades.^{1–6} Much of the earlier theoretical work focused on energy switching and stability of solitons in coupled waveguide structures. For instance, it has been shown that, in a dual-core coupler, symmetry breaking typically occurs such that a symmetric soliton becomes unstable when its energy exceeds a threshold value.^{2,3}

More recently, closely spaced waveguide arrays (lattices) have attracted considerable attention owing to their strong link with photonic crystals as well as to intriguing phenomena that arise from their collective wave propagation behavior.^{7,8} An example is the formation of discrete solitons and bandgap structures, which have been demonstrated in a number of experiments.^{9–15} In particular, it has been shown that, in fabricated waveguide lattices with strong coupling, discrete solitons centered in the center of a waveguide (on-site excitation) are stable, while those centered in the middle between waveguides (off-site excitation) are unstable.^{14,15} Closely related research with optically induced photonic lattices¹⁶ has shown that an even-mode soliton or an in-phase dipolelike soliton is always unstable.^{12,17}

In this Letter we study experimentally off-site excitation in a weakly coupled lattice created by optical induction. When a Gaussian-like probe beam is launched between two lattice sites, its energy switches mainly to the two closest waveguide channels evenly, leading to a symmetric beam profile. However, as the intensity of the probe beam exceeds a threshold value, the probe beam evolves into an asymmetric beam profile, akin to that which results from symmetry breaking in a double-well potential.^{2,3} Should the probe beam experience no or only weak nonlinearity, such symmetry breaking in the beam profile would not occur, regardless of the increase in

its intensity. When two probe beams are launched in parallel into two off-site locations, they form symmetric or antisymmetric (dipolelike twisted^{12,17,18}) soliton states, depending on their relative phase. A transition of the intensity pattern from on-site to off-site locations is also observed as the lattice is excited by a quasi-one-dimensional plane wave, which may be related to excitation of symmetric (first band) and antisymmetric (second band) Bloch states in the lattices.^{10,19,20}

The experimental setup for our study is similar to that used for creation of spatial soliton pixels.¹⁶ A partially spatially incoherent beam (488 nm) is generated by use of a rotating diffuser. A biased photorefractive crystal (SBN:60, 6 mm × 8 mm × 5 mm) is employed to provide noninstantaneous saturable self-focusing nonlinearity. To generate a two-dimensional waveguide lattice we use an amplitude mask to spatially modulate the otherwise uniform beam after the diffuser. The mask is then imaged onto the input face of the crystal, thus creating a pixellike input intensity pattern. This lattice beam is ordinarily polarized; thus it induces a nearly linear waveguide array, which remains invariant during propagation.^{11–13} An extraordinarily polarized coherent beam (either 488 or 632.8 nm) is used as a probe beam propagating collinearly with the lattice. When required, the probe beam is split by a Mach–Zehnder interferometer to create two beams, which we can make either mutually coherent with a controlled phase relation or mutually incoherent by adjusting a piezoelectric transducer mirror installed in the interferometer.

First, we launch a single Gaussian beam (488 nm) as a probe into the middle of two lattice sites located in the vertical direction (illustrated as P₁ in Fig. 1). The choice of vertical rather than horizontal direction is made to prevent possible asymmetry of the beam profile induced by soliton self-bending. When the *e*-polarized probe beam propagates collinearly with the lattice through the crystal, we observe a transition from a symmetric to an asymmetric beam profile

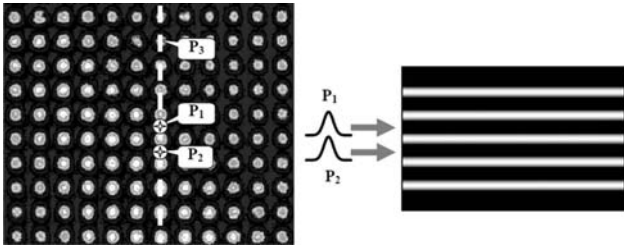


Fig. 1. Illustration of input locations of probe beams in a two-dimensional waveguide lattice.

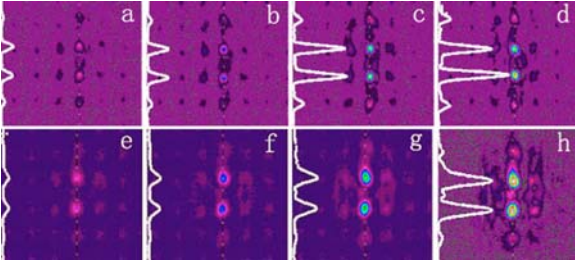


Fig. 2. (Color online) Off-site probing with a single Gaussian beam at 488 (top) and 632.8 (bottom) nm. a–h, Output intensity patterns of the probe beam at intensities (normalized to the lattice intensity) of a, 0.1; b, 0.2; c, 0.4; d, 0.5; e, 0.2; f, 0.4; g, 1.0; h, 2.0.

as the intensity of the probe beam is increased gradually while all other experimental conditions remain unchanged. Typical experimental results are presented in Fig. 2 (top), which were obtained with a lattice of $35 \mu\text{m}$ spacing (as shown at the left in Fig. 1). When the intensity of the probe beam is low, the energy of the probe tunnels evenly into two waveguides (Figs. 2a–2c). However, above a threshold value of input intensity, the output intensity pattern becomes asymmetric (Fig. 2d). The bifurcation from symmetric to asymmetric output is also clearly visible in the vertical beam profile illustrated at the left in each figure, which we obtained here by changing only the beam intensity without offsetting the beam position. To demonstrate that such a transition was induced by nonlinearity, all experimental conditions were kept unchanged, except that the 488 nm probe was replaced by a 632.8 nm probe. The beam at 632.8 nm experiences much weaker nonlinearity than does the 488 nm beam, simply because the former is at a much less photosensitive wavelength for our crystal. As expected, such a dynamic transition did not occur with the 632.8 nm probe, regardless of the increase in its intensity. In fact, even if the intensity of the probe beam was increased to twice that of the lattice beam, the probe profile remained symmetric, as shown in Fig. 2h.

Next, we split the Gaussian probe beam into two mutually incoherent beams with a Mach–Zehnder interferometer in which one of the mirrors was driven by a piezoelectric transducer at a frequency much faster than the crystal can respond to. When only one of the beams exiting from the interferometer was sent to an off-site position, we adjusted the beam's intensity such that a single beam alone did not lead to an asymmetric beam profile. Adding the other beam at the same location resulted in an overall asymmet-

ric beam profile. When the two beams were sent into two separate off-site locations (P_1 and P_2 in Fig. 1) rather than overlapped, we effectively had a three-well potential for the probe beams in the weak-coupling region. The energy of each probe beam alone tunneled into two adjacent waveguides evenly, as shown in Figs. 3a and 3b. We then opened up both beams and recorded the intensity pattern both immediately and after a new steady state had been reached. From Figs. 3c and 3d, one can see clearly that more energy from the probe beams moved to the central site owing to the noninstantaneous nonlinearity experienced by the probe beams. In fact, when we blocked one beam and quickly recorded the intensity pattern of the other beam, we noted that each beam profile became slightly asymmetric at this new steady state, with the preferred direction of energy tunneling toward the central site. In this case, the asymmetry of the top beam was similar to that shown in Fig. 2d, but the beam profile of the bottom beam had opposite asymmetry simply because the effective waveguide in the central site was stronger. Without the pairing beam, each beam alone will evolve into an asymmetric beam profile such as that in Fig. 2d once its intensity is increased above a threshold value. (The corresponding symmetry-breaking numerical simulation for off-site excitation of a single beam is shown at the right in Fig. 3; the waveguides are centered at $x = -9, -3, 3, 9$, etc.)

Naturally, one wonders what would happen if the two probe beams were made mutually coherent with a different phase relation. By controlling the dc voltage applied to the piezoelectric transducer mirror, we made the two beams exiting the interferometer either in phase or out of phase with each other. Keeping all other experimental conditions unchanged, we obtained quite different steady states between in-phase and out-of-phase excitation, as illustrated in Fig. 4. In the in-phase case, most of the energy flows into the central lattice site (Fig. 4a), whereas in the out-of-phase case the energy flows mainly into the two lateral sites in the vertical direction (Fig. 4b). Radiation to other nearby lattice sites owing to waveguide coupling is also visible. Intuitively, one may consider these new steady states to be a result of constructive and destructive interference, but they correspond to symmetric (in-phase) and antisymmetric

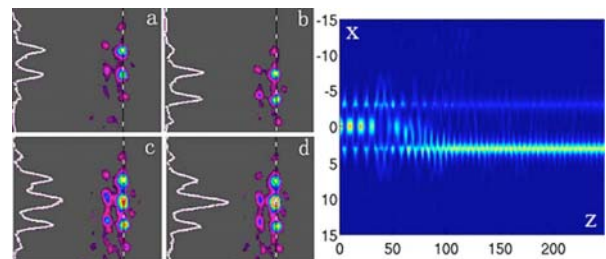


Fig. 3. (Color online) Left, off-site probing with two mutually incoherent beams. a, b, Output of a beam alone; c, d, output of two combined beams at 1 and 30 s, respectively. Right, numerical simulation of a single probe beam launched initially in the middle of two lattice sites located at $x = -3.0$ and $x = 3.0$ for 250 spatial steps of evolution (corresponding to ~ 50 cm propagation distance).

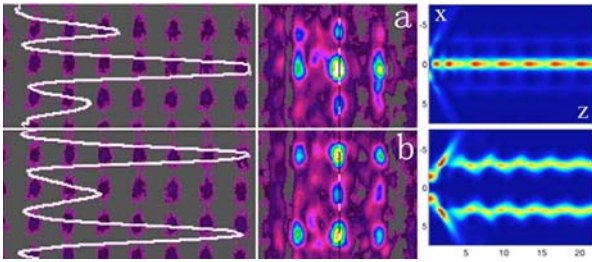


Fig. 4. (Color online) Off-site probing with two mutually coherent beams. Shown are the combined input beam profile (left) and the intensity pattern (middle) for, a, in-phase and, b, out-of-phase excitation. Right, simulation of dynamic evolution of two in-phase and out-of-phase beams launched at two off-site locations ($x = -1.5$ and $x = 1.5$).

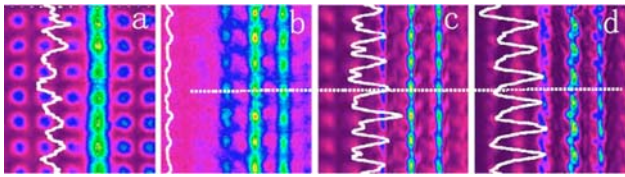


Fig. 5. (Color online) Probing with a stripe beam: a, combined input of lattice and stripe beams; b–d, output of the stripe beam at normalized intensities of b, 0.2 and 0.8 after c, 1 s and, d, 30 s.

(twisted) soliton states as defined for lattice solitons.^{17,18} Here the solitons are excited in an effectively three-well potential as embedded in a weakly coupled waveguide lattice. In fact, we theoretically investigated this issue, using a continuum model based on saturable photorefractive nonlinearity with an effective three-well potential. We found that in this setting any state with multiple in-phase beams (all centered on site) is always unstable. However, both symmetric states (corresponding to a single beam on site) and antisymmetric states (corresponding to two out-of-phase beams on two different sites) can be linearly stable. Typical results from simulations are included in Fig. 4 (right), where the top figure shows the evolution of two Gaussian beams launched at $x = -1.5$ and $x = 1.5$ (while the three waveguides are centered at $x = -3, 0, 3$). It can be seen that the two beams (although they are excited at off-site locations) evolve quickly into either a single beam (for the in-phase case) at the central site or two beams (for the out-of-phase case) at the two lateral sites.

As mentioned above, for a single beam excitation in waveguide lattices, the odd solitons (centered on a lattice site) are stable but the even ones (centered between two lattice sites) are not.^{12,14,15} Symmetry breaking in double-well potentials is well known,^{2,3} but in a fully periodic potential it may no longer be possible. Instead, an even-symmetry mode is indeed unstable, but it can be transformed into an odd-symmetry mode through an asymmetric beam profile.^{14,15} Such a transition is what we observed in our experiment (Fig. 2). In addition, twisted- (or dipole-) mode solitons (centered between two lattice sites but with an out-of-phase relation) were indeed predicted and found to be stable.^{12,17,18} Here we ob-

served such antisymmetric solitons by off-site excitation of two probe beams simultaneously.

Finally, we launched a stripe beam (akin to a quasi-1D plane wave) to cover many lattice sites in the vertical direction (shown in Fig. 5a and as P3 in Fig. 1). When the intensity of the probe beam was increased, we observed a shifting of its intensity peaks from on-site (Figs. 5b and 5c) to off-site (Fig. 5d) locations as the beam experienced higher nonlinear self-action and bending. This may be related to excitation of different Bloch states in the lattices.^{10,19,20}

This work was supported by National Natural Science Foundation (60328406, 10334010) and Ministry of Education (704012, PCSIRT) of China and by the U.S. National Science Foundation, Air Force Office of Scientific Research, and Petroleum Research Fund. We thank D. Frantzeskakis, D. Neshev, T. Kapitula, and J. Yang for discussions. Z. Chen is also with San Francisco State University, San Francisco, California. Z. Chen's email is zchen@stars.sfsu.edu.

References

1. D. N. Christodoulides and R. I. Joseph, *Opt. Lett.* **13**, 794 (1988).
2. E. M. Wright, G. I. Stegeman, and S. Wabnitz, *Phys. Rev. A* **40**, 4455 (1989).
3. M. Romangoli, S. Trillo, and S. Wabnitz, *Opt. Quantum Electron.* **24**, S1237 (1992).
4. N. N. Akhmediev and A. V. Buryak, *J. Opt. Soc. Am. B* **11**, 804 (1994).
5. A. B. Aceves, M. Santagiustina, and C. Angelis, *J. Opt. Soc. Am. B* **14**, 1807 (1997).
6. P. G. Kevrekidis, K. O. Rasmussen, and A. R. Bishop, *Int. J. Mod. Phys. B* **15**, 2833 (2001).
7. D. N. Christodoulides, F. Lederer, and Y. Silberberg, *Nature* **424**, 817 (2003).
8. D. Campbell, S. Flach, and Y. S. Kivshar, *Phys. Today* **57**, 43 (January 2004).
9. H. S. Eisenberg, Y. Silberberg, R. Morandotti, A. R. Boyd, and J. S. Aitchison, *Phys. Rev. Lett.* **81**, 3383 (1998).
10. D. Mandelik, H. S. Eisenberg, Y. Silberberg, R. Morandotti, and J. S. Aitchison, *Phys. Rev. Lett.* **90**, 053902 (2003).
11. J. W. Fleischer, M. Segev, N. K. Efremidis, and D. N. Christodoulides, *Nature* **422**, 147 (2003).
12. D. Neshev, E. Ostrovskaya, Y. Kivshar, and W. Krolikowski, *Opt. Lett.* **28**, 710 (2003).
13. H. Martin, E. D. Eugenieva, Z. Chen, and D. N. Christodoulides, *Phys. Rev. Lett.* **92**, 123902 (2004).
14. R. Morandotti, U. Peschel, J. S. Aitchison, H. S. Eisenberg, and Y. Silberberg, *Phys. Rev. Lett.* **83**, 2726 (1999).
15. U. Peschel, R. Morandotti, J. M. Arnold, J. S. Aitchison, H. S. Eisenberg, Y. Silberberg, T. Pertsch, and F. Lederer, *J. Opt. Soc. Am. B* **19**, 2637 (2002).
16. Z. Chen and K. McCarthy, *Opt. Lett.* **27**, 2019 (2002).
17. J. Yang, I. Makasyuk, A. Bezryadina, and Z. Chen, *Opt. Lett.* **29**, 1662 (2004).
18. S. Darmanyan, A. Kobayakov, and F. Lederer, *JETP* **86**, 682 (1998).
19. A. A. Sukhorukov, D. Neshev, W. Krolikowski, and Y. S. Kivshar, *Phys. Rev. Lett.* **92**, 093901 (2004).
20. F. Fedele, J. Yang, and Z. Chen, *Stud. Appl. Math.* **115**, 279 (2005).

Ultraviolet photorefractive effect in Mg-doped near-stoichiometric LiNbO₃

Dengsong Zhu, Jingjun Xu ^{*}, Haijun Qiao, Yanli Shi, Feng Gao, Wei Li, Bo Fu, Guaquan Zhang, Ke Zheng

The Key Laboratory of Advanced Technique and Fabrication for Weak-Light Nonlinear Photonics Materials, Ministry of Education, Nankai University, Tianjin 300457, People's Republic of China

Received 27 November 2005; received in revised form 8 May 2006; accepted 19 May 2006

Abstract

The ultraviolet photorefractive effect of Mg-doped near-stoichiometric LiNbO₃ crystals prepared by vapor transport equilibration (VTE) technique was studied at 351 nm. It was found in the near-stoichiometric LiNbO₃ crystals that the ultraviolet photorefractive effect could be enhanced greatly with the increase of Mg concentration. Based on the activation energy of dark decay of the photorefractive grating, possible centers responsible for the ultraviolet photorefractive effect were also discussed.

© 2006 Elsevier B.V. All rights reserved.

Keywords: Photorefractive; Lithium niobate; Stoichiometric; Ultraviolet

1. Introduction

Lithium niobate (LiNbO₃) is one of the most important photorefractive materials due to its many important applications, e.g., holographic volume storage, optical image and signal processing, coherent optical amplification, and phase-conjugation [1,2]. However, most of these applications have been studied in the visible. With the development of the ultraviolet light source, it is possible and necessary to study the photorefractive effect of LiNbO₃ in the ultraviolet. In 2000, Xu et al. found an enhancement of photorefractive effect in highly Mg-doped congruent LiNbO₃ in the ultraviolet [3]. Afterwards, Qiao et al. reported highly Zn and In doped congruent LiNbO₃ crystals to have excellent ultraviolet photorefractive characteristics [4]. These materials were believed to be good materials with optical damage resistance since 1980 [5–10] and the results of [3,4] extended the potential applications of them greatly. Nevertheless, these abnormal phenomena are still not fully understood.

In this paper, we further studied the ultraviolet photorefractive effect in Mg-doped near-stoichiometric LiNbO₃ crystals and discussed possible centers responsible for the ultraviolet photorefractive effect based on the activation energy of dark decay of the photorefractive grating.

2. Experiment

Three LiNbO₃ crystals doped with 0.2, 1.0, and 2.0 mol% Mg, hereafter denoted SMg0.2, SMg1.0, and SMg2.0, respectively, were grown by the conventional Czochraski method from the congruent melt. The positive direction of the *c*-axis was determined by the pyroelectric effect [11]. The vapor transport equilibration (VTE) technique [12,13] was introduced to increase the [Li]/[Nb] ratio of the crystals and due to the limitation of VTE technique, the thickness of the samples was less than 1 mm. The measured [Li]/[Nb] ratios of three samples by the Raman linewidth of the *E* mode (152 cm⁻¹) [14] are listed in Table 1. From the results of optical damage testing at 488 nm, it was found that the Mg concentration was above threshold in SMg2.0.

Experiments were performed with an Ar⁺ laser working at 351 nm. A schematic representation of the experimental

^{*} Corresponding author. Tel.: +86 2266229028; fax: +86 2266229310.
E-mail addresses: jjxu@nankai.edu.cn, zhudengsong@mail.nankai.edu.cn (J. Xu).

Table 1
Materials and photorefractive parameters of the samples at 351 nm

Samples	SMg0.2	SMg1.0	SMg2.0
Thickness along the <i>b</i> -axis (mm)	0.70	0.70	0.75
Mg concentration (mol%)	0.2	1.0	2.0
[Li ₂ O] (mol%)	50.18	50.04	49.55
Two-wave coupling gain ^a Γ (cm ⁻¹)	3.26	7.74	11.87
Diffraction efficiency ^b η (%)	0.52	1.37	3.1
Refraction index change ^b Δn ($\times 10^{-5}$)	1.08	1.76	2.48
Photoconductivity sensitivity ^b S (cm/J)	0.13	0.32	7.80
Response time ^c τ_e (s)	27.11	13.20	0.69
Effective carrier density N_{eff} ($\times 10^{16}$ cm ⁻³)	0.55	0.98	1.37
Activation energy E_A (eV)	0.29 ± 0.04	0.16 ± 0.02	0.13 ± 0.02

^a The intensity ratio between the signal and reference beam $I_S:I_R$ was 1:11 and the total incident light intensity $I_R + I_S$ was 191 mW/cm². The grating period Λ was 0.54 μm .

^b Two equal recording intensity $I_S = I_R = 57$ mW/cm² and the grating period Λ was 0.54 μm .

^c The response time constants were measured under the ultraviolet illumination of 57 mW/cm².

arrangement is shown in Fig. 1. The holographic gratings were written by the signal beam S and reference beam R with extraordinary polarization. The grating wave vector was kept parallel to the *c*-axis of crystal. The formation and decay process of the gratings were monitored by a weak He–Ne laser beam (632.8 nm) at the Bragg angle. The diffraction efficiency η of the holographic grating was measured by simply blocking the reference beam after saturation and η was defined as

$$\eta = \frac{I_d}{I_d + I_t}, \quad (1)$$

where I_d and I_t were the diffracted and the transmitted light intensity of the signal beam, respectively. The two-wave coupling gain Γ was defined as

$$\Gamma = \frac{1}{d} \ln \left(\frac{I'_S I_R}{I_S I'_R} \right), \quad (2)$$

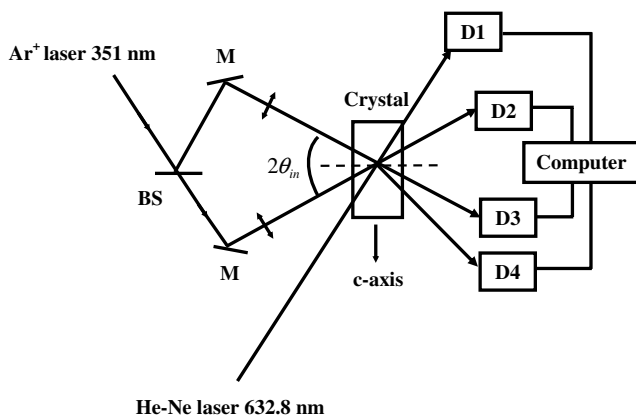


Fig. 1. Experimental set-up for ultraviolet photorefractive effect. M, mirror; BS, beam splitter; D1–D4, detectors; and $2\theta_{\text{in}}$, the intersection angle between the signal and reference beams in crystal.

where d was the thickness of the sample and I'_S, I'_R and I_S, I_R were the transmitted intensities of the signal beam S and reference beam R with and without coupling, respectively.

3. Results

The two-wave coupling experiment was performed with the setup as shown in Fig. 1. The total incident light intensity I ($I = I_S + I_R$) was 191 mW/cm², the ratio of intensity between the signal and reference beam $I_S:I_R$ was 1:11. The grating period was 0.54 μm corresponding to the intersection angle of signal and reference beam in air. The measuring coupling gain coefficient Γ was 11.78 cm⁻¹ in SMg2.0, 7.74 cm⁻¹ in SMg1.0, and 3.26 cm⁻¹ in SMg0.2, which are listed in Table 1. In the experimental process, for all the samples, the signal beam S propagates at an incline with respect to the $-c$ -axis direction. It was found that the intensity of signal beam S increased with time and saturated to a certain value when the reference beam R was switched on. Accordingly, the energy was unidirectionally transferred from $+c$ to $-c$ -axis direction, as also reported in Zn and In doped LiNbO₃ [4,15]. It could be reasonably concluded that the diffusion was the dominant mechanism and the dominant charge carriers were electrons during the ultraviolet photorefractive processes in the three samples [2].

The diffraction efficiency η was measured according to Eq. (1). When measuring, we set signal and reference beams of equal light intensity ($I_S = I_R = 57$ mW/cm²) were used in order to get a large optical modulation. The ultraviolet photorefractive characteristics of the three samples are listed in Table 1. The refractive index change Δn was calculated from the diffraction efficiency, according to [16]

$$\eta = \sin^2 \left(\frac{\pi \Delta n d}{\lambda \cos \theta_{\text{in}}} \right), \quad (3)$$

where $2\theta_{\text{in}}$ was the intersection angle between the signal and reference beams in crystal, λ was the wavelength of the probe beam in vacuum. The response time constant τ_e was defined as the time when the diffraction efficiency decays to $1/e$ of its initial value with the reference beam R to erase the grating. The photorefractive sensitivity S was defined as

$$S = \frac{1}{I d} \left. \frac{d\sqrt{\eta}}{dt} \right|_{t=0}, \quad (4)$$

where I ($I = I_S + I_R$) was the total incident intensity. From the experimental results in Table 1, it can be seen that the ultraviolet photorefractive effect was enhanced greatly with the increase of Mg concentration in our samples. The sample SMg2.0 showed the strongest photorefractive effect, whose refraction index change Δn , the response time τ_e , the coupling gain Γ and the photorefractive sensitivity S were 2.48×10^{-5} , 0.69 s, 11.87 cm⁻¹, and 7.80 cm/J, respectively. The results indicated that SMg2.0 was a better photorefractive material and more suitable for the dynamic and real-time holographic application than the other two samples in the ultraviolet.

Because the diffusion was the dominant mechanism, the photorefractive effect was mainly affected by the effective charge density [3,4]. The relation between the two-wave coupling gain Γ and the beam-crossing angle was described by [17].

$$\Gamma = \frac{A \sin \theta \cos 2\theta_{\text{in}}}{(1 + B^{-2} \sin^2 \theta) \cos \theta_{\text{in}}}, \quad (5)$$

where 2θ and $2\theta_{\text{in}}$ were the intersection angle between the signal and reference beams in air and in crystal, respectively, $A = \gamma_{\text{eff}} \xi (8\pi^2 n^3 k_B T / e \lambda^2)$ and $B = (e \lambda / 4\pi) (N_{\text{eff}} / \epsilon \epsilon_0 k_B T)^{1/2}$, where ξ was electron-hole competition factor, n was the refractive index, e was the elementary charge and N_{eff} was the effective charge density. The dependence of two-wave coupling gain Γ on the grating period Λ ($\Lambda = \lambda / 2 \sin \theta$) was measured and is shown in Fig. 2. By fitting the results with Eq. (5), we could obtain the effective carrier density N_{eff} . The fitting curves are also shown in Fig. 2. The fitting results yielded the N_{eff} was $0.55 \times 10^{16} \text{ cm}^{-3}$ for the sample SMg0.2, $0.98 \times 10^{16} \text{ cm}^{-3}$ for SMg1.0, and $1.37 \times 10^{16} \text{ cm}^{-3}$ for SMg2.0. The results indicated a noticeable increase of N_{eff} with increase of Mg-doped concentration, which caused a greater ultraviolet photorefractive effect in SMg2.0. This conclusion is consistent with the previous result in Mg, Zn, and In doped congruent LiNbO₃ [3,4].

In order to clarify the possible photorefractive centers responsible for the ultraviolet photorefractive effect, the activation energy was calculated from measurements of the temperature dependence of the dark decay time. The dark decay time constant τ of the grating was defined as the time when Δn decayed to $1/e$ of its initial value in the darkness. The crystal temperature was set from 23 °C to 140 °C. The temperature dependence of τ obeyed the Arrhenius law:

$$\tau^{-1} = \tau_0^{-1} \exp\left(-\frac{E_A}{k_B T}\right), \quad (6)$$

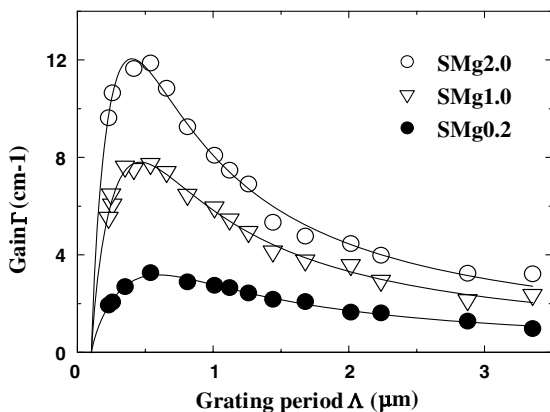


Fig. 2. Grating period Λ dependence of gain Γ . The intensity ratio between the signal and reference beam $I_S:I_R$ was 1:11 and the total incident light intensity $I_R + I_S$ was 191 mW/cm². Symbols: measured results; solid lines: theoretically fitting curves.

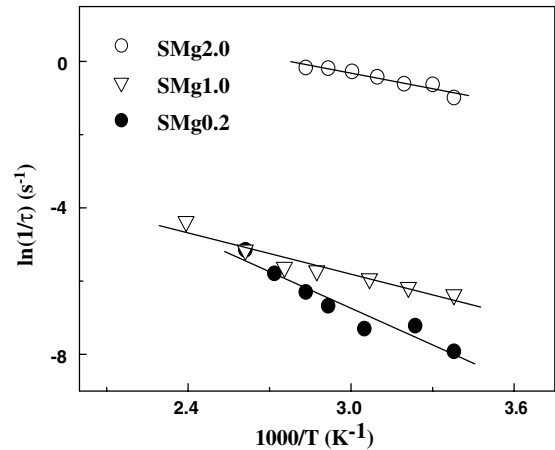


Fig. 3. Arrhenius plots of the dark decay time constant for SMg0.2, SMg1.0 and SMg2.0, respectively. The fitting activation energies were 0.29 ± 0.04 eV, 0.16 ± 0.02 eV, and 0.13 ± 0.02 eV.

where T was the absolute temperature of the crystal, k_B was the Boltzmann constant, and E_A was the activation energy. Fig. 3 shows the curves of τ versus T for SMg0.2, SMg1.0, and SMg2.0. The solid lines are the least-square fits of our experimental results by Eq. (6). The fitting results yielded the activation energy, E_A being 0.29 ± 0.04 eV for SMg0.2, 0.16 ± 0.02 eV for SMg1.0, and $0.13 \text{ eV} \pm 0.02$ eV for SMg2.0, which are listed in Table 1. The results indicated that E_A may correspond to shallow photorefractive centers due to its small value.

4. Discussion

Up to now, whether the dominant carrier in LiNbO₃ in ultraviolet is hole or electron is still under dispute [4,15,18–20]. In our samples, the energy was unidirectionally transferred from $+c$ to $-c$ -axis direction, and a large coupling gain coefficient Γ was observed. This indicated that diffusion was the dominant mechanism and the dominant charge carriers were electrons. Shallow photorefractive centers in LiNbO₃ have been studied extensively because of recent interests in non-volatile two-color recording.

In light of the Li-site vacancy model [21], Mg ions would replace the antisite Nb (Nb_{Li}) and force them to their original sites. For SMg0.2, because of the low concentration of Mg, in term of Ref. [22], it was thought that Mg ions would primarily replace the antisite Nb (Nb_{Li}) and force them to their original sites, Fe ions remain at Li sites. As the concentration of Nb_{Li} antisite defects decreased greatly; electrons would be trapped by Nb_{Nb} and formed the small free polaron $\text{Nb}_{\text{Nb}}^{4+}$ [23]. The $\text{Nb}_{\text{Nb}}^{4+}$ could act as the shallow photorefractive center and the activation energy of $\text{Nb}_{\text{Nb}}^{4+}$ was 0.29 ± 0.04 eV according to the Arrhenius plot. This value was close to the thermal activation energy of 0.24 eV and 0.29 eV for small free polaron $\text{Nb}_{\text{Nb}}^{4+}$ in reduced Mg doped and Zn doped LiNbO₃, respectively [24]. Sun-arno et al. also reported that in In doped congruent LiNbO₃ there was small free polaron $\text{Nb}_{\text{Nb}}^{4+}$ which was

responsible for the observed monoexponential decay behavior [25].

Ref. [26] reported that Fe ions also changed their sites and formed $\text{Fe}_{\text{Nb}}^{2-/3-}$ with the concentration of Nb_{Li} decreasing. For SMg1.0 and SMg2.0, it was thought there was $\text{Fe}_{\text{Nb}}^{2-/3-}$ defect as the shallow photorefractive center and its average activation energy was about 0.15 ± 0.02 eV according to the Arrhenius plots. Winnacker et al. reported that $\text{Fe}_{\text{Nb}}^{2-/3-}$ serves as a hole donor whose energy level is located at 0.11 eV below the conduction band [27].

Our results showed that the shallow photorefractive center with an increase of concentration of Mg would change from $\text{Nb}_{\text{Nb}}^{4+}$ to $\text{Fe}_{\text{Nb}}^{2-/3-}$. It should be noted that in Ref. [22] $\text{Fe}_{\text{Nb}}^{2-/3-}$ defect could be formed at above threshold concentration. In Ref. [26], however, it could be formed under threshold concentration. From what had been discussed above, it was thought that $\text{Fe}_{\text{Nb}}^{2-/3-}$ was not formed in SMg0.2, whereas it was formed in SMg1.0 where concentrations of Mg were both under threshold concentration.

5. Conclusion

In summary, we have studied the ultraviolet photorefractive effect of Mg-doped near-stoichiometric LiNbO_3 crystals produced by the Czochralski method and VTE treatment. We found that the ultraviolet photorefractive effect could be enhanced greatly with the increase of Mg concentration in the near-stoichiometric LiNbO_3 . The analysis of the activation energy indicated that under ultraviolet light, the shallow photorefractive center with an increase of concentration of Mg would change from $\text{Nb}_{\text{Nb}}^{4+}$ to $\text{Fe}_{\text{Nb}}^{2-/3-}$.

Acknowledgements

This work was supported by the “973” project of China (No. G1999033004), the Cultivation Fund of the Key Scientific and Technical Innovation Project of Chinese Ministry of Education (No. 704012), the Key Project of Chinese Ministry of Education (No. 105043), and the Program for Changjiang Scholars and Innovative Research Team in University.

References

- [1] A. Räuber, Chemistry and physics of lithium niobate, in: E. Kaldis (Ed.), Current Topics in Materials Science, vol. 1, North-Holland, Amsterdam, 1978, p. 481.
- [2] P. Günter, J.P. Huignard (Eds.), Photorefractive Materials and Their Applications, vols. I and II, Springer-Verlag, Heidelberg, 1989.
- [3] J. Xu, G. Zhang, F. Li, X. Zhang, Q. Sun, S. Liu, F. Song, Y. Kong, X. Chen, H. Qiao, J. Yao, L. Zhao, Opt. Lett. 25 (2000) 129.
- [4] H. Qiao, J. Xu, G. Zhang, X. Zhang, Q. Sun, G. Zhang, Phys. Rev. B 70 (2004) 094101.
- [5] G.G. Zhong, J. Jin, Z.K. Wu, IEEE Cat no. 80 CH 1561-0613 (1980).
- [6] D.A. Bryan, R. Gerson, H.E. Tomaschke, Appl. Phys. Lett. 44 (1984) 847.
- [7] T.R. Volk, V.I. Pryalkin, N.M. Rubinina, Opt. Lett. 15 (1990) 996.
- [8] T.R. Volk, N.M. Rubinina, Ferroelectr. Lett. Sect. 14 (1992) 37.
- [9] T.R. Volk, M. Wöhlecke, N. Rubinina, N.V. Razumovskii, F. Jermann, C. Fischer, R. Böwer, Appl. Phys. A 60 (1995) 217.
- [10] Y. Kong, J. Wen, H. Wang, Appl. Phys. Lett. 66 (1995) 280.
- [11] G.D. Boyd, R.C. Miller, K. Nassau, W.L. Bond, A. Savage, Appl. Phys. Lett. 5 (1964) 234.
- [12] P.F. Bordui, R.G. Norwood, D.H. Jundt, M.M. Feyer, J. Appl. Phys. 71 (1992) 875.
- [13] A. Gröne, S. Kapphan, J. Phys. Chem. Sol. 56 (1995) 687.
- [14] M. Wöhlecke, G. Corradi, K. Betzler, Appl. Phys. B 63 (1996) 323.
- [15] H. Qiao, J. Xu, Y. Tomita, D. Zhu, B. Fu, G. Zhang, G. Zhang, Opt. Mater., in press, doi:10.1016/j.optmat.2006.01.016.
- [16] H. Kogelnik, Bell Syst. Tech. J. 48 (1969) 2909.
- [17] M.D. Ewbank, R.R. Neurgaondar, W.K. Cory, J. Feinberg, J. Appl. Phys. 62 (1987) 374.
- [18] R. Orłowski, E. Kraetzig, Sol. State Commun. 27 (1978) 1351.
- [19] R. Jungen, G. Angelow, F. Laeri, C. Grabmaier, Appl. Phys. A 55 (1992) 101.
- [20] F. Laeri, R. Jungen, G. Angelow, U. Vietze, T. Engel, M. Wurtz, D. Hilgenberg, Appl. Phys. B 61 (1995) 351.
- [21] N. Iyi, K. Kitamura, Y. Yajima, S. Kimura, Y. Furukawa, M. Sato, J. Sol. State Chem. 118 (1995) 148.
- [22] H. Feng, W. Jin, H. Wang, S. Han, Y. Xu, J. Phys. Chem. Sol. 51 (1990) 397.
- [23] O.F. Schirmer, O. Thiemann, M. Wöhlecke, J. Phys. Chem. Sol. 52 (1991) 185.
- [24] B. Faust, H. Müller, O.F. Schirmer, Ferroelectrics 153 (1994) 297.
- [25] S. Sunarno, Y. Tomita, G. Zhang, Appl. Phys. Lett. 81 (2002) 4505.
- [26] A. Böckert, H. Donnerbergt, O.F. Schirmert, X.Q. Feng, J. Phys. 2 (1990) 6865.
- [27] A. Winnacker, R.M. Macfarlane, Y. Furukawa, K. Kitamura, Appl. Opt. 41 (2002) 4891.

Ultraslow Gaussian pulse propagation induced by a dispersive phase coupling in photorefractive bismuth silicon oxide crystals at room temperature

Fang Bo, Guoquan Zhang *, Jingjun Xu

*Photonics Center, College of Physics Science, Nankai University, Weijin Road 94, Tianjin 300071, China
The Key Laboratory of Advanced Technique and Fabrication for Weak-Light Nonlinear Photonics Materials, Ministry of Education, Nankai University, Tianjin 300457, China
Tianjin Key Laboratory of Photonics Materials and Technology for Information Science, Nankai University, Tianjin 300457, China*

Received 2 July 2005; received in revised form 29 November 2005; accepted 6 December 2005

Abstract

By use of the highly dispersive phase coupling effect in a photorefractive wave mixing process, we have observed ultraslow propagation of a single Gaussian light pulse with a group velocity ~ 0.5 m/s in a photorefractive $\text{Bi}_{12}\text{SiO}_{20}$ crystal at room temperature. The ultraslow Gaussian pulse is amplified due to an intensity coupling effect but keeping its Gaussian profile with high fidelity. The group velocity of the Gaussian pulse can be controlled to a large extent. This technique is useful for controllable optical delay lines.

© 2006 Elsevier B.V. All rights reserved.

Keywords: Ultraslow; Phase coupling; Photorefractive; Dispersive; Group velocity

1. Introduction

Due to an overwhelming desire for a fundamental understanding of physical laws governing light propagation and the promise of many applications, such as controllable optical delay lines, optical memories and information processing, great endeavors have been made to develop techniques to manipulate light propagation. Both superluminal [1,2] and subluminal [2–16] light propagation have been demonstrated via various techniques. A breakthrough on ultraslow light was accomplished first by Hau et al. [4] in an ultracold sodium atomic gas by use of the electromagnetically induced transparency (EIT) effect. Later ultraslow light propagation and even completely stopped light pulses were demonstrated in the Bose–Einstein condensates [4,5], in the atomic vapors [6,7] and in Pr-doped Y_2SiO_5 crystals

[8] using the EIT effect. However, complicated and rigorous experimental requirements, such as single-frequency lasers with a bandwidth \sim MHz or less and an extremely narrow operating spectral range put serious limitations onto such techniques for practical applications. Techniques based on mechanisms other than the EIT effect were proposed recently [2,9–13]. Among them the most representative ones are the ultraslow light propagation in solids at room temperature via the coherent population oscillation effect [2,10] and that via the temporal evolution of the photorefractive (PR) grating buildup in a degenerate two-wave mixing process [11,12]. The system requirements of these techniques are relatively simple as compared with those based on the EIT effect. On the other hand, the output signal pulse usually experiences serious distortion because the frequency components of the pulse are not uniformly delayed and attenuated/amplified. Podivilov et al. [11] showed that the delayed Gaussian pulse durations followed linearly the input pulse durations when the input Gaussian pulse durations were much longer than

* Corresponding author. Tel./fax: +86 22 23499944.
E-mail address: zhanggq@nankai.edu.cn (G. Zhang).

the response time of the PR degenerate two-wave mixing process. Deng et al. [12] tried to eliminate the distortion of the ultraslow light pulse by use of the multiple pump beams, in which each pump beam was tuned to the different frequency component of the signal pulse so that every frequency component of the signal pulse was delayed and amplified with the same amount by the corresponding pump beam. Recently, Odoulov et al. [13] delayed Gaussian pulses without severe broadening effect by using pump pulses of identical temporal profile as that of signal pulses. The pulses were delayed through a degenerate PR two-wave mixing with a negligible intensity coupling effect using electron-hole competition in $\text{Sn}_2\text{P}_2\text{S}_6$ and CdTe crystals.

In the previous papers [14,15], we proposed a simple technique to produce steady-state ultraslow light based on a dispersive phase coupling (PHC) effect. As an example, we demonstrated an amplified ultraslow light with a group velocity $V_g \sim 0.05$ m/s by using the highly dispersive PR-PHC effect in a $\text{Bi}_{12}\text{SiO}_{20}$ (BSO) crystal [16]. This technique offers a large controllability over the group velocity and a broad effective operating spectral range. Furthermore, a conventional laser can be used to achieve such PHC-induced ultraslow lights. We achieved the ultraslow light in the quasi-continuous-wave (quasi-cw) regime, therefore, a sinusoidally modulated probe light was used in the experiments. Nevertheless, it would be more interesting to slow down a single pulse in view of practical applications. In this paper, we have demonstrated the PHC-induced ultraslow single Gaussian pulse with high profile fidelity in a PR BSO crystal even with a cw pump beam. The factors that may induce the pulse profile distortion have been discussed. We have also discussed the differences in the propagation properties of the ultraslow lights between the quasi-cw and the pulse cases.

2. Experimental setup

Two mutually coherent and vertically polarized 532-nm beams, a strong cw pump beam and a weak signal Gaussian pulse, were overlapped and coupled in a BSO crystal ($5.2 \times 5.7 \times 5.7$ mm), as shown in Fig. 1. The pump was shifted in angular frequency by Ω using a sawtooth-volt-

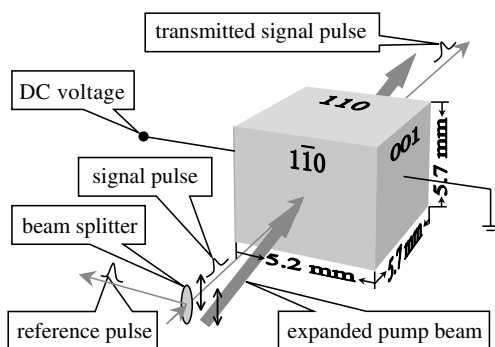


Fig. 1. Schematic diagram of the experimental setup.

age-driving piezo-mirror, and then expanded and collimated in order to illuminate the BSO crystal uniformly [17]. The signal Gaussian pulse was generated via an electro-optic modulator and its duration T (defined as the time constant of the Gaussian pulse) was controlled by a personal computer. Both the signal pulse and the pump propagated approximately along the $1\bar{1}0$ -direction of the BSO crystal (along the 5.7-mm side). The time-delay Δt experienced by the transmitted signal pulse was measured by monitoring and comparing the temporal trace of the transmitted signal pulse and that of a reference pulse which was a portion of the incident Gaussian pulse reflected by a beam splitter before the entrance facet of the BSO crystal. A direct current (DC) voltage was applied along the 001-direction of the BSO crystal.

3. Results and discussion

Fig. 2 shows typical temporal traces of the transmitted signal pulse (the solid curves) and the reference pulse (the dashed curves) with the pump off (a) and on (b), respectively. In the experiments, we used a pump intensity $I_p = 34$ mW/cm², an input intensity ratio of the pump to the peak of the signal pulse $\gamma = I_p/I_{\text{smax}} = 1400$, an external DC electric field $E = 8$ kV/cm, a grating spacing $\Lambda = 21.3$ μm , a pulse duration $T = 34$ ms and a frequency-shift of the pump $\Omega/2\pi = 18$ Hz, respectively. It is evident that the transmitted signal pulse is substantially delayed (see Fig. 2(b)) when the cw pump is on because of the highly dispersive PR-PHC effect. The time-delay Δt was measured to be ~ 11.2 ms, corresponding to a $V_g \sim 0.5$ m/s. It was found that, although the delayed signal pulse was amplified because of an energy transfer from the pump via the PR intensity coupling effect, it was of high Gaussian profile

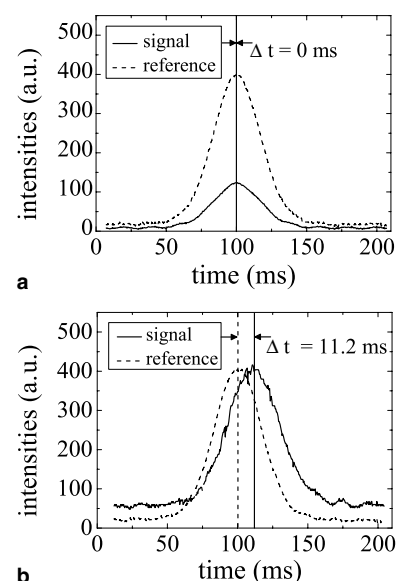


Fig. 2. Typical temporal traces of the reference pulses (dashed curves) and the transmitted signal pulses (solid curves) with the pump off (a) and on (b), respectively.

fidelity with only a slight ripple and broadening effect (see Fig. 2(b)). The slight profile ripple may come from an imperfect profile of the driving sawtooth voltage and the environmental vibration. The profile broadening effect of the delayed pulse originates mainly from the high order dispersion of the PHC effect and the broad frequency bandwidth of the Gaussian pulse itself. It is substantially suppressed when the frequency bandwidth of the input Gaussian pulse is much narrower than the bandwidth of the frequency window of the PHC effect with a positive dispersion slope. The bandwidth of the frequency window depends on the response rate of the PHC process. The faster the response rate of the PR-PHC process, the broader the bandwidth of the frequency window of the PR-PHC effect with a positive dispersion slope. Therefore, the profile broadening effect can be eliminated by employing a pulse with a long pulse duration T or a PR material with a fast response rate, as will be discussed in more detail in the following. In addition, the beam amplification effect and the memory effect of the PR gratings may also contribute to the pulse broadening partially. Note that the high fidelity of the ultraslow pulse was achieved with a cw pump beam, in contrast to that in Ref. [13] in which a pump pulse with an identical temporal profile as that of the signal pulse was used in order to suppress the broadening effect of the delayed pulse.

As is the quasi-cw case [14–16], the group velocity of a single pulse is also controllable to quite a large extent through adjusting experimental parameters, such as I_p , E and T . Fig. 3(a) shows the dispersion curves of V_g for the

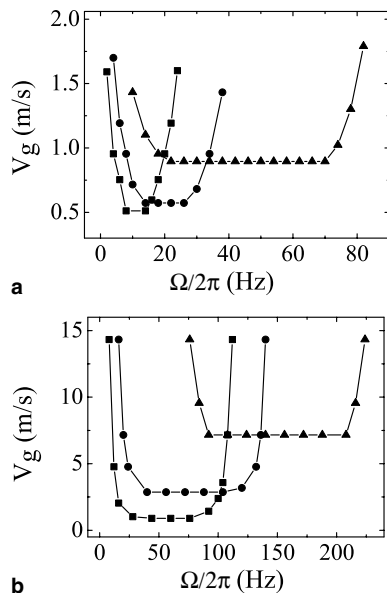


Fig. 3. Measured dispersion curves of V_g for a single Gaussian pulse at different conditions. (a) shows the results for $E = 8$ kV/cm with I_p to be 34 mW/cm² (squares), 68 mW/cm² (circles) and 152 mW/cm² (triangles), respectively. (b) is the results for $I_p = 152$ mW/cm² with E set at 8 kV/cm (squares), 6 kV/cm (circles) and 4 kV/cm (triangles), respectively. Other parameters γ , A and T for both cases were set to be 1400 , 21.3 μ m and 34 ms, respectively. The curves are guided by the experimental data.

signal pulse at different I_p with $E = 8$ kV/cm, $\gamma = 1400$, $A = 21.3$ μ m and $T = 34$ ms, respectively. It is clearly seen that ultraslow pulse propagation is limited within a narrow effective Ω -window $\Delta\Omega$, where the PHC coefficient dispersion curve has a steep positive slope [14,15]. It is the narrowness of this spectral window $\Delta\Omega$ that results partially in the profile broadening and distortion of the delayed pulse in the case of a short pulse, as discussed in the previous paragraph. Also, a lower I_p usually leads to a smaller achievable minimal V_g and a narrower $\Delta\Omega$ because of the proportionality of the response rate of the PHC to I_p [15]. Nevertheless, it is worthy of mention that it is possible to have a smaller V_g at a higher I_p in the short pulse case, where the coupling between the signal pulse and the pump is more effective at a higher intensity because of a larger ratio of pulse duration T to the response time constant τ of the PHC process [15]. The PHC between the signal pulse and the pump was found to be more effective at a higher E . This results in a lower V_g at a higher E , as shown in Fig. 3(b). As expected, $\Delta\Omega$ is broader at a lower E because of a faster response rate due to a shorter drift length of photoexcited electrons.

The pulse duration T also has an effect on V_g because of the slow response rate of the PHC process. The PHC is more effective with a longer pulse duration (especially when T is much less than τ) but it finally saturates when T is comparable to or much longer than τ . Fig. 4 shows a typical dependence of V_g on T with I_p , γ , E , A and $\Omega/2\pi$ set to be 152 mW/cm², 1400 , 8 kV/cm, 21.3 μ m and 60 Hz, respectively. As expected, V_g decreases with the increase of T but finally reaches the minimal with T longer than ~ 30 ms. Similar dependence of V_g on T was also observed by Podivilov et al. [11]. We notice that the pulse profile distortion grows with the decrease of T and it becomes serious when T is much less than τ . In this case, the spectral bandwidth of the Gaussian pulse is much broader than $\Delta\Omega$, therefore, the frequency components of the pulse cannot be uniformly delayed and amplified [12]. To delay short pulses while keeping their profile fidelity, high pump intensities or fast-response-rate PR materials, such as quantum well and semiconductor should be employed. We also note that the group velocity of a single pulse is much larger than

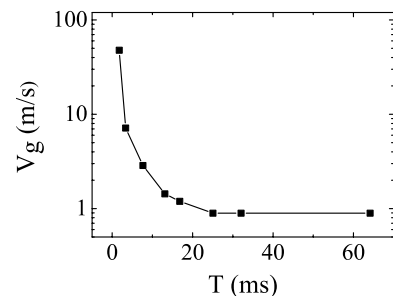


Fig. 4. Measured T -dependence of V_g for a single Gaussian pulse. The values for I_p , γ , E , A and $\Omega/2\pi$ were set at 152 mW/cm², 1400 , 8 kV/cm, 21.3 μ m and 60 Hz, respectively. The curve is guided by the experimental data.

that in the quasi-cw case under the similar experimental conditions. This may be due to the fact that the interaction duration between the pulse and the pump in the single pulse case is determined entirely by the pulse duration, while the PHC effect accumulates one pulse after another because of the memory effect of the PR gratings and therefore is enhanced in the quasi-cw case. In addition, the PR-PHC process is more complicated in the single pulse case than that in the quasi-cw case because the frequency components of a single Gaussian pulse are more complicated than those of a sinusoidally modulated wave in the quasi-cw case. To describe the dynamic propagation properties of a single pulse in the presence of a dispersive PHC effect, a modification to the theory of the PHC-induced ultraslow light in the quasi-cw case is necessary, which is currently under way in our laboratory.

4. Conclusions

In summary, we have decelerated a single Gaussian pulse down to ~ 0.5 m/s while keeping its high profile fidelity with a cw pump beam in BSO crystals at room temperature by using the highly dispersive PR-PHC effect. The group velocity of a Gaussian pulse is proved to be controllable to a great extent by changing the experimental conditions, such as the pump intensity, the strength of the externally applied electric field and the pulse duration. The delayed Gaussian pulse keeps its temporal profile when the pulse duration is comparable to or much longer than the response time of the dispersive PR-PHC process. The ultraslow Gaussian pulse is amplified due to an intensity coupling effect. Such a technique may be useful for optical delay lines as well as acousto-optic devices.

Acknowledgments

This work is supported by NSFC (60308005 and 10334010), NCET-04-0234, the Key Project of Chinese Ministry of Education (104054), and the Cultivation Fund of the Key Scientific and Technical Innovation Project, Ministry of Education of China (704012).

References

- [1] L.J. Wang, A. Kuzmich, A. Dogariu, *Nature* 406 (2000) 277.
- [2] M.S. Bigelow, N.N. Lepeshkin, R.W. Boyd, *Science* 301 (2003) 200.
- [3] S.E. Harris, *Phys. Today* 50 (7) (1997) 36.
- [4] L.V. Hau, S.E. Harris, Z. Dutton, C.H. Behroozi, *Nature* 397 (1999) 594.
- [5] Ch. Liu, Z. Dutton, C.H. Behroozi, L.V. Hau, *Nature* 409 (2001) 490.
- [6] M.M. Kash, V.A. Sautenkov, A.S. Zibrov, L. Hollberg, G.R. Welch, M.D. Lukin, Y. Rostovtsev, E.S. Fry, M.O. Scully, *Phys. Rev. Lett.* 82 (1999) 5229.
- [7] D.F. Phillips, A. Fleischhauer, A. Mair, R.L. Walsworth, *Phys. Rev. Lett.* 86 (2001) 783.
- [8] A.V. Turukhin, V.S. Sudarshanam, M.S. Shahriar, J.A. Musser, B.S. Ham, P.R. Hemmer, *Phys. Rev. Lett.* 88 (2002) 023602.
- [9] L. Deng, E.W. Hagley, M. Kozuma, D. Akamatsu, M.G. Payne, *Appl. Phys. Lett.* 81 (2002) 1168.
- [10] M.S. Bigelow, N.N. Lepeshkin, R.W. Boyd, *Phys. Rev. Lett.* 90 (2003) 113903.
- [11] E. Podivilov, B. Sturman, A. Shumelyuk, S. Odoulov, *Phys. Rev. Lett.* 91 (2003) 083902.
- [12] Zh. Deng, P.R. Hemmer, *SPIE* 5362 (2003) 81.
- [13] A. Shumelyuk, K. Shcherbin, S. Odoulov, B. Sturman, E. Podivilov, K. Buse, *Phys. Rev. Lett.* 93 (2004) 243604.
- [14] G. Zhang, R. Dong, J. Xu, *Chin. Phys. Lett.* 20 (2003) 1725.
- [15] G. Zhang, R. Dong, F. Bo, J. Xu, *Appl. Opt.* 43 (2004) 1167.
- [16] G. Zhang, F. Bo, R. Dong, J. Xu, *Phys. Rev. Lett.* 93 (2004) 133903.
- [17] Ph. Refregier, L. Solymar, H. Rajbenbach, J.P. Huignard, *J. Appl. Phys.* 58 (1985) 45.



Observation of superluminal and slowdown light propagation in doped lithium niobate crystals

Feng Gao, Jingjun Xu ^{*}, Haijun Qiao, Qiang Wu, Yin Xu, Guoquan Zhang

*TEDA Applied Physics School, Nankai University, Tianjin 300457, PR China
Photonics Center, Nankai University, Tianjin 300071, PR China*

Received 17 December 2004; received in revised form 3 July 2005; accepted 12 July 2005

Abstract

We investigate the group velocity of light in a one-dimensional volume grating inside lithium niobate crystals doped with different impurities. The superluminal and slowdown light propagations are both observed in the crystals. The relationships between the group refractive index and the grating amplitude and phase shift are presented and discussed. © 2005 Elsevier B.V. All rights reserved.

PACS: 42.25.Fx; 42.40.Eq; 42.25.Gy; 42.40.Lx; 42.40.Pa

Keywords: Group velocity; Volume grating; Lithium niobate

Optical waves in a volume grating behave similarly to electrons in the energy-band structure. For example, their group velocity is lowered to zero at the band edge [1]. Such a periodic structure exhibits strong group velocity dispersion, as studied on a GaAs–AlAs periodic-layered medium [2] and on a fiber Bragg grating [3]. There is also study on the slowing down of the group velocity of light by a volume grating in a photorefractive crystal of lithium niobate [4], which can

be explained by a change in the effective refractive index due to the grating [4]. Gratings with different origins may affect propagation behaviors of light in different ways, so in this paper we experimentally investigate the group velocity in the volume gratings with different origins as a result from different dopants in the crystal and try to find how gratings with different origins affect the results.

According to the coupled-mode theory [5,6], the complex amplitude of an optical wave passing through a reflection grating under the off Bragg condition is

^{*} Corresponding author. Tel./fax: +862266229419.
E-mail address: fenggao@nankai.edu.cn (F. Gao).

$$A(z) = A(0) \exp \left(-i \frac{\Delta k}{2} z \right) \times \frac{s \cosh s(L-z) - i \frac{\Delta k}{2} \sinh s(L-z)}{s \cosh sL - i \frac{\Delta k}{2} \sinh sL}, \quad (1)$$

where $A(z)$ is the complex amplitude of the transmitted beam and L is the interacting length along the direction of grating wave vector. s is given by $s = [\kappa^2 - (\frac{\Delta k}{2})^2]^{\frac{1}{2}}$ in which $\kappa = \frac{\pi n_1}{\lambda}$ is the coupling constant, n_1 is the index modulation of the grating, and Δk defined as $\Delta k = 2n \frac{\omega}{c} \cos \theta - \frac{2\pi}{\Lambda}$ is the phase mismatch, where θ is the mismatch angle, n is the refractive index of the crystal, ω is the angular frequency of the incident beam and Λ is the grating period. Eq. (1) follows immediately that the phase shift of the beam transmitting out of the crystal's grating by

$$\Phi(z) = \frac{\pi}{\Lambda} z + \tan^{-1} \left[-\frac{\Delta k}{2s} \tanh s(L-z) \right] + \tan^{-1} \left[\frac{\Delta k}{2s} \tanh sL \right], \quad (2)$$

The phase shift at $z = L$ is then given by [4]

$$\Phi = \frac{\pi}{\Lambda} L + \tan^{-1} \left[\frac{\Delta k}{2s} \tanh sL \right]. \quad (3)$$

By differentiating the phase shift per unit length with respect to ω , we obtain the effective group velocity of light propagating through the grating as [4]

$$V_g(L) = v_g \frac{(\frac{\Delta k}{2})^2 - \kappa^2 \cosh^2 sL}{(\frac{\Delta k}{2})^2 - \kappa^2 \frac{\sinh sL}{sL} \cosh sL}, \quad (4)$$

where v_g defined as $v_g = c/n$ is the group velocity of electromagnetic waves in the host medium in the absence of the volume grating. We also define the effective refractive index n_{eff} as $n_{\text{eff}} = c/V_g$. If n_{eff} is larger than n , it corresponds to the slowdown light propagation, while if smaller, it is the case of superluminal light propagation. Because we record the reflection grating in a small incident angle to avoid the surface back reflection affecting the result of the experiment, according to the Kogelnik formula, the diffraction efficiency η in our experiment could be given by

$$\eta = \tanh^2 \left(\frac{\kappa L}{\cos \alpha} \right), \quad (5)$$

where α is the incident angle of the recording beams outside the crystal relative to the normal of crystal surface. From Eqs. (4) and (5), we can easily get the relationship of V_g as a function of η and Δk .

In Fig. 1, we present the normalized effective group velocity V_g/v_g depending on η and Δk . V_g/v_g is larger than 1 or smaller than 1 corresponding to the case of superluminal light propagation and the case of slowdown light propagation, respectively. In Fig. 1, we take L as 10 mm, which corresponds to the length of the samples #a and #b in the z -axis direction. It can be seen that the normalized group velocity is not obviously deviant from 1 when η is small, i.e., no obvious propagating time change can be observed, for example, point A in Fig. 1. At a certain Δk , a fairly large change of the normalized group velocity should be observed when η is high enough, for example, at point B. It is also seen clearly that the result is sensitive to the phase mismatch. From Fig. 1, we can also see that the linear properties between the normalized group velocity and η can be roughly fulfilled when η is small and Δk is fixed, and if the fixed phase mismatch Δk is large enough, η can be up to 0.8 and this quasi-linear properties still keeps. Therefore, it could be roughly described as $V_g/v_g = n/n_{\text{eff}} = a\eta + 1$, where a is fitting constants. When $a < 0$, it is corresponding to the case of slowdown light propagation, otherwise to the case of superluminal light

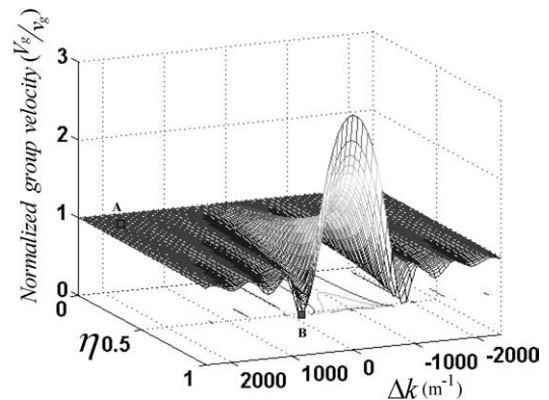


Fig. 1. The dependence of the normalized group velocity (V_g/v_g) on the diffraction efficiency η and the phase mismatch Δk .

propagation. This formula can be transformed to $n_{\text{eff}} = n/(a\eta + 1)$. We should find that the temporal evolution of the effective refractive index n_{eff} is coincident with the diffraction efficiency η in the case of slowdown light propagation, while it is opposite to that of η in the case of superluminal light propagation in the experiment.

In the experiment, we measured the diffraction efficiency and the effective refractive index. It is a very common and useful method of measuring the propagating time difference of the probe beam to get the probe beam's group velocity, and a single pulse usually serves as a probe beam if its group velocity is low enough to ignore the system error from the dispersive pulse broadening, for example, in the experiment of EIT (Electromagnetically induced transparency) [7,8]. The volume grating in our experiment has chromatic dispersion large enough to cause obviously dispersive pulse broadening, but the group velocity can not be reduced as low as that in EIT materials, in which the probe beam's propagating time difference is at least 10^{-8} s [7] and even 10^{-4} s [8]. Therefore, it is not suitable to choose a single pulse as a probe beam in our experiment, and we have to introduce an optical wave with a narrow bandwidth other

than use a single pulse as in EIT, so as to avoid the system error from the dispersive pulse broadening and ensure the measurement accuracy of the propagating time change from the difference of the light's group velocity in the crystal. In the experiment, we used a temporal beat beam, which was obtained by means of optical non-degenerate coherence between two beams at different frequencies out of an acousto-optic modulator (AO). The experimental setup is shown in Fig. 2. An output laser beam from an Ar⁺ laser at 514.5 nm was split into two beams. One of them directing in the way of path2 was used to record a photorefractive reflection volume grating in the crystal. The other beam in the direction of path1 was diffracted by an acousto-optic modulator (AO) operating at ~70 MHz. The first order diffracted beam and the undiffracted beam out of acousto-optic modulator were recombined via a beam splitter (BS2). Thus, at the same modulation frequency of ~70 MHz, two sinusoidally modulated beat beams were formed by means of the non-degenerate coherence. One acted as a reference, the other as the probe beam passing through the volume grating under the off-Bragg condition. The probe beam transmitting out of the crystal (the signal) and the

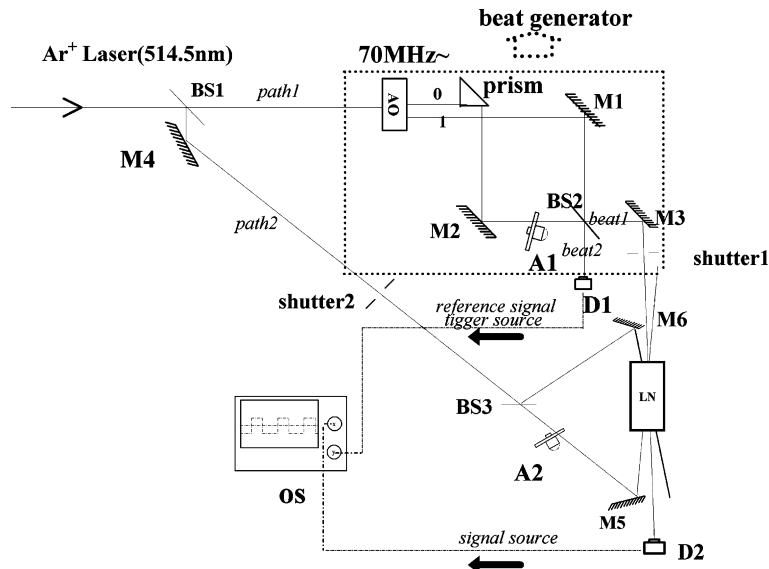


Fig. 2. Experimental configuration: AO is operating at the frequency of ~70 MHz. M1–M6, mirrors; BS1–BS3, beam splitters; A1–A2, attenuators; D1–D2, detectors; shutter1–shutter2, shutter; prism, act as a mirror; OS, oscilloscope.

reference beam were detected and the waveforms of them were monitored by an oscilloscope (OS). In this way, the time change of the probe beam propagating through the crystal during the grating building could be observed by the phase difference between the reference and the signal, from which the effective refractive index (consequently the group velocity) in the propagating direction of the probe beam inside the crystal could be determined. It is also seen clearly that the result is sensitive to the phase mismatch, and it is important to make sure that the change of the phase mismatch consequently the change of the group velocity comes from the building of the grating. In the experiment, we prepared different initial phase mismatch conditions by tuning the incident angle of the beating beam in order to observe both the slowdown and superluminal light propagations. Once an incident angle was chosen, we kept all the components in Fig. 2 fixed to preserve an unchanged phase mismatch except for the additional influence from the building process of the grating. During the grating building process we blocked one of the recording beams from time to time and measured the transmitted and diffracted beams of the other recording beam to calculate the diffraction efficiency. Then, we blocked the two recording beams and turned on the probe beam immediately to measure the phase difference of the signal and the reference beam. The probe beam was opened only for a very short interval to minimize the erasure of the grating. The typical time lag between the two measurements is less than

5 s in the experiment. All above is to ensure the accuracy of the measurement.

To study the relationship between gratings with different origins and the effective refractive index, we chose three lithium niobate crystals with different dopants. These crystals are referred as crystal #a doped with 0.025 wt% Fe, #b codoped with 0.05 wt% Fe and 0.8 mol% Mg, and #c codoped with 0.15 wt% Fe and 0.01 wt% Mn, respectively. The linear dimensions ($x \times y \times z$) of the three crystals were 10 mm \times 10 mm \times 10 mm, 20 mm \times 5 mm \times 10 mm, and 5 mm \times 5 mm \times 25 mm, respectively. Typical experimental results of slowdown and superluminal light propagation in the three samples are shown in Figs. 3–5 in which time dependences of the effective refractive index n_{eff} and diffraction efficiency η in the build-up process of the gratings are both presented. In the experiment, the time counter is stopped when the two recording beams are blocked, thus the time lag between the diffraction efficiency and the effective refractive index is much smaller than the total time of the build-up process. We neglect the time lag in the figures. In the process, n_1 is growing with time which results in the changes of both η and n_{eff} . Figs. 3(a), 4(a) and 5(a) show the case of slowdown light propagation while Figs. 3(b), 4(b) and 5(b) indicate the case of superluminal light propagation. The result of the superluminal case is achieved with the probe beam introduced at the Bragg angle of the grating and the Δk is almost zero. The result of the slow light case is achieved with the probe beam in the direction where its

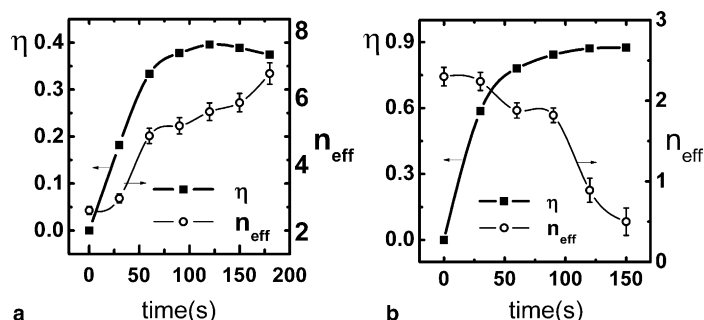


Fig. 3. Time dependence of the effective refractive index n_{eff} and the diffraction efficiency η during the building of the grating in the sample #a. (a) The data of slowdown light propagation at the $\Delta k \approx 628 \text{ m}^{-1}$; (b) The data of superluminal light propagation at the $\Delta k \approx 0 \text{ m}^{-1}$. The lines are just guides to eyes.

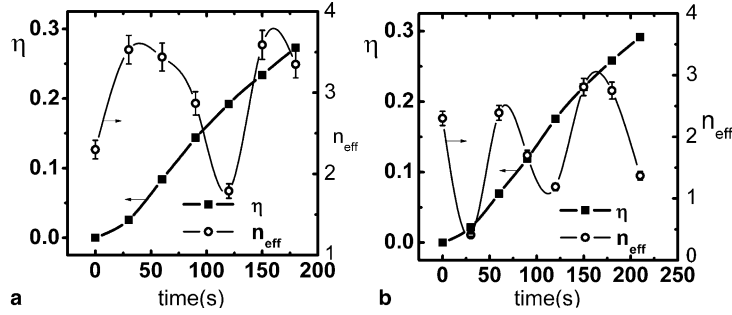


Fig. 4. Time dependence of the effective refractive index n_{eff} and diffraction efficiency η in the crystal #b. (a) The data of slowdown light propagation at the $\Delta k \approx 628 \text{ m}^{-1}$; (b) The data of superluminal light propagation at the $\Delta k \approx 0 \text{ m}^{-1}$. The lines are just the guide to eyes.

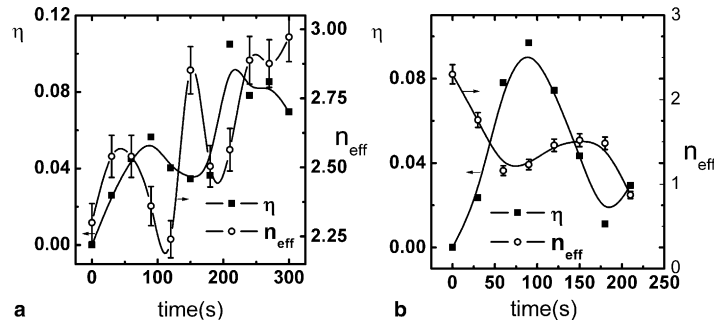


Fig. 5. Time dependence of the effective refractive index n_{eff} and diffraction efficiency η in the crystal #c. (a) The data of slowdown light propagation at the $\Delta k \approx 251 \text{ m}^{-1}$; (b) The data of superluminal light propagation at the $\Delta k \approx 0 \text{ m}^{-1}$. The lines are just the guide to eyes.

transmission is the largest in the immediate vicinity of the Bragg angle when the grating has been built up, for example, point B in Fig. 1, where $sL = i\pi$, i.e., $\Delta k = 2(\kappa^2 + (\pi/L)^2)^{\frac{1}{2}}$. In the theory, this direction corresponds to the Δk which gives almost the slowest group velocity [4]. It is also noticed that κ is much smaller than π/L , thus $\Delta k \approx 2\pi/L$.

From Figs. 3 and 5, i.e., in the crystals #a and #c, It is seen that the temporal evolution of the effective refractive index n_{eff} is more or less coincident with the diffraction efficiency η in the case of slowdown light propagation, while it is opposite to that of η in the case of superluminal light propagation. This agrees the theoretical prediction of $n_{\text{eff}} = n/(a\eta + 1)$. We also note that there is obvious difference among the results of the three LiNbO₃ crystals. The largest n_{eff} , the highest saturation diffraction efficiency η , and the slowest light

velocity as low as $c/6$ are observed in the crystal #a, and during the grating building process, the temporal evolution of n_{eff} rises or falls with η as the theoretical prediction. The change of the normalized group velocity is larger than the theoretical result shown in Fig. 1. This remains unclear now. Since the crystal #a is doped with iron, a fairly strong bulk photovoltaic field is always induced during the grating buildup process. Therefore, the grating is probably driven to move by the photovoltaic field, which may bring an additional phase shift due to the Doppler effect other than this mechanism. This may possibly bring some influence on the measurements. In addition, It is also found that the fanning effect in the crystal #a is another affecting factor. For example, due to the fanning, η slightly falls down during the growth of n_{eff} grows at the end of the curves in Fig. 3(a), which does not agree with the theoretical

analysis. On the other hand, we obtained a monotonic temporal buildup result for η in the crystal #b. But it is also found that n_{eff} oscillated somewhat chaotically in both slowdown light propagation and superluminal light propagation cases in this crystal. The crystal #b is co-doped with iron and magnesium, and we suppose that both the bulk photovoltaic field and the diffusion field contribute to the formation of the grating. As it is well known, the photovoltaic effect and the diffusion fields are related to the local and non-local responses, respectively. Therefore, the phase shift between the interference fringe and the light-induced index grating is more complicated so that such a result is obtained. It has been investigated that the group velocity changes in photorefractive two wave mixing [9]. We take it as one of the other mechanisms involved into the group velocity change with both larger phase shift and more obvious coupling between the probe beam and its reflection from the grating, which are both due to the non-local responses from the existence of magnesium. It is suggested that this mechanism together with the mechanism of Eq. (4) took effect in the crystal and made the temporal change of group velocity irregular whilst the temporal change of η is regular. Also, we observed the vibrating η during the grating buildup process in the crystal #c. We attribute it to the result of the co-existence of a phase grating created by the photorefractive effect and a photochromic grating due to co-doping with iron and manganese [10]. The phase grating has relative movement to the photochromic grating temporally dependent due to photovoltaic field which makes n_1 oscillate temporally and influence the η and the n_{eff} to oscillate temporally. It is seen from the Fig. 5 that n_{eff} mainly shows correspondences to the temporal evolution of η for some time ahead in the build-up process the grating. We can describe the above relationship as $n_{\text{eff}}(t) = n / (a\eta(t + t_0) + 1)$, where a is fitting constants, t_0 (positive in the result) means that the n_{eff} is some time ahead relative to the η . This is probably caused by the difference that n_{eff} is phase-sensitive to the probe beam while η is amplitude-sensitive to the probe beam. At the beginning, the two gratings are overlapped. When the relative movement happens between the two overlapped gratings,

the change of the total refractive index modulation will affect the phase of the probe beam earlier than the amplitude of it, which results in t_0 . The detail process of the relative movement of the grating is too complex to analysis and need further investigation.

In summary, we have experimentally investigated the superluminal light and slowdown light propagations through photorefractive volume gratings in lithium niobate crystals doped with different dopants. Besides the diffraction efficiency and the phase mismatch due to the off-Bragg angle, we found that the gratings with different mechanism origins are also of great influence on the results. The relationships between the effective refractive index and the gratings with different origins are also studied and discussed, which deserve further investigation.

Acknowledgments

This work was supported by National Advanced Materials Committee of China (Grant 2001AA313020), the National Natural Science Foundation of China (Grants 60308005 and 0378013 and 60278006) and the Key Project of the National Natural Science Foundation of China (Grants 1999033004).

References

- [1] C. Kittel, Quantum Theory of Solids, Wiley, New York, 1968.
- [2] M. Scalora, R.J. Flynn, S.B. Reinhardt, R.L. Fork, Phys. Rev. E 54 (1996) 1078.
- [3] B.J. Eggleton, C.M. de Sterke, R.E. Slusher, J. Opt. Soc. Am. B 16 (1998) 587.
- [4] Shiuan Huei Lin, Ken Y. Hsu, Pochi Yeh, Opt. Lett. 25 (2000) 1582.
- [5] H. Kogelnik, Bell Syst. Tech. J 48 (1969) 2909.
- [6] P. Yeh, Optics of Layered Media, Wiley, New York, 1993.
- [7] A. Kasapi, M. Jain, G.Y. Yin, S.E. Harris, Phys. Rev. Lett 74 (1995) 2447.
- [8] Lene Vestergaard Hau, S.E. Harris, Zachary Dutton, Cyrus H. Behroozi, et al., Nature 397 (1999) 594.
- [9] Zhang Guo-Quan, Dong Rong, XU Jing-Jun, Chin. Phys. Lett. 20 (10) (2003) 1725.
- [10] K. Buse, A. Adibi, D. Psaltis, Nature 393 (1998) 665.

W.-P. ZANG
 J.-G. TIAN[✉]
 Z.-B. LIU
 W.-Y. ZHOU
 F. SONG
 C.-P. ZHANG

High-accuracy finite-difference beam-propagation method for cylindrical geometry

The MOE Key Lab of Advanced Technique & Fabrication for Weak-Light Nonlinear Photonics Materials, and Tianjin Key Lab of Photonics Materials & Technology for Information Science, Nankai University, Tianjin 300457, P.R. China

Received: 18 January 2005/Revised version: 28 August 2005
 Published online: 30 November 2005 • © Springer-Verlag 2005

ABSTRACT A high-accuracy finite-difference beam-propagation method (HAFD-BPM) based on high-accuracy divided-difference formulas is presented. The truncation error in this HAFD-BPM is reduced to $o(\Delta r)^4$ in the transverse direction, whereas the error in a conventional FD-BPM is typically $o(\Delta r)^2$. Gaussian beam propagation in vacuum and nonlinear medium is simulated by this new method and conventional one. The comparison between them in computing time and accuracy reveals the advantage of this new method. As an example, this method is applied to the simulation of blow-up in self-focusing of a Gaussian beam.

PACS 42.65.Hw; 42.25.Bs; 02.70.Bf

1 Introduction

The beam-propagation method (BPM) has been established well as a versatile numerical tool for simulation and analysis of electromagnetic wave propagation in guided-wave photonic devices and nonlinear media [1–6]. Owing to its high accuracy and computing efficiency, the finite-difference BPM (FD-BPM) is currently more widely used than the fast-Fourier-transformation BPM [7, 8]. It has been shown that the accuracy of conventional FD-BPM strongly depends on the number of transverse grid points [3] due to the typical transverse discrete errors of $o(\Delta r)^2$.

In this paper, we present a new FD-BPM that is based on the high-accuracy divided-difference formulas to reduce the truncation error to $o(\Delta r)^4$ in transverse direction. Its computing time will increase because the matrix changes from tridiagonal matrix to pentadiagonal matrix, but it is worthy since a greater improvement in computing accuracy can be obtained. Numerical simulations of a Gaussian beam propagation in nonlinear media reveal the advantage of this new method. As an application, we have used this new scheme to simulate the blow-up in self-focusing of a Gaussian beam.

2 Numerical methods

We write the field envelop as $E = E_0\psi$, and E_0 is the field amplitude at $(z, r) = (0, 0)$. Applying slow varying

envelope approximation, we can write the partial differential equation that describes the propagation of the electric field envelope in a nonlinear medium as:

$$\frac{\partial \psi}{\partial \bar{z}} = \frac{1}{4i} L_r + \frac{1}{4i} p(\psi) \psi, \quad (1a)$$

with

$$L_r = \left(\frac{\partial^2 \psi}{\partial \bar{r}^2} + \frac{1}{\bar{r}} \frac{\partial \psi}{\partial \bar{r}} \right), \quad (1b)$$

where the transverse components are normalized to the beam waist radius in r direction, $\bar{r} = r/w_0$, the longitudinal distance is normalized to the Rayleigh length, $\bar{z} = z/z_0$, $z_0 = kw_0^2/2$ the Rayleigh length is, k is wave-vector, and $p(\psi)$ is nonlinear coupling function.

Let $\psi^l(\bar{r})$ be the complete solution to (1) at $\bar{z} = \bar{z}^l$, so the solution at $\bar{z}^l = \bar{z}^l + \Delta \bar{z}$ can be written in terms of $\psi^l(\bar{r})$ as

$$\psi^{l+1} = \exp \left[\frac{\Delta \bar{z}}{4i} L_r + \frac{1}{4i} \int_{\bar{z}^l}^{\bar{z}^{l+1}} p(\psi) d\bar{z} \right] \psi^l. \quad (2)$$

Above equation can be rewritten in a second-order accuracy form by symmetrical split operator

$$\psi^{l+1} \approx \exp \left[\frac{\Delta \bar{z} L_r}{8i} \right] \exp \left[\bar{p}(\psi) \Delta \bar{z} \right] \exp \left[\frac{\Delta \bar{z} L_r}{8i} \right] \psi^l, \quad (3a)$$

$$\bar{p}(\psi) = \frac{1}{4i \Delta \bar{z}} \int_{\bar{z}^l}^{\bar{z}^{l+1}} p(\psi) d\bar{z}. \quad (3b)$$

The symmetry in (3) is actually very important since after the first upgrading of the phase the half steps of propagation can be combined into single propagation step according to the following rule:

$$\exp \left(\frac{\Delta \bar{z} L_r}{8i} \right) \exp \left(\frac{\Delta \bar{z} L_r}{8i} \right) = \exp \left(\frac{\Delta \bar{z} L_r}{4i} \right). \quad (4)$$

The algorithm for propagating the field over a distance $\Delta \bar{z}$ thus consists of an incrementing of the phase in accordance with nonlinear medium changes, followed by a vacuum

✉ Fax: 86-22-23499981, E-mail: jitian@nankai.edu.cn

propagation of the resulting field over a distance $\Delta\bar{z}$, i.e. solving the equation

$$\frac{\partial\psi}{\partial\bar{z}} = \frac{1}{4i}L_r\psi. \quad (5)$$

Using the Crank–Nicholson scheme, the (5) can be derived as follows:

$$\left(1 - \frac{L_r\Delta\bar{z}}{8i}\right)\psi^{l+1} = \left(1 + \frac{L_r\Delta\bar{z}}{8i}\right)\psi^l. \quad (6)$$

The discrete field at the lattice point $\bar{r} = m\Delta\bar{r}$ and $\bar{z} = l\Delta\bar{z}$ will be represented by ψ_m^l . The first derivative term and second derivative term for \bar{r} with the accuracy of $o(\Delta\bar{r})^2$ can be derived as follows [9]:

$$\frac{\partial\psi}{\partial\bar{r}} = \frac{\psi_{m+1} - \psi_{m-1}}{2\Delta\bar{r}}, \quad (7a)$$

$$\frac{\partial^2\psi}{\partial\bar{r}^2} = \frac{\psi_{m+1} - 2\psi_m + \psi_{m-1}}{\Delta\bar{r}^2}. \quad (7b)$$

Meanwhile, the first derivative term and second derivative term for \bar{r} with the accuracy of $o(\Delta\bar{r})^4$ are

$$\frac{\partial\psi}{\partial\bar{r}} = \frac{-\psi_{m+2} + 8\psi_{m+1} - 8\psi_{m-1} + \psi_{m-2}}{12\Delta\bar{r}}, \quad (8a)$$

$$\frac{\partial^2\psi}{\partial\bar{r}^2} = \frac{-\psi_{m+2} + 16\psi_{m+1} - 30\psi_m + 16\psi_{m-1} - \psi_{m-2}}{12\Delta\bar{r}^2}. \quad (8b)$$

For the conventional FD-BPM, substituting (7) into (6) and collecting terms, the following finite-difference equations can be derived:

$$A_m\psi_{m-1}^{l+1} + B_m\psi_m^{l+1} + C_m\psi_{m+1}^{l+1} = F_m^l, \quad (9a)$$

$$F_m^l = A_m^*\psi_{m-1}^l + B_m^*\psi_m^l + C_m^*\psi_{m+1}^l. \quad (9b)$$

The coefficients in the last equations are expressed as follows:

$$A_m = \left(\frac{2m-1}{2m+1}\right), \quad B_m = \frac{2m}{(2m+1)}\left(\frac{1}{i\rho} - 2\right), \quad C_m = 1, \quad (10)$$

where $\rho = \frac{\Delta\bar{z}}{8(\Delta\bar{r})^2}$.

To avoid the singularity at $\bar{r} = 0$ L'Hospital rule must be applied, and $\psi_{-1}^l = \psi_1^l$ (first derivative with \bar{r} is zero at $\bar{r} = 0$) is assumed. The expressions for A_0, B_0, C_0 become:

$$A_0 = 0, \quad B_0 = \frac{1}{4i\rho} - 1, \quad C_0 = 1. \quad (11)$$

To satisfy the boundary conditions for $\bar{r} = (N-1)\Delta\bar{r}$, we set $\psi_N^l = 0$, which is equivalent to adding a sharp reflecting boundary at the edge of the numerical window. In order to keep $\psi_N^l = 0$, the size of numerical window has to be at least four times larger than beam size for Gaussian beams.

The numerical scheme described by (9)–(11) is the essence of the Crank–Nicholson method, and when numerically implemented involved solving (9), the matrix of coefficients for (9) is the so-called tridiagonal matrix; and therefore the computation of (9) can be easily performed analytically

using Thomas algorithm and involves only $(2N-1)$ floating-point operations of multiplications and divisions [10].

Meanwhile, for the HAFD-BPM, substituting (8) into (6) and collecting terms, the following finite-difference equations can be derived:

$$O_m\psi_{m-2}^{l+1} + P_m\psi_{m-1}^{l+1} + Q_m\psi_m^{l+1} + R_m\psi_{m+1}^{l+1} + S_m\psi_{m+2}^{l+1} = T_m^l, \quad (12a)$$

$$T_m^l = O_m^*\psi_{m-2}^l + P_m^*\psi_{m-1}^l + Q_m^*\psi_m^l + R_m^*\psi_{m+1}^l + S_m^*\psi_{m+2}^l. \quad (12b)$$

The coefficients in the above equations are expressed as follows:

$$O_m = \left(\frac{2m-1}{2m+1}\right), \quad P_m = -16\left(\frac{2m-1}{2m+1}\right),$$

$$Q_m = \frac{2m}{2m+1}\left(30 + \frac{1}{\rho_P}\right), \quad R_m = -16, \quad S_m = 1,$$

$$\rho_P = \frac{\Delta\bar{z}}{96i(\Delta\bar{r})^2}. \quad (13)$$

To avoid the singularity at $\bar{r} = 0$ L'Hospital rule must be applied, and assume that $\psi_{-1}^l = \psi_1^l$ and $\psi_{-2}^l = \psi_2^l$. The expressions for $O_0, P_0, Q_0, R_0, S_0, O_1$ become:

$$O_0 = O_1 = P_0 = 0, \quad Q_0 = \frac{1}{4\rho_P} + 15,$$

$$R_0 = -16, \quad S_0 = 1. \quad (14)$$

The numerical scheme described by (12)–(14) is the essence of the HAFD-BPM, and when numerically implemented involved solving the system is the so-called pentadiagonal matrix. Because this matrix is a constant coefficient matrix in numerical simulation, we only need to decompose this matrix into one time by LU decomposition method. These triangular matrixes are also tridiagonal matrixes. A two-step strategy can be applied to solving the system efficiently and only need $(4N-3)$ floating-point operations of multiplications and divisions [10].

3 Numerical results

As an illustration of this new method, we analyze the propagation of a Gaussian beam with form $\psi = \exp(-\bar{r}^2)$ in vacuum and a nonlinear medium with the nonlinear coupling function $p(\psi) = |\psi|^2$. Two main parameters of the Gaussian beam were computed numerically and then compared with the analytical values. They are beam size that is evaluated as the second moment of intensity

$$w(z) = \left[\frac{2\pi \int_0^\infty \bar{r}^2 I(\bar{r}, \bar{z}) \bar{r} d\bar{r}}{2\pi \int_0^\infty I(\bar{r}, \bar{z}) \bar{r} d\bar{r}}\right]^{1/2}, \quad (15)$$

and the total power of beam:

$$P(z) = 2\pi \int_0^\infty I(\bar{r}, \bar{z}) \bar{r} d\bar{r}. \quad (16)$$

For Gaussian beam propagating in vacuum, a true percent relative error ε_t is defined as:

$$\varepsilon_t = \left| \frac{\text{analytical value} - \text{numerical value}}{\text{analytical value}} 100\% \right|, \quad (17)$$

where the subscript t denotes that the error is normalized to a true value. Meanwhile, for Gaussian beam propagating in a nonlinear medium, the percent relative error ε_a is define as:

$$\varepsilon_a = \left| \frac{\text{high accuracy approximation} - \text{current approximation}}{\text{high accuracy approximation}} 100\% \right|, \quad (18)$$

where the subscript a denotes that the error is normalized to an approximate value.

4 Discussion

4.1 Propagation in vacuum

First, we discuss the Gaussian beam propagation in vacuum. In order to reduce the error introduced by $\Delta\bar{z}$, we choose step size in propagation direction to be $\Delta\bar{z} = 0.005$.

The true percent relative error ε_t of the beam radius of Gaussian beam propagating in the air for FD-BPM and HAFD-BPM is shown in Fig. 1. It is seen that the computing accuracy by HAFD-BPM is better than that by FD-BPM for same transverse step size $\Delta\bar{r}$. In order to compare conveniently the computing accuracy of the two methods, we define R_e as the ratio of HAFD-BPM's ε_t to FD-BPM's:

$$R_e = \frac{\text{The true percent relative error of HAFD-BPM}}{\text{The true percent relative error of FD-BPM}}. \quad (19)$$

It is seen in Fig. 2 that minimum R_e is 0.02 and maximum R_e is 0.12. Therefore, the computing accuracy of HAFD-BPM increases by one or two order of magnitude under the same transverse step size $\Delta\bar{r}$, compared with FD-BPM. The optimal step size of $\Delta\bar{r}$ lies in a range from 0.05 to 0.1.

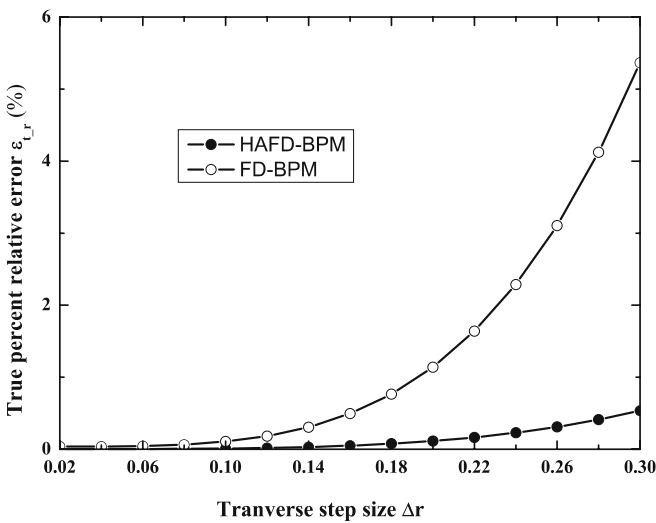


FIGURE 1 The true percent relative errors of beam radius $\varepsilon_{t,r}$ as a function of transverse step sizes $\Delta\bar{r}$ for HAFD-BPM and FD-BPM

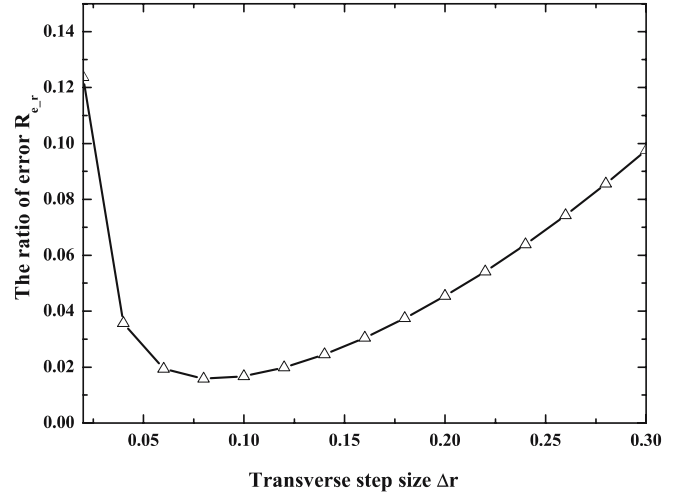


FIGURE 2 The ratio of error $R_{e,r}$ of beam radius for FD-BPM and HAFD-BPM as a function of transverse step sizes $\Delta\bar{r}$

The true percent relative error ε_t of the power of Gaussian beam propagating in the air for FD-BPM and HAFD-BPM is shown in Fig. 3. It is seen in Fig. 4 that minimum R_e is 0.015 when $\Delta\bar{r}$ equals to 0.06 and maximum R_e is 0.135 when $\Delta\bar{r}$ equals to 0.3. Therefore the computing accuracy of HAFD-BPM increases by one or two order of magnitude under the same transverse step size $\Delta\bar{r}$, compared with FD-BPM. The optimal step size of $\Delta\bar{r}$ is 0.06.

4.2 Propagation in nonlinear medium

We choose the step size in propagation direction to be $\Delta\bar{z} = 0.005$ and the distance of beam propagation to be $5z_0$. The relationship between percent relative error ε_a (see (18)) and transverse step size $\Delta\bar{r}$ is shown in Fig. 5. The true percent relative error ε_t of the power of Gaussian beam propagating in the case of nonlinearity FD-BPM and HAFD-BPM is shown in Fig. 6. The maximum percent relative error is $\varepsilon_a = 6$ for FD-BPM and $\varepsilon_a = 0.5$ for HAFD-BPM. It is seen in Fig. 7 that

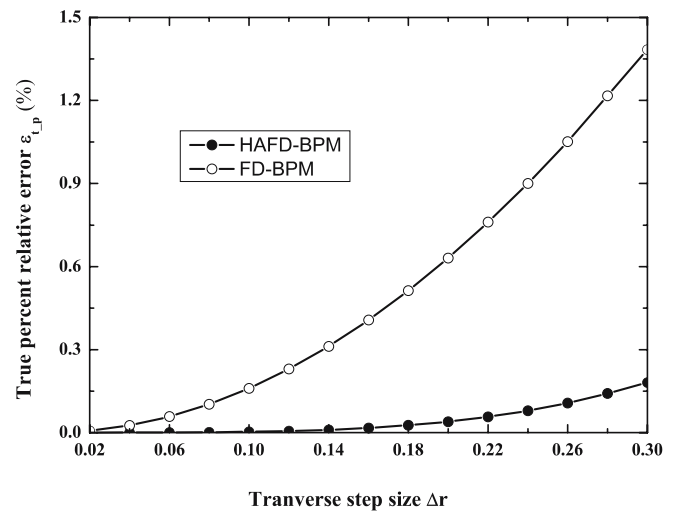


FIGURE 3 The true percent relative errors of power $\varepsilon_{t,p}$ as a function of transverse step sizes $\Delta\bar{r}$ for HAFD-BPM and FD-BPM

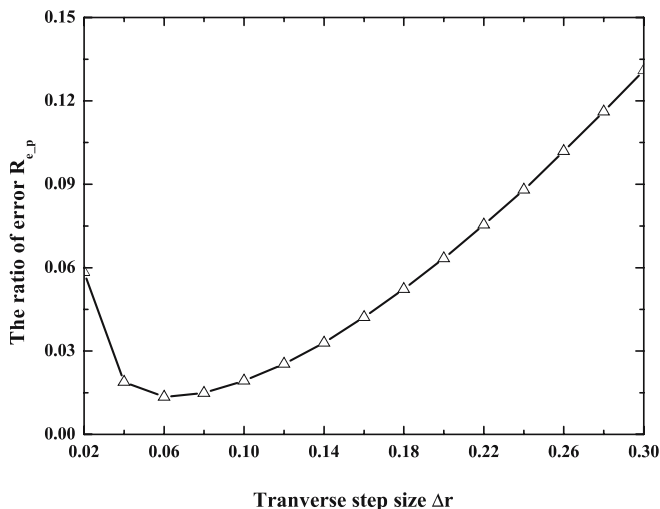


FIGURE 4 The ratio of error $R_{e,p}$ of power for FD-BPM and HAFD-BPM as a function of transverse step sizes $\Delta\bar{r}$

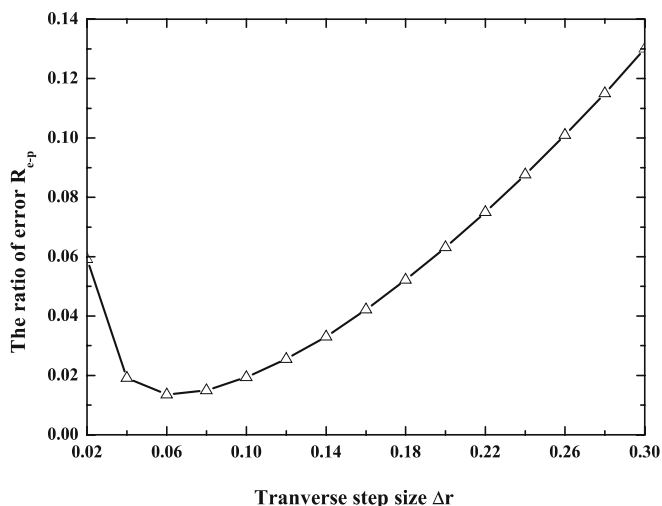


FIGURE 7 The ratio of error $R_{e,p}$ of power for FD-BPM and HAFD-BPM as a function of transverse step sizes $\Delta\bar{r}$ in the case of nonlinearity

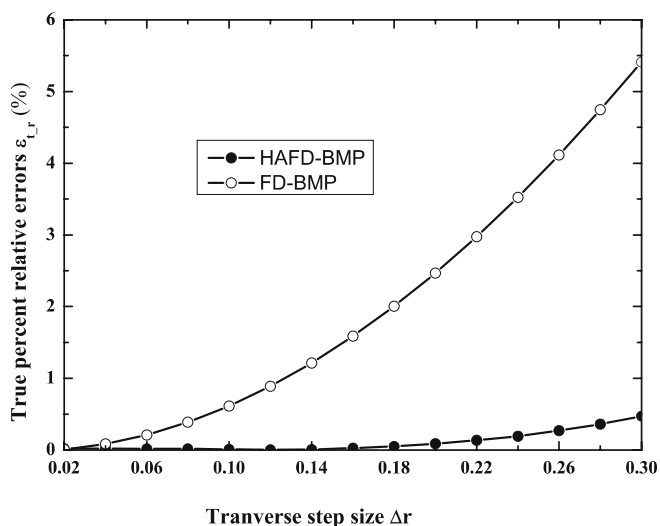


FIGURE 5 The true percent relative errors of beam radius $\varepsilon_{L,r}$ as a function of transverse step sizes $\Delta\bar{r}$ for HAFD-BPM and FD-BPM in the case of nonlinearity

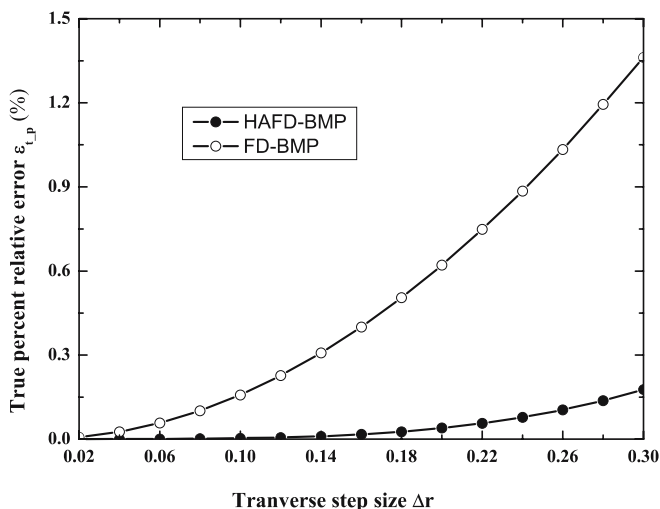


FIGURE 6 The true percent relative errors of power $\varepsilon_{L,p}$ as a function of transverse step sizes $\Delta\bar{r}$ for HAFD-BPM and FD-BPM in the case of nonlinearity

minimum R_e is 0.02 when $\Delta\bar{r}$ equals to 0.08 and maximum R_e is 0.135 when $\Delta\bar{r}$ equal to 0.3. Therefore, the computing accuracy of HAFD-BPM increases by one or two orders of magnitude under the same transverse step size $\Delta\bar{r}$, compared with FD-BPM. The optimal step size of $\Delta\bar{r}$ is 0.08.

To compare the computing speed of both methods, the CPU time required per propagation step is evaluated on a PC. The ratio of computing time required by the two method R_{time} for some transverse step size $\Delta\bar{r}$ is shown in Fig. 8. We can see that the computing time is about two times longer than that of FD-BPM. But it is worthy because the computing accuracy of HAFD-BPM increases one or two order of magnitude, compared with FD-BPM.

4.3 Blow-up in self-focusing

As an application of this new scheme, we use it to simulate the blow-up in self-focusing of a Gaussian beam. Under very general conditions on $p(\psi)$ of (1a), the Cauchy problem has a unique local solution $\psi(r, z)$ with

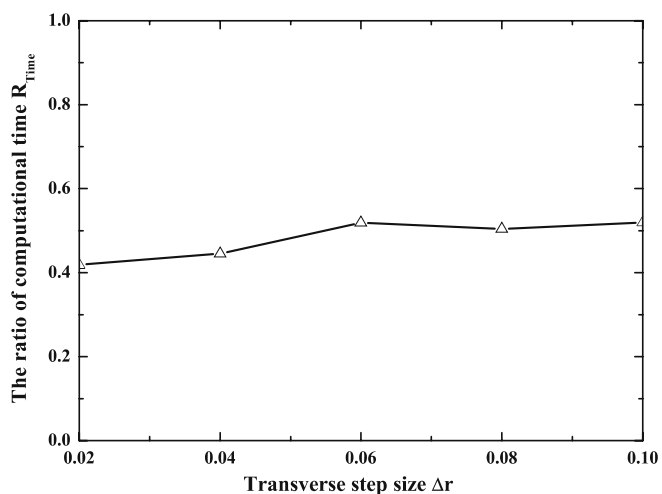


FIGURE 8 The ratio of computation time R_{time} for FD-BPM and HAFD-BPM as a function of transverse step sizes $\Delta\bar{r}$

$z \in [0, Z)$. A basic problem is whether these solutions can be continued to $Z = \infty$, that is, to a global solution in r . When the solution is not global, we speak of collapse or blow-up. When the solutions are global but develop “strong peaks” during evolution, one speaks of quasi-collapse processes. In the quasi-collapsing examples there is not a full collapse, but the amplitude grows in a localized spatial region leading to a spike of the amplitude of solution, which is difficult to describe using standard numerical scheme. This is also the case during real collapse processes, where the scheme must be able to integrate the solution up to the vicinity of the collapse point and even to detect the existence of the singularity, a fact which is not known a priori in some cases.

Let $p(\psi) = 6|\psi|^2$, $\Delta r = 0.01$, $\Delta z = 10^{-4}$ and the initial value of electric field be $\psi(0, r) = \exp(-r^2)$, we can obtain the relation between on-axis electric field and propagation distance, as shown in Fig. 9. The inset figure gives the detail around collapse point. For FD-BPM and HAFD-BPM, we can get the expressions as followings, respectively

$$\psi(z + \Delta z, r) = \psi(z, r) + O(\Delta z)^2 + O(\Delta r)^2, \quad (20a)$$

$$\psi(z + \Delta z, r) = \psi(z, r) + O(\Delta z)^2 + O(\Delta r)^4. \quad (20b)$$

When propagating to the vicinity of collapse point, the amplitude of ψ increases drastically, this leads to a drastic increase of truncation errors due to Δr and Δz . So the amplitude oscillation of ψ in vicinity of collapse point is an artificial effect that arising from truncation error of Δr and Δz . If step size decreases, this artificial effect also decreases. In order to get the approximate position of collapse point, we must set a criterion. The amplitude of electric field must increase monotonously with propagation distance. If this rule is broken, it can be thought that collapse point has reached. The position of collapse point as a function of Δr is shown in Fig. 10 for FD-BPM and HAFD-BPM, where the step size is set to be $\Delta z = 10^{-6}$. It can be seen that using HAFD-BPM we can approach the collapse point better than using FD-BPM. The position change of collapse point with Δz is also shown

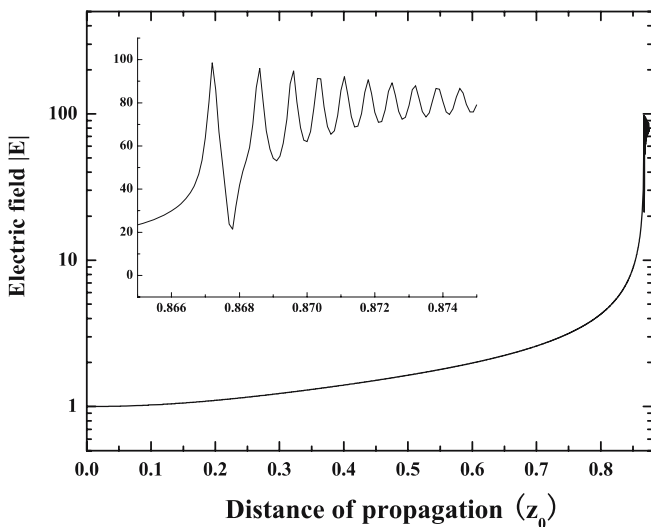


FIGURE 9 The on-axis electric field as a function of propagation distance

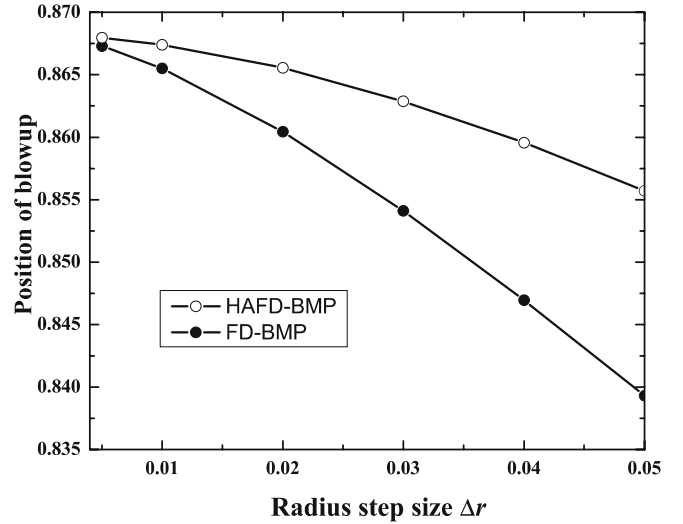


FIGURE 10 The position of collapse point as a function of Δr for FD-BPM and HAFD-BPM

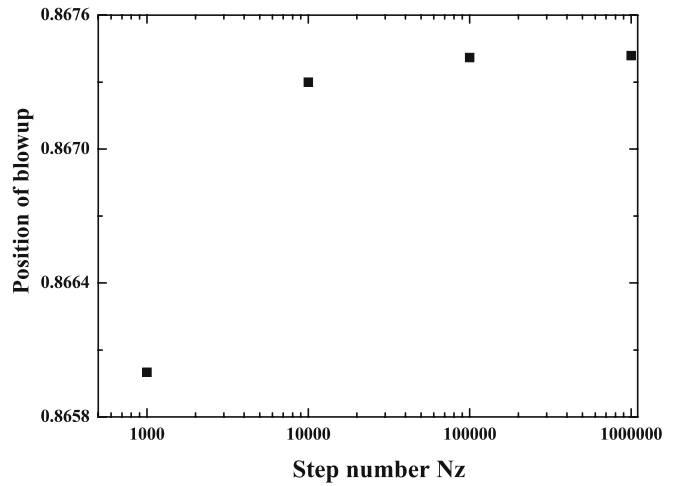


FIGURE 11 The positions of collapse point as a function of Δz for HAFD-BPM

in Fig. 11 for HAFD-BPM, where $\Delta r = 0.01$. It can be seen in Fig. 11 that the best approach to the collapse point can be achieved by reducing the step size Δz .

5 Conclusion

A high-accuracy finite-difference beam-propagation method (HAFD-BPM) based on high-accuracy divided-difference formulas is presented. The Gaussian beam propagating in vacuum and nonlinear medium by this new method and conventional method is simulated. Compared with FD-BPM, it is worthy that its computing accuracy gets a great improvement although its computing time increases a little. As an application, we use this new scheme to simulate the blow-up in self-focusing of a Gaussian beam.

ACKNOWLEDGEMENTS This research is supported by project 60025512 supported by the National Natural Science Foundation of China, the Preparatory Project of the National Key Fundamental Research Program (grant 2004CCA04400), Natural Science Foundation of Tianjin (grant 043601211), and the Fok Ying Tung Education Foundation (grant 71008).

REFERENCES

- 1 M.D. Feit, J.A. Fleck, Appl. Opt. **19**, 1154 (1980)
- 2 M.D. Feit, J.A. Fleck, Opt. Lett. **14**, 662 (1989)
- 3 D.I. Kvosh, S. Yang, D.J. Hagan, E.W. Vanstryland, Appl. Opt. **38**, 5168 (1999)
- 4 W.P. Zang, J.G. Tian, Z.B. Liu, W.Y. Zhou, C.P. Zhang, G.Y. Zhang, Appl. Phys. B **77**, 529 (2003)
- 5 W.P. Zang, J.G. Tian, Z.B. Liu, W.Y. Zhou, F. Song, C.P. Zhang, Opt. Comm. **244**, 71 (2005)
- 6 W.P. Zang, J.G. Tian, Z.B. Liu, W.Y. Zhou, F. Song, C.P. Zhang, Appl. Opt. **43**, 4408 (2004)
- 7 Y. Chung, N. Dagli, IEEE J. Quantum Electron. **QE-26**, 1335 (1990)
- 8 K. Kawano, T. Kitoh, *Introduction to Optical Waveguide Analysis* (Wiley, New York 2001) Chapt. 5
- 9 S.C. Chapra, R.P. Canale, *Numerical methods for Engineers* (McGraw-Hill, New York 1998) Chapt. 23
- 10 S.C. Chapra, R.P. Canale, *Numerical methods for Engineers* (McGraw-Hill, New York 1998) Chapt. 10

Nonlinear Absorption and Nonlinear Refraction of Self-Assembled Porphyrins

Zhi-Bo Liu,[†] Yi-Zhou Zhu,[‡] Yan Zhu,[‡] Shu-Qi Chen,[†] Jian-Yu Zheng,[‡] and Jian-Guo Tian^{*†}

The Key Laboratory of Advanced Technique and Fabrication for Weak-Light Nonlinear Photonics Materials, Ministry of Education and TEDA Applied Physical School, Nankai University, Tianjin 300457, China, and State Key Laboratory of Elemento-Organic Chemistry, College of Chemistry, Nankai University, Tianjin, 300071, China

Received: March 23, 2006; In Final Form: June 7, 2006

Nonlinear refraction and nonlinear absorption of self-assembled porphyrins in the nanosecond and picosecond regimes were studied at 532 nm by the Z-scan technique. First, a marked difference in nonlinear refraction was observed between self-assembled zinc porphyrins and free base porphyrins; however, the effects of self-assembly and metallization on nonlinear absorption are small. Second, an enhancement of nonlinear absorption was observed for the monomeric components of self-assembled structures by adding pyridine, while their nonlinear refractions remained almost unchanged as pyridine was added. It is expected that the metallization and addition of ligand can provide more convenient routes to alter the optical nonlinearities of porphyrins than the modifications of molecular structures of traditional covalent-bond organic materials.

Introduction

Organic compounds and organometallic complexes with π -electron delocalization have received significant attention in the last two decades because of their large and fast nonlinear optical response and potential applications in optical communication, data processing, optical switching, and so forth.^{1,2} Porphyrins are promising candidates for such nonlinear optical (NLO) materials in view of not only large π -conjugated systems but also versatile modifications of structures and various possibilities of the central metal ion.^{3,4} Most reports about optical nonlinearities of porphyrins, up to now, have been focused on reverse saturable absorption (RSA) between Soret and Q absorption bands,^{5–15} off-resonant third-order nonlinearities, and two-photon absorption (TPA).^{16–27} For example, under off-resonant conditions, a linear porphyrins array linked by butadiyne has been shown to exhibit among the largest $\chi^{(3)}$ values in any organic materials.¹⁷ Anderson et al.¹² reported triply linked porphyrin with the extended region of RSA from the visible to near-infrared range. Recently, a large number of porphyrins with different molecular structures were reported on their RSA,^{13–15} off-resonant third-order nonlinearities, and TPA.^{21–26} However, the reports on nonlinear refraction of porphyrins in the region of RSA are few.

With the development of porphyrins,²⁸ a supramolecular porphyrins system with large third-order optical nonlinearities and strong TPA has been obtained by using the complementary coordination of imidazolyl to the zinc of imidazolylporphyrinatozinc(II) in the noncoordinating solvent chloroform.^{19,20} The self-assembly of porphyrins greatly enhanced the off-resonant third-order nonlinearities and TPA for per-porphyrin unit. In the region of RSA, to our knowledge, the effects of self-assembly and ligand on optical nonlinearities of supramolecular porphyrins are not reported yet.

In this paper, we studied both nonlinear refraction and nonlinear absorption of self-assembled porphyrins by using a

Z-scan method²⁹ at 532 nm in nanosecond and picosecond regimes. Compared with free base porphyrins, self-assembled zinc porphyrins have a marked difference of nonlinear refraction and but little difference of nonlinear absorption. Furthermore, the effects of the coordination solvent pyridine on optical nonlinearities of self-assembled zinc porphyrins were also observed. An enhancement of RSA was obtained by the addition of pyridine. However, the addition of pyridine cannot affect the nonlinear refraction of zinc porphyrins. We used a five-level model to simulate experimental data.

Experimental Section

Materials. Molecular structures of porphyrins studied in this work are shown in Scheme 1. Since zinc porphyrins appended with nitrogen ligands can interact with each other to form complementary dimers or multi-composites, porphyrins **1b** and **2b** to which 2-imidazolyl groups are directly attached were self-assembled to afford complementary dimers **3** and **4**.¹⁹ Since the coordination bond can be cleaved in coordinating solvent, self-assembled porphyrin dimers can be dissociated to monomers by the addition of pyridine, and porphyrin monomers **5** and **6** can be obtained.²⁸

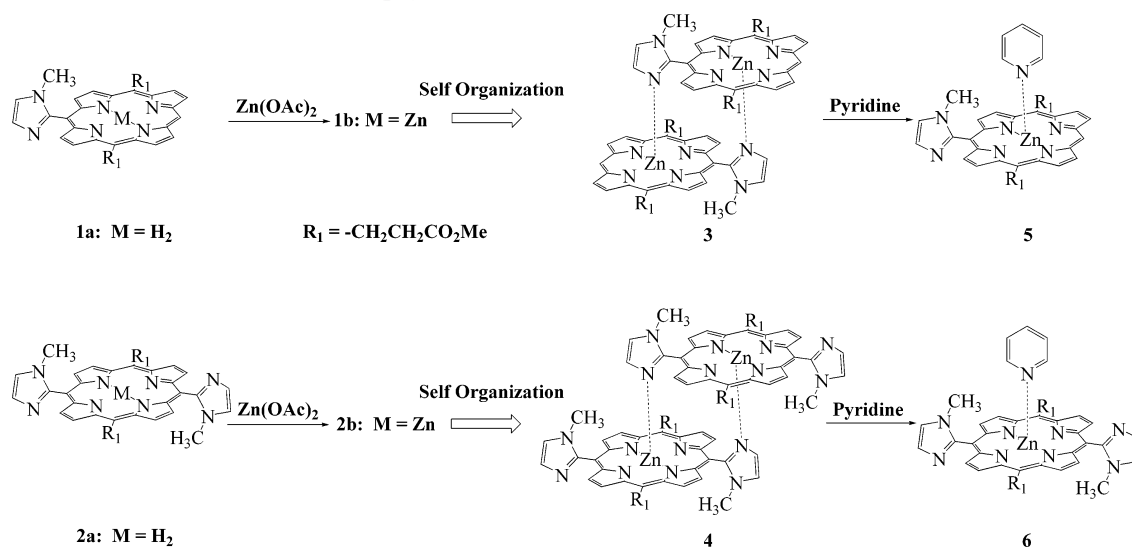
Measurements. Electronic absorption spectra were recorded on a UV spectrophotometer (Cary 300). Nonlinear refraction and reverse saturable absorption were measured by using the closed- and open-aperture Z-scan.²⁹ A Q-switched Nd:YAG laser (Continuum Surelite-II) and a mode-locked Nd:YAG laser (Continuum model PY61) were used to generate 5-ns pulses and 30-ps pulses with a repetition rate of 10 Hz at 532 nm, respectively. The spatial profiles of optical pulses were nearly Gaussian obtained by spatial filtering. The beam waist was 18 μm and 20 μm for 5-ns pulses and 30-ps pulses, respectively. The incident and transmitted pulse energies were measured simultaneously with two energy detectors (Moletron J3S-10). At every position, an average of 50 incident pulses which are not beyond $\pm 5\%$ fluctuation was taken by a computer. The sample solutions poured in a 1-mm quartz cuvette were used with the same concentration of 2×10^{-4} mol/L. The on-axis

* Author to whom correspondence should be addressed. E-mail: jjtian@nankai.edu.cn.

[†] TEDA Applied Physical School, Nankai University.

[‡] College of Chemistry, Nankai University.

SCHEME 1: Molecular Structures of Porphyrins Studied in This Work



peak intensity at focus is 1.12×10^9 W/cm² for 5-ns pulses and 4.11×10^9 W/cm² for 30-ps pulses.

Synthesis of Self-Assembled Porphyrins. In a 1000-mL four-neck round-bottom flask, 0.94 g (4 mmol) of 5-(2-methoxycarbonyl-ethyl) dipyrromethane was dissolved in 600 mL of chloroform, bubbled with nitrogen for 15 min. To this solution, the mixture of 0.24 g (2.1 mmol) of 1-methyl-2-imidazolecarboxyaldehyde, 0.8 g (7 mmol) of trifluoroacetic acid in 100 mL of chloroform and 0.16 g (37%, 2 mmol) of formaldehyde, 0.92 g (20 mmol) of ethyl alcohol in 100 mL of chloroform were added simultaneously in 15 min at 40 °C. The resulting solution was stirred for 30 min, then 1.8 g (8 mmol) of DDQ was added. The mixture was passed through an aluminum oxide column after 1 h. Further purification was carried out on a silica gel column. The second red band was collected to afford **1a** 5-(1-methyl-2-imidazolyl)-10,20-bis(2-methoxy-carbonyl-ethyl)porphyrin (yield: 5%). The compound **1a** was treated with a saturated zinc acetate/methanol solution to give porphyrin zinc complex **3**. **1a** ¹H NMR (300 MHz, CDCl₃) δ 10.151 (s, 1H), 9.567 (d, *J* = 4.8 Hz, 2H), 9.517 (d, *J* = 4.8 Hz, 2H), 9.393 (d, *J* = 4.8 Hz, 2H), 8.849 (d, *J* = 4.8 Hz, 2H), 7.697 (d, *J* = 1.2 Hz, 1H), 7.491 (d, *J* = 1.2 Hz, 1H), 5.345 (t, *J* = 8.1 Hz, 4H), 3.748 (s, 6H), 3.517 (t, *J* = 8.1 Hz, 4H), 3.382 (s, 3H), -2.970 (s, 2H). FT-IR (KBr) *v* 3283, 3104, 2987, 2948, 2836, 1733, 1561, 1466, 1434, 1405, 1339, 1308, 1278, 1246, 1224, 1145, 956, 919, 851, 796, 731. ESI-MS *m/z* 563 [M + H]⁺, 1125 [2M + H]⁺. **3** ESI-MS *m/z* 625 [M + H]⁺, 1249 [2M + H]⁺.

The third red band collected was proved to be **2a** 5,15-bis(1-methyl-2-imidazolyl)-10,20-bis(2-methoxycarbonyl-ethyl)porphyrin (yield: 5%). The zinc complex **4** was gained by treating **2a** with a saturated zinc acetate/methanol solution. **2a** ¹H NMR (300 MHz, CDCl₃) δ 9.532 (d, *J* = 5.1 Hz, 4H), 8.878 (m, 4H), 7.716 (m, 2H), 7.519 (m, 2H), 5.360 (t, *J* = 8.4 Hz, 4H), 3.770 (s, 6H), 3.527 (m, 10H), -2.780 (s, 2H). FT-IR (KBr) *v* 3304, 3187, 3131, 3109, 2989, 2946, 2838, 1732, 1632, 1561, 1473, 1440, 1403, 1347, 1280, 1250, 1192, 1142, 1040, 980, 805, 734, 708. ESI-MS *m/z* 643 [M + H]⁺, 1285 [2M + H]⁺. **4** ESI-MS *m/z* 705 [M + H]⁺, 1409 [2M + H]⁺.

Results and Discussions

Absorption Measurements. The absorption spectra of **1a**, **2a**, **3**, and **4** shown in Figure 1a present the characteristic bands

of porphyrins. The Soret bands of **1a** and **2a** are located around 411 and 417 nm, respectively. In the dimers of **3** and **4**, two porphyrins take a slipped co-facial form, and excitonic coupling between two porphyrin chromophores characteristically splits the Soret band. The Soret bands were split into twin peaks at 407 and 430 nm for **3** and at 411 and 436 nm for **4** due to exciton interaction originating from a slipped co-facial arrangement.³⁰ Additionally, the Soret bands of both free base and self-assembled zinc porphyrin with two imidazolyls (**2a** and **4**) have a red-shift compared with those with one imidazolyl (**1a** and **3**).

The degree of dissociation of dimers **3** and **4** depends on the amount of pyridine added. The split Soret bands of the CHCl₃ solution of dimers **3** and **4** can gradually turn into a single peak

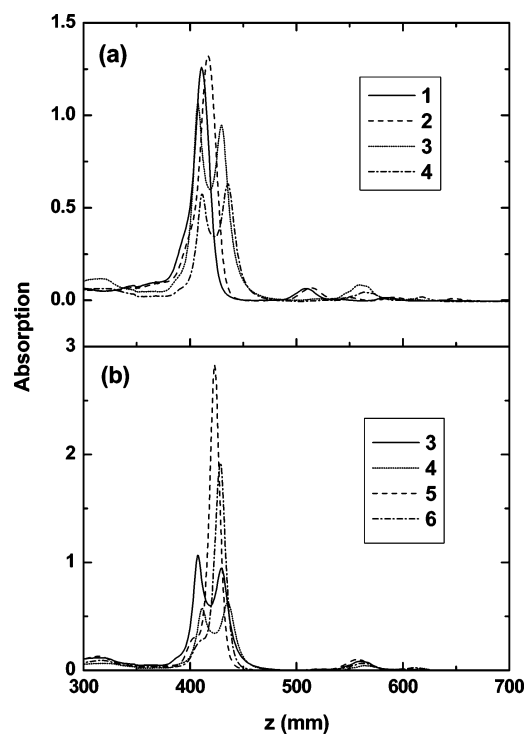


Figure 1. (a) UV absorption spectra of free base porphyrins (**1a** and **2a**) and self-assembled zinc porphyrins (**3** and **4**); (b) UV absorption spectra of **3**, **4**, **5**, and **6**.

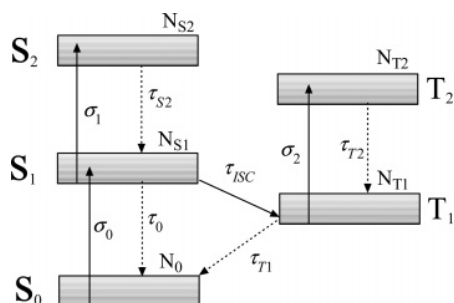
TABLE 1: Linear and Nonlinear Optical Properties of 1a, 2a, 3, 4, 5, 6, 7 (TPP), 8 (ZnTPP), and 9 (ZnTPP–pyridine)

	Soret band λ_{\max} (nm)	Q-band λ_{\max} (nm)	σ_0 (10^{-17} cm 2)	picosecond pulses			nanosecond pulses		
				σ_1 (10^{-17} cm 2)	σ_{T_1} (10^{-17} cm 2)	τ_0 (ns)	σ_2 (10^{-17} cm 2)	σ_{T_2} (10^{-17} cm 2)	τ_{ISC} (ns)
1a	411	509, 584	1.24	4.1	-2.2	0.15	2.6	-1.8	8.0
2a	417	514, 590	1.62	4.5	-2.1	0.15	3.2	-1.8	6.0
3	407, 430	559, 609	1.32	3.0		0.25	1.9	-1.1	2.5
4	411, 435	564, 618	1.55	3.1		0.25	2.7	-1.1	2.0
5	423	557, 601	1.57	6.1		0.55	3.6	-1.0	1.7
6	428	562, 611	1.65	5.6		0.64	4.3	-1.1	1.5
7	418	514, 548	1.75	5.8	-1.6	0.30	4.8	-1.2	10.0
8	419	547, 584	2.65	4.2		0.45	3.5	-0.8	3.0
9	429	563, 602	2.45	4.1		0.85	2.9	-0.9	1.5

along with the addition of pyridine. When the volume ratio of pyridine to CHCl_3 is larger than 1:4, the change of absorption bands is so small that we can consider that the dimers **3** and **4** were completely dissociated to monomers **5** and **6**. In our experiments, we used volume 1:1 mixture solvent of pyridine and CHCl_3 . For the monomeric imidazolylporphyrinatozinc **5** and **6**, a single peak in the Soret bands is observed as shown in Figure 1b. We can see from Figure 1 that the Q-bands of porphyrins studied in this work cover the region from 500 to 650 nm. Therefore, the laser at 532 nm used in the experiments just excites Q-bands. At this wavelength, the ground-state absorption cross-sections σ_0 of all porphyrins are shown in Table 1. As we will discuss later, a difference of optical nonlinearities between them is also observed when pyridine is added.

Effects of Metallization on Optical Nonlinearities. A large third-order optical nonlinearity of this self-assembled porphyrin system under the one-photon off-resonant condition has been observed by using femtosecond pulses.^{19,20} Our work presented here involves the excited-state optical nonlinearities of self-assembled porphyrin between Soret and Q absorption bands. Through Z-scan measurements using a picosecond pulsed laser, we can obtain both the absorption and refraction cross-sections of the singlet excited state. However, we cannot determine the triplet absorption and refraction cross-sections since the triplet state cannot become populated within the picosecond pulse duration because an intersystem crossing from the second excited singlet state to the first excited triplet state is typically on the order of a nanosecond for the materials used in our experiments. Hence, to study the triplet-state absorption and refraction, a nanosecond pulsed laser has to be used. The photophysical parameters of **1a**, **2a**, **3**, and **4** measured in our experiments are summarized in Table 1.

For a nanosecond pulsed laser, a five-level model, as shown in Figure 2, can depict the excited-state absorption (ESA) process in porphyrins and other dyes. Generally, after the initial excitation of this five-level system the first excited singlet state S_1 is populated. From this state the electrons may be subsequently excited into S_2 within the pulse duration of the laser. Once arriving at S_2 , they will rapidly relax to S_1 again. From

**Figure 2.** Five-level model of excited-state optical nonlinearities.

S_1 , the population can also undergo an intersystem crossing to the first excited triplet state T_1 with a time constant τ_{ISC} and thereafter be excited into T_2 . Similar to S_2 , this state relaxes to T_1 rapidly. An efficient RSA material whose transmission decreases as the incident intensity increases should have a high ratio (>1) of the absorption cross-sections of the excited states σ_1 and σ_2 ($T_1 \rightarrow T_2$ and $S_1 \rightarrow S_2$) to the ground state σ_0 ($S_0 \rightarrow S_1$). Rate equations of the five-level model can be written as³¹

$$\frac{dN_{S_0}}{dt} = -\frac{\sigma_0 I N_{S_0}}{\hbar\omega} + \frac{N_{S_1}}{\tau_0} + \frac{N_{T_1}}{\tau_{T_1}} \quad (1a)$$

$$\frac{dN_{S_1}}{dt} = -\frac{\sigma_1 I N_{S_1}}{\hbar\omega} + \frac{\sigma_0 I N_{S_0}}{\hbar\omega} - \frac{N_{S_1}}{\tau_0} - \frac{N_{S_1}}{\tau_{ISC}} + \frac{N_{S_2}}{\tau_{S_2}} \quad (1b)$$

$$\frac{dN_{S_2}}{dt} = \frac{\sigma_1 I N_{S_1}}{\hbar\omega} - \frac{N_{S_2}}{\tau_{S_2}} \quad (1c)$$

$$\frac{dN_{T_1}}{dt} = -\frac{\sigma_2 I N_{T_1}}{\hbar\omega} + \frac{N_{S_1}}{\tau_{ISC}} - \frac{N_{T_1}}{\tau_{T_1}} \quad (1d)$$

$$\frac{dN_{T_2}}{dt} = \frac{\sigma_2 I N_{T_1}}{\hbar\omega} - \frac{N_{T_2}}{\tau_{T_2}} \quad (1e)$$

where N_i represents the population in the i state ($I = S_0, S_1, S_2, T_1, T_2$), I is input laser intensity, and τ_0 is the time constant of the population's transition from S_1 to S_0 . If the sample length L is less than z_0 , the equations that govern the irradiance and the phase change can be written as³²

$$\frac{dI}{dz} = -\alpha I = -(\sigma_0 N_{S_0} + \sigma_1 N_{S_1} + \sigma_2 N_{T_1}) I \quad (2a)$$

$$\frac{d\phi}{dz} = k\Delta n = \sigma_{T_1} N_{S_1} + \sigma_{T_2} N_{T_1} \quad (2b)$$

where $k = 2\pi/\lambda$ is the wave vector, λ is the laser wavelength, and σ_{T_1} and σ_{T_2} are the singlet and triplet excited-state refractive cross-sections, respectively.

If the picosecond pulsed laser is used, the five-level model (S_0, S_1, S_2, T_1 , and T_2) can be simplified into a three-level model (S_0, S_1 , and S_2) since the intersystem crossing time τ_{ISC} is about the order of a few nanoseconds and is much larger than the pulse duration τ_p . It is difficult to obtain analytical solutions of these time- and space-dependent differential equations. Here we used the standard Runge–Kutta fourth-order method to solve eqs 1,2 numerically, and the irradiance and phase change of the laser beam at the exit face of the sample can be obtained. Then, by applying Huygens's principle and a zeroth-order

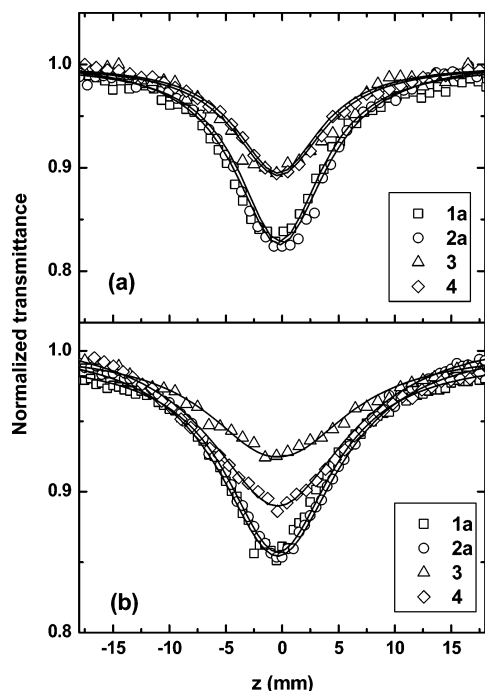


Figure 3. Open-aperture Z-scan curves of **1a**, **2a**, **3**, and **4** for the cases of picosecond pulses (a) and nanosecond pulses (b). The solid lines are the fittings obtained by a five-level model.

Hankel transformation, we can obtain the far-field electric field at the aperture plane and the Z-scan curves. By theoretically simulating the open- and closed-aperture Z-scan experimental data, we can obtain the values of σ_1 , σ_{r1} , and τ_0 in the case of 30-ps pulses, and σ_2 , σ_{r2} , and τ_{ISC} in the case of 5-ns pulses.¹⁰

The RSA properties of free base and zinc porphyrins (**1a**, **2a**, **3**, and **4**) dissolved in CHCl_3 are shown in Figure 3a (with 30-ps pulse duration) and Figure 3b (with 5-ns pulse duration), where open-aperture Z-scan curves were measured. The solid lines are the theoretical fittings obtained by using a five-level model. There is no obvious difference in the open-aperture Z-scan curves of **1a** and **2a** for both picosecond and nanosecond pulses. This implies that the influence of the imidazolyl is weak for free base porphyrin. It can also be seen clearly in Figure 3 that the metallization of the zinc atom results in a decrease of RSA in the cases of picosecond pulses and nanosecond pulses. This indicates that the metallization affects the absorption of both singlet and triplet excited states, since the RSA is dominated by absorption of singlet excited states in the case of picosecond pulses and by absorption of triplet excited states in the case of nanosecond pulses. For the self-assembled zinc porphyrins with one imidazolyl **3** and two imidazolyls **4**, their characteristics of RSA are similar in the case of picosecond pulses. However, **4** has a larger RSA than **3** in the case of nanosecond pulses. The difference of RSA between **3** and **4** in the case of nanosecond pulses may be due to the influence of imidazolyl on the absorption cross-section of T_1 .

In the region between Soret and Q-bands, such as at 532 nm, most reports on porphyrins were concentrated on studies of RSA, but their properties of nonlinear refraction are seldom reported so far. We studied the nonlinear refraction of self-assembled porphyrins in the RSA region. Figure 4 gives the nonlinear refraction Z-scan curves of **1a**, **2a**, **3**, and **4** obtained by dividing closed-aperture Z-scan data by corresponding open-aperture Z-scan data. The solid lines are the theoretical fittings by eq 3, and the relative parameters of σ_{r1} and σ_{r2} are given in Table 1. For free base or self-assembled zinc porphyrins, the

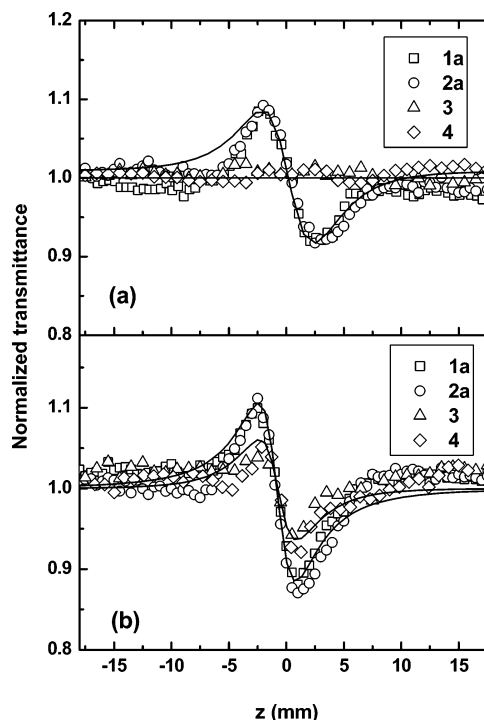


Figure 4. Nonlinear refraction Z-scan curves of **1a**, **2a**, **3**, and **4** in CHCl_3 for the cases of picosecond pulses (a) and nanosecond pulses (b). The solid lines are obtained by using equations (2).

effect of imidazolyl on nonlinear refraction is too small to cause an observable change of nonlinear refraction Z-scan curves as shown in Figure 4. In the case of picosecond pulses, the contribution of the singlet excited state to nonlinear refraction is dominant, and using eq 3 to numerically fit the data of Figure 4a then yields $\sigma_{r1} = -2.2 \times 10^{-17} \text{ cm}^2$ for **1a** and $\sigma_{r1} = -2.1 \times 10^{-17} \text{ cm}^2$ for **2a**. No obvious nonlinear refraction was observed in the solution of self-assembled zinc porphyrins **3** and **4**, and this implies that the nonlinear refraction arising from the singlet excited state is very small. To our knowledge, it is the first time that the disappearance of nonlinear refraction was observed through the metallization at 532 nm.

To determine the nonlinear refractive cross-section of the triplet excited state σ_{r2} , we performed closed-aperture Z-scans using a nanosecond pulsed laser and fitted the experimental data, as shown in Figure 4b. This yielded a σ_{r2} of $-1.8 \times 10^{-17} \text{ cm}^2$ for free base porphyrins (**1a** and **2a**) and $-1.1 \times 10^{-17} \text{ cm}^2$ for self-assembled zinc porphyrins (**3** and **4**). The metallization of the zinc atom also caused a decrease of nonlinear refraction like its effect on RSA. However, it can be seen from Table 1 that the decrease of σ_{r2} due to the metallization is smaller than that of σ_{r1} , indicating that the effect of metallization on the singlet excited state is larger than that on the triplet excited state. In the case of nanosecond pulses, the thermal effect should be generally taken into account for the measurements of nonlinear refraction. The thermal effect arises from acoustic wave propagation caused by medium density change after local heating, and its buildup time is determined by the time required for a sound wave to propagate across beam size, $\tau_{ac} = \omega_0/c_s$, where c_s is the velocity of sound in the medium. In our experimental condition, the value of τ_{ac} (≈ 20 ns) is much larger than the duration of pulses $\tau_p = 5$ ns. Therefore, the thermal effect can be neglected when the nanosecond pulsed laser is used.^{33,34}

For self-assembled zinc porphyrins such as **4**, Yoshiaki Kobuke et al.^{19,20,27} have employed the femtosecond time-

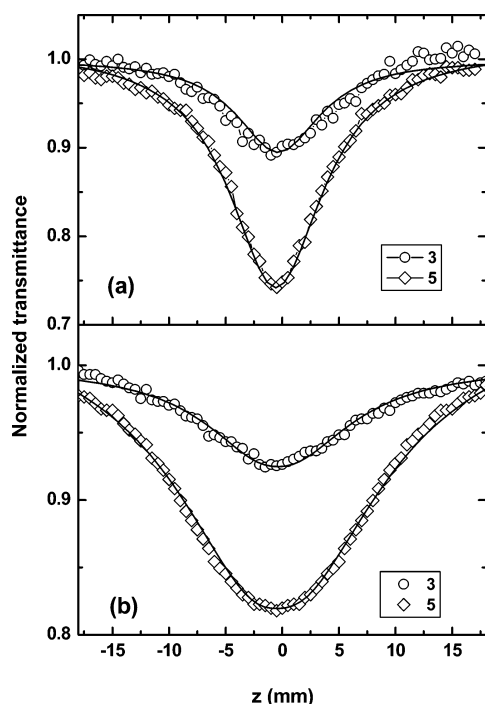


Figure 5. Open-aperture Z-scan curves of **3** and **5** in the cases of picosecond pulses (a) and nanosecond pulses (b).

resolved optical Kerr effect and Z-scan methods to measure the third-order optical nonlinearities in the off-resonance condition. The optical nonlinearities from electronic polarization in the off-resonance condition, which involves the distortion of the electron cloud about an atom or molecule by the optical field, was obtained and the susceptibility $|\chi_{yyyy}^{(3)}|$ is 2.4×10^{-14} esu at 800 nm with a concentration of 1.5×10^{-4} M.

Effect of Ligand on Optical Nonlinearities. In our experiments, the coordination solvent pyridine was added in the CHCl_3 solutions of self-assembled zinc porphyrin. Since the coordination bond can be cleaved by adding a coordinating solvent, the dimers **3** and **4** were dissociated to monomers **5** and **6** with the addition of pyridine, which leads to a transition of Soret bands from the split band into a single peak, as shown in Figure 1b. Besides the induced change of linear absorption, the addition of coordination solvent can also result in a change of RSA for self-assembled zinc porphyrins. Figure 6 gives the open-aperture Z-scan curves of **3** and **5** in the cases of picosecond pulses (part a) and nanosecond pulses (part b), respectively. The results are summarized in Table 1. The values of excited-state absorption cross-sections are raised to 6.1×10^{-17} from 3.0×10^{-17} cm^2 for σ_1 and to 3.4×10^{-17} from 1.9×10^{-17} cm^2 for σ_2 , respectively, when pyridine was added in porphyrins **3**. For zinc porphyrins **4** with two imidazolyls, an enhancement of both singlet and triplet excited-state absorption cross-sections can also be found in Table 1 when pyridine was present. Meanwhile, it can be seen from Table 1 that the change of the ground-state absorption cross-section σ_0 is small when pyridine is added. The fixity of σ_0 and the enhancement of σ_1 and σ_2 can cause the improvement of figure of merit (σ_1/σ_0 and σ_2/σ_0) that is an important parameter in the application of optical limiting.

The enhancement of RSA may arise from the significantly different symmetries between the monomers (**5** and **6**) and the assemblies (**3** and **4**). The different symmetries will cause different electronic distributions. For assemblies (**3** and **4**), the Soret band corresponding to higher singlet excited-state S_2 is nondegenerate depending on the head-to-tail and face-to-face

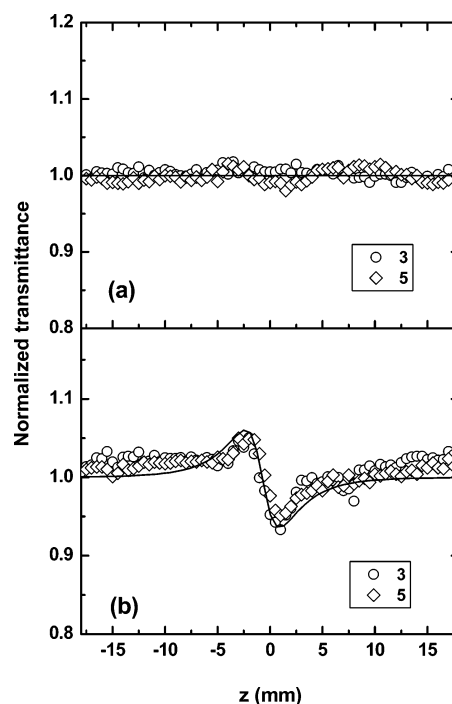


Figure 6. Nonlinear refraction Z-scan curves of **3** and **5** in the cases of picosecond pulses (a) and nanosecond pulses (b).

orientations of transition dipoles.³⁰ In the monomers (**5** and **6**), however, the Soret band is degenerate due to symmetry. The different electronic distributions may result in different properties of RSA between the monomers (**5** and **6**) and the assemblies (**3** and **4**). Furthermore, the cooperative assembly of the dimers results in a robust system that likely remains together as the heat is dissipated from the supramolecular compounds. Conversely, the axial coordination of pyridine by zinc porphyrins is quite weak so the pyridine probably transiently comes off the metalloporphyrins.³⁵

The Z-scan experiments of **1a** and **2a** with the addition of pyridine have also been performed, and no obvious change was observed because there is no coordination interaction between free base porphyrins and pyridine.

The nonlinear refraction Z-scan curves of **3** and **5** are shown in Figure 6. Opposite to RSA, the addition of pyridine cannot result in an observable change of nonlinear refraction for both one imidazolyl and two imidazolyls porphyrins, and the values of σ_{r1} and σ_{r2} of **5** and **6** are shown in Table 1. This illustrates that the complementary coordination of ligands to zinc has no contribution to nonlinear refraction, but it does have a large influence on RSA in the cases of both picosecond and nanosecond pulses. For picosecond pulses, although singlet and triplet excited-state absorption cross-sections are enhanced when pyridine is added, the nonlinear refraction was still absent. Therefore, the disappearance of nonlinear refraction should be mainly caused by the metallization of zinc.

The Z-scan experiments were also carried out for simple zinc and free base tetraphenylporphyrins (ZnTPP and TPP) in CHCl_3 . The change of nonlinear refraction is similar to that of self-assembled porphyrins, indicating that the metallization of zinc can mainly affect nonlinear refraction. However, no obvious change of RSA was obtained by adding pyridine into ZnTPP in the case of picosecond pulses.³⁶ In the case of nanosecond pulses, the addition of pyridine in ZnTPP resulted in a small decreasing of RSA,³⁶ which is different from enhancement of

RSA in the self-assembled porphyrin system. The data of TPP (7), ZnTPP (8), and ZnTPP–pyridine (9) are given in Table 1.

It is very interesting that the coordination of pyridine to zinc porphyrins can only affect their properties of RSA, and their nonlinear refraction cannot be obviously altered. Oppositely, the demetallization of the zinc atom at the center of porphyrin rings can mainly result in a decrease of nonlinear refraction. To realize the control of optical nonlinearities and find materials with large optical nonlinearities, more efforts have been undertaken to establish the relationship between structure and nonlinear optical response for organic molecules in order that materials in particular applications can be rationally designed and synthesized.^{3,11} The ligands substitution in the supramolecular porphyrin system provides a convenient approach to alter optical nonlinearities of porphyrins. It can be realized much more easily and flexibly than modifying molecular structure of traditional covalent bond organic materials.^{19,20} Furthermore, through the combination of the addition of pyridine and the metallization of the zinc atom, nonlinear refraction and RSA can be adjusted solely.

Conclusions

In summary, this work points out that metallization and coordination of solvent to zinc have large effects on nonlinear refraction and RSA for imidazolylporphyrins. In the picosecond regime, a drastic decrease of nonlinear refraction was observed in self-assembled zinc porphyrins. The change of nonlinear refraction is mainly attributed to the metallization. An enhancement of RSA was obtained by adding pyridine to self-assembled zinc porphyrins in the cases of both picosecond and nanosecond pulses. In this supramolecular system, the molecular length and the structure of the central π -conjugation system are easily modified. The flexible control of linear and nonlinear optical properties can be realized by using different noncovalent bonds. Efforts are being undertaken to further enhance and characterize optical nonlinearities of supramolecular porphyrins.

Acknowledgment. The authors acknowledge the support of the Preparatory Project of the National Key Fundamental Research Program (Grant 2004CCA04400), the Natural Science Foundation of China (Grants 10574075, 20172028, and 20421202), and the Program for Changjiang Scholars and Innovative Research Team in University.

References and Notes

- (1) Prasad, P. N.; Williams, D. J. *Introduction to Nonlinear Optical Effects in Molecules and Polymers*; Wiley: New York, 1991.
- (2) Nalwa, H. R.; Miyata, S. *Nonlinear Optics of Organic Molecules and Polymers*; CRC Press: Boca Raton, FL, 1997.
- (3) Torre, G. D. L.; Vazquez, P.; Agullo-Lopez, F.; Torres, T. *Chem. Rev.* **2004**, *104*, 3723.
- (4) Calvete, M.; Yang, G. Y.; Hanack, M. *Synth. Met.* **2004**, *141*, 231.
- (5) Blau, W.; Byrne, H.; Dennis, W. M.; Kelly, J. M. *Opt. Commun.* **1985**, *56*, 25.
- (6) Henari, F. Z.; Blau, W. J.; Milgram, L. R.; Yahioglu, G.; Phillips, D.; Lacey, J. A. *Chem. Phys. Lett.* **1997**, *267*, 229.
- (7) Rao, S. V.; Naga Srinivas, N. K. M.; Rao, D. N.; Giribabu, L.; Maiya, B. G.; Philips, R.; Kumar, G. R. *Opt. Commun.* **2000**, *182*, 255.
- (8) Ono, N.; Ito, S.; Wu, C. H.; Chen, C. H.; Wen, T. C. *Chem. Phys.* **2000**, *262*, 467.
- (9) McEwan, K. J.; Bourhill, G.; Robertson, J. M.; Anderson, H. L. *J. Nonlinear Opt. Phys. Mater.* **2000**, *9*, 451.
- (10) Kiran, P. P.; Reddy, D. R.; Maiya, B. G.; Dharmadhikari, A. K.; Kumar, G. R.; Desai, N. R. *Appl. Opt.* **2002**, *41*, 7631.
- (11) McEwan, K.; Lewis, K.; Yang, G. Y.; Chng, L. L.; Lee, Y. W.; Lau, W. P.; Lai, K. S. *Adv. Funct. Mater.* **2003**, *13*, 863.
- (12) McEwan, K.; Fleitz, P.; Rogers, J.; Slagle, J.; McLean, D.; Akdas, H.; Katterle, M.; Blake, I.; Anderson, H. *Adv. Mater.* **2004**, *16*, 1933.
- (13) McKerns, M. M.; Sun, W.; Lawson, C. M. *J. Opt. Soc. Am. B* **2005**, *22*, 852.
- (14) Jiang, L.; Lu, F.; Li, H.; Chang, Q.; Li, Y.; Liu, H.; Wang, S.; Song, Y.; Cui, G.; Wang, N.; He, X.; Zhu, D. *J. Phys. Chem. B* **2005**, *109*, 6311.
- (15) Neto, N. M. B.; Boni, L. D.; Mendonca, C. R.; Misoguti, L.; Queiroz, S. L.; Dinelli, L. R.; Batista, A. A.; Zilio, S. C. *J. Phys. Chem. B* **2005**, *109*, 17340.
- (16) Kandasamy, K.; Shetty, S. J.; Puntambekar, P. N.; Srivastava, T. S.; Kundu, T.; Singh, B. P. *J. Porphyrins Phthalocyanines* **1999**, *3*, 81.
- (17) Kuebler, S. M.; Denning, R. G.; Anderson, H. L. *J. Am. Chem. Soc.* **2000**, *122*, 339.
- (18) Screen, T. E.; Thorne, J. R. G.; Denning, R. G.; Bucknall, D. G.; Anderson, H. L. *J. Am. Chem. Soc.* **2002**, *124*, 9712.
- (19) Ogawa, K.; Zhang, T.; Yoshihara, K.; Kobuke, Y. *J. Am. Chem. Soc.* **2002**, *124*, 22.
- (20) Ogawa, K.; Ohashi, A.; Kobuke, Y.; Kamada, K.; Ohta, K. *J. Am. Chem. Soc.* **2003**, *125*, 13356.
- (21) Ikeda, C.; Yoon, Z. S.; Park, M.; Inoue, H.; Kim, D.; Osuka, A. *J. Am. Chem. Soc.* **2005**, *127*, 534.
- (22) Drobizhev, M.; Stepanenko, Y.; Dzenis, Y.; Karotki, A.; Rebane, A.; Taylor, P. N.; Anderson, H. L. *J. Phys. Chem. B* **2005**, *109*, 7223.
- (23) Kim, D. Y.; Ahn, T. K.; Kwon, J. H.; Kim, D.; Ikeue, T.; Aratani, N.; Osuka, A.; Shigeiwa, M.; Maeda, S. *J. Phys. Chem. A* **2005**, *109*, 2996.
- (24) Collini, E.; Ferrante, C.; Bozio, R. *J. Phys. Chem. B* **2005**, *109*, 2.
- (25) Ahn, T. K.; Kwon, J. H.; Kim, D. Y.; Cho, D. W.; Jeong, D. H.; Kim, S. K.; Suzuki, M.; Shimizu, S.; Osuka, A.; Kim, D. *J. Am. Chem. Soc.* **2005**, *127*, 12861.
- (26) Rath, H.; Sankar, J.; Prabhuraja, V.; Chandrashekar, T. K.; Nag, A.; Goswami, D. *J. Am. Chem. Soc.* **2005**, *127*, 11608.
- (27) Ogawa, K.; Ohashi, A.; Kobuke, Y.; Kamada, K.; Ohta, K. *J. Phys. Chem. B* **2005**, *109*, 22003.
- (28) Satake, A.; Kobuke, Y. *Tetrahedron* **2005**, *61*, 13.
- (29) Sheik-Bahae, M.; Said, A. A.; Wei, T. H.; Hagan, D. J.; Van Stryland, E. W. *IEEE J. Quantum Electron.* **1990**, *26*, 760.
- (30) Kobuke, Y.; Miyaji, H. *J. Am. Chem. Soc.* **1994**, *116*, 4111.
- (31) Wei, T. H.; Huang, T. H.; Wu, T. T.; Tsai, P. C.; Lin, M. S. *Chem. Phys. Lett.* **2000**, *318*, 53.
- (32) Wei, T. H.; Hagan, D. J.; Sence, M. J.; Van Stryland, E. W.; Perry, J. W.; Coulter, D. R. *Appl. Phys. B* **1992**, *54*, 46.
- (33) Kovsh, D. I.; Hagan, D. J.; Van Stryland, E. W. *Opt. Express* **1999**, *4*, 315.
- (34) Liu, Z. B.; Zhou, W. Y.; Tian, J. G.; Chen, S. Q.; Zang, W. P.; Song, F.; Zhang, C. P. *Opt. Commun.* **2005**, *245*, 377.
- (35) Retsek, J. L.; Drain, C. M.; Kirmaier, C.; Nurco, D. J.; Medforth, C. J.; Smith, K. M.; Sazanovich, I. V.; Chirvony, V. S.; Fajer, J.; Holten, D. *J. Am. Chem. Soc.* **2003**, *125*, 9787.
- (36) Kimball, B. R.; Nakashima, M.; DeCristofano, B. S.; Srinivas, N. K. M. N.; Premkiran, P.; Rao, D. N.; Panchangam, A.; Rao, D. V. G. L. N. *Proc. SPIE* **2000**, *4106*, 264.

Effect of Small-Angle Scattering on the Integer Quantum Hall Plateau *

SHU Qiang(舒强)¹, LIN Yao-Wang(林耀望)^{1,2}, XING Xiao-Dong(邢晓东)¹, YAO Jiang-Hong(姚江宏)¹,
PI Biao(皮彪)¹, SHU Yong-Chun(舒永春)^{1**}, WANG Zhan-Guo(王占国)^{1,2}, XU Jing-Jun(许京军)¹

¹The Key Laboratory of Advanced Technique and Fabrication for Weak-Light Nonlinear Photonics Materials (Ministry of Education), Nankai University, Tianjin 300457

²Key Laboratory of Semiconductor Materials Science, Institute of Semiconductors, Chinese Academy of Sciences, Beijing 100083

(Received 30 September 2005)

A GaAs/AlGaAs two-dimensional electron gas (2DEG) structure with the high mobility of $\mu_{2K} = 1.78 \times 10^6 \text{ cm}^2/\text{Vs}$ has been studied by low-temperature Hall and Shubnikov de Hass (SdH) measurements. Quantum lifetimes related to all-angle scattering events reduced from 0.64 ps to 0.52 ps after illuminating by Dingle plots, and transport lifetimes related to large-angle scattering events increasing from 42.3 ps to 67.8 ps. These results show that small-angle scattering events become stronger. It is clear that small-angle scattering events can cause the variation of the widths of the quantum Hall plateaus.

PACS: 71.20.Nr, 72.2.Jv

The integer quantum Hall effect (IQHE) has been studied extensively, experimentally as well as theoretically, over the last two decades.^[1-3] It is now well established that it is a result of the unique energy structure of two-dimensional electron gas (2DEG) in the presence of magnetic field B and the ubiquitous presence of localized states, which cannot transport electrical current across the sample.^[4] After the discovery of the IQHE, a linear decrease of the plateau widths with increasing current^[5] and with increasing temperature^[6] has been measured. Recently, the dependence of widths of the integer quantum Hall plateaus on quantum lifetimes has been reported by Gottwaldt *et al.*^[7] They demonstrated that the widths of the spin-split quantum plateaus can be determined by quantum lifetimes of the electrons, whereas transport lifetimes are not directly related to the widths of the integer quantum Hall plateaus. Quantum lifetimes increases with carrier concentrations after illuminating also has been reported by Lo *et al.*^[8] However, effects of main factor on quantum Hall plateaus have not been reported.

In this Letter, we report that quantum lifetimes decrease and transport lifetimes increase with the increasing electron density and mobility after illuminating due to the persistent photoconductivity (PPC) effect. The transport lifetime τ_t is dependent on large angle scattering events, and the quantum lifetime τ_q is dependent on all angle scattering events. These indicate that the small-angle scattering would increase to dominate the variation of integer quantum Hall plateaus.

The sample was prepared by an RIBER Compact

21 T molecular beam epitaxy (MBE) machine using solid sources on a semi-insulating GaAs substrate.^[9] It consists of a 1.2- μm -thick undoped GaAs buffer layer, an undoped 220- \AA -thick $\text{Al}_x\text{Ga}_{1-x}\text{As}$ ($x = 0.28$) spacer layer, a 550- \AA -thick $\text{Al}_x\text{Ga}_{1-x}\text{As}$ ($x = 0.28$) layer with Si-doped of $1 \times 10^{18} \text{ cm}^{-3}$, and a cap layer with 75- \AA -thick Si-doped GaAs. In the measurement, Ohmic contacts were formed by alloying AuGe and Ni at 450°C. The sketch of the cross section of the layer structures is shown in Fig. 1.

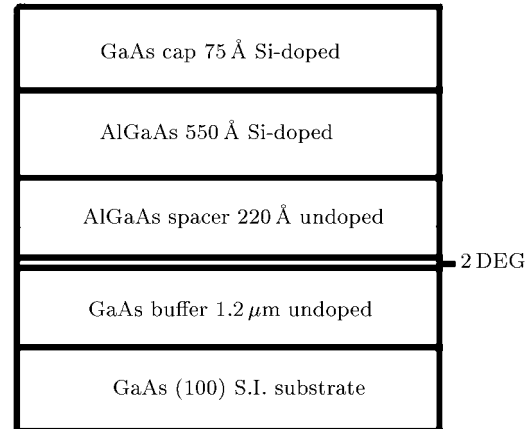


Fig. 1. Cross section of the layer structures of the sample.

Quantum lifetimes can be measured by the amplitudes of the Shubnikov de Hass (SdH) oscillations.^[10,11] In 2DEG systems and in the case of a GaAs/AlGaAs structure, the SdH oscillation amplitudes read^[12]

* Supported by the National Natural Science Foundation of China under Grant No 60476042, Programme for Changjiang Scholars and Innovative Research Team in University, TEDA School, Nankai University.

** Email: shuyc@nankai.edu.cn

©2005 Chinese Physical Society and IOP Publishing Ltd

$$\Delta R_{xx}(B) = 4R_0 K(B, T) \exp\left(-\frac{\pi}{\omega_c \tau_q}\right), \quad (1)$$

where R_0 is the zero-field resistance, $\omega_c = eB/m^*$ is the angular cyclotron frequency, m^* is the electron cyclotron effective mass, τ_q is the quantum lifetime (according to the collision broadening of Landau levels), and $K(B, T)$ is the thermal damping factor (according to the thermal broadening of the levels) given by

$$K(B, T) = \frac{2\pi^2 K_B T / \hbar \omega_c}{\sinh(2\pi^2 K_B T / \hbar \omega_c)}. \quad (2)$$

Here \hbar is Planck's constant, K_B is Boltzmann's constant, and τ_q can be extracted experimentally from Dingle plots exhibiting $\ln Z$ versus the inverse magnetic field, where Z is given by

$$Z = \left(\frac{\Delta R}{R}\right) \frac{1}{4K(B, T)} = \exp\left(-\frac{\pi}{\omega_c \tau_q}\right). \quad (3)$$

The SdH measurements of the sample are taken for a magnetic field up to 2 T (Tesla) and a temperature at 2 K. The electron mobility and electron density are extracted from the Hall measurements at 2 K. In our experiment, a standard commercial light-emitting diode (LED) was used as a light source for the persistent photoconductivity effect (PPC) to change electron densities. The SdH oscillation spectrum of the GaAs/AlGaAs heterostructure sample at 2 K is shown in Fig. 2. The variation of the sample resistance R_{xx} with magnetic field B exhibits the typical 2DEG behaviour.

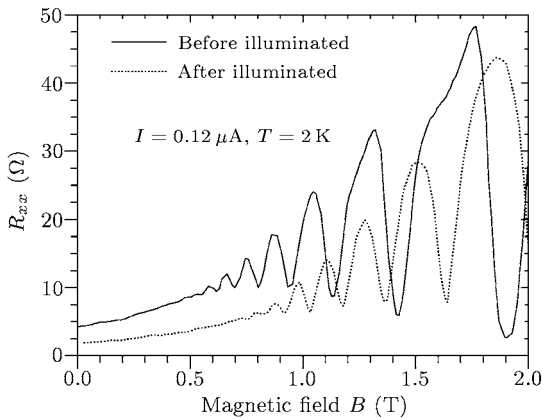


Fig. 2. A typical SdH oscillation spectrum of the sample at 2 K.

Dingle plots for the sample are presented in Fig. 3. Quantum lifetimes τ_q are calculated by linear fits using Eq. (1).

Transport lifetimes τ_t were obtained by

$$\tau_t = m^* \sigma / n e^2, \quad (4)$$

where n is the density of carriers, e is the electron charge, and m^* is electron effective mass. The results of our experiment and theoretical calculation are listed in Table 1.

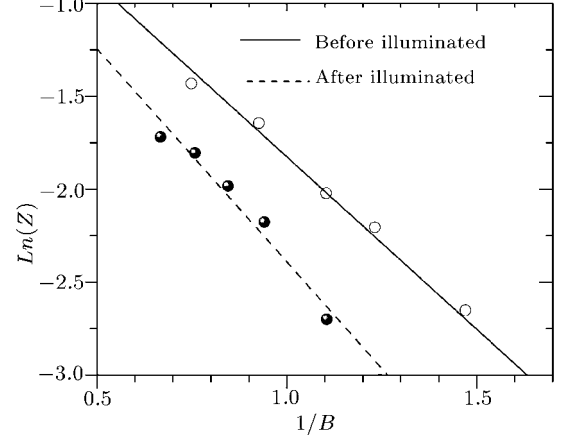


Fig. 3. Dingle plots for the sample by using Eq. (3).

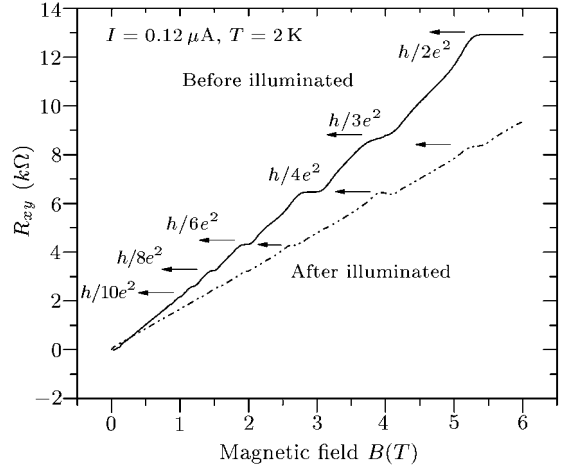


Fig. 4. The QHE curves for the sample at 2 K.

As can be found from Table 1, the transport lifetime increases from 42.3 ps to 67.8 ps, and the quantum lifetime decreases from 0.64 ps to 0.52 ps after the sample is illuminated. The ratio between the transport and the quantum lifetime varies from 66.1 to 130.4. The transport lifetime τ_t is dependent on large angle scattering events whereas the quantum lifetime τ_q is dependent on all angle scattering events.^[13,14] The transport lifetimes τ_t increases with the increasing electron density and mobility, which means that large angle scattering events are reduced due to the free-carrier increasing to screen the ionized impurity potential.^[15] Whereas quantum lifetimes decrease after illuminating, which implies that all-angle scattering increases. It is obvious that small-angle scattering enhances after illuminating.

Table 1. Low-temperature measure results of the sample.

	Density n (10^{11} cm^{-2})	Mobility μ (10^4 $\text{cm}^2/\text{V}\cdot\text{s}$)	Transport lifetime τ_t (ps)	Quantum lifetime τ_q (ps)	τ_t/τ_q	Plateau width at $i = 6$ (T)
Before illuminated	2.88	111	42.3	0.64	66.1	0.0577
After illuminated	3.76	178	67.8	0.52	130.4	0.0352

During the magnetic field up to 6 T, Hall measures were performed both in dark and after illuminating at 2 K. As shown in Fig. 4, the widths of the quantum Hall plateaus can be determined by

$$\rho_{xy} = h(ie^2) \pm 0.1 \text{ k}\Omega, \quad (5)$$

where h is Planck's constant and i is an integer plateau number. The results are shown in Fig. 4. As can be seen in Fig. 4, there is no evidence for the fractional quantum Hall effect, and the widths of the plateaus narrowed after illuminating. For example, at $i = 6$ plateau, the width of the plateau is 0.0577 T before illuminating, whereas the width becomes 0.0352 T after illuminating (Table 1). It is believed that the variety is caused by the increasing small-angle scattering events.

In conclusion, the SdH oscillations have been observed in a GaAs/AlGaAs 2DEG structures at 2 K, and quantum lifetimes have been determined by Dingle plots. The widths of the integer quantum Hall plateaus have been obtained. The width is 0.0577 T before illuminating and 0.0352 T after illuminating at the $i = 6$ plateau. It is found from the Dingle plots that Quantum lifetimes related to all-angle scattering events reduce from 0.64 ps to 0.52 ps, and transport lifetimes related to large-angle scattering events increase from 42.3 ps to 67.8 ps. It is clear that small-angle scattering can cause the variation of the widths of the quantum Hall plateaus.

The authors would like to thank Professor Lü Li for low-temperature Hall and Shubnikov de Hass measurement.

References

- [1] Von K K, Dorda G, and Pepper M 1980 *Phys. Rev. Lett.* **45** 494
- [2] Tsui D C and Gossard A C 1981 *Appl. Phys. Lett.* **38** 550
- [3] Zheng H Z, Choi K K, Tsui D C and Weimann G 1985 *Phys. Rev. Lett.* **55** 1144
- [4] Huckestein B 1995 *Rev. Mod. Phys.* **67** 357
- [5] Pudalov V M and Semenchinskii S G 1984 *JETP Lett.* **39** 576
- [6] Pudalov V M and Semenchinskii S G 1984 *Solid State Commun.* **51** 19
- [7] Gottwaldt L, Kpierz, Ahlers F J et al 2003 *J. Phys.: Condens. Matter* **15** 5073
- [8] Ikai L, Mitchel W C, Ahoujja M, Cheng J P, Fathimulla A and Mier H 1994 *Appl. Phys. Lett.* **66** 754
- [9] Shu Q, Shu Y C, Wang Z G et al 2006 *Acta Phys. Sin.* **55** 368 (in Chinese)
- [10] Isihara A and Smrôka L 1986 *J. Phys.: Condens. Matter* **19** 6777
- [11] Zhang C P, Yang F H, Zheng H Z et al 2004 *Chin. Phys. Lett.* **21** 915
- [12] Coleridge P T, Stoner R and Fletcher R 1989 *Phys. Rev. B* **33** 1120
- [13] Harrang J P, Higgins R J, Goodall R K et al 1985 *Phys. Rev. B* **32** 8126
- [14] Das Sarma S and Stern F 1985 *Phys. Rev. B* **32** 8442
- [15] Hirakawa K, Sakaki H and Yoshino J 1986 *Surf. Sci.* **170** 440

Eu^{3+} 离子在微晶玻璃研究中的探针作用*

余 华¹⁾²⁾ 孙 健¹⁾ 刘宝荣¹⁾ 宋 杰¹⁾ 赵丽娟^{1)2)†} 许京军¹⁾²⁾

1) (南开大学物理科学学院光子学中心, 天津 300071)

2) (弱光非线性光子学材料先进技术及制备教育部重点实验室, 天津市信息光子材料与
技术重点实验室, 南开大学泰达应用物理学院, 天津 300457)

(2006 年 1 月 4 日收到; 2006 年 4 月 14 日收到修改稿)

制备出单掺 Eu^{3+} 离子的氟氧化物玻璃陶瓷系列样品, 利用 Eu^{3+} 离子作为荧光探针, 通过热处理前后 Eu^{3+} 离子发射光谱中电偶极子跃迁与磁偶极子跃迁强度比值的变化表征在玻璃材料中微晶是否形成, 分析了 Eu^{3+} 离子荧光发射谱中电偶极子跃迁与晶体场对称性的关系, 进一步表征了稀土离子所处微晶晶格场的变化。

关键词: 微晶玻璃, 探针, Eu^{3+} 离子

PACC: 8140, 3200, 6170T

1. 引 言

在玻璃制造业中, 玻璃结晶会影响玻璃材料的透明度, 这是玻璃技术人员一直试图克服的问题. 1957 年美国 Corning 公司的 Stookey 发现, 在玻璃制备过程中, 如果将其结晶尺寸限制在德布罗意波长范围内, 晶体颗粒对光的散射损失可忽略, 其产品的透明度不变, 并且这种玻璃比常规玻璃具有更好的机械性能和热稳定性, 称之为玻璃陶瓷^[1-6]. 上世纪 70 年代, Auzel 等人^[7]利用特殊工艺在常规的氧化物玻璃中嵌入稀土离子掺杂的氟化物, 以提高稀土离子的上转换荧光效率, 但受当时工艺条件的限制, 氧化物中的氟化物微晶颗粒尺寸较大, 影响玻璃的透明度, 使这种上转换激光材料的研究搁浅. 1992 年, Tanabe 研究小组^[8]在氟化物玻璃中掺入少量的氧和磷, 试图提高氟化物玻璃的化学稳定性和机械强度, 同时保持稀土离子的上转换荧光效率, 但实验结果表明, 少量的氧和磷会产生声子边带, 使稀土离子相邻能级之间的多声子弛豫概率大大增加, 导致上转换荧光效率的大幅度降低. 1993 年 Sumita 公司的 Wang 和 Ohwaki^[9]将 Auzel 的制备方法加以改进, 报道了在 $30\text{SiO}_2 \cdot 15\text{Al}_2\text{O}_3 \cdot 24\text{PbF}_2 \cdot 20\text{CdF}_2 \cdot 10\text{YbF}_3 \cdot \text{ErF}_3$ 透明玻璃陶瓷中通过热处理形成氟化物纳米微晶

$\text{Pb}, \text{Cd}, \text{F}_2, \text{Er}, \text{Yb}$ 溶于其中, 利用高温热处理工艺使氧化物中的氟化物微晶尺寸缩小至纳米量级, 解决了玻璃失透的问题. 与氧化物玻璃相比, 热处理后稀土离子的上转换荧光强度提高近两个数量级, 这一结果为实现紧凑型固体上转换激光器开辟了新途径. 稀土离子掺杂的氟氧化物玻璃陶瓷材料是将掺有稀土离子的氟化物微晶包埋于氧化物基质材料中, 使其既具有氟化物的低声子能量, 又具有氧化物的高机械强度、高稳定性和易于加工的特点; 氟化物微晶中的稀土离子间距离被限制在纳米范围内, 具有独特的上转换和下转换辐射通道, 从而在上转换发光、三维显示等方面有很好的应用前景^[10, 11].

氟氧化物玻璃陶瓷在上转换效率上较传统的氧化物玻璃材料提高了近两个数量级, 主要原因在于通过热处理在氧化物基质中生成了纳米数量级的氟化物微晶, 提高了溶解在氟化物微晶中的稀土离子的上转换发光效率, 所以微晶能否有效的形成是该类材料在后续研究和应用的前提条件. 除了使用 X 射线和荧光光谱的方法证明氟化物微晶存在于玻璃陶瓷中之外, Kawamoto^[10]等人还利用 Eu^{3+} 离子作为“探针”研究了在 $50\text{SiO}_2 \cdot 50\text{PbF}_2 \cdot x\text{ErF}_3$ 玻璃陶瓷中稀土离子发光与微晶的关系, 结合热处理前后发射光谱的变化, 得出稀土离子有效的溶解在热处理后形成的氟化物微晶中. 本文采用了用 Eu^{3+} 离子代替

* 国家自然科学基金(批准号: 10574074), 教育部科技创新工程重大项目培育基金(批准号: 704012), 基金委重点项目(批准号: 10334010), 国际合作重点项目(批准号: 2005DFA10170), 长江学者和创新团队发展计划资助的课题.

† 通讯联系人. E-mail: zhaolj@nankai.edu.cn

上转换发光中心 Er^{3+} 离子作探针的方法来证明稀土离子存在于嵌入玻璃陶瓷中的氟化物微晶中,以及表征稀土离子周围晶体场的变化,值得一提的是 Eu^{3+} 离子发射光谱的变化除了可以表征微晶的形成,还可以定性地表征晶体场变化的趋势。

2. 实 验

准确称取一定比例的 SiO_2 , Al_2O_3 , PbF_2 , CdF_2 , Eu_2O_3 试剂,除 CdF_2 (>95%) 以外,各原材料纯度均在 99.99% 以上. 在玛瑙研钵中充分混合研磨,然后装入白金坩埚. 在 1000 °C 下灼烧 120min, 高温下将熔融的玻璃液迅速倾倒在铁盘上进行急冷,得到透明的氟氧化物玻璃材料,然后在材料的核化温度下进行热处理,热处理的时间为 8h. 材料的组成分别为 $30\text{SiO}_2 \cdot 15\text{Al}_2\text{O}_3 \cdot x\text{PbF}_2 \cdot (50-x)\text{CdF}_2 \cdot 5\text{Eu}_2\text{O}_3$ ($x = 50, 40, 28, 10, 0$ 编号分别为 C, D, E, F, G), A 样品与 E 样品的组成完全一致,但是未经过热处理. 将所有样品双面抛光处理后进行测量,样品尺寸为 $10.0\text{mm} \times 10.0\text{mm} \times 2.5\text{mm}$. 荧光光谱的测试使用 SPEX Fluorolog-2 型分光光度计. X 射线衍射谱的测量使用的是 D/Max-2500 型 X 射线衍射仪, Cu 靶,扫描速度为 $4^\circ/\text{min}$.

3. 实验结果与分析

2.1. Eu^{3+} 离子的发光性质

Eu^{3+} 离子的电子组态为 $4f^6 5s^2 5p^6$, 外层有 6 个

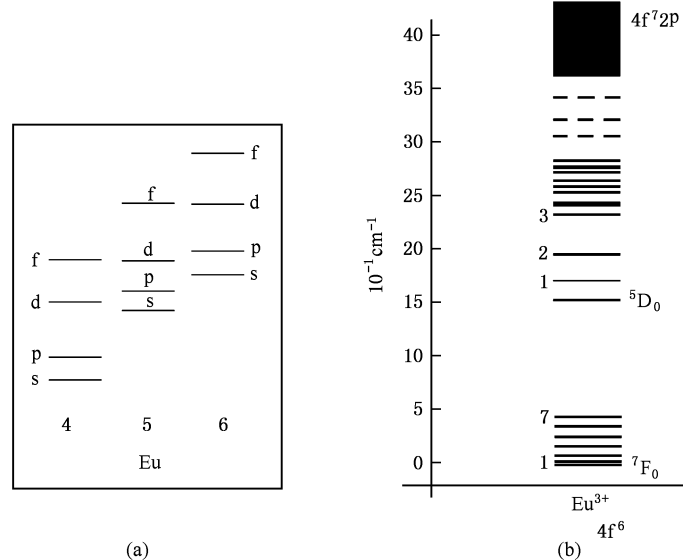


图 1 Eu^{3+} 离子能级图

4f 电子,处于基态的电子要求所有自旋平行. 对于高一点的能级,结构比较复杂,其中 5D_0 是最低的激发态,通常都是从这里开始向下跃迁,产生发光. Eu^{3+} 离子的能级结构如图 1(b) 所示.

各个能级之间遵循跃迁的选择定则. 对于多电子的重原子来讲,跃迁只能发生在宇称性不同的能态之间. Eu^{3+} 离子光谱项是由 4f 电子形成的, l 相同,即宇称性一样,因此 $4f \rightarrow 4f$ 能级间的电偶极子的跃迁是禁戒的. 对于磁偶极子,宇称选择定则正好相反,4f 各能级之间的跃迁是磁偶极子跃迁引起的,但是这种跃迁能量很弱. 然而,当 Eu^{3+} 离子偏离晶格对称中心和受周围场的扰动,以及相反宇称组态与 f^6 组态的混合,宇称选择定则会被部分解除,电偶极子跃迁成为可能. 其中 Eu^{3+} 离子的 $^5D_0 \rightarrow ^3F_2$ 跃迁是一些对环境变化比较敏感的跃迁,称为“超灵敏跃迁”,这种跃迁选择规则遵循 $|\Delta J| = 2, |\Delta L| \leq 2, \Delta S = 0$, 一般认为这是由于强度参数中的 τ_2 对离子周围环境的灵敏性引起的^[12],因此基于这种离子光谱的特殊性,人们将 Eu^{3+} 离子作为荧光探针引入.

3.2. Eu^{3+} 离子在氟氧化物玻璃中的探针效应

Eu^{3+} 离子发光对其晶体场环境极其敏感. Eu^{3+} 离子的发射谱中主要有两个发射峰,通过对 Eu^{3+} 离子的能级结构的计算可知 590nm 左右的两个峰为 $^5D_0 \rightarrow ^3F_1$ 的磁偶极子的跃迁. 614nm 左右的若干峰对应 $^5D_0 \rightarrow ^3F_2$ 的电偶极子跃迁. 电偶极跃迁与晶场的对称性密切相关,而晶场的对称性对磁偶极跃迁

影响不大,所以电偶极跃迁与磁偶极跃迁的比率可以用来表征稀土离子周围晶场的变化^[10].另一方面,在镧系元素中,其系列元素半径大小基本上相似,用相同摩尔百分率的 Eu^{3+} 离子来替换原来的上转换发光离子 Er^{3+} ,对氟化物的微晶结构影响不大,然后通过 Eu^{3+} 离子发光的变化来判断稀土离子周围环境的变化,从而模拟上转换发光 Er^{3+} 离子的晶场环境的变化,由此可以判断氟化物微晶的结构.

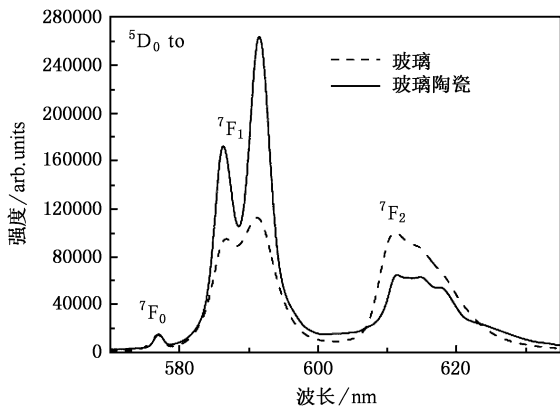


图2 393nm激发下玻璃和玻璃陶瓷样品中 Eu^{3+} 离子的发射光谱

对于掺 Eu^{3+} 离子的系列样品,393nm激发时我们得到了图2的结果,从图中可以得出, Eu^{3+} 离子的发射曲线在玻璃中较在玻璃陶瓷中发生较大的强度变化,这定性地说明了 Eu^{3+} 离子周围的晶格场环境发生了一定程度的变化.正如上面所提到的,从 Eu^{3+} 离子的电偶极子跃迁与磁偶极子跃迁强度的比值可以判断 Eu^{3+} 离子所处的晶格场环境,由于奇对称场的哈密顿函数为零,所以 Eu^{3+} 离子的电偶极子跃迁与磁偶极子跃迁强度的比值越接近于零,就说明所处的晶格场的对称性越高,在玻璃和玻璃陶瓷中, Eu^{3+} 离子的电偶极子跃迁与磁偶极子跃迁强度的比值分别为 1.07 : 1 和 0.48 : 1,这明显地说明了 Eu^{3+} 离子周围的晶格场环境在玻璃陶瓷中较在玻璃中具有更高的对称性.在玻璃中,稀土离子处于氧化物的玻璃网状结构中,周围的环境很不对称.当样品进行热处理之后,玻璃基体中均匀的形成了一定数量的 $\text{Pb}_x\text{Cd}_{1-x}\text{F}_2$ 微晶, $\text{Pb}_x\text{Cd}_{1-x}\text{F}_2$ 的结构为面心立方^[13,14],稀土离子处于这样的晶格场环境中与处于玻璃的网状结构环境中具有更高的结构对称性.电偶极子跃迁的禁戒解除与对称性有着密切的关系,对称性越差电偶极子跃迁禁戒解除得越彻底,其跃迁强度相应也越强,故此在对称性较差的玻璃结构

中,电偶极子跃迁强度与磁偶极子跃迁强度基本上相等(1.07 : 1);当热处理之后,电偶极子跃迁强度显著变弱,与磁偶极子跃迁强度的比值变为 0.48 : 1,这说明 Eu^{3+} 离子周围的晶体场环境对称性提高,电偶极子跃迁禁戒的解除变得不彻底,所以表现出跃迁强度变弱.这也说明在我们的玻璃样品中形成了掺有稀土离子的微晶.

通过 XRD 的测试,同样也证实了玻璃样品经过热处理之后形成了微晶,如图3所示.从图中可以看出,热处理之后,样品的 XRD 谱峰由原来的波包形状(A)变成了有尖锐衍射峰的形状,这表明样品中出现了晶化的现象,图中尖锐的衍射峰形对应面心立方的 $\text{Pb}_x\text{Cd}_{1-x}\text{F}_2$ 结构,并随着 CdF_2 含量的逐渐增大衍射峰位并没有发生较大改变,这表明在氟氧化物玻璃陶瓷中所形成的微晶结构仍然保持 $\text{Pb}_x\text{Cd}_{1-x}\text{F}_2$ 结构, $\text{Pb}_x\text{Cd}_{1-x}\text{F}_2$ 结构类似于 $\beta\text{-PbF}_2$ 的面心立方结构, Cd^{2+} 离子取代了 Pb^{2+} 的格位,并随着 Cd^{2+} 离子的含量增加而逐渐发生畸变, $\text{Pb}_x\text{Cd}_{1-x}\text{F}_2$ 的模型结构图参阅文献[14].通过 XRD 谱图可以看出,随着 CdF_2 含量的逐渐增大玻璃波包背低逐渐增大,并且衍射峰位发生略微的移动.这在结构上说明所形成的面心立方的 $\text{Pb}_x\text{Cd}_{1-x}\text{F}_2$ 结构开始发生畸变,发生畸变的大小可以通过以下公式予以计算:

$$\sin^2 \theta = \frac{\lambda^2}{4a^2} (h^2 + k^2 + l^2), \quad (1)$$

其中, a 是晶格常数, h, k, l 是晶面指数. C, D, E 样品中的晶格常数分别为 0.587nm, 0.583nm 和 0.541nm.

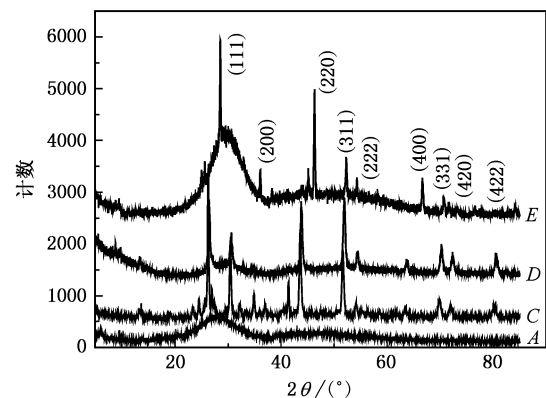


图3 玻璃(A)和玻璃陶瓷(微晶组成为 $30\text{SiO}_2 \cdot 15\text{Al}_2\text{O}_3 \cdot x\text{PbF}_2 \cdot (50-x)\text{CdF}_2 \cdot 5\text{Eu}_2\text{O}_3$) (C) $x=50$, (D) $x=40$, (E) $x=28$) 的 X 射线衍射谱

用 Eu^{3+} 离子的探针效应同样也可以表征纳米

微晶尺寸的变化而引起稀土离子周围晶体场的变化. 如图 4 所示. 通过不同的 Pb 和 Cd 的比, 峰的相对强度也有了明显的变化. 值得注意的是随着 Cd 离子的增加, 在玻璃陶瓷中非常敏感的 ${}^5\text{D}_0 \rightarrow {}^7\text{F}_2$ 的电偶极跃迁较 ${}^5\text{D}_0 \rightarrow {}^7\text{F}_1$ 的磁偶极跃迁能量明显增加. 电偶极跃迁与磁偶极跃迁的比率是衡量玻璃结构是否是中心对称的重要指标. 与前面所提到的在玻璃和玻璃陶瓷中 ${}^5\text{D}_0 \rightarrow {}^7\text{F}_2$ 的电偶极跃迁与 ${}^5\text{D}_0 \rightarrow {}^7\text{F}_1$ 的磁偶极跃迁比例的变化可以推断, 此时晶场的对称性减弱. 从结果可以看出, 当氟化物微晶中不含 CdF_2 时电偶极跃迁与磁偶极跃迁的比率大约是 1:2, ${}^5\text{D}_0 \rightarrow {}^7\text{F}_1$ 的磁偶极跃迁占主导地位. Eu^{3+} 离子处于对称中心. 随着 Cd 离子的增加, ${}^5\text{D}_0 \rightarrow {}^7\text{F}_1$ 的磁偶极跃迁较 ${}^5\text{D}_0 \rightarrow {}^7\text{F}_2$ 的电偶极跃迁所占比重明显减小. 也说明此时 Eu^{3+} 离子处于的晶场环境对称性降低. 同时电偶极跃迁的波峰开始出现多个小峰, 表现出了精细结构. 说明微晶结构的变化, 引起了 Eu^{3+} 离子能级的劈裂. 直到在氟化物中完全不含 PbF_2 时比率减小到大约是 0.4:1. 也就是说, 在样品 C 中, 晶场对于 Eu^{3+} 离子的对称度是很高的, 随着氟化物中 CdF_2 含量的增大, 微晶晶场的对称性逐渐减小, 样品 E 中, 稀土离子周围的对称性最差; CdF_2 的核化温度高达 485 $^\circ\text{C}$, 而 PbF_2 的核化温度仅有 310 $^\circ\text{C}$ ^[15], 所以当 CdF_2 的含量进一步增大时, 由于 CdF_2 自身具有较高的核化温度, 这时玻璃材料中微晶的形成随着 CdF_2 含量的增大变得越来越困难, 稀土离子周围的晶体场状况也趋于无序化, 对称性降低, 在光谱的表征上表现为电偶极跃迁的禁戒解除得越来越彻底, 跃迁强度逐渐增大, 如图 4 所示; 在结构上, 由于拥有较高核化温度 CdF_2 的含量逐渐增大(从样品 C 到样品 E), 那么形成微晶的趋势是减小的, 越来越多的稀土 Eu^{3+} 离子所处的晶场环境变为对称性变差的微晶晶场和无定形的玻璃晶场, 在图 3 中表现为衍射峰的半宽度的变宽和衍射杂散峰以及背景玻璃基质衍射包络的出现. 这些表征稀土 Eu^{3+} 离子周围晶场对称性逐渐变差的结构信息在光谱上则是表现在 Eu^{3+} 离子的发射光谱中(图 4) 电偶极跃迁与磁偶极跃迁的比率的逐渐增大.

以上结论说明, Eu^{3+} 离子完全可以作为稀土离子探针用来研究晶场的变化, 随着样品中 $\text{PbF}_2/\text{CdF}_2$ 比值的减小, Eu^{3+} 离子中电偶极跃迁与磁偶极跃迁

的比率的逐渐增大, 说明随着 $\text{PbF}_2/\text{CdF}_2$ 比值的减小, 晶场的对称性逐渐降低. 在我们所提出的模型中, 氟化物微晶结构的基本框架是由 $\text{Pb}_x\text{Cd}_{1-x}\text{F}_2$ 结构构成的, 所以当样品中的氟化物仅仅包含 PbF_2 时, Eu^{3+} 离子的电偶极跃迁与磁偶极跃迁的比率较小, 说明此时晶场的对称性还是比较高的(相对于所有系列玻璃陶瓷样品来说), 随着 $\text{PbF}_2/\text{CdF}_2$ 比值的减小, Cd 离子在氟化物微晶中所占的比例增加以及自身较高核化温度的影响, 微晶的变形逐渐增大, 形成越发困难, 晶场对称性逐渐降低.

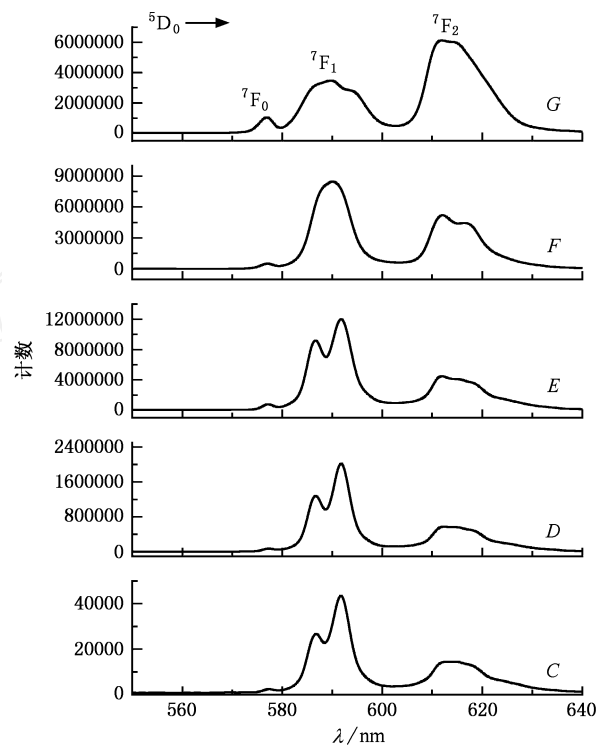


图 4 Eu^{3+} 离子在组成为 $30\text{SiO}_2 \cdot 15\text{Al}_2\text{O}_3 \cdot x\text{PbF}_2 \cdot (50-x)\text{CdF}_2 \cdot 5\text{Eu}_2\text{O}_3$ ($x=50, 40, 28, 10, 0$ 编号分别为 C, D, E, F, G) 中的发射光谱

4. 结 论

Eu^{3+} 离子中电偶极子的跃迁发射强度对于晶体场对称性的变化较为敏感, 当周围晶体场的对称性越低, 电偶极子的跃迁禁戒解除的程度越大, 相应跃迁发射强度越大. 通过分析玻璃材料在热处理前后 Eu^{3+} 离子中电偶极子与磁偶极子跃迁发射强度比值与体场对称性的关系, 得出: 氟氧化物玻璃在热处理之后有效的形成了微晶, 且稀土离子溶解在其中; 通过改变微晶化学剂量比, Eu^{3+} 离子中电偶极子与磁偶极子跃迁发射强度比值的变化分析了微晶的晶体

场对称性的变化. 所以, Eu^{3+} 离子完全可以作为离子探针应用于微晶玻璃中微晶是否形成的探测, 模拟

其他稀土离子的掺入研究晶体场环境的变化以及对称性的变化.

- [1] Grubb S, Bennett K W, Cannon R S *et al* 1992 *Opt. & Photon News* **3** 42
- [2] Johnson L F, Guggenheim H 1971 *Appl. Phys. Lett.* **19** 44
- [3] Silversmith A J, Lenth W, Macfarlane R M *et al* 1987 *Appl. Phys. Lett.* **51** 1977
- [4] Antipenko B M, Dumbravyanu R V, Perlin Yu E *et al* 1985 *Opt. Spectrosc. (USSR)* **59** 377
- [5] McFarlane R A 1994 *J. Opt. Soc. Am. B* **11** 871
- [6] Jackson S D, King T A 1998 *Opt. Lett.* **23** 1462
- [7] Auzel F, Pecile D, Morin D 1975 *J. Electrochem. Soc.* **122** 101
- [8] Tanabe S, Yoshii S, Hirao K, Soga N 1992 *Phys. Rev. B* **45** 4620
- [9] Wang Y H, Ohwaki J C 1993 *Appl. Phys. Lett.* **63** 3268
- [10] Kawamoto Y, Kanno R, Qiu J 1998 *J. Mater. Sci.* **33** 63
- [11] Meng J, Zhao L J, Yu H *et al* 2005 *Acta Phys. Sin.* **54** 1442 (in Chinese) [孟 婕、赵丽娟、余 华等 2005 物理学报 **54** 1442]
- [12] Meng Q G, Zhang H J 1999 *J. Inorg. Mater.* **14** 630 (in Chinese) [孟庆国、张洪杰 1999 无机材料学报 **14** 630]
- [13] Kukkonen L L, Reaney I M, Furniss D *et al* 2001 *J. Non-Crystal. Solids* **290** 25
- [14] Yu H, Zhao L J, Meng J *et al* 2005 *Chin. Phys.* **14** 1799
- [15] Dejneka M J 1998 *MRS. Bulletin* 57-62

Eu^{3+} luminescence in neoceramic glass as ion microprobe *

Yu Hua¹⁾²⁾ Sun Jian¹⁾ Liu Bao-Rong¹⁾ Song Jie¹⁾
Zhao Li-Juan^{1)2)†} Xu Jing-Jun¹⁾²⁾

1) (Photonics Center , College of Physical Science , Nankai University , Tianjin 300071 , China)

2) (Tianjin Key Lab of Photonics Material and Technology for Information Science and The Key Lab of Advanced Technique and Fabrication For Weak-Light Nonlinear Photonics Materials , Ministry of Education , TEDA Applied Physics School , Nankai University , Tianjin 300457 , China)

(Received 4 January 2006 ; revised manuscript received 14 April 2006)

Abstract

In oxyfluoride glass-ceramics , the fluoride nanocrystals doped with rare earth ions were dispersed in an oxide network. The emission of Eu^{3+} has high sensitivity to different crystal field and is suitable for microstructure research in neoceramic glass. Different oxyfluoride glass ceramics doped with Eu^{3+} were prepared. The variation of the emission spectra of Eu^{3+} in different glass ceramics confirms the applicability of Eu^{3+} ions in neoceramic glass as microprobe before and after heat treatment.

Key words: neoceramic glass , probe , Eu^{3+}

PACC: 8140 , 3200 , 6170T

* Project supported by the National Natural Scientific foundation of China (Grant No. 10574074) , the Changjiang Scholars and Innovative Research Team in University and the Cultivation Fund of the Key Scientific and Technical Innovation Project from the Ministry of Education of China (Grant Nos. 704012 , NSFC(10334010)) and the Key International S&T Cooperation Project (Grant No. 2005DFA10170) .

† Corresponding author. E-mail : zhaolj @nankai . edu . cn

调制掺杂 GaAs/AlGaAs 2DEG 材料持久光电导 及子带电子特性研究*

舒 强¹⁾ 舒永春^{1)†} 张冠杰¹⁾ 刘如彬¹⁾ 姚江宏¹⁾ 皮 彪¹⁾
邢晓东¹⁾ 林耀望¹⁾²⁾ 许京军¹⁾ 王占国¹⁾²⁾

1) (南开大学泰达应用物理学院, 南开大学弱光非线性光子学材料及其先进制备技术教育部重点实验室, 天津 300457)

2) (中国科学院半导体研究所半导体材料科学重点实验室, 北京 100083)

(2005 年 7 月 12 日收到; 2005 年 8 月 3 日收到修改稿)

在掺 Si 的 GaAs/AlGaAs 二维电子气(2DEG)结构中, 得到 $\mu_{2K} = 1.78 \times 10^6 \text{ cm}^2 / (\text{V} \cdot \text{s})$ 的高迁移率. 在低温(2K)和高磁场(6T)的条件下, 对样品进行红光辐照, 观察到持久光电导(PPC)效应, 电子浓度在光照后显著增加. 通过整数量子霍尔效应(IQHE)和 Shubnikov-de Haas (SdH) 振荡的测量, 研究了 2DEG 的子带电子特性. 样品在低温光照后 2DEG 中第一子带和第二子带的电子浓度同时随电子总浓度的增加而增加; 而且电子迁移率也明显提高. 同时, 通过整数霍尔平台的宽度对光照前后电子的量子寿命变短现象作了理论分析.

关键词: 二维电子气, 量子霍尔效应, SdH 振荡, 持久光电导效应

PACC: 7230D, 7220J, 7340H

1. 引 言

在过去的 20 年里, 人们已经对掺 Si 的 GaAs/AlGaAs 高电子迁移率二维电子气(2DEG)结构的持久光电导效应进行了大量的实验及理论研究^[1,2]. 发现在一些 III-V 族化合物半导体中, 当样品在低温(2K)下被光照(红外或者可见光)后, 其电子浓度会明显增加. 这主要是由于 DX 中心的存在. DX 中心是一个复杂的深能级缺陷, 涉及到施主(Donor)和某个未知的缺陷(X). 在低温时 DX 中心的能级在费米能级之下, 被电子占据. 光辐照后吸收能量被激发而进入量子阱的导带内, 光辐照停止后, 电子在低温中没有足够的能量越过势垒, 所以量子阱中的导带内电子增加. 这种现象被称为持久光电导(PPC)效应. 1968 年, Craford 在研究 GaAs_{1-x}P_x 时观察到这个现象^[3]. 随后人们相续又在 AlGaAs(Te)^[4], ZnCdTe(CI)^[5] 和 AlN(Si)^[6] 结构中得到了 PPC 效应. 1977 年, Nelson 在 n 型 Al_xGa_{1-x}As 结构中观察到了 PPC 效应^[7]. 随后人们对于这个现象进行了大量的实验

和理论研究^[8]. 由于和 PPC 效应相关的 DX 中心是一个深能级缺陷, 它的存在对于器件的性能有很大的影响, 所以人们对于 PPC 的研究有很大的兴趣.

在调制掺杂 GaAs/AlGaAs 异质结构中, 垂直于界面电子的运动被限制在紧靠界面的极窄的势阱中, 而在平行于界面的方向上可做自由运动, 形成 2DEG. 横向磁阻的 Shubnikov-de Haas(SdH) 振荡曲线和量子霍尔效应曲线是研究半导体中电子迁移性质的很好工具. Fang 和 Howard 在研究掺 Si 金属氧化物半导体场效应晶体管(MOSFET)时发现, 在低温下, 由于电子对阳离子杂质的屏蔽作用, 电子浓度的增加导致 2DEG 的迁移率增加^[9]. 在 AlGaAs/GaAs 结构中的 2DEG 更容易研究, 因为在掺 Si 的 MOSFET 结构中的一些例如谷间散射和表面粗糙度散射等散射机理在这些结构中可以被忽略. Stomer 等人发现当电子浓度超过一定数值时, 霍尔迁移率由于子带间散射的开始而减小了^[10]. 他们认为迁移率的下降是由于第二子带比第一子带有更低的迁移率, Mori 和 Ando 通过理论计算给予了证明^[11]. 在进一步的研究中, 人们得到第二子带的散射时间比第一子带的散射时间更短^[12]. 但 Smith 和 Fang 认为一般第一

*国家自然科学基金(批准号:60476042), 长江学者和创新团队发展计划和南开大学泰达学院资助的课题.

† E-mail: shuyc@nankai.edu.cn

子带的电子一般更靠近界面,因而更靠近 AlGaAs 层的电离杂质,它们将有比第二子带更强的散射,所以,第二子带中电子的弛豫时间比第一子带的更长,迁移率比第一子带的更大^[13].

2. 样品结构

实验中使用的样品是通过分子束外延(MBE)的方法生长的调制掺杂(Si)的 GaAs/Al_xGa_{1-x}As (x = 0.28) 结构. 其结构为半绝缘的 GaAs 衬底(S. I. Substrate); 1.2μm 的 GaAs 缓冲层; 220Å 的不掺杂的 Al_xGa_{1-x}As (x = 0.28) 隔离层; 上面是 550Å 的 Al_xGa_{1-x}As 的 Si 掺杂层、最上面是 75Å 的 Si-GaAs 盖层. 结构图如图 1 所示. AlGaAs 的禁带宽度大于

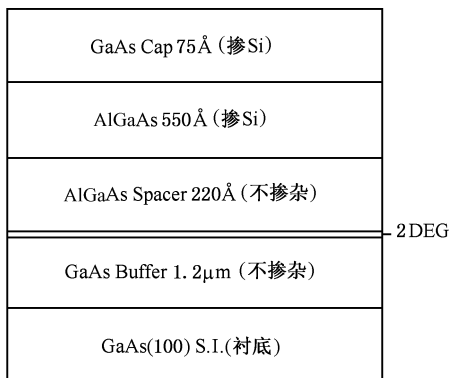


图 1 样品结构示意图

GaAs ($E_g | Al_{0.22}Ga_{0.78}As = 1.70eV$, $E_g | GaAs = 1.24eV$), 这种带隙的差异导致了在异质界面带边断续,重掺杂的 AlGaAs 层中的电子将转移到非掺杂的 GaAs 一侧,而电离施主仍留在 AlGaAs 一侧. 界面附近能带发生弯曲, AlGaAs 一侧形成势垒, GaAs 一侧

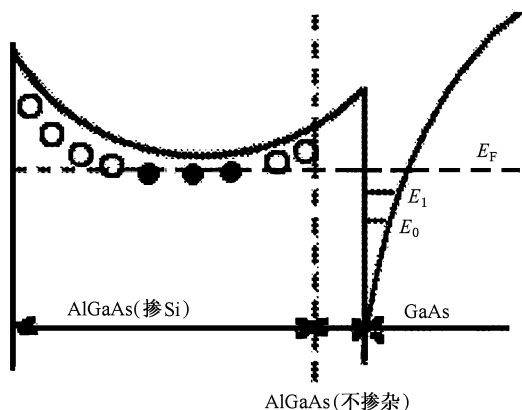


图 2 样品导带示意图

形成准三角势阱. 其中不掺杂的 AlGaAs 层减弱了势阱中电子与电离施主之间的库仑作用(杂质散射), 使电子的迁移率增加. 光照后得到 $\mu_{2K} = 1.78 \times 10^6 cm^2/(V \cdot s)$ 的高迁移率. 其导带示意图如图 2 所示.

3. 实验结果与讨论

在强磁场(6T)和低温(2K)的条件下,我们测量了样品在光照前后的量子霍尔平台和 SdH 振荡曲线,研究了 2DEG 中电子迁移特性. 实验中使用的辐照光是红光. 辐射前后,均得到了很好的整数量子霍尔平台. 在实验中没有发现和分数霍尔效应相关的平台. 光照前后的结果如图 3 所示.

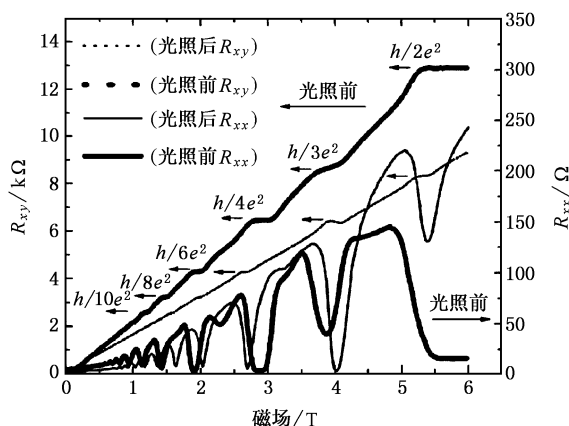


图 3 光照前后霍尔效应及 SdH 振荡曲线

当 $\hbar\omega_c > k_B T$, 即低温高磁场的条件下, 样品横向磁阻由振动项和非振动项组成 $\rho = \rho_{oscillatory} + \rho_{nonoscillatory}$, 其中振荡项 $\rho_{oscillatory}$ 对于 2DEG 的研究起重要作用. 这时 2DEG 受到量子阱的限制以及磁场作用, 处于由量子阱限制造成的量子化能级和由磁场作用而形成的分立朗道能级中. 当朗道能级越过费米能级时, 横向磁阻会产生振荡现象. 对于一个特定的由量子阱限制造成的量子化子能级 (E_i), 磁阻的振荡 ($\delta\rho_{xx}$) 能被表达成^[14]

$$\delta\rho_{xx} = 2\bar{\sigma}_{xx} \frac{(\omega_i \tau_i)^2}{1 + (\omega_i \tau_i)^2} \exp\left[-\frac{\pi}{\omega_i \tau_i}\right] \frac{\xi_i}{\sinh(\xi_i)} \times \cos\left[2\pi \frac{E_F - E_i}{\hbar\omega_i} + \phi_i\right], \quad (1)$$

下标 i 指的是第 i 个子带, 这是由量子阱限制造成的量子化子能级. $\omega_i = eB/m_i^*$ 是角回旋频率; m_i^* 是电子回旋有效质量; τ_i 是电子弛豫时间; $\bar{\sigma}_{xx}$ 是平均

磁导率; ϕ_i 是第 i 个子带的相; $\xi_i = 2\pi^2 k_B T / \hbar\omega_i$. k_B 是玻耳兹曼常数; $\hbar = h/2\pi$ (h 是普朗克常数).

费米能级和第 i 子带最小值的差为

$$\Delta E_i = E_F - E_i = \frac{\pi \hbar n_i}{m_i} \quad (2)$$

n_i 是由量子阱限制造成的第 i 个量子化子能级的电子浓度. 把(2) 式代入(1) 式可得到

$$\begin{aligned} \delta\rho_{xx} = & 2\bar{\sigma}_{xx_i} \frac{(\omega_i \tau_i)^2}{1 + (\omega_i \tau_i)^2} \exp\left[-\frac{\pi}{\omega_i \tau_i} \frac{\xi_i}{\sinh(\xi_i)}\right] \\ & \times \cos\left[2\pi \frac{\hbar n_i}{2e} \frac{1}{B} + \phi_i\right]. \end{aligned} \quad (3)$$

因而 SdH 曲线随 $1/B$ 振荡的频率仅同 2DEG 的电子浓度 n_i 有关系,

$$f_{\text{SdH}} = \frac{\hbar n_i}{2e}. \quad (4)$$

在磁场从 0.3T 到 5.2T 的范围内, 从对应的 $1/B$ 的区间里取 1024 个点, 对 SdH 振荡曲线做了以相等的 $1/B$ 为间距的快速傅里叶变换 (FFT). 经快速傅里叶变换后的图中有两个峰值振幅, 这说明 2DEG 中有两个子带被占据^[15]. 由(4) 式知其对应的两个频率是由这两个子带的电子浓度决定的. 结果如图 4(光照前) 和图 5(光照后) 所示.

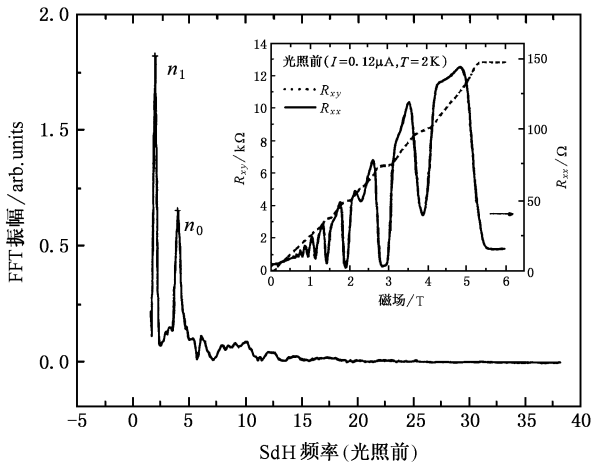


图 4 光照前的 SdH 数据的傅里叶变换图(小图为光照前的 SdH 及霍尔效应图)

在实验测量中, 得到光照前 2DEG 的总电子浓度 (n_T) 为 $2.28 \times 10^{11} \text{ cm}^{-2}$, 而光照后为 $3.76 \times 10^{11} \text{ cm}^{-2}$, 增加为将近原来的 1.65 倍. 根据方程(4) 和傅里叶变换的结果可得到, 光照后第二子带的电子浓度 (n_1) 从 $0.94 \times 10^{11} \text{ cm}^{-2}$ 增加到了 $1.30 \times 10^{11} \text{ cm}^{-2}$; 而第一子带的电子浓度 (n_0) 从 $1.94 \times 10^{11} \text{ cm}^{-2}$ 增加到 $2.46 \times 10^{11} \text{ cm}^{-2}$. 如表 1 所示.

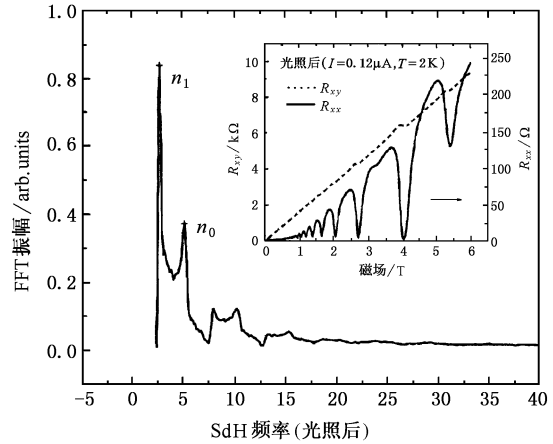


图 5 光辐照后的 SdH 数据的傅里叶变换图(小图为辐照前的 SdH 及霍尔效应图)

表 1 电子浓度

	n_0/cm^{-2}	n_1/cm^{-2}	n_T/cm^{-2}
光照前	1.94×10^{11}	0.94×10^{11}	2.28×10^{11}
光照后	2.46×10^{11}	1.30×10^{11}	3.76×10^{11}

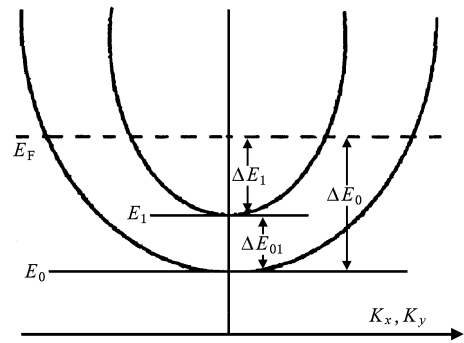


图 6 样品结构能级示意图

这说明当 2DEG 中总电子浓度增加时, 两个子带的电子浓度都增加^[15]. 说明电子在进行子能级填充时, 第一子带还没全部填满第二子带已经开始填充. 但光照使 DX 中心的深能级杂质被激发, 第一子带得以继续填充. 我们利用 $m^* = 0.067 m_0$ (m^* 为 GaAs 材料中的电子有效质量, $m_0 = 9.108 \times 10^{-31} \text{ kg}$ 为电子的惯性质量), 以及方程(2), 可粗略估计两个子带和费米能级的能量间隔. 费米能级和第一子带和第二子带的能级间隔分别为 $\Delta E_0 = 8.88 \text{ meV}$ 和 $\Delta E_1 = 4.69 \text{ meV}$. 两能级间隔 $\Delta E_{01} = 4.19 \text{ meV}$. 其能级关系如图 6 所示.

在经过 FFT 后的图中, 其峰值的高低代表着各自能带中电子量子寿命的长短. 从图 4 和图 5 中可

得到,第二子带的峰值(对应于 n_1)要比第一子带的峰值(对应于 n_0)高,所以第二子带中电子的量子寿命比第一子带中的长,受到的散射比第一子带小.样品经光照后,各自能带的峰值均较光照前有所减小,说明光照前后电子的量子寿命减小.在具有两个子带的系统中,影响电子量子寿命的主要是子带间散射的大小和电子对阳离子的屏蔽作用的强弱.由于两个子带的电子浓度的增加所引起电子子带间散射的影响超过了对阳离子屏蔽作用的影响^[16].

当载流子的量子寿命 τ_q 减小时,说明 2DEG 中载流子的散射增加.因此,朗道能级展宽了,电子自旋态的相对空间分布就减小.磁场中电子的自旋分裂是由于塞曼能 E_s 引起的,

$$E_s = s(\mu_B B + E_{ex}), \quad (5)$$

这里 s 是自旋量子数 ($\pm 1/2$), μ_B 是波尔磁子, E_{ex} 是交换能量.并且 E_{ex} 由其朗道能级中两个自旋态的布局的不同决定,

$$E_{ex} \propto n_N \uparrow - n_N \downarrow. \quad (6)$$

电子自旋态空间分布的减小导致 E_{ex} 的减小.所以电子自旋分裂朗道能级对应的磁场范围减小,即自旋分裂量子霍尔平台所对应的磁场范围减小.故霍尔平台的宽度也减小^[17].

从实验结果中可看到(如图 1),光照后,整数霍尔平台的宽度变窄.以填充因子 $i = 6$ 为例.光照前,其平台宽度(这里以平台处磁阻的变化同磁阻的比值小于 0.1% 为标准来计算其宽度)是 0.0577T;而

在光照后是 0.0352T.减小将近 64%.而光照前后,第一子带的峰值从 0.651 减小到 0.372,减小 75%;第二子带的峰值从 1.323 减小到 0.838,减小 58%.光照前后峰值变化的均值同平台宽度的变化值相当.说明光照前后电子量子寿命变短(FFT 图中的峰值变小)和整数霍尔平台宽度变窄相符.

4. 结 论

在低温(2K)下,对掺 Si 的 GaAs/AlGaAs 高电子迁移率 2DEG 结构进行光照,其具有明显的持久光电导 (PPC) 效应,电子浓度在光照后从 $2.28 \times 10^{11} \text{ cm}^{-2}$ 增加到 $3.76 \times 10^{11} \text{ cm}^{-2}$.测量样品的霍尔电阻和横向磁阻,得到了整数量子霍尔效应 (IQHE) 和 SdH 振荡曲线;对 SdH 振荡曲线进行快速傅里叶变换后,得到样品在低温光照后第一子带和第二子带的电子浓度同时增加;分别从 $1.94 \times 10^{11} \text{ cm}^{-2}$ 增加到 $2.46 \times 10^{11} \text{ cm}^{-2}$ 和从 $0.94 \times 10^{11} \text{ cm}^{-2}$ 增加到 $1.30 \times 10^{11} \text{ cm}^{-2}$.估算了费米能级和两个子带之间的能级间隔 $\Delta E_{01} = 4.19 \text{ meV}$.光照后两个子带中电子的量子寿命均有所减小,以光照前后 $i = 6$ 为例的整数霍尔平台宽度变化进一步解释了这个现象.

在该项研究工作中,得到中国科学院物理研究所吕力教授和国家纳米技术与工程研究院单诗诚高级工程师的大力支持,在此表示深深的谢意.

- [1] Chadi D J, Chang K J 1988 *Phys. Rev. Lett.* **61** 873
- [2] Xiao X F, Kang J Y 2001 *Acta Phys. Sin.* **51** 138 (in Chinese) [肖细凤,康俊勇 2001 物理学报 **51** 138]
- [3] Craford M G, Stillingman G E, Rossi J A, Holonyak N 1968 *Phys. Rev.* **168** 867
- [4] Lang D V, Logan R A, Jaros M 1979 *Phys. Rev. B* **19** 1015;
- [5] Burkley B C, Khosla R P, Fischer J R, Losee D L 1976 *J. Appl. Phys.* **47** 1095
- [6] Zeisel R, Bayerl M W, Gennenwein S T B *et al* 2000 *Phys. Rev. B* **61** 16283
- [7] Nelson R J 1977 *Appl. Phys. Lett.* **31** 351
- [8] Fletcher R, Zaremba E, D'lorio M, Foxon C T, Harris J J 1990 *Phys. Rev. B* **41** 10649
- [9] Fang F F, Howard W E 1966 *Phys. Rev. Lett.* **16** 797;
- [10] Stormer H L, Gossard A C, Weigmann W 1982 *Solid State Commun.* **41** 707
- [11] Mri S, Ando T 1980 *J. Phys. Soc. Jpn.* **48** 865
- [12] Lruyi S 1987 *Phys. Rev. Lett.* **58** 2263
- [13] Smith III T P, Fang F F 1988 *Phys. Rev. B* **37** 4303
- [14] Ikai Lo, Mitchel W C, Perrin R E, Messham R L, Yen M Y 1990 *Phys. Rev. B* **43** 11787
- [15] Ando T 1982 *J. Phys. Soc. Jpn.* **51** 3893
- [16] Ikai Lo, Mitchel W C, Aboujja M, Cheng J P, Fathimulla A, Mir H 1995 *Appl. Phys. Lett.* **66** 755
- [17] Gottwaldt L, Pierz K, Schweitzer L, Gobel E O 2003 *J. Phys.: Condens. Matter* **15** 5073

Study of persistent photoconductivity and subband electronic properties of the two-dimensional electron gas in modulation doped GaAs/AlGaAs structure *

Shu Qiang¹⁾ Shu Yong-Chun^{1)†} Zhang Guan-Jie¹⁾ Liu Ru-Bin¹⁾ Yao Jiang-Hong¹⁾
Pi Biao¹⁾ Xing Xiao-Dong¹⁾ Lin Yao-Wang¹⁾²⁾ Xu Jing-Jun¹⁾ Wang Zhan-Guo¹⁾²⁾

1) (Key Laboratory of Advanced Technique and Fabrication for Weak-Light Nonlinear Photonics Materials of Ministry of Education, and TEDA Applied Physics School, Nankai University, Tianjin 300457, China)

2) (Key Laboratory of Semiconductor Materials Science, Institute of Semiconductors, Chinese Academy of Sciences, Beijing 100083, China)

(Received 12 July 2005; revised manuscript received 3 August 2005)

Abstract

We obtained the high mobility of $\mu_{2K} = 1.78 \times 10^6 \text{ cm}^2/\text{V} \cdot \text{s}$ in Si-doped GaAs/AlGaAs two-dimensional electron gas (2DEG) structures. After the sample was illuminated by a light-emitting diode in magnetic fields up to 6 T at $T = 2 \text{ K}$, we did observe the persistent photoconductivity effect and the electron density increased obviously. The electronic properties of 2DEG have been studied by Quantum Hall-effect and Shubnikov-de Haas (SdH) oscillation measurements. We found that the electron concentrations of two subbands increase simultaneously with the increasing total electron concentration, and the electron mobility also increases obviously after being illuminated. At the same time, we also found that the electronic quantum lifetime becomes shorter, and a theoretical explanation is given through the widths of integral quantum Hall plateaus.

Keywords: two-dimensional electron gas, quantum Hall effect, SdH oscillations, persistent photoconductivity

PACC: 7230D, 7220J, 7340H

* Project supported by the National Natural Science Foundation of China (Grant No. 60476042), Program for Changjiang Scholars and Innovative Research Team in University and TEDA School Nankai University.

† E-mail: shuyc@nankai.edu.cn

不同淀积厚度 InAs 量子点的喇曼散射*

张冠杰¹ 徐波² 陈涌海² 姚江宏¹ 林耀望^{1,2} 舒永春^{1,†} 皮彪¹
邢晓东¹ 刘如彬¹ 舒强¹ 王占国^{1,2} 许京军¹

(1 南开大学弱光非线性光子学材料先进技术及制备教育部重点实验室, 天津 300457)
(2 中国科学院半导体研究所 半导体材料科学重点实验室, 北京 100083)

摘要: 利用喇曼散射方法在 77 K 温度下对不同淀积厚度的 InAs/GaAs 量子点材料进行了研究. 在高于 InAs 体材料 LO 模的频率范围内观察到了量子点的喇曼特征峰, 分析表明应变效应是影响 QD 声子频率的主要因素. 实验显示, 随着量子点层淀积厚度 L 的增加, InAs 量子点的声子频率由于应变释放发生红移. 在加入 InAlAs 应变缓冲层的样品中, 类 AlAs 声子峰随 L 增大发生了蓝移, 从侧面证实了 InAs 量子点层的应变释放过程.

关键词: 量子点; 喇曼散射; 应变效应; 限制效应

PACC: 6322; 6855; 7865P

中图分类号: TN244

文献标识码: A

文章编号: 0253-4177(2006)06-1012-04

1 引言

随着化学气相沉积 (CVD) 和分子束外延 (MBE) 技术的发展, 各种材料体系的外延生长日趋成熟^[1,2]. 其中, 以量子点 (QD) 材料作为有源区的光电材料以其潜在的优势而备受人们关注^[3]. 在量子点的各种生长方法中, 基于 S-K 模式的自组织生长是近年来研究的热点. S-K 生长模式利用衬底和外延层之间的晶格失配及其所引起的应变场驱使量子点自组织生长, 在生长过程中, 三维岛状结构的形成释放了应变产生的弹性能, 因此量子点材料具有结构完整、缺陷位错少的优点. 但是, 对器件性能起关键作用的点密度、尺寸和均匀性相对较难控制, 而这些均与生长过程中的材料应变密切相关.

喇曼散射方法是研究应变的有力工具之一, 并且已越来越多地应用于超晶格、量子点等材料的研究. 由于量子点波函数的扩展性, 弛豫过程涉及到来自量子点结构不同区域的多种声子效应, 因此喇曼散射方法所获得的量子点结构的声子谱, 对理解材料内部信息, 进而获得更高质量的量子点具有重要意义. InAs/GaAs 体系量子点材料由于在半导体激光器、红外探测器等方面有比较好的应用前景而得到了广泛的重视, InAs 岛状结构的声子谱研究也已见诸报道. Zanelatto 等人^[4]利用喇曼散射研究了生长于 GaAs 衬底上的自组织 InAs 量子点的布局情况; Galzerani 等人^[5]在不同条件下生长了 InAs 量

子点, 比较了掺杂和未掺杂、单层和多层、退火和未退火样品之间的喇曼谱特征; Pusep 等人^[6]通过共振喇曼实验观察到了生长于 GaAs 衬底上的金字塔形 InAs 量子点尖端的界面振动模, 由此分析了材料应变对喇曼谱的强烈影响; Ibanez 等人^[7]研究了多层堆垛 InAs/GaAs 量子点, 发现随隔离层厚度减小, 量子点喇曼峰由于弹性应变的释放而向低频方向移动; Artús 等人^[8]研究了淀积厚度为 1.4 ~ 1.9 ML 的 InAs 量子点样品的喇曼频移, 并将之归因于材料晶格失配引起的压应力.

本文对生长于 GaAs 上的 InAs 量子点材料进行了研究. 使用 MBE 设备生长了淀积厚度为 1.7 ~ 2.7 ML 的量子点材料, 并利用低温背散射对样品进行了喇曼散射实验. 通过 QD 声子频率的移动, 结合量子点形貌的观察结果进一步讨论了材料生长过程中量子点形状和应力的变化关系.

2 实验

实验所用样品均是在 RIBER Compact21T 型 MBE 设备上采用 S-K 生长模式制备的. 在 GaAs (001) 半绝缘衬底上, 580 °C 下首先生长 100 nm 的 GaAs 缓冲层, 之后降温至 480 °C 进行量子点有源区的生长. A, B, C, D 样品中, InAs 层的淀积厚度 L 分别为 1.7 ML, 1.9 ML, 2.1 ML 和 2.7 ML, 生长速率均为 0.1 ML/s. 为进行比较, 另一组结构类似但有 GaAs 盖层的样品中在 InAs 岛上面继续覆盖了

*国家自然科学基金(批准号:60476042)和天津市应用基础研究(批准号:06 YFJ ZJ C01100)资助项目

†通信作者. Email:shuyc@nankai.edu.cn

2005-09-25 收到, 2006-03-02 定稿

3ML 的 $\text{In}_{0.2}\text{Al}_{0.8}\text{As}$ 和 5nm 的 $\text{In}_{0.2}\text{Ga}_{0.8}\text{As}$, 以起到应力缓冲的作用.

在材料的生长过程中, 当 InAs 达到临界厚度附近(约 1.7ML), 反射高能电子衍射仪(RHEED)图形从线状变为燕尾状, 表明材料正从二维层状生长向三维岛状生长过渡. 利用 Renishaw RM2000 型微区喇曼光谱仪采用背散射几何配置在 77 K 下测量了样品的喇曼散射谱, 激发光源为 514.5nm 的 Ar^+ 离子激光器.

3 结果与讨论

表面形貌测试显示量子点的尺寸和密度随着淀积厚度的改变而发生变化. 图 1 所示为不同淀积厚度下量子点的平均直径和平均高度. 随着 InAs 厚度的增加, QD 的尺寸逐渐增大. 图 2 显示了量子点平均直径与平均高度的比值变化. 由图可见, 随着量子点的平均高度从 2.5nm 逐渐增大到 5nm 左右, QD 的尺寸纵横比则呈现下降趋势, 量子点形状逐渐改变.

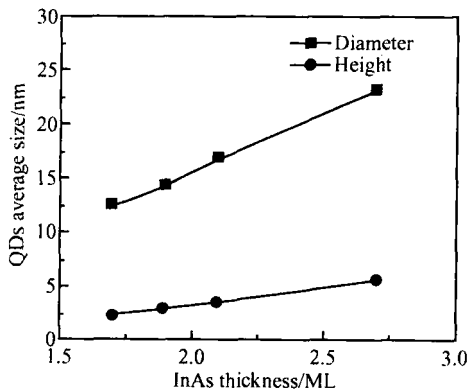


图 1 各样品中量子点的平均直径和平均高度
Fig.1 Average diameter and height of QDs

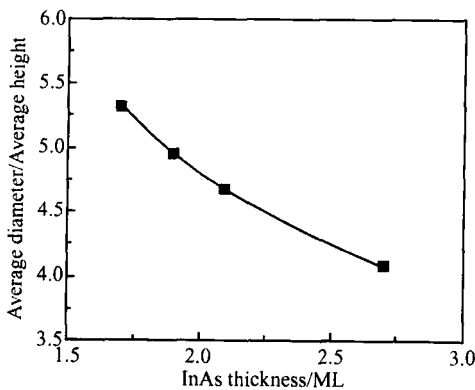


图 2 量子点尺寸纵横比随淀积厚度的变化
Fig.2 Diameter/height ratio of QDs with InAs thickness

77 K 下测量了样品的光致发光(PL)谱, 图 3 为样品 C 和样品 D 的 PL 谱比较, 其中 $\sim 1.1\text{eV}$ 和 $\sim 1.2\text{eV}$ 处的两个发光峰分别对应 InAs 量子点的基态和激发态跃迁^[9]. 从图中可见, 样品 D 基态发光峰强度明显增大, 且与样品 C 发光峰相比, 其半高宽变窄, 量子点材料的发光质量得到提高. 由于 InAs 淀积厚度增加导致量子点尺寸和应力分布的变化, 其基态和激发态的发光峰均出现了轻微的红移^[10].

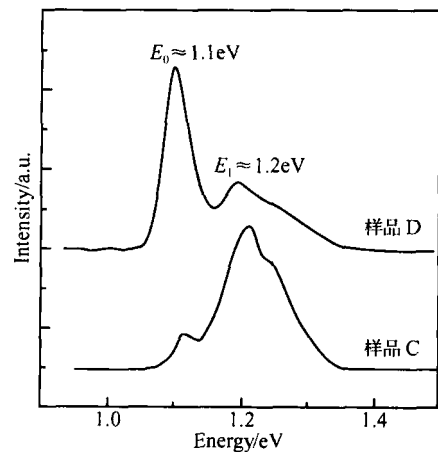


图 3 77K 下样品 C, D 的 PL 谱
Fig.3 PL spectra of samples C and D at 77 K

图 4 中将不同淀积厚度的四个样品的低温喇曼散射谱进行了比较. 各个样品中, 位于 293cm^{-1} 处的 GaAs LO 模均为强度最大的峰, 270cm^{-1} 处的较弱峰来源于本应禁戒的 GaAs TO 模^[11]在非完全背散射配置下的泄漏. 在低于 GaAs TO 模的频率范围内, 有另外一个喇曼特征峰, 虽然其强度相对微弱, 但在 InAs 淀积量超过临界厚度 ($\geq 1.7\text{ML}$) 的几个样品中都可以观察到, 并且其频率位置随样品 InAs 淀积厚度增加而发生移动, 证实了该峰既不是类 GaAs 界面模的信号, 也不是浸润层(WL)声子的贡献, 而是来源于样品中的量子点声子^[8,12].

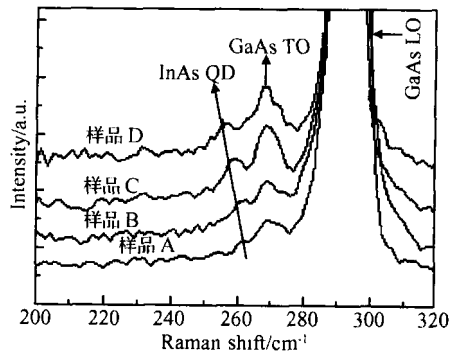


图 4 77 K 下四样品的喇曼散射谱对比
Fig.4 Raman spectra of the four samples at 77 K

与 InAs 体材料相比, QD LO 模频率发生了较大程度的蓝移. 一般而言, In 组分、应变效应和限制效应均可能使量子点的声子频率发生移动. Chu 等人^[12]认为, 生长温度较高时 ($\geq 530^\circ\text{C}$), 由于界面处 In 和 Ga 的互混, 导致 InGaAs 混晶形成, 使声子振动频率很大程度上决定于材料中的 In 含量. 而事实上, 由于 $\text{In}_x\text{Ga}_{1-x}\text{As}$ 声子谱所具有的双模行为, 且对于 x 较大的情况, 类 InAs 声子频率相对其体材料将向低频轻微移动^[13], 考虑到我们样品较低的生长温度, 基本可以排除 In, Ga 界面混晶对 QD 声子频率的影响.

下面考虑应变效应和限制效应对 InAs LO 的影响. 对 InAs/GaAs 体系, 压应变将导致喇曼峰频率相对于体材料蓝移, 限制效应将使喇曼峰红移. 特别是对于量子点层上方有覆盖层的情况, 量子点声子三维受限, 须考虑限制效应引起的频移, 即在计算中引入 $\Delta\omega_{\text{on}}$ 项. 而在无覆盖层样品中, 则限制效应可以忽略, 应变效应导致的频移可表示为^[14]:

$$\Delta\omega_{\text{tr}} = -326.9\varepsilon$$

其中 内建应变系数 ε 主要由晶格失配度决定, 对于 InAs/GaAs 体系, $\varepsilon \approx -6.9\%$. 利用这种方法, 得到压应变效应将使 InAs LO 模产生约 22cm^{-1} 的频移. 实验测得的结果 ($\omega(L=1.7\text{ML}) \approx 261.5\text{cm}^{-1}$) 也证实了除应变效应外, 其他因素对 QD 声子模频率的影响较小.

图 4 显示了随 InAs 层厚增加, 量子点喇曼峰相对于体材料声子 ($242 \pm 1\text{cm}^{-1}$, 77K)^[15] 的频移量变化情况. 随着 InAs 的淀积量增大, QD 声子峰向低频方向移动, 这与 Art ūs 等人^[8]的研究结果有所差异. 在 Art ūs 等人的实验中, InAs 层的淀积厚度为 $1.4 \sim 1.9\text{ML}$, 并且随 InAs 厚度增大, 其 LO 模频率发生一定程度的蓝移. 首先, 与该报道中的样品相比, 我们实验中所用的生长温度较高 (480°C), InAs 岛具有较大的平均高度和较小的尺寸纵横比, QD 形状更接近于金字塔形. 因而, 量子点形成过程和岛状结构的应力分布均与文献[8]中的样品具有明显差异. 另一方面, Art ūs 等人的样品结构中包含 25nm 的 GaAs 盖层, 则其产生的限制效应会对 QD 声子频率带来与应变效应相反的影响.

在不考虑边界能的情况下, 采用 S-K 模式的量子点生长过程中系统的总能量可表示为:

$$E = \Delta E_{\text{surface}} + \Delta E_{\text{elastic}}$$

即系统总能量 E 决定于表面能 $\Delta E_{\text{surface}}$ 与弹性应变能 $\Delta E_{\text{elastic}}$ 之和. 当 InAs 淀积量到达临界厚度后, 为了使系统的总能量 E 为最小值, 只有通过三维生长减小 $\Delta E_{\text{elastic}}$, 这也是自组织量子点生长的驱动力. 在我们的样品中, 随着 InAs 淀积量的增加, 根据 AFM 形貌观察的统计分析表明三维岛尺寸的横纵

比减小, 三维生长的趋势越来越显著, 很大程度上释放了 InAs QD 内应变, 从而导致其 Raman 峰出现红移. 图 5 中近似线性的频移关系显示, 弹性应变的释放是影响量子点喇曼峰频率位置的主要因素^[17,16].

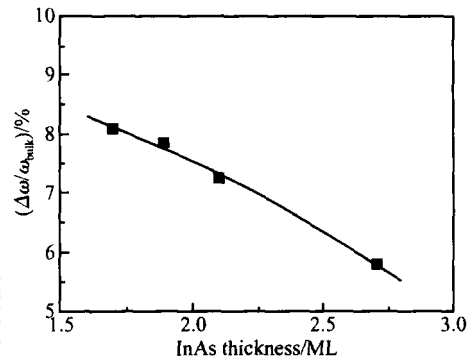


图 5 量子点声子频移量与 InAs 淀积厚度的关系

Fig. 5 QD phonon-frequency shift as a function of InAs thickness L

对另一组在 InAs QD 和 GaAs 盖层间加入应变缓冲层的样品的实验显示, 随 InAs 层淀积厚度增大, 来源于与 InAs 层相邻的 $\text{In}_{0.2}\text{Al}_{0.8}\text{As}$ 层的类 AlAs LO 模信号向高频方向移动, 如图 6 所示. 这一现象同样证实了在岛状结构生长过程中, 不同淀积厚度量子点层的应变发生了显著变化.

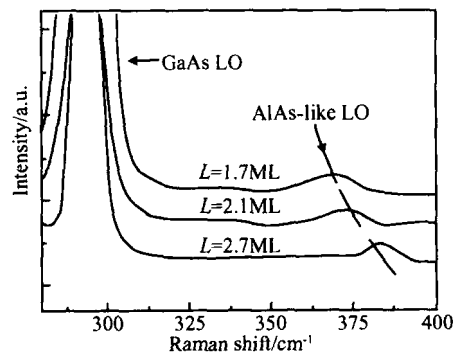


图 6 随 InAs 淀积厚度增加 AlAs-like LO 模的频率移动

Fig. 6 Frequency shift of AlAs-like LO mode as InAs thickness increases

4 结论

对淀积厚度不同的 InAs/GaAs 量子点材料进行了背散射喇曼实验. 在 77K 下, 观察到的 QD 声子模较 InAs 体材料 LO 模向高频方向发生了较大的频移, 通过计算分析, 认为应变效应对喇曼峰频率的移动产生较大影响. 随着量子点层淀积厚度 L 的增加, InAs LO 模发生红移, 我们分析了材料中量子点尺寸和形状的变化, 认为 QD 横纵比减小引起

的应变释放是影响其频移的主要因素。

参考文献

- [1] Hu Huiyong, Zhang Heming, Dai Xianying, et al. Growth of strained $\text{Si}_{1-x}\text{Ge}_x$ layer by UV/ UHV/ CVD. Chinese Journal of Semiconductors, 2005, 26(4) : 641
- [2] Zhang Guanjie, Shu Yongchun, Pi Biao, et al. Compatibility study on growing high quality modulation doped GaAs and InP/ InP epilayers by solid source molecular beam epitaxy. Journal of Synthetic Crystals, 2005, 34(3) : 395
- [3] Zhao Fengai, Zhang Chunling, Wang Zhanguo. Semiconductor quantum dots and their potential applications. Physics, 2004, 33(4) : 249 (in Chinese) [赵凤瑗, 张春玲, 王占国. 半导体量子点及其应用. 物理, 2004, 33(4) : 249]
- [4] Zanelatto G, Pusep Y A, Moshegov N T, et al. Raman study of the topology of InAs/ GaAs self-assembled quantum dots. J Appl Phys, 1999, 86(8) : 4387
- [5] Galzerani J C, Pusep Y A. Raman spectroscopy characterization of InAs self-assembled quantum dots. Physica B, 2002, 316/ 317 : 455
- [6] Pusep Y A, Zanelatto A, Silva S W, et al. Raman study of interface mode subjected to strain in InAs/ GaAs self-assembled quantum dots. Phys Rev B, 1998, 58(4) : R1770
- [7] Ibanez J, Patane A, Henini M, et al. Strain relaxation in stacked InAs/ GaAs quantum dots studied by Raman scattering. Appl Phys Lett, 2003, 83(15) : 3069
- [8] Art ús L, Cusco R, Hernandez S, et al. Quantum-dot phonons in self-assembled InAs/ GaAs quantum dots: Dependence on the coverage thickness. Appl Phys Lett, 2000, 77(22) : 3556
- [9] Grundmann M, Heitz R, Ledentsov N, et al. Electronic structure and energy relaxation in strained InAs/ GaAs quantum pyramids. Superlattices and Microstructures, 1996, 19(2) : 81
- [10] Wang Xiaodong, Wang Hui, Wang Hailong, et al. Study of self-assembled InAs quantum dots grown on low temperature GaAs epi-layer. J Infrared Millim Waves, 2000, 19(3) : 177 (in Chinese) [王晓东, 汪辉, 王海龙, 等. 低温 GaAs 外延层上生长 InAs 量子点的研究. 红外与毫米波学报, 2000, 19(3) : 177]
- [11] Milekhin A G, Toropov A I, Bakarov A K, et al. Vibrational spectroscopy of InAs and AlAs quantum dot structures. Physica E, 2004, 21 : 241
- [12] Chu L, Zrenner A, Bichler M, et al. Raman spectroscopy of In (Ga)As/ GaAs quantum dots. Appl Phys Lett, 2000, 77(24) : 3944
- [13] Groenen J, Carles R, Landa G, et al. Optical-phonon behavior in $\text{Ga}_{1-x}\text{In}_x\text{As}$: The role of microscopic strains and ionic plasmon coupling. Phys Rev B, 1998, 58(16) : 10452
- [14] Groenen J, Mlayah A, Carles R, et al. Strain in InAs islands grown on InP(001) analyzed by Raman spectroscopy. Appl Phys Lett, 1996, 69(7) : 943
- [15] Carles R, Saint-Cricq N, Renucci J B, et al. Raman scattering in $\text{InP}_{1-x}\text{As}_x$ alloys. J Phys C, 1980, 13 : 899
- [16] Tenne D A, Bakarova A K, Toropova A I, et al. Raman study of self-assembled InAs quantum dots embedded in AlAs: influence of growth temperature. Physica E, 2002, 13 : 199

Raman Scattering of InAs Quantum Dots with Different Deposition Thicknesses*

Zhang Guanjie¹, Xu Bo², Chen Yonghai², Yao Jianghong¹, Lin Yaowang^{1,2}, Shu Yongchun^{1,†}, Pi Biao¹, Xing Xiaodong¹, Liu Rubin¹, Shu Qiang¹, Wang Zhanguo^{1,2}, and Xu Jingjun¹

(1 Key Laboratory of the Ministry of Education of Advanced Techniques and Fabrication of Weak-Light Nonlinear Photonics Materials, Nankai University, Tianjin 300071, China)

(2 Key Laboratory of Semiconductor Material Science, Institute of Semiconductors, Chinese Academy of Sciences, Beijing 100083, China)

Abstract : The Raman scattering of InAs/ GaAs self-assembled quantum dots (QDs) with different InAs thicknesses is investigated. The vibrational mode, which can be assigned to QD phonons, is observed. Analysis indicates that strain is the most important factor that influences the InAs QD frequency. As the InAs deposition thickness L increases, the InAs-like LO mode frequency decreases, which we attribute to the relaxation of the strain in the QD layer. In another sample with an InAlAs strain buffer layer, the AlAs-like LO mode shows a blue shift as L increases. This also supports the proposed strain relaxation process in QDs.

Key words : quantum dots; Raman scattering; strain effect; confinement effect

PACC : 6322; 6855; 7865P

Article ID : 0253-4177(2006)06-1012-04

*Project supported by the National Natural Science Foundation of China (No. 60476042) and the Applied Basic Research Foundation of Tianjin (No. 06 YFJ ZJ C01100)

†Corresponding author. Email: shuyc@nankai.edu.cn

Received 25 September 2005, revised manuscript received 2 March 2006

©2006 Chinese Institute of Electronics



Poly(3,4-ethylene dioxythiophene) : Poly(styrene sulfonate) 的 共振拉曼光谱研究

林海波, 徐晓轩*, 王 斌, 吴彬麟, 许家林, 俞 钢, 张存洲

南开大学泰达应用物理学院, 天津 300457

摘要 通过拉曼光谱方法分别对 PEDOT:PSS 掺杂和去掺杂状态进行了详细分析。实验结果表明, 去掺杂的 PEDOT:PSS 由于其在激发波长附近的吸收增强而引起了共振效应, 拉曼信号得到大幅度增强, 可见, 以 633 nm (He-Ne) 激光为激发波长的拉曼光谱是研究 PEDOT:PSS 掺杂状态的有效方法。此外, 显微拉曼光谱也是分析聚合物发光二极管器件内各层材料的有效手段。

关键词 PEDOT:PSS; 共振拉曼光谱; 聚合物发光二极管

中图分类号: TN 312. 8; TN27

文献标识码: A

文章编号: 1000-0593(2006)04-0646-03

引 言

在过去的 30 年里, 研究工作者合成和研制出众多的导电共聚物, 其中 Poly(3,4-ethylene dioxythiophene) (PEDOT) 就是一种比较成功的聚合物导电材料, 并广泛用于各种电子器件中^[1]。它与其他同样功能的聚合物材料相比有自己的特点: 具有较低的氧化电势; 适中的禁带宽度; 具有稳定的氧化态。此外, 无论通过化学方法还是电化学方法制备的氧化 PEDOT 都具有较高的电导率 ($400 \sim 600 \text{ S} \cdot \text{cm}^{-1}$), 当制备成为氧化薄膜时, 具有较高的透明度^[2]。但是 PEDOT 是一种难溶的聚合物, 这一缺陷严重影响了 PEDOT 的应用。然而, 将 PEDOT 与水溶高分子电解质 Poly(styrene sulfonate) (PSS) 聚合掺杂后, 这一缺陷可以被克服, 从而产生一种水溶聚合物 PEDOT:PSS。作为聚合物发光二极管 (PLEDs) 中普遍使用的一种空穴传输层^[3], PEDOT:PSS 对提高器件的性能具有重要意义, 而它的化学组份和材料掺杂状态将直接影响到它的导电性能^[4], 从而影响到 PLEDs 的工作性能, 由此可见, 一种能够有效和灵敏地分析 PEDOT:PSS 的化学结构和掺杂状态的方法很有应用价值。

拉曼光谱技术作为一种无损测量手段, 在过去的几十年里遍及材料科学, 化学, 物理学, 生物学, 医学和环境科学等众多科学领域。我们使用的显微共焦拉曼光谱仪, 可以提供 μm 数量级精度的化学和结构方面的信息, 不但可以进行样品表面的化学结构信息分析, 还可以在纵深方向上进行测

量^[5], 能够得到物质材料表面以下不同深度的结构信息; 拉曼光谱的激发波长具有可选择性, 可以通过选择波长来避免荧光对拉曼光谱信号的影响; 另外, 通过适当选择波长, 可以利用拉曼光谱的共振增强效应^[6, 7], 由此提高光谱信号的信噪比, 这是红外光谱所不具有的特点和优势。

1 实验部分

聚合物薄膜的拉曼光谱是由英国 Renishaw 公司的 MK1000 型显微共焦拉曼光谱仪测得, 激发波长为 633 nm, 采用 180° 背散射式收集, 到达薄膜处的激光功率约 2 mW, 采用 $\times 50$ (N. A. = 0.75) 普通显微物镜聚焦于样品表面, 光斑尺寸约为 $1 \mu\text{m}$; 拉曼光谱采集的积分时间在 $100 \sim 200 \text{ s}$, 当采用更长的积分时间, 在显微镜下未观察到激光损伤, 同时为了避免激光对聚合物薄膜造成的光老化, 实验中尽量采用较低的激光功率; 收集信号中的瑞利散射光被两块全息窄带滤光片去除, 所以只有拉曼散射光最终被光栅分光并被制冷 CCD 探测器接收; 由于薄膜被甩膜于玻璃基底上, 所以采集过程中, 拉曼信号收到玻璃的荧光影响, 实验结果已经做了基底去除。吸收光谱是通过美国 Ocean Optic 公司的 SD1000 型光纤光谱仪测量的。我们实验中用到的掺杂的 PEDOT:PSS 是由华南理工大学材料学院高分子光电材料及器件研究所提供的, 通过用水合肼在高温下处理得到去掺杂的 PEDOT:PSS^[8]。

收稿日期: 2005-01-08, 修订日期: 2005-04-06

基金项目: 国家教育部“振兴计划”项目(A01504)资助

作者简介: 林海波, 1977 年生, 南开大学泰达应用物理学院在读博士研究生 * 通讯联系人

2 结果及讨论

以可见-近红外光作为拉曼光谱的激发源时, 共轭聚合物的拉曼共振效应可以表示成(1)式^[9]

$$\beta \propto \left[\frac{\nu_p^2 + \nu_0^2}{(\nu_p^2 - \nu_0^2)^2} \right]^2 \quad (1)$$

其中 $\beta(\text{cm}^2 \cdot \text{molecule}^{-1} \cdot \text{sr}^{-1})$ 是微分拉曼散射截面; $\nu_p(\text{cm}^{-1})$ 表示材料中电子在分子轨道中的跃迁频率; $\nu_0(\text{cm}^{-1})$ 表示拉曼光谱的激发频率。可以看到, 当激发波长的频率接近材料中电子在分子轨道中跃迁的频率时, 微分拉曼散射截面急剧增加, 从而有效增加拉曼光谱的有效信号强度。图1给出了掺杂和去掺杂 PEDOT:PSS 的吸收光谱比较, 从图中可以看到, 与掺杂状态的 PEDOT:PSS 材料不同, 去掺杂的 PEDOT:PSS 在 620 nm 附近出现了一个较强的吸收带^[10], 这意味着选择适当的拉曼激发波长, 如 He-Ne(633 nm), 将使去掺杂的 PEDOT:PSS 受益于拉曼共振效应。

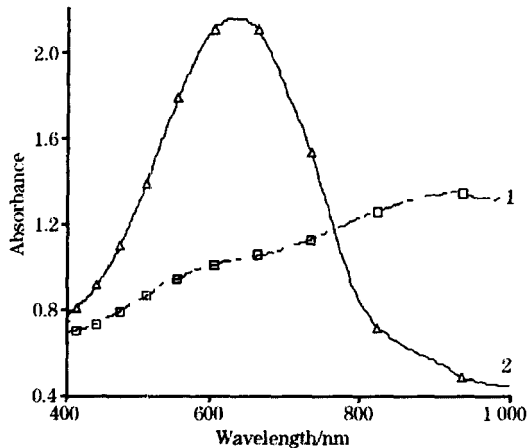


Fig 1 Comparison of absorbance spectra between doping and dedoping PEDOT:PSS
1: doped PEDOT; 2: dedoped PEDOT

对于实际的 PLEDs 器件来说, 由于 PEDOT:PSS 的掺杂状态决定材料的导电特性, 所以也严重影响 PLEDs 器件的工作性能, 而且有工作表明去掺杂的 PEDOT:PSS 也是造成 PLEDs 器件中黑斑缺陷的原因之一, 制约着 PLEDs 的应用。对于封装的器件, 由于所有聚合物材料都以夹层形式封于阳极(透明的导电 ITO 玻璃)和金属阴极之间, 红外光谱等测试手段的测量将受到局限, 而显微共焦拉曼由于其光谱采集系统具有共焦的特点, 使得这种光谱测量方法在纵向上具有较高的分辨本领($\sim 1 \mu\text{m}$), 而且拉曼光谱工作波段可以穿过玻璃基底, 对内部各种聚合物材料的化学结构特性进行分析。

图2给出了掺杂和去掺杂的拉曼光谱比较。插图是 PEDOT 的化学结构式, 可以看到 PEDOT 的骨架也具有共轭结构, 而 PSS 则不具有这种共轭结构^[3]。可以看到, 去掺杂 PEDOT 的拉曼光谱在相对强度上强于掺杂 PEDOT:PSS 的拉曼光谱, 这是由于共振拉曼效应的影响。从图中可见, 掺杂 PEDOT 在 1426 cm^{-1} 附近有个很宽的振动峰, 通过曲线拟合可知这个主峰是由 $1458, 1443, 1426, 1399$ 和 1357 cm^{-1} 五个峰叠加而成的。聚合物 PSS 虽然在 PEDOT:PSS 中的比重占支配地位, 但在拉曼光谱上并不表现出很强的特征峰, 此外, 玻璃基底的荧光也影响了 PSS 微弱拉曼信号的表现。而去掺杂的 PEDOT 在 1424 cm^{-1} 处有一个很强的共振振动峰, 这是因为随着 PEDOT 掺杂程度的下降, $\pi \rightarrow \pi^*$ 带在 620 nm 处的吸收急剧增加(如图1), 而拉曼光谱的激发波长 633 nm 正好落在这一吸收带内, 使得去掺杂 PEDOT 拉曼光谱信号受益于共振效应而得到增强。在长波段 $1500 \sim 1600 \text{ cm}^{-1}$ 内, 两种氧化状态的 PEDOT 都有两个明显的特征峰, 对于掺杂的氧化态, 两个特征峰分别处于 1530 和 1563 cm^{-1} 处, 而且它们的强度接近; 而去掺杂的氧化态, 两个特征峰出现在 1512 和 1548 cm^{-1} 处, 且 1512 cm^{-1} 的强度要明显强于 1548 cm^{-1} 的特征峰。因此通过拉曼光谱可以有效并灵敏地区分 PEDOT 的掺杂态和去掺杂态。

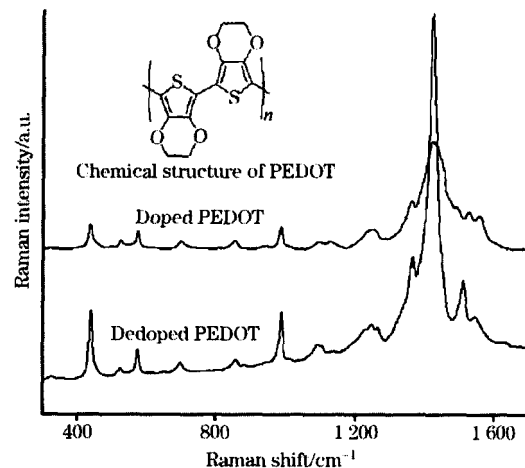


Fig 2 Comparison of Raman spectra between doping and dedoping PEDOT:PSS. Chemical structure of PEDOT is shown in the insert

总之, PEDOT:PSS 是一种良好的、稳定的导电材料, 由于掺杂和去掺杂状态分别具有不同的电学特性, 可以根据不同的实际需要选择不同的掺杂状态。从吸收光谱上看, 与掺杂状态的 PEDOT:PSS 不同, 去掺杂的 PEDOT:PSS 在 620 nm 附近出现了较强的吸收带, 所以适当选择拉曼激发波长, 可以利用共振拉曼效应研究 PEDOT 掺杂状态, 这是一种快捷、灵敏的方法。

参 考 文 献

- [1] Arias A C, et al. Phys. Rev. B, 1999, 60: 1854.
- [2] Louwet F, et al. Synthetic Metals, 2003, 135: 115.
- [3] Cao Y, et al. Synthetic Metals, 1997, 87: 171.
- [4] Tomas Johansson, et al. Synthetic Metals, 2002, 129: 269.
- [5] XU Xiao-xuan, LIN Hai-bo, WU Zhong-chen, et al (徐晓轩, 林海波, 武中臣, 等). J. Infrared and Millimeter Waves (红外与毫米波学报), 2003, 22(1): 63.
- [6] YAN Xun-ling, DONG Rui-guo, WANG Qiu-guo (闫循领, 董瑞国, 王秋国). Spectroscopy and Spectral Analysis (光谱学与光谱分析), 2004, 24(5): 576.
- [7] ZHENG Jun-wei, GU Ren-ao, LU Tian-hong (郑君伟, 顾仁敖, 陆天虹). Spectroscopy and Spectral Analysis (光谱学与光谱分析), 2000, 20(5): 689.
- [8] Peter K H Ho, et al. Nature, 2000, 404: 481.
- [9] Kim Ji-Seon, et al. Adv. Mater., 2002, 14: 206.
- [10] Lapkowski M, et al. Synthetic Metals, 2000, 110: 79.

Study of Poly (3,4-Ethylene Dioxythiophene) :Poly (Styrene Sulfonate) by In-Situ Resonance Raman Spectroscopy

LIN Hai-bo, XU Xiao-xuan*, WANG Bin, WU Bin-lin, XU Jia-lin, YU Gang, ZHANG Cun-zhou
TEDA Applied Physics School, Nankai University, Tianjin 300457, China

Abstract Poly (3,4-ethylene dioxythiophene) (PEDOT) : Poly (styrene sulfonate) (PSS) has attracted a lot of interest for application in organic electronics due to good stability and high electronic conductivity in its doped state. Indeed, thin layers of PEDOT:PSS was regularly used in light emitting diodes (PLEDs) as hole injection and transportation layer. Here, Doping and dedoping states of PEDOT:PSS were studied by absorbance spectra and Raman spectra. A new absorption band centered at 620 nm was observed on dedoped PEDOT:PSS. Consistently, Raman signals of dedoped PEDOT:PSS are resonantly intensified since the Raman excitation wavelength (633 nm) is set in the enhanced absorption band. So it gives a sensitive way to study the doping and dedoping states of PEDOT:PSS. Furthermore, for the encapsulated polymer light-emitting diodes, Raman spectroscopy is a powerful way to study the polymer layers inside the devices.

Keywords PEDOT:PSS; Resonant Raman spectra; Polymer light-emitting diodes

(Received Jan. 8, 2005; accepted Apr. 6, 2005)

*Corresponding author

乳腺组织形态基元共焦显微拉曼光谱的研究

于 舸¹, 徐晓轩², 吕淑华³, 张存洲², 宋增福⁴, 张春平²

1. 北京石油化工学院数理教学部, 北京 102617
2. 南开大学物理科学学院光子学中心, 天津 300071
3. 天津医科大学肿瘤医院, 天津 300060
4. 北京大学物理学院, 北京 100871

摘要 利用共焦显微拉曼方法, 测定了乳腺组织切片的 Mapping 拉曼谱, 光谱采样体积达到 μm 尺度。通过对这些共焦拉曼谱与商业提纯肌动蛋白、胶原等生物物质做出的谱的分析比较, 分离出了来自细胞质、细胞间质、脂肪以及乳腺沉积物这些组织形态基元的拉曼谱; 用 K 阶簇分析方法, 还获得了细胞核基元谱; 基元谱与提纯化学物质谱的相关分析印证了组织形态基元谱的来源。还分析总结了这些组织形态基元谱的特征。这些工作为深入理解组织形态与其拉曼谱的关系以及乳腺组织形态拉曼模型的建立奠定了基础。

关键词 共焦显微拉曼光谱; 乳腺; 组织形态基元; Mapping; K 阶簇分析; 相关分析

中图分类号: O657.3 **文献标识码**: A **文章编号**: 1000-0593(2006)05-0869-05

引言

乳腺癌是导致女性死亡的主要恶性肿瘤之一。因此, 早期作出正确诊断对疾病的治疗、治愈具有决定性的意义。目前在临床可结合多种方法对肿瘤进行诊断, 但最终确定肿瘤的良、恶性程度等通常需要做具有一定创伤性的活体组织切片病理学检查。然而, 非量化的病理学诊断过程繁琐, 往往受人为因素影响, 而且组织切片的病理表明 70%~90% 又是良性的^[1]。显然, 寻求一种具有分子化学成分分析能力的原位诊断方法是非常必要的。前期的研究成果表明, 傅里叶变换红外拉曼光谱能在分子水平揭示乳腺肿瘤组织与正常组织的差别^[2-7], 但无法确定产生这些谱(宏观谱)特征的化学和组织形态学的根源。乳腺组织癌变引起的早期变化, 发生在显微水平, 因此有必要研究微观组织形态基元(Morphological elements)细胞核、细胞质、细胞间质等拉曼光谱特征及变化, 以提取生物组织的化学和结构信息, 进而更好地理解其宏观谱的变化并为发展拉曼诊断方法奠定基础。目前这方面的研究工作已有报道^[8, 9]。本文采用了具有空间分辨率的共焦显微拉曼光谱方法, 在前期研究工作的基础上^[10], 进一步测定乳腺组织切片的 Mapping 拉曼光谱, 光谱采样体积达到 μm 尺度。通过对所测显微拉曼光谱的分析、对比, 发现了乳腺组织形态基元细胞核、细胞质、细胞间质等的拉曼光

谱, 并研究这些基元谱的光谱学特征。

1 实验部分

1.1 样品

32 例乳腺组织样品全部取自天津肿瘤医院手术切除的新鲜标本。经病理科检验证实正常组织 3 例, 良性肿瘤 11 例, 乳腺癌组织 18 例。标本离体后用生理盐水冲洗净血渍, 取材于肿瘤中心部位约为 1.0 cm^3 大小的组织样品, 放置于 $-20\text{ }^\circ\text{C}$ 的 LEICA CM1900 显微切片机中, 切成 $10\text{ }\mu\text{m}$ 的组织切片贴在氟化钙基片上, 并用空气吹干, 用于测量拉曼显微光谱。与这些切片相邻的切片做成 $7\text{ }\mu\text{m}$ 厚, 放在玻璃片上 HE 染色, 进行病理学检查。

购于 Sigma 公司的生物物质: 脱氧核糖核酸 DNA、核糖核酸 RNA、肌动蛋白、I 型胶原、甘油三油酸酯、 β 胡萝卜素和胆固醇、卵磷脂。实验前, 将这些生物样品置于冰箱 $2\sim 4\text{ }^\circ\text{C}$ 的冷藏室中保存。

1.2 实验仪器与测量

使用 Renishaw 公司的 M KI-2000 型显微拉曼光谱仪, 配备有 LEICA 的显微镜及三维微动平台, 平台横向 (x, y 轴) 分辨率为 $1\text{ }\mu\text{m}$, 纵向 (z 轴) 分辨率为 $2\text{ }\mu\text{m}$, 光谱分辨率为 2 cm^{-1} , 激发光为氩氦激光 633 nm , 输出功率为 30 mW 。仪器的波数轴用硅的谱线进行校准, 强度轴用钨灯的光谱来校

收稿日期: 2005-02-21, 修订日期: 2005-05-22

基金项目: 国家教育部“振兴计划”资助项目

作者简介: 于 舸, 女, 1962 年生, 北京石油化工学院数理教学部副教授, 博士

准。拉曼谱仪在共焦状态下具有三维空间分辨能力,其共焦原理如图 1 所示。显微镜采用无穷远共轭方式,显微镜焦点与探测器的接收点组成一对共轭点。样品放置在物镜的焦平面上,物镜后光谱仪狭缝前有一个透镜,狭缝位于此透镜的焦平面上, Renishaw 公司的共焦显微拉曼光谱仪没有共焦针孔,其光谱仪入射狭缝代替了共焦针孔作为一个维度方向上的空间滤波器,再利用 CCD 像面上方向与狭缝垂直的像元行数作为另一个维度方向上的空间滤波器。在垂直于狭缝方向上,超出狭缝外的光被狭缝滤除,沿狭缝方向上的光进入谱仪,在 CCD 上形成一个谱带,谱带的高度为沿狭缝方向上被照明的部分狭缝通过谱仪成像而成。通过限制 CCD 上被采集的谱带高度,即可实现垂直于狭缝方向的空间滤波。狭缝越小、CCD 上被采集的像素行数越少,其共焦效果越好。

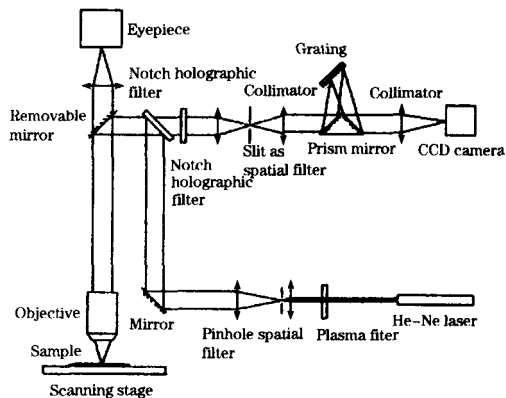


Fig 1 Diagram of the confocal system

本实验中,使用的共焦条件是:狭缝宽度为 $15\ \mu\text{m}$, CCD 上像元行数为 5 行,采用大数值孔径 ($N.A. = 0.75$) 50 倍物镜,样品上聚焦光斑直径约为 $1\ \mu\text{m}$,光谱采样体积约为 $\sim 2\ \mu\text{m}^3$ 。

显微镜装备的微动平台是由计算机控制的 x, y, z 三维运动定位系统,因此,能够按照预先定义在 (x, y) 平面上实现阵列的 Mapping 定点测量,并能在测量中实现样品聚焦平面的精确定位 (z 轴)。应用这种方法,我们获取了十多幅拉曼 Mapping, 2 000 多个拉曼谱,这些成像的典型面积为 $30\ \mu\text{m} \times 30\ \mu\text{m}$,在 x, y 轴方向的步长为 $2\ \mu\text{m}$,每个测量点的信号收集时间为 $60 \sim 80\ \text{s}$ 。室温设置为 $(22 \pm 2)\ \text{C}$ 。所有拉曼光谱来自正常、良性肿瘤和癌变乳腺组织样品。另外,还测定了购买的生物物质的拉曼谱。

1.3 数据处理

在 Matlab 6.5 软件环境下,自行编制了数据处理程序。

对 Mapping 谱数据和纯化学物质的谱数据进行预处理。用 $633\ \text{nm}$ 波长激发的拉曼光谱含有较强的荧光背景,收集拉曼散射光的 CCD 经常受到宇宙射线的照射,同时还含有随机噪声等,预处理的目的是去除基底和宇宙射线、增加信噪比。预处理的方法是:(1)通过导数滤波去除宇宙射线;(2)通过多项式拟合去除基底;(3)通过九点 Savitzky-Golay 平滑滤波去除高频噪声。为了对乳腺组织的谱进行主因素分

析,还对谱数据做了方差归一化处理。

对经过预处理的 Mapping 谱做主因素 (PC) 分析。先计算出全部主因素,然后保留前面重要的、去掉后面不重要的主因素,使得保留下来的主因素能够涵盖谱数据样本差异的 99% 以上,通常保留下来的主因素有 $30 \sim 150$ 个。依据每个谱在这些主因素上的得分,对谱数据做 K 阶簇分析 (K -means cluster analysis)。簇的数量通过试验来确定,每个 Mapping 数据都试着分 2 簇、3 簇直到 10 簇,通过观察每次分析的轮廓图、各个簇平均谱等来确定最佳的簇数量。簇分析后,我们得到各个簇的分布图、簇平均谱及总平均谱等。

2 结果与分析

我们分析了经过预处理的 Mapping 谱的特征,并与商业提纯的肌动蛋白、胶原等生物物质的拉曼光谱进行了比较,分离出了来自细胞质、细胞间质、脂肪以及乳腺沉积物这些组织形态基元的拉曼谱,并研究了这些基元谱与提纯化学物质谱的相关性,相关系数见表 1。

Table 1 Correlation coefficients of Raman spectra from morphological elements and commercial available chemicals

Correlation	Morphologically derived fat vs triolein	Cell cytoplasm vs actin	Extracellular matrix vs collagen (type I)	Cell nucleus vs DNA
Correlation coefficients	0.984 3	0.917 5	0.978 7	0.866 8
p value	0	0	0	0

2.1 细胞质基元谱

细胞质由细胞质基质和细胞器构成,细胞质基质的主要成分是肌动蛋白,肌动蛋白主要分布于细胞质基质中^[11]。因此,以肌动蛋白拉曼光谱为主要特征的谱一定来自于细胞质,称之为细胞质基元谱。先前的研究表明,细胞质的拉曼谱不容易获得,原因可能是肌动蛋白的拉曼散射截面较小、浓度较低。本实验获得了少量的具有肌动蛋白谱特征的细胞质的拉曼谱,见图 2a。图中所示为 6 个患者的 12 幅谱的平均谱。图 2b 显示了购于 Sigma 公司的肌动蛋白拉曼光谱,二者非常相似。位于 $1\ 660 \sim 1\ 250\ \text{cm}^{-1}$ 处的酰胺 I, III 谱线, $1\ 449\ \text{cm}^{-1}$ 处的 CH_2, CH_3 变形振动模, $1\ 338\ \text{cm}^{-1}$ 处色氨酸的谱线 (CH_2 变形振动), 以及 $1\ 002\ \text{cm}^{-1}$ 处的苯丙氨酸的谱线 ($\text{C}-\text{C}$ 对称伸缩振动) 都显著地出现在图 2a 和 2b 中^[2, 12, 13]。肽链骨架 $\text{C}-\text{C}$ 对称伸缩振动的低强度谱带 $\sim 938\ \text{cm}^{-1}$ 也出现在其中。酰胺 I, III 带的强振动峰以及肽链骨架的弱振动峰的出现,表明肌动蛋白空间构象的无序性。

此基元谱和肌动蛋白谱的相关系数为 0.917 5,显著性水平 p value < 0.05 (见表 1),它们高度相关,进一步证实了这种基元谱来自细胞质,肌动蛋白是细胞质谱的主要贡献者^[18]。

2.2 细胞间质基元谱

细胞间质 (Extracellular matrix) 又被称之为结缔组织, 它不仅能为细胞提供支撑网络作用, 而且还参与细胞的黏附、迁移以及细胞内基因的表达等活动。其主要成分是结构蛋白、具有特殊功能的黏附蛋白以及聚糖分子, 胶原是其最主要的蛋白质成分。胶原的氨基酸组成不同寻常, 脯氨酸 (12%)、羟脯氨酸 (9%)、甘氨酸残基 (33%) 的含量特别高。胶原由三条左手螺旋的多肽链缠绕、右旋, 形成绳索样右手超螺旋结构, 其中脯氨酸和羟脯氨酸可限制多肽链旋转。三螺旋结构常有 4-羟脯氨酸, 产生氢键及氧桥, 使三股螺旋结构相对牢固。

胶原具有强拉曼散射截面, 信号强特征明显, 具有胶原特征的拉曼谱比较常见并且容易分辨。胶原蛋白集中分布在细胞间质中, 以胶原蛋白为主要特征的谱主要来自于细胞间质。图 2c 显示了细胞间质基元谱, 它来自 8 个患者的 272 幅谱的平均谱; 图 2d 则显示了购买的 I 型胶原的拉曼光谱, 二者十分相似, 表明了 I 型胶原是细胞间质谱的主要贡献者^[8]。其中强谱带酰胺 I、III 分别位于 1 668, 1 245 和 1 270 cm^{-1} , 可归属于三股螺旋构象的极性和非极性区域, 中强度谱带 920 和 874 cm^{-1} 来源于脯氨酸和羟脯氨酸的 C-C 伸缩振动模^[12], 后者是胶原的特征谱带。

细胞间质基元谱和 I 型胶原谱的相关系数为 0.978 7 ($p < 0.05$), 也显示了两谱的高度一致性。

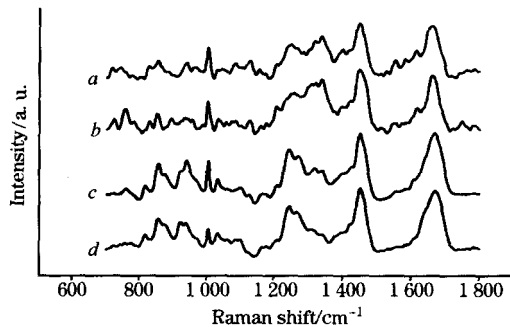


Fig 2 Comparison of (a) cell cytoplasm and (b) actin; (c) extracellular matrix and (d) purified collagen (type I)

2.3 脂肪基元谱

脂肪是正常乳腺组织拉曼谱的最大贡献者之一, 其拉曼散射截面极强、含量较丰富。图 3a 显示了脂肪基元谱, 它是取自 5 位患者的 8 幅乳腺组织脂肪谱的平均。其特征峰分别是 1 298 cm^{-1} (CH_2 扭转和摆动振动)、1 437 cm^{-1} (CH_2 剪切振动)、1 654 cm^{-1} ($\text{C}=\text{C}$ 伸展振动) 以及 1 743 cm^{-1} ($\text{C}=\text{O}$ 伸展振动)^[2, 9, 12]。与购买的甘油三酸酯的拉曼谱比较 (见图 3b), 显示出甘油三酸酯是脂肪在人体组织中存在的主要形式。二者很高的相关系数 (0.984 3) 也证明了这个结论。

2.4 乳腺组织中 β 胡萝卜素和钙化点的谱

用 633 nm 波长激发时, 乳腺组织中 β 胡萝卜素具有共振增强效果, 产生极强的拉曼信号。其特征峰分别位于 1 154 和 1 521 cm^{-1} 附近^[2, 8, 12] (见图 4a)。与购买的纯 β 胡萝卜素

相比 (见图 4b), 组织形态基元的 β 胡萝卜素谱中还含有少量的脂肪成分, 它常与脂肪共存。为了获取纯 β 胡萝卜素的拉曼谱, 我们确认用购买的 β 胡萝卜素样品能够较好地代替组织中的 β 胡萝卜素, 用于乳腺组织建模研究。

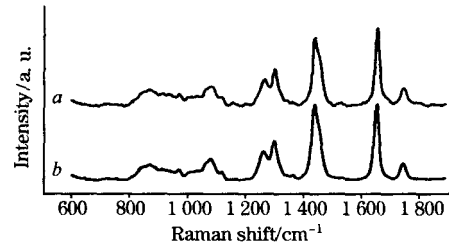


Fig 3 Comparison of (a) morphologically derived fat and (b) purified triolein

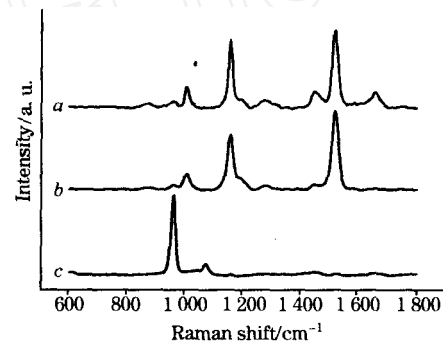


Fig 4 Spectra of breast deposits and purified β carotene
a: β carotene in breast tissues sample;
b: Purified β carotene;
c: Calcium hydroxyapatite in breast tissues sample

乳腺组织中另一种常见的沉积物就是钙化, 通常认为是细胞分泌物、降解的结果。它常与癌变相联系, 钙化点的大小、形状、数量和分布是乳腺癌临床诊断的直接征像之一。文献报道 X 线片上钙化的出现率为 30%~50%, 病理上为 60%~85%。钙化的化学成分是氢氧磷灰石的钙盐, 它们都有很强的拉曼散射截面。但在冰冻切片中, 钙化的组织主要用于病理分析, 通常不会给我们做研究, 所以我们只获得了几幅钙化的谱。图 4c 显示的是四幅钙化谱的平均谱, 该谱主要由两个特征谱线 960 和 1 070 cm^{-1} 组成, 经文献确认^[13, 14], 该谱主要是由羟基磷酸钙贡献的。其中位于 960 cm^{-1} 处的强特征峰归属于 PO 基团对称伸缩振动, 而位于 1 070 cm^{-1} 处的低强度谱线归属于 CO 基团对称伸缩振动。

2.5 细胞核基元谱

DNA 是细胞核的特征成分, 尽管提纯的 DNA 是强拉曼散射体 (见图 5b), 但在实验中很难直接测到以 DNA 谱为主要特征的细胞核基元谱。其主要原因我们认为是 DNA 凝聚在很小的体积中, 即使落在采样范围内其所占采样体积的比例也很小, 因此它的拉曼信号比其他成分弱许多, 无法成为谱的主要贡献者。在本研究中我们利用 K 阶簇分析方法获得了细胞核基元的拉曼谱。

图 5a 显示了一个由 208 幅谱组成的 Mapping 谱数据的

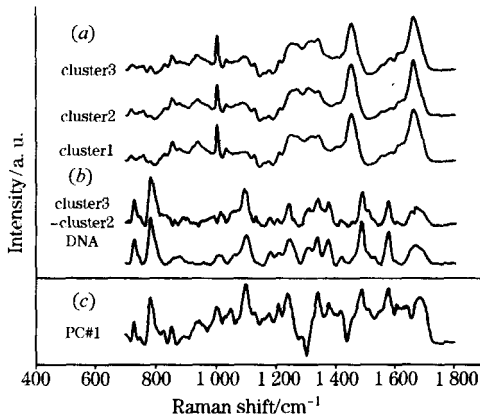


Fig 5 a: average spectra of cluster 1 to 3; b: difference spectrum of cluster 3 and 2, DNA spectrum; c: the first principal component calculated for the data set

K 阶簇分析的簇平均谱, 共分 3 簇。 K 阶簇分析依据前 80 个主因素分值, 约 80% 数据落在前两个主因素中。病理分析对照表明, 这些谱来源于乳腺正常的上皮组织。

在簇 3 (图 5a Cluster 3) 的平均谱中 DNA 拉曼特征峰 728, 782, 1 096 和 1 575 cm^{-1} 都存在, 说明这一簇主要代表了来自含有上皮组织细胞核区域的谱, 簇 1, 2 谱中 DNA 的

贡献较少。簇 3 和 2 的差谱 (见图 5b) 具有较多 DNA 谱特征, 尽管它还含有少量组蛋白相关的特征。差谱与 DNA 谱的相关系数为 0.866 8 ($p=0$), 具有较好的相似性, 因此可以确定, 该差谱能够代表乳腺组织细胞核基元拉曼谱。其中, 归属于 DNA 碱基基团腺嘌呤 (A)、鸟嘌呤 (G) 的拉曼特征峰位于 728 cm^{-1} (A) 和 1 575 cm^{-1} (A, G) 附近, 属于 PO_2^- 骨架磷酸离子基团的对称伸缩振动的谱线出现在 1 096 cm^{-1} , 以及指定为 O—P—O 骨架磷酸二酯的对称伸缩振动谱线出现在 782 cm^{-1} 附近^[9, 12, 15]。

主因素值也反映出不同簇谱之间的差异主要是 DNA 的贡献。由本组数据计算出来的第一种主因素值的图 5c 与 DNA 谱主要特征相似。

3 结 论

上述结果表明, 利用共焦显微拉曼方法, 能够做出细胞核、细胞质、细胞间质等乳腺组织形态基元的拉曼光谱; 这些基元谱与其特有的生化成分谱的相似性印证了基元谱的来源。本文进一步分析总结了这些组织形态基元谱的特征。这些工作为更好地理解乳腺组织形态及其与拉曼谱的关系及建立乳腺组织形态拉曼模型奠定了基础, 为实现原位诊断提供了组织形态的化学信息。

参 考 文 献

- [1] Johnson J , Dalton R , Wester S , et al. Archives of Surgery , 1999 , 134 : 712.
- [2] Alfano R R , Liu C H , Sha W L , et al. Lasers Life Sci. , 1991 , 4 : 23.
- [3] Frank C J , Redd D C B , Gansler T S , et al. Analytical Chemistry , 1994 , 66(3) : 319.
- [4] Frank C J , McCreery R L. Analytical Chemistry , 1995 , 67(5) : 777.
- [5] Manoharan R , Shafer-Peltier K E , Perelman L , et al. Photochemistry and Photobiology , 1998 , 67(1) : 15.
- [6] Jackson M , Mansfield J R , Dolenko B , et al. Cancer Detection and Prevention , 1999 , 23(3) : 245.
- [7] LING Xiao-feng , LI Wei-hong , SONG Yuan-yuan , et al (凌晓锋 , 李维红 , 宋苑苑 , 等). Spectroscopy and Spectral Analysis(光谱学与光谱分析) , 2000 , 20(5) : 692.
- [8] Shafer-Peltier K E , Haka A S , Fitzmaurice M , et al. J. Raman Spectrosc. , 2002 , 33 : 552.
- [9] Kneipp J , Schut T B , Kliffen M , et al. Vibrational Spectroscopy , 2003 , 32 : 67.
- [10] YU Ge , XU Xiao-xuan , NIU Yun , et al (于 舸 , 徐晓轩 , 牛 昀 , 等). Spectroscopy and Spectral Analysis(光谱学与光谱分析) , 2004 , 24(11) : 1359.
- [11] QIAN Kai-xian , SHAO Jian-zhong , LI Ya-nan (钱凯先 , 邵健忠 , 李亚南). Principles of Cellular Biochemistry(细胞生物化学原理). Hangzhou : Zhejiang University Press(杭州 : 浙江大学出版社) , 1999 . 298.
- [12] Anita M J , Rebecca R K. Journal of Biomedical Optics , 1996 , 1 : 1.
- [13] Radi M J. Archives of Pathology and Laboratory Medicine , 1989 , 113 : 1367.
- [14] Kodati V R , Tomasi G E , Turumin J L , et al. Appl. Spectrosc. , 1990 , 44 : 1408.
- [15] LI Guang , YANG Hong-ying , XU Yi-ming , et al (李 光 , 杨红英 , 许以明 , 等). Science in China C(中国科学 C) 2002 , 32(2) : 177.

Confocal Raman Microspectroscopic Study of Human Breast Morphological Elements

YU Ge¹ , XU Xiao-xuan² , L Ü Shu-hua³ , ZHANG Cun-zhou² , SONG Zeng-fu⁴ , ZHANG Chun-ping²

1. Department of Mathematics and Physics , Beijing Institute of Petrochemical Technology , Beijing 102617 , China
2. Photonics Center , Institute of Physics , Nankai University , Tianjin 300071 , China
3. Tumour Hospital , Tianjin Medical University , Tianjin 300060 , China
4. College of Physics , Peking University , Beijing 100871 , China

Abstract Breast tissue sections were examined by means of confocal Raman spectroscopy with an excitation wavelength of 633 nm. Acquired using a microscopic mapping approach with the sample volume of $\sim 2 \mu\text{m}^3$, these spectra were compared with the ones of the commercially available actin , DNA , collagen (type I) , triolein etc. Some spectra were distinguished and identified and characterize the morphological elements like cell cytoplasm , extracellular matrix etc. The cell nucleus spectrum was also obtained by *K*-means cluster analysis. The correlation analysis showed that the spectrum from a morphological element is highly correlated with that from the corresponding purified chemical. The spectroscopic characterization of these morphological elements was then investigated. This study is helpful to understanding the chemical/ morphological basis of the Raman spectrum and designing the Raman microspectroscopic model of human breast tissue.

Keywords Confocal Raman microspectroscopy ; Breast ; Morphological elements ; Mapping ; *K*-means cluster analysis ; Correlation analysis

(Received Feb. 21 , 2005 ; accepted May 22 , 2005)

文章编号: 1001-3806(2006)04-0351-04

光抽运垂直外腔面发射激光器特性与研究进展

张冠杰¹, 舒永春^{1*}, 刘如彬¹, 舒强¹, 林耀望^{1,2}, 姚江宏¹, 王占国^{1,2}, 许京军¹

(1 南开大学 弱光非线性光子学材料先进技术及制备教育部重点实验室, 天津 300457; 2 中国科学院 半导体研究所 半导体材料科学重点实验室, 北京 100083)

摘要: 介绍了光抽运半导体垂直外腔面发射激光器的结构特点、设计原理及其性能优势, 综合评述该领域的最新研究进展, 并探讨该类型激光器的发展前景和技术发展方向。

关键词: 光电子学; 垂直外腔面发射激光器; 光抽运; 分布布拉格反射镜; 超短脉冲

中图分类号: TN248.4 **文献标识码:** A

Characteristics and development of optical pumping vertical-external-cavity surface-emitting lasers

ZHANG Guan-jie¹, SHU Yong-chun¹, LIU Ru-bin¹, SHU Qiang¹, LIN Yaowang^{1,2}, YAO Jiang-hong¹,
WANG Zhan-guo^{1,2}, XU Jing-jun¹

(1. Key Laboratory of Advanced Technique and Fabrication for Weak-Light Nonlinear Photonics Materials of Ministry of Education, Nankai University, Tianjin 300071, China; 2. Key Laboratory of Semiconductor Materials Science, Institute of Semiconductors, the Chinese Academy of Sciences, Beijing 100083, China)

Abstract: The properties and advantages of optical pumping semiconductor vertical-external-cavity surface-emitting laser (VECSEL) are introduced and the latest device development is demonstrated. On the basis of these analyses, the application potential and technology direction in the areas are pointed out.

Key words: optoelectronics; vertical-external-cavity surface-emitting laser (VECSEL); optical pumping; distributed Bragg reflector (DBR); ultra short pulse

引 言

近几十年来, 各类半导体激光器的性能在不断提高, 但也均存在着缺点, 限制了其进一步发展。传统的半导体二极管激光器技术已经相当成熟, 能高效可靠地产生大功率光束, 但其固有缺点是很难获得圆形衍射极限的基横模输出光束; 垂直腔面发射激光器 (vertical cavity surface-emitting laser, VCSEL) 具有理想的圆形输出光束, 但在单横模下工作很难达到大功率。垂直外腔面发射激光器 (vertical-external-cavity surface-emitting laser, VECSEL)^[1] 有望克服上述缺点, 现在已受到了越来越广泛的关注。

与传统的半导体激光器不同, VECSEL 具有类似于 VCSEL 的增益结构, 再通过与固体激光器相近的外腔结构进行选模输出, 可形成圆形高斯 TEM₀₀ 模式的输出光束, 克服了固体激光器光束质量不理想的缺点。与 VCSEL 相比, VECSEL 突破了功率限制, 单横模输

出功率可达几百毫瓦, 同时在高效实现腔内倍频的前提下简化了谐振腔内的结构, 从而降低了激光器晶片生长和加工的难度。

VECSEL 可采用成熟的大功率半导体激光器做抽运源, 称为光抽运垂直外腔面发射激光器 (OPS-VECSEL)。与电抽运激光器相比, OPS-VECSEL 不使用 p-n 结或电接触, 既降低了串联电阻上的电能损耗, 又增加了器件的可靠性。宽抽运带宽 (大于 40nm) 和极短的抽运吸收长度 (约 1μm ~ 2μm) 确保抽运光的有效吸收, 消除了二极管激光器抽运的严格波长限制。此外, OPS-VECSEL 使用无掺杂的半导体材料, 降低了由于自由载流子吸收造成的光学损耗。可以说, OPS-VECSEL 结合了二极管抽运固体激光器和 VCSEL 的构造方法, 吸取了二者的优点。

良好的空间光强分布、大的输出功率范围、体积小、光束质量好等突出优点, 使 OPS-VECSEL 具有广阔的应用范围, 并已在高速激光打印、高密度光存储、超快激光、激光雷达等方面显示出诱人的前景。本文将就光抽运垂直外腔面发射激光器的特性进行介绍, 综述目前最新的研究进展。在此基础上, 分析了该类型激光器的发展潜力和技术发展方向。

作者简介: 张冠杰 (1979-), 男, 博士研究生, 主要研究方向为纳米光电材料与器件。

* 通讯联系人。E-mail: shuyc@nankai.edu.cn

收稿日期: 2005-06-29; 收到修改稿日期: 2005-08-10

InAlAs 量子点材料的 AFM 和拉曼散射研究

张冠杰¹ 陈涌海² 姚江宏¹ 舒强¹ 刘如彬¹ 舒永春¹ 王占国^{1,2} 许京军¹

(¹ 天津市南开大学弱光非线性光子学材料先进技术及制备教育部重点实验室, 天津 300457)
(² 中国科学院半导体研究所半导体材料科学重点实验室, 北京 100083)

摘要 对分子束外延(MBE)自组织生长的 InAlAs 量子点材料进行了拉曼散射实验。结合原子力显微镜(AFM)对量子点形貌观察的结果,分析了 InAlAs 量子点生长过程中尺寸、密度和均匀性的改变,并研究了三维岛的结构对拉曼谱线的影响。对 InAlAs 淀积厚度不同样品的拉曼谱分析表明,岛状结构的尺寸纵横比与类 GaAs LO 模和类 AlAs LO 模的半高全宽有密切关系。不同偏振下的拉曼实验证实了该结构中的光学声子在 $Z(X, X)\bar{Z}$ 偏振条件下为非拉曼活性。

关键词 光电子学与激光技术; 量子点; 拉曼散射; 声子; 互混效应

中图分类号: TN244

AFM and Raman Scattering Study of InAlAs Quantum Dots

ZHANG Guanjie¹ Chen Yonghai² YAO Jianghong¹ SHU Qiang¹ LIU Rubin¹

SHU Yongchun¹ WANG Zhanguo^{1,2} XU Jingjun¹

(¹ Key Laboratory of Advanced Technique and Fabrication for Weak-light Nonlinear Photonics Materials, Ministry of Education, Nankai University, Tianjin 300457)
(² Key Laboratory of Semiconductor Materials Science, Institute of Semiconductors, The Chinese Academy of Sciences, Beijing 100083)

Abstract Raman scattering investigation of InAlAs/AlGaAs quantum dots (QDs) grown by molecular beam epitaxy (MBE) is reported. The changes of QDs size, density and uniformity in their growing process from the AFM images are analyzed together with the FWHM of Raman peaks. Moreover, the relation between the Raman lines and the structure characteristics of QDs is studied. Comparing those samples with different InAlAs thicknesses, it is found that the width/height ratio has some relation with the widening of GaAs-like LO and AlAs-like LO modes. It also confirms that this kind of phonons is Raman inactive in the $Z(X, X)\bar{Z}$ polarization.

Key words opto-electronics and laser technology; quantum dot; Raman scattering; phonon; intermixing effect

1 引言

近年来,以自组织量子点材料作为有源区的光电器件由于其独特的性能和广泛的应用前景而备受人们关注^[1-3]。其中,量子点激光器和探测器在理论上具有优于量子阱器件的诸多优势,因而引起了研究人员的兴趣^[4-6]。一般而言,大多数自组织生长的量子点都有较

大的横向尺寸(约几十纳米)和较小的纵向尺寸(约几纳米)。这种接近“量子盘”的形状使点在生长方向的限制作用非常强,而水平方向的限制作用相对较弱。但是,自组织量子点的尺寸、密度和均匀性相对较难控制,并对器件性能造成了很大的影响。因此,研究自组织量子点在生长过程中形貌及结构的变

化对获得更高质量的材料进而获得性能优异的器件具有重要意义。

拉曼散射是研究与晶格振动相关的声子行为的最有力工具之一,并且已逐渐应用于超晶格、量子点等材料的研究^[7,8]。众所周知,量子点材料的拉曼光谱表现出与相应结构体材料不同的性质,如拉曼峰强度、线宽等改变,频移、界面

收稿日期: 2005-08-13; 收到修改稿日期: 2006-01-10

基金项目: 国家自然科学基金(No.60476042)资助项目

作者简介: 张冠杰(1979-),男,天津市人,博士研究生,主要研究方向为纳米光电材料与器件。

E-mail: centaur@mail.nankai.edu.cn

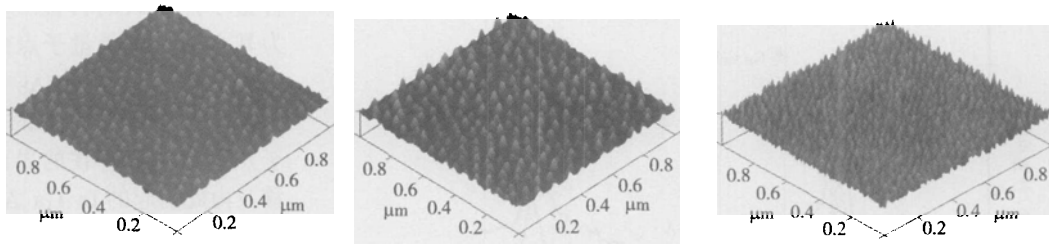


图 1 A、B、C 三个样品的 AFM 图

模的出现等等。目前,量子点的拉曼研究比较多地集中于 InAs/GaAs、InAs/InP 等材料体系。Zanelatto G 等人^[9]利用拉曼散射研究了生长于 GaAs 衬底上的自组织 InAs 量子点的布局情况;Galzerani J C 等^[10]在不同条件下生长了 InAs 量子点,并比较了掺杂和未掺杂、单层和多层、退火和未退火样品之间的拉曼谱特征。Groenen J 等人^[11]利用拉曼散射方法研究了 InP 衬底上 InAs 量子点的应力变化,并且分析了拉曼特征峰频率变化的原因。

InAlAs 量子点材料可以用作红光波段量子点激光器以及红外探测器的有源区^[12,13],具有很好的应用前景和研究价值。但是由于 Al 组分的存在,使 InAlAs 量子点的尺寸明显超过 InAs 量子点,且均匀性也变差^[14],这就增加了 InAlAs 量子点材料的研究难度。因此,虽然围绕量子点材料的拉曼散射实验已有很多报道,但是在国内外文献中,对生长于 $Al_xGa_{1-x}As$ 材料上

InAlAs 量子点的拉曼研究还很少。本文中,我们利用拉曼散射的实验方法,结合 AFM 的测试结果,分析了不同淀积厚度 InAlAs 量子点材料自组织生长过程中结构的变化特征。

2 样品生长与实验

实验所用的样品均是在 Riber Compact21 MBE 设备上采用 S-K 生长模式制备的。具体结构为:在 GaAs(001)半绝缘衬底上,首先生长 200nm 的 GaAs 缓冲层,然后再生长 200nm 的 $Al_{0.3}Ga_{0.7}As$ 。有源区为生长在 AlGaAs 上的 5 层周期结构 InAlAs 量子点, $Al_{0.3}Ga_{0.7}As$ 隔离层厚度为 10nm。A、B、C 样品 InAlAs 层的淀积厚度 d 分别为 4ML、4.5ML 和 5ML (ML, monolayer)。通过控制恒定的 In 源束流,使 In 组分固定在 0.7 左右。InAlAs 量子点层 AlGaAs 隔离层的生长温度为 500℃,其余层的生长温度为 580℃。

在材料的生长过程中,利用反射高能电子衍射仪(RHEED)图形从线到点的转变来确定从二维层状生长到三维岛状生长的转变。对于我们生长的材料,这种转变发生在 InAlAs 覆盖厚度约 3.6ML 处。AFM 测试是在 DI Nanoscope4 型多功能扫描探针显微镜上进行的。我们利用 Renishaw RM2000 型微区拉曼光谱仪,采用背散射几何配置常温下测量了样品的拉曼散射谱,激发光源为 632.8nm 的 Ar⁺ 离子激光器。

3 结果与讨论

图 1 显示了三个样品的 AFM 形貌图。AFM 测试显示,A 和 B 样品量子点具有近似透镜的圆盘形状,而 C 样品的量子点接近椭球形。随着淀积厚度的增加,量子点的密度大幅度提升,其中,C 样品的密度达到 $1.1 \times 10^{11} \text{ cm}^{-2}$,为 A 样品的 10 倍左右。值得注意的是,三个样品相比较,B 样品具有比较好

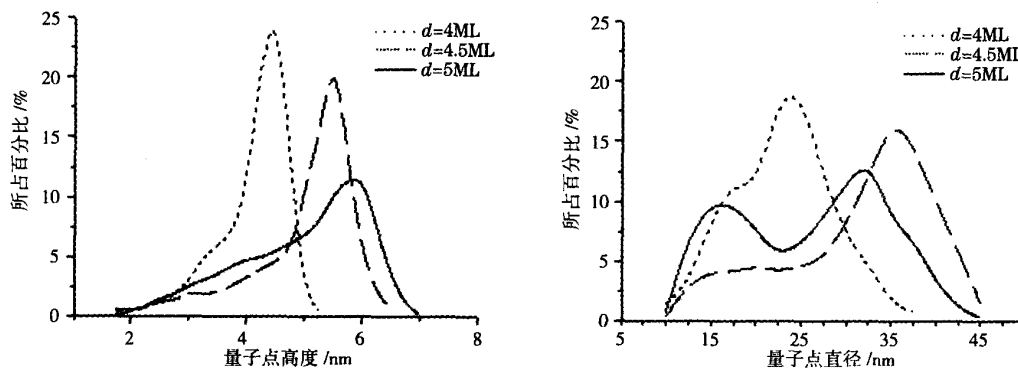


图 2 量子点高度(左图)和直径(右图)随淀积厚度的变化

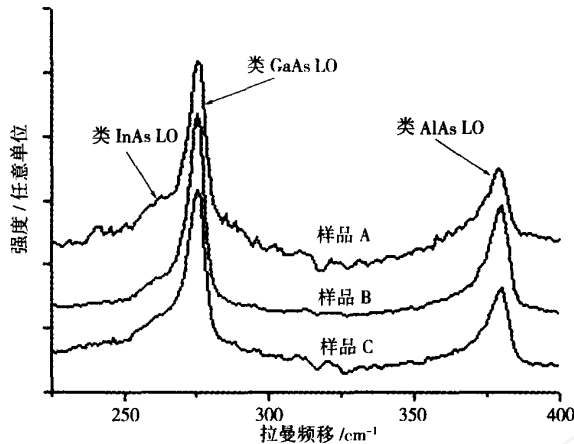


图 3 A、B、C 三样品的拉曼谱比较

的均匀性,而 C 样品中比较明显地出现了两种尺寸的量子点,图 2 为根据 AFM 图像统计的随淀积厚度不同,量子点高度和直径的变化情况。其中,在淀积厚度较大的 C 样品中,不同大小量子点的存在使量子点尺寸显示出双模分布的趋势。

通过分析以上数据,可以对 InAlAs 合金量子点的生长过程获得进一步的认识。在三维岛状生长的初始阶段,随着淀积厚度的增加,点的尺寸逐渐变大,密度也有小幅度增加,此时量子点仍呈近似透镜的圆盘形状。这一阶段内,由于刚刚超过临界厚度不久,量子点的尺寸普遍较小,依靠浸润层的应变积累,三维岛逐渐自组织成形并变大,岛的形成使成核位置附近的应变得到释放,也使得这些位置成为 InAlAs 优先淀积的区域^[10]。当 InAlAs 层达到一定厚度以后,量子点的横向尺寸变化不十分明显,但随着 InAlAs 的进一步淀积和 In 组分偏析的加剧,更多的 In 向邻近量子点扩散,原本较大的点间空隙部分开始获得更多的淀积元素,表现为外延层的增厚和更多成核中心的出现^[10],因此量子点密度得到大幅度提升。同时,一部分较小的量子点的出现,导致了量子点的不均匀分布,在图 2 中 C 样品出现了比

较明显的双峰现象。

图 3 给出了 Z (X,Y)Z̄ 退偏振条件下 C 样品的拉曼散射谱。在图中我们观察到两个主要的光学声子模,它们分别位于约 274cm⁻¹ 和 379cm⁻¹ 附近。考虑到背散射几何配置下 TO 模的禁忌,及 InAlAs 合金材料所具有的声子双模行为^[17], 379cm⁻¹ 处的拉曼峰应对应类 AlAs-LO 模。274cm⁻¹ 处强度较大的峰为类 GaAs LO 模,AlGaAs 层中 Al 组分的存在使其频率位置低于体材料 GaAs LO 模(295cm⁻¹)^[18]。注意到在该峰左侧有一强度相对微弱的肩峰(~261cm⁻¹),应来源于 QD 的类 InAs LO 模^[12,19]。与 InAs 体材料的 LO 模相比,拉曼谱中的类 InAs 声子模位置向高频方向发生了蓝移,这种较大幅度的频移符

合量子点材料的特征^[11,21],一般认为其主要来源是量子点内部的压应力作用。但在 InAlAs 量子点材料中,另一个需要考虑的原因是量子点边缘位置存在的界面原子迁移及由此引起的 In、Ga、Al 互混^[10]。在自组织生长过程中,某些材料区域(如隔离层/量子点界面等位置)甚至有出现四元混晶的可能。当然,量子点对声子的限域效应同样会对拉曼峰的位置产生影响,但与纯 InAs 量子点相比,由于 InAlAs 岛尺寸较大,这种影响要小得多。从图 3 中可见,不同淀积厚度的三个样品,拉曼峰的频率位置差异很小,这说明在 InAlAs 量子点材料中,三维岛形状变化引起限域效应的差异对拉曼谱的影响远小于混晶组分这一因素。

图 4 显示了随着淀积厚度的增加,谱线拉曼峰的半高全宽变化。由图可见在三个样品中 B 样品具有最窄的半高全宽(<1.0meV),而 A 样品和 C 样品与之相比出现不同程度的展宽。Zanelatto 等人^[9]认为,界面模的谱线特征与量子点边缘的形状差异及岛状结构的均匀性有关,可以认为,在类 GaAs 和类 AlAs 信号中,至少有部分来自于界面模声子的贡献,谱线半高全宽的变化来源于不同样品中 AlGaAs 隔层与三维岛之间界面声

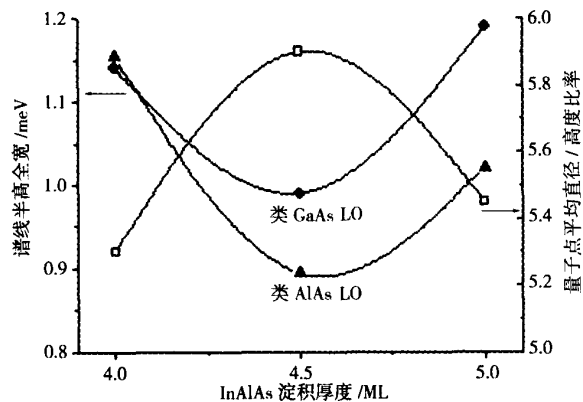


图 4 量子点尺寸纵横比以及谱线半高全宽随 QD 淀积厚度的变化

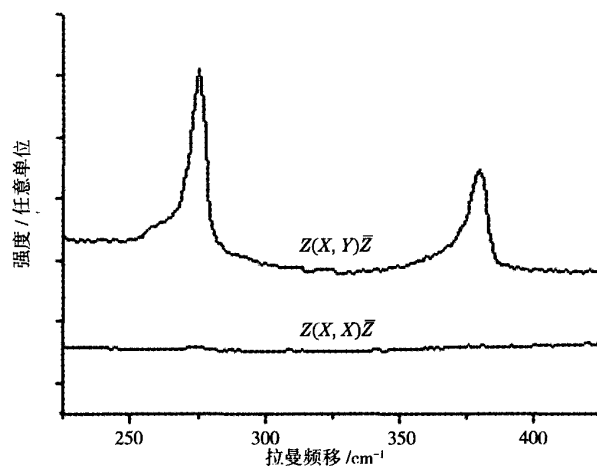


图5 不同偏振条件下的拉曼谱比较

子振动强度的差异。图4中另一条曲线反映的是不同InAlAs层厚下量子点尺寸纵横比(三维岛平均直径与平均高度之比)的变化。很明显,它和拉曼峰半高全宽变化具有恰好相反的趋势。这说明,从量子点底部到顶部的边缘界面越陡峭,其界面声子振动越明显,从而使拉曼峰出现展宽,这与Zanelatto等人的观点相一致。反之,对于形状

愈趋于扁平的量子点材料,界面束缚能级愈趋于单一,对应不同频率的散射跃迁几率就愈小。由于不同形状的量子点在各种器件应用中具有相异的性质,上述结果为我们提供了一种判断InAlAs/AlGaAs合金量子点材料中三维岛结构特征的方法。

此外,我们还研究了不同偏振条件下的拉曼散射结果。从图5中

可见,在 $Z(X,X)\bar{Z}$ 偏振条件下基本观察不到拉曼散射峰。这也证实了InAlAs合金量子点材料仍符合典型的闪锌矿结构半导体材料的基本特征,即在此种偏振条件下是非拉曼活性的。这与Artus L等人对InAs/GaAs量子点的研究结果^[12]相一致。

4 结论

使用分子束外延方法自组织生长了淀积厚度不同的InAlAs/AlGaAs量子点材料,并利用拉曼散射的方法对材料进行了研究。根据原子力显微镜的测试结果和拉曼谱图中量子点声子峰的半高全宽差异,详细讨论了量子点生长过程中尺寸、均匀性的变化,发现量子点尺寸的纵横比与拉曼峰半高全宽的变化趋势具有明显的关联性。此外,验证了InAlAs/AlGaAs量子点合金材料的光学声子在 $Z(X,X)\bar{Z}$ 偏振条件下为非拉曼活性。

参考文献

- 1 Rubin M E, Medeiros-Ribeiro G, O'Shea J J *et al.* Imaging and spectroscopy of single InAs self-assembled quantum dots using ballistic electron emission microscopy [J]. *Phys. Rev. Lett.*, 1996, **77**(26):5268-5271
- 2 Lin Y Y, Singh J. Self-assembled quantum dots: A study of strain energy and intersubband transitions [J]. *J. Appl. Phys.*, 2002, **92**(10):6205-6210
- 3 Lee C D, Park C, Lee H J *et al.* Formation of self-assembled GaAs/AlGaAs quantum dots by low-temperature epitaxy [J]. *Appl. Phys. Lett.*, 1998, **73**(2):2615-2617
- 4 Le D T, Morath C P, Norton H E *et al.* High responsivity, LWIR dots-in-a-well quantum dot infrared photodetectors [J]. *Infr. Phy. Techn.*, 2003, **44**(5):517-526
- 5 Moldavskaya L D, Shashkin V I, Drozdov M N *et al.* Infrared lateral photoconductivity of InGaAs quantum dot heterostructures grown by MOCVD [J]. *Phys. E*, 2003, **17**:634-635
- 6 Zhang J Z, Galbraith I. Intraband absorption for InAs/GaAs quantum dot infrared photodetectors [J]. *Appl. Phys. Lett.*, 2004, **84**(11):1934-1936
- 7 Menendez-Proupin E, Trallero-Giner C, Ulloa S E. Resonant Raman scattering in self-assembled quantum dots [J]. *Physical Rev. B*, 1999, **60**(24):16747-16757
- 8 Pusep Y A, Zanelatto A, Silva S W *et al.* Raman study of interface mode subjected to strain in InAs/GaAs self-assembled quantum dots [J]. *Phys. Rev. B*, 1998, **58**(4):1770-1773
- 9 Zanelatto G, Pusep Y A, Moshegov N T *et al.* Raman study of the topology of InAs/GaAs self-assembled quantum dots [J]. *J. Appl. Phys.*, 1999, **86**(8):4387-4389
- 10 Galzerani J C, Pusep Y A. Raman spectroscopy characterization of InAs self-assembled quantum dots. *Physica B*, 2002,

316-317:455-458

- 11 Groenen J, Mlayah A, Carles R *et al.*. Strain in InAs islands grown on InP (001) analyzed by Raman spectroscopy [J]. *Appl. Phys. Lett.*, 1996, **69**:943-945
- 12 Artus L, Cusco R, Hernandez S *et al.*. Quantum-dot phonons in self-assembled InAs/GaAs quantum dots: Dependence on the coverage thickness [J]. *Appl. Phys. Lett.*, 2000, **77**(22):3556-3558
- 13 徐波, 刘会口, 王占国等, 应变自组装 InAlAs 量子点材料和红光量子点激光器[J]. 固体电子学研究与进展, 2002, **22**(2):199-201
- 14 Zhongzhe S, Fengqi L, Ding D *et al.*. Self-assembled InAs and In_{0.9}Al_{0.1}As quantum dots on (001)InP substrates grown by molecular beam epitaxy (MBE) [J]. *J. Cryst. Growth*, 1999, **204**:24-28
- 15 Kim M D, Lee D H, Kim T W *et al.*. Formation process for and strain effect in InAs quantum dots grown on GaAs substrates by using molecular beam epitaxy [J]. *Solid State Commun.*, 2004, **130**(7):473-476
- 16 Zhuang Q D, Li J M, Zeng Y P *et al.*. Structural characterization of InGaAs/GaAs quantum dots superlattice infrared photodetector structures[J]. *J. Cryst. Growth*, 1999, **200**:375-381
- 17 Liu B L, Xu Z Y, Liu H Y *et al.*. Strong temperature dependence of photoluminescence properties in visible InAlAs quantum dots [J]. *J. Cryst. Growth*, 2000, **220**:51-55
- 18 Holtz M, Seon M, Brafman O *et al.*. Pressure dependence of the optic phonon energies in Al_xGa_{1-x}As [J]. *Phys. Rev. B*, 1996, **54**(12):8714-8720
- 19 Chu L, Zrenner A, Bichler M *et al.*. Raman spectroscopy of In (Ga)As/GaAs quantum dots [J]. *Appl. Phys. Lett.*, 2000, **77**(24):3944-3946

欢迎成为《中国光学期刊网》企业会员

为进一步提高服务水平,中国光学期刊网从 2006 年起在信息服务上实行会员制度,凡光电子、激光、光通信等相关的企业均可申请成为中国光学期刊网的企业会员,中国光学期刊网将为企业会员提供优质超值的专业服务。

一、会员企业享受的服务包括:

- 1) 企业名称在中国光学期刊网首页的会员企业栏目中出现,并链接到企业自己的网址。
- 2) 会员企业可获赠光学类期刊一份,全年 12 册,在《中国激光》《光学学报》《激光与光电子学进展》《Chinese Optics Letters》中任选一种。
- 3) 可免费在本站“特别推荐”栏目发布文字信息(含广告)10 条,每篇不过 2000 字。
- 4) 如在中国光学期刊网发布广告,可享受广告报价的 80% 优惠。
- 5) 优先或免费参加光学期刊网组织的各类学术和业务活动。
- 6) 可免费阅读本网站期刊全文 300 篇次。

二、会员义务:

1. 注册时向中国光学期刊网递交企业真实信息。
2. 每年交纳会员费 2800 元,会员资格从交费之日起计算,一年有效。
3. 不得将中国光学期刊网提供给会员的信息转给第三方使用。
4. 尊重并保护本网及论文作者的知识产权。
5. 在本网发布信息必须遵守中华人民共和国相关法律法规。

三、成为企业会员的步骤:

- ① 注册成为中国光学期刊网的一般用户,也可以直接填写广告投放申请表单,说明您的意向。
- ② 来信 mail@opticsjournal.net 告知您已经注册成功。并请告知选择何种期刊及收刊地址、联系人。
- ③ 银行汇款 2800 元至下列帐户:
开户行:工商银行上海嘉定支行营业部 户名:中国科学院上海光学精密机械研究所
帐号:1001700809026400195
- ④ 联系人:郑继承; 电话:021-69918253; Email:expert@mail.siom.ac.cn



1 器件原理

图 1 显示了典型的 OPS-VECSEL 结构示意图,其核

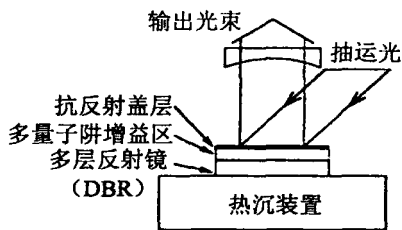


图 1 OPS-VECSEL 结构示意图

心部分是包含多量子阱增益区和多层分布反馈布拉格反射镜 (DBR) 增益结构的激光谐振腔。为使模斑尺寸能适应腔内每个工作组件的大小需要,谐振腔可被设计成 V 形、Z 形或 W 形等多种形式。如图 1 所示,入射抽运光聚焦至 VECSEL 芯片上,在高反射率的 DBR 镜和外部球面镜之间形成激光振荡,多量子阱提供增益,外镜控制激光器在单横模下工作。

图 2 显示了 VECSEL 谐振腔内有源区的能带图,

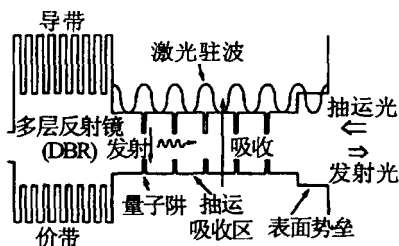


图 2 典型 OPS-VECSEL 有源区的能带图

展示了激光器工作原理。这个结构类似于 VCSEL,但是要将其中一个 DBR 反射镜替换成透明的窗口层。工作区由一系列周期性的量子阱结构将势垒层分开,每个周期厚度为半波长。量子阱置于激光驻波的波腹,形成谐振的周期增益结构。抽运吸收区的势垒层通过带间跃迁吸收入射光,产生的电子和空穴扩散至量子阱并被其俘获,提供激光器的光增益。最右侧的

AlGaAs 窗口层接收入射光,并提供了一个更高的表面势垒,阻止载流子扩散到芯片表面而发生无辐射复合。紧邻着量子阱的高反射率多层 DBR 反射镜作为激光器的一个腔镜,一般要求其最大反射率达到 99% 以上。

2 OPS-VECSEL 研究进展

2.1 不同波长范围与材料体系的 VECSEL

对 OPS-VECSEL 而言,激光器工作波长和抽运波长能根据设计选择。几种成熟的半导体材料体系,如 InGaAs-AlGaAs-GaAs^[2], InGaAs-InGaAsP-GaAs^[3] 和 InGaAsP-InP^[4],都可以用来制造不同波长的激光器。

多数 VECSEL 都是在 GaAs 衬底上制作,使用高折射率比值的 GaAs/AlAs 反射镜,用于近红外方面的应用。这些激光器主要工作在两个波长段:使用晶格匹配 GaAs/AlGaAs 量子阱的激光器,工作波长为 850nm 左右^[5];使用压应变 InGaAs/GaAs 量子阱的激光器,波长在 1000nm 附近^[6]。但最近的报道显示,其它材料体系的 VECSEL 可实现从红外到可见光的不同波长范围的应用。

红光 VECSEL 已有报道,它使用应变 InGaP 量子阱,带有一个 AlGaInP DBR,以 660nm 绿光氩离子激光器作为抽运源,可以输出超过 200mW 功率的光束^[7]。紫光输出也由 PARK 等人^[8]实现,他们的器件使用 GaN 基材料,带有一个蓝宝石谐振腔,实际上构成了一个微腔 VECSEL,该激光器在室温下输出 391nm 的激光。

以 InP 为衬底可制造工作波长在 1.5μm 附近的器件。在这个材料体系里,VECSEL 遇到了与 VCSEL 同样的难题:由于波长较长,DBR 各层的折射率也会有所降低,要求反射镜厚度更大;并且在这种结构的材料中,吸收和散射不能忽略,反射镜的总反射率就会受到影响。近年来,生长技术的提高推动了高反射率和低电子阻抗 InP/InAlGaAs DBR 的发展,利用这种工艺

表 1 VECSEL 工作波长范围及其结构特征

λ / 衬底	DBR	量子阱	功能特性
391nm	介电 SiO ₂ / HfO ₂	InGaN / GaN	335nm 三倍频 Nd:YAG 激光器抽运 ^[8]
660nm (GaAs)	AlGaInP	InGaP	514nm 氩离子激光器抽运 ^[7]
670nm (GaAs)	AlGaAs	InGaP / InGaAsP / GaAs	532nm Nd:YAG 激光器抽运 ^[3]
850nm ~ 870nm (GaAs)	AlAs / AlGaAs	GaAs / AlGaAs	670nm LD 抽运大功率 ^[5] 660nm Kr ⁺ 激光器为抽运源 ^[12]
960nm ~ 1030nm (GaAs)	AlAs / AlGaAs	InGaAs / GaAs	808nm LD 抽运 ^[13] SESAM 锁模 大功率 ^[2] 发射近 500fs 的孤子波 ^[14]
1.3μm	AlAs / GaAs	GaInAs / GaAs	810nm LD 抽运源、大功率 ^[10]
1.5μm (InP)	InAlAs / GaInAs InP / InGaAs	InGaAs / InGaAsP InGaAsP	980nm LD 抽运 ^[9] SESAM 锁模 ^[4]
2.3μm (GaSb)	GaSb / AlAsSb	GaInAsSb AlGaAsSb	室温下 830nm LD 抽运 ^[11]

可制造出均匀的 VECSEL 增益结构,并成功地在 7°C 温度下连续工作^[19]。总体来说,与 GaAs 器件相比, InP 器件具有低的特征温度和高的热阻,受到更为严格的热问题限制。近来,以稀氮四元化合物 GaInNAs 为基础的 1.3 μm 激光器设计也已得到发展并成功实现,其 1.3 μm 波长的连续输出功率达 0.6W^[10]。

在长波长范围, CERUTTI 等人^[11]报道了工作在 2 μm ~2.5 μm 波段的 GaSb 基 VECSEL。这种波长的激光器因对 CH₄ 和 CO 等污染物有强烈的吸收峰,在大气探测方面有较高的应用价值。他们研制的光抽运 VECSEL 激光器可以在 350K 温度下连续运转,工作波长为 2.3 μm ,室温下最大输出功率为 7mW,特征温度为 70K,入射抽运的阈值强度为 800W/cm²。

表 1 中列出了现有报道的 VECSEL 的工作波长范围,以及每个装置中量子阱和反射镜的结构及功能特性。

2.2 大功率 OPS-VECSEL 的研究

1997 年, KUZNETSOV 的小组第 1 次实现了以二极管激光器抽运产生大功率和高质量光束的 VECSEL^[11],工作波长为 980nm。其结构为:在最顶端使用 30 对 Al_{0.8}Ga_{0.2}As/GaAs 多层镜面作为反射镜;增益区由 Al_{0.08}Ga_{0.92}As 抽运吸收层,和 8nm 厚的位于光驻波波腹位置的压应变 In_{0.16}Ga_{0.84}As 量子阱组成 (13 对)。该激光器在 TEM₁₁ 模式的输出功率为 0.69W;与单模光纤耦合,在 TEM₀₀ 模式下输出功率为 0.37W。HOLM 等人^[15]以 AlGaAs/GaAs 晶格匹配材料为基础,研制了工作波长为 870nm 的 VECSEL。相对于应变 InGaAs/GaAs 系统,这个量子阱结构系统表现出较低的分增益和特征温度相关性。由一对极化耦合 670nm 二极管提供 850mW 功率的抽运能量,实现了 0.15W 的输出功率。

ALFORD 等人^[15]提出了将热量从工作区通过 DBR 直接释放的技术,有效地提高了激光器的输出功率。他把一个无镀层的蓝宝石窗口与 VECSEL 增益部分的前表面相连,蓝宝石起热扩散平板作用。利用该技术,其 985nm 的 InGaAs/GaAs VECSEL 抽运区域直径达到 500 μm 以上,实现了最大功率为 1.6W 的连续输出。HASTIE 等人^[3]将热扩散平板技术应用到 850nm 的 GaAs/AlGaAs VECSEL,使用 SiC 代替蓝宝石作为热扩散平板,观察到在 TEM₀₀ 模式下的最大输出功率是 0.5W。此后的工作中,他们还报道了一台使用 810nm 波长光纤耦合激光器作为抽运源,微片温度维持在 20°C 的 InGaAs/GaAs VECSEL,获得了功率 1.7W、波长 980nm 的输出光。将微片冷却到 0°C 后,激光器输出功率增加到 2.5W,光斑为圆形对称分布。

最新的研究成果已体现出 OPS-VECSEL 达到更高

功率的潜力。LUTGEN 等人^[2]报道使用一个 808nm 光纤耦合二极管激光器做为抽运源的 InGaAs/GaAs VECSEL 工作波长为 1 μm 。由于外延生长的高质量、高精度、低散射损失和高有效增益,最大输出功率达到了 8W,光-光转换总效率达到了 41%。CHILLA 等人^[16]使用 InGaAs/GaAs 有源区制成波长为 980nm 的 VECSEL,它使用 3 台光纤耦合二极管激光器组成阵列,可向增益结构输入 70W 的净抽运能量,抽运光的光斑直径在 500 μm ~900 μm 之间变化,输出功率达迄今为止最高的 30W。

2.3 超短脉冲发生的 SESAM 锁模 VECSEL

锁模 VECSEL 可以作为超短脉冲的高质量和高平均功率光谱源,脉冲仅传播几微米厚度,避免了强烈的色散和自相位调制,因而成为研究的热点。VECSEL 锁模的早期研究是在 100MHz 重复频率的锁模抽运源同步抽运基础上进行的,例如 Nd:YAG 或 Ti³⁺:Al₂O₃ 激光器。第 1 台脉冲主动锁模 VECSEL^[5]由常用的二极管激光器连续抽运,长腔具有 168MHz 往返频率,在二次谐波频率 336MHz 处锁模,观测到持续时间达 100ps~120ps 的脉冲。

现在出现了一种非常简单的锁模激光器,就是通过半导体饱和吸收镜 (SESAM) 将 VECSEL 被动锁模,产生超短脉冲,其结构示意图如图 3 所示。第 1 台

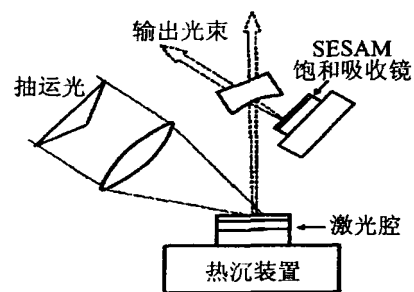


图 3 SESAM 锁模 VECSEL 结构示意图

SESAM 锁模 VECSEL 由 HOOGLAND 等人^[13]设计实现,其使用 InGaAs/GaAs 增益结构,发射波长为 1000nm~1040nm。SESAM 锁模增益结构位于一个不对称的 V 形腔末端,由一个 $\lambda/2$ 抗谐振腔和 20nm 厚 In_{0.2}Ga_{0.8}As 量子阱构成。SESAM 大约会产生 1.3% 的低强度损耗,响应时间分为两部分,包括 130fs 的快速响应时间和 4ps 的慢恢复时间。腔内工作一个来回的重复频率为 4.4GHz,与纳秒级别的载流子寿命相适应。该激光器脉冲为双曲正割自相关的形状,半峰全宽 (FWHM) 为 22ps。HÄRNG 等人^[17]报道了平均输出功率超过 200mW、发射波长为 963nm 的 InGaAs/GaAs VECSEL,发射近转换极限脉冲的 FWHM 为 3.2ps。他们随后又研制了平均输出功率达 950mW 的 952nm 激光器,脉冲重复频率为 6GHz^[18]。当处于最

高输出功率时,输出脉冲变得相当长,具有双曲正割形状,FWHM为15.3ps。

近几年,一些更新颖的技术也开始应用于SESAM的研究,提高了激光器的性能。例如,GARNACHE等人^[14]采用了具有快速非线性响应量子阱吸收结构的SESAM,获得了1030nm波长的VECSEL,得到重复频率为1.2GHz,接近转换限制的477fs准孤子脉冲。另一些研究中,锁模VECSEL的饱和吸收装置使用自组织InAs/GaAs量子点,获得了比量子阱系统更宽的吸收曲线和更均匀的光谱特性,显示出良好的前景。

3 OPS-VECSEL的发展方向与展望

OPS-VECSEL的研究工作在许多新的方向可以被丰富地拓展,这种激光器在未来很有可能被广泛地应用于多种用途。最重要的两个突破点仍然是VECSEL的高性能和小型化。

由于OPS-VECSEL腔内功率高,腔内倍频会有很高效率。采用多抽运和增益元件,激光器能达到数瓦的输出功率,同时具有优异的光束质量。使用可调的外部光栅或微观结构镜,有望实现激光器的可调大功率工作。这样,VECSEL无疑会在要求衍射极限光束质量和大功率高效光源方面的应用大受欢迎。进一步研究饱和吸收装置,将很可能实现锁模OPS-VECSEL在更大功率量级下工作。除此之外,OPS-VECSEL在其它波长和材料体系的工作也应该进一步探索研究,例如,波长为1550nm的InGaAsP/InP激光器、使用铋化物半导体材料的中红外激光器、AlInGaP/GaAs红光激光器、蓝色到紫外的AlInGaP/GaN激光器,等等。

另一方面,为了OPS-VECSEL的商品化,要求高效、小型化和更可靠的封装。在小型化超快脉冲源领域,VECSEL具有相当大的发展潜力。注入抽运通过精细的晶片设计,实现介质功率器件的优化,有可能制造带有复杂谐振腔的高度小型化的VECSEL设备。OPS-VECSEL集成外腔是一种非常理想,也有可能实现的结构,集成抽运激光器的可能性也值得进一步探讨。在这些集成结构中,反射镜将与增益结构整合,结合其它非线性和光谱滤波功能,将有望发展出带有高级功能的超小型器件。

参 考 文 献

- [1] KUZNETSOV M, HAKMI F, SPRAGUE R *et al* High power (>0.5W CW) diode-pumped vertical-external-cavity surface-emitting semiconductor lasers with circular TEM₀₀ beams [J]. IEEE Photonics Technology Letters, 1997, 9(8): 1063~1065.
- [2] LUTGEN S, ALBRECHT T, BRICK P *et al* 8W high-efficiency continuous-wave semiconductor disk laser at 1000 nm [J]. A P L, 2003, 82(21): 3620~3622.
- [3] HASTIE J E, CALVEZ S, DOWSON M D. High power CW red VECSEL with linearly polarized TEM₀₀ output beam [J]. Optics Express, 2005, 13(1): 77~81.
- [4] HOOGLAND S, GARNACHE A, SAGNES I *et al* Picosecond pulse generation with 1.5pm passively mode-locked surface-emitting semiconductor laser [J]. Electron Lett, 2003, 39(1): 846~847.
- [5] HOLM M A, BURNS D, CUSUMANO P *et al* High-power diode-pumped AlGaAs surface-emitting laser [J]. Appl Opt, 1999, 38(27): 5781~5784.
- [6] KUZNETSOV M, HAKMI F, SPRAGUE R *et al* Design and characteristics of high-power (0.5W CW) diode-pumped vertical-external-cavity surface-emitting semiconductor lasers with circular TEM beams [J]. IEEE Journal of Selected Topics in Quantum Electronics, 1999, 5(3): 561~573.
- [7] LINDER N, KARNUTSCH C, LUFT J *et al* High power 660nm optically pumped semiconductor thin disk laser [A]. IEEE/LEOS Summer Topics [C]. Ingenieria: IEEE, 2002. 5~6.
- [8] PARK S H, KM J, JEON H *et al* Room-temperature GaN vertical-cavity surface-emitting laser operation in an extended cavity scheme [J]. A P L, 2003, 83(11): 2121~2123.
- [9] SYMONDS C, SAGNES I, GARNACHE A *et al* Continuous-wave operation of monolithically grown 1.5μm optically pumped vertical-external-cavity surface-emitting lasers [J]. Appl Opt, 2003, 42(33): 6678~6681.
- [10] HOPKINS J M, SMITH S A, JEON C W *et al* 0.6W CW GaInAs vertical external-cavity surface emitting laser operating at 1.32μm [J]. Electron Lett, 2004, 40(1): 30~31.
- [11] CERUTTIL, GARNACHE A, GENTY F *et al* Low threshold, room temperature laser diode pumped Sb-based VECSEL emitting around 2.1μm [J]. Electron Lett, 2003, 39(3): 290~292.
- [12] HASTIE J E, HOPKINS J M, CALVEZ S *et al* 0.5W single transverse-mode operation of an 850nm diode-pumped surface-emitting semiconductor laser [J]. IEEE Photonics Technology Letters, 2003, 15(7): 894~896.
- [13] HOOGLAND S, DHANJAL S, TROPPER A C *et al* Passively mode-locked diode-pumped surface-emitting semiconductor laser [J]. IEEE Photonics Technology Letters, 2000, 12(9): 1135~1137.
- [14] GARNACHE A, HOOGLAND S, TROPPER A C *et al* Sub-500-fs soliton-like pulse in a passively mode-locked broadband surface-emitting laser with 100mW average power [J]. A P L, 2002, 80(21): 3892~3894.
- [15] ALFORD W J, RAYMOND T D, ALLERMAN A A. High power and good beam quality at 980nm from a vertical external-cavity surface-emitting laser [J]. J O S A, 2002, B19(4): 663~666.
- [16] CHILLA J, BUTTERWORTH S, ZEITSCHEL A *et al* High power optically pumped semiconductor lasers [J]. Proc SPIE, 2004, 5332: 143~150.
- [17] HÄRNG R, PASCHOTTA R, GNIE *et al* Picosecond surface-emitting semiconductor laser with >200mW average power [J]. Electron Lett, 2001, 37(12): 766~767.
- [18] HÄRNG R, PASCHOTTA R, ASCHWANDEN A *et al* High-power passively mode-locked semiconductor lasers [J]. IEEE J Q E, 2002, 38(9): 1268~1275.